A theory of seismic wave propagations

—To decipher seismic waveforms—

Kiwamu Nishida

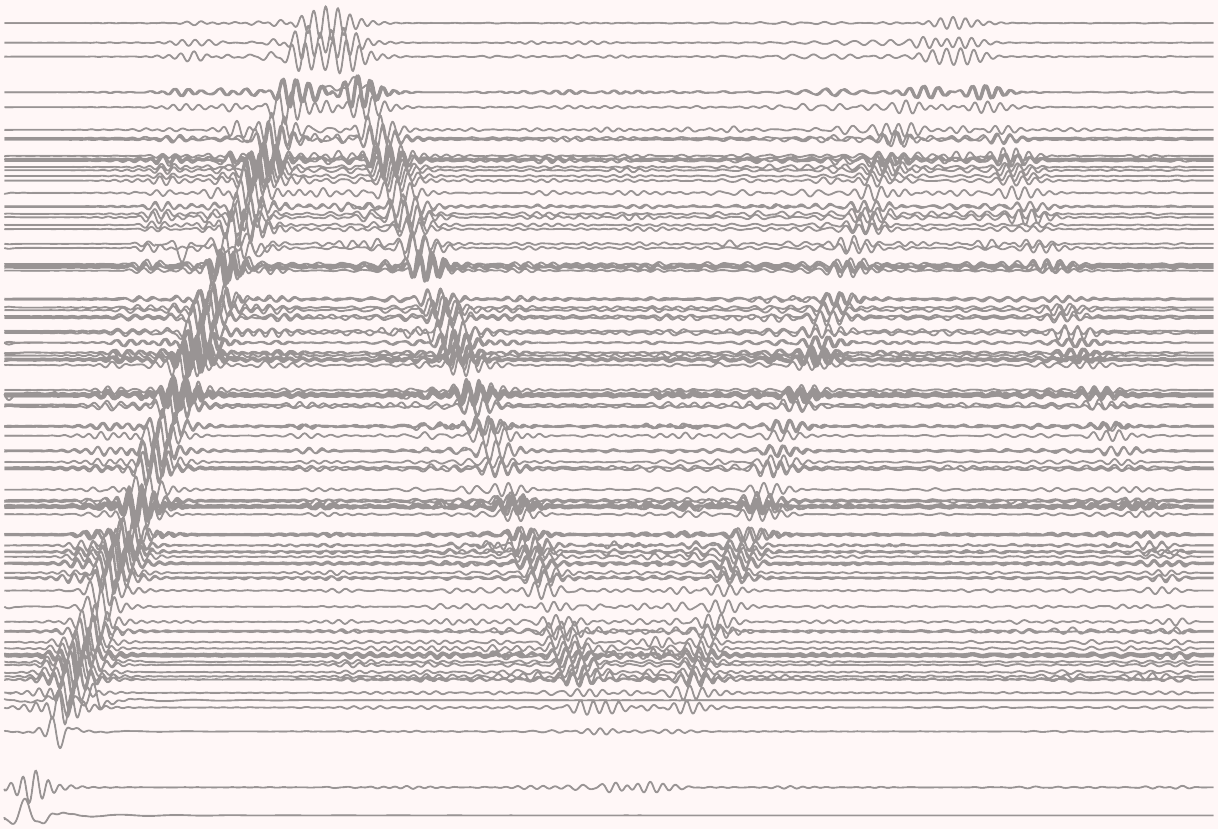

March 24, 2026

The waveform on the cover is a broadband observation record of the 2010 Maule earthquake in Chile. Rayleigh waves circulating the Earth can be seen. See Chapter 8 for details.

Suggested Citation
Kiwamu Nishida (2026), *A theory of seismic wave propagations —To decipher seismic waveforms—*, Lecture Notes (Draft),
Available at: https://www.eri.u-tokyo.ac.jp/people/knishida/eng/seismology.html

Contents

Introduction

Chapter 1

There are many different fields of research in this world. When we study a new research field, what is the most rewarding aspect? Of course, there is no right answer to this question. However, if I were to venture a guess, I would say it is the new perspective that changes how we view the world. For example, let us say you learn about geology. You will discover that you can decipher millions of years of history from geological clues in a landscape you have never previously paid attention to. The act of observation is not as simple as it seems; rather, the act of observing itself already involves an implicit modeling of how one perceives nature. Therefore, it is impossible to avoid viewing phenomena through the lens of a particular model. This lecture covers a branch of geophysics. How does geophysics expand our horizons?

Physics is the study of symmetry and universality. In geophysics, we observe physical information about the Earth and extract knowledge from it. Symmetry and universality serve as crucial criteria for interpretation. Consider a situation where the data seem too complex to understand. Even in such a case, once we recognize the governing laws, previously unseen symmetries may unexpectedly emerge. If you appreciate this approach, the observed phenomena can appear as beautifully intricate as a kaleidoscope. But if you do not understand the underlying theory, they will just look like a mess.

Let us imagine a scene where the wind creates ripples on the surface of a river. If you have a basic understanding of the physics of water waves, you can observe the dispersion of the waves and see how they change depending on the water depth. If there is a current in the river, you can also observe its effect on wave propagation. Suppose that there is a duck swimming in the river (Fig. 1.1). First, you might notice that the duck is swimming faster than the wave speed, thereby creating a shock wave. You may also notice that the wedge-shaped wavefront behind the duck is not a straight line as expected for a simple shock wave. This distortion occurs because the group velocity differs from the phase velocity (due to dispersion), causing the wave shape to change continuously. Then you might also notice that the angle formed by the wedge-shaped wake behind the duck remains constant regardless of the swimming speed. Thus, with some background in physics, you will be able to decipher information about the waves step by step. The purpose of this lecture is to learn the physical foundation necessary to interpret such wave information.

In this chapter, I will first explain what seismology deals with and then discuss the importance of understanding seismic wave propagation in this context. This is followed by an overview of

Figure 1.1: Waves made by ducks. Such waves are generally called wake waves, and the ripples are described by the Kelvin pattern.

what is covered in seismic wave theory.

§1.1 How to interpret waveforms of recorded seismograms

In this section, we review briefly the basics of seismic wave propagation.

Seismology[note 1)] does not solely cover research on earthquakes but also generally encompasses **seismic** wave propagation within the Earth. Broadly speaking, we can categorize the research areas of seismology into two main fields. The first is **how geophysical phenomena excite seismic waves**. From the observed seismic records, seismologists infer physical processes such as earthquakes, volcanic activity, and landslides[note 2)]. The second field is the **seismic exploration**

[note 1)] The term "seismology" originated from ancient Greek ($\sigma\epsilon\iota\sigma\mu\acute{o}\varsigma$ (seism*ós*, "earthquake") and $\lambda o\gamma\acute{\iota}\alpha$ (-log*ía*, "study of").

[note 2)] Of course, other disciplines such as geology and geochemistry are also crucial for understanding earthquakes and

https://www.eri.u-tokyo.ac.jp/people/knishida/eng/seismology.html

of the Earth's interior.

When we observe a natural phenomenon, we implicitly assume a model. For example, most seismologists historically focused on "earthquake" data. Of course, the "earthquake" itself as a faulting process is an important topic, and the "earthquake" also illuminates the Earth's interior. Seismologists, therefore, recognized the seismic wavefield excited by an "earthquake" as a signal, whereas they treated the seismic wavefield excited by other phenomena—including ocean swells, human activities, and so on—as noise. Depending on the explicit or implicit model adopted, we call a phenomenon described by the model a signal, and vice versa. What is "noise" to someone could be a "signal" to others.

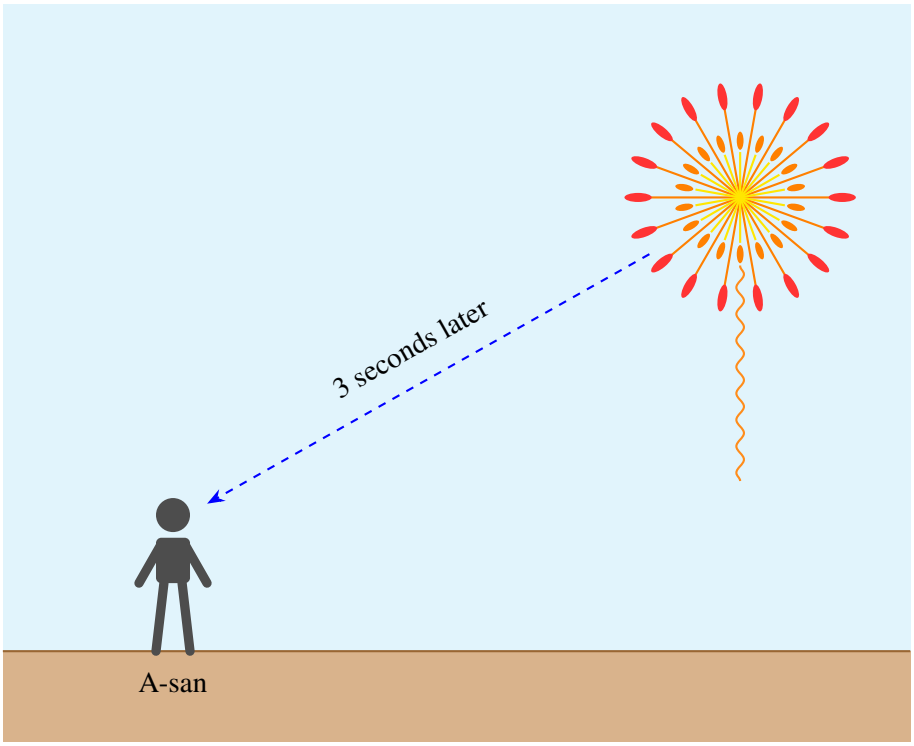

Figure 1.2: Schematic figure of seismic wave field at an instance excited by an earthquake. We can see the concentric shape, which shows the propagation.

Here we consider a simple example. When enjoying fireworks on a summer night, we often notice the lag time between the visual flash and the sound of the explosion. This lag originates from the difference in propagation speeds between light and sound (Figure 1.2). This situation is similar to the seismic wave field of P- and S-waves: P-wave corresponds to light, and S-wave corresponds to sound. One can infer the distance between the observer and the firework by the lag. This estimation uses the same principle as locating the hypocenter of an earthquake from seismograms. When we know the distance in advance, we can infer sound velocity from the measured lag time. This method has also played an important role in understanding the Earth's

volcanic activities.

interior. Seismic waves travel fast in hard materials and slowly in soft materials. Therefore, seismic waves generated by an earthquake reach the observation point earlier if they travel through hard regions, and later if they travel through soft regions. From this difference in arrival times, we can investigate which parts of the Earth's interior are hard and which are soft. In fact, many studies have been conducted to estimate the Earth's internal structure using numerous seismic waveforms.

For seismological investigations, the theoretical background of seismic wave propagation is indispensable. Looking back at the history of seismic observation, seismometers were sparsely distributed in space but recorded data continuously over time. By utilizing these observational data ingeniously, seismologists have studied seismic phenomena and the Earth's internal structure. In recent years, however, geophysics, including seismology, has experienced an explosion in data volume. In fact, observations with more than 1,000, or even 10,000 seismic sensing nodes have become a reality. Furthermore, new measurement technologies that capture wavefields spatially, such as Distributed Acoustic Sensing (DAS), have emerged. The question of what insights can be gained from observing the entire wavefield continuously in space will be a crucial perspective for the future of seismology. In order to fully leverage these new spatial observation data, it will become increasingly important to acquire the physical foundations for understanding seismic wavefields.

In this lecture, I will introduce a **systematic framework for interpreting seismic wavefields**.[note 3)].

In the last ten years, numerical methods for calculating seismic wavefields in a 3-D heterogeneous medium have become common. As numerical computation methods become more sophisticated, the entire analysis often tends to become a black box. However, even if one can reproduce the wavefield strictly numerically, it cannot be said to be truly understood without the ability to physically decode it. In a sense, the fundamentals of seismic wave theory have become even more critical. The primary aim of this lecture is to equip you with the fundamental physical intuition required to understand such seismic waves.

§1.2 Outline of this lecture

In Chapter 3, I will introduce Green's function for understanding wave propagation in an infinite medium. Then, I will explain the representation theorem as a generalization of Huygens' principle. These provide us with a foundational framework for understanding wave propagation.

Chapter 4 explains how the excitation of seismic waves can be represented based on the representation theorem. Without delving deeply into the physics of the seismic source, I will explain how the seismic source process can be represented as an equivalent force system.

As a first step to understanding wave propagation in a realistic medium, we will review the

[note 3)] Research on seismic wave propagation has historically developed as a branch of applied mathematics. For example, Jeffreys, who is famous for the reference 1-D structure (Jeffreys and Bullen), is also known as a great applied mathematician (e.g., WKBJ approximation and Bayesian statistics). Although classic textbooks of seismology focus on techniques using complex analysis to calculate waveforms, this lecture emphasizes a more intuitive explanation.

https://www.eri.u-tokyo.ac.jp/people/knishida/eng/seismology.html

effects of a free surface in Chapter 5. Reflections and conversions are key to this understanding. In general, a wave propagation problem in a semi-infinite medium is known as Lamb's problem. Under certain conditions, analytic formulations can be obtained. The Rayleigh wave fundamentally originates from the effects of the free surface.

Next, in Chapter 6, we will consider wave propagation in a two-layer medium. First, reflections and transmissions at the internal boundary will be analyzed. Based on this framework and our knowledge of reflections and refractions, we will interpret the wave propagation of direct waves, head waves, and reflected waves in a two-layer medium. Love waves can exist in a two-layer medium, although they cannot exist in a simple semi-infinite homogeneous medium.

Chapter 7 describes ray theory, which is a vital framework for understanding complex elastic wave propagation in a multi-layer medium. The theory originated from optics, and its mathematical and physical treatments have been firmly established.

In Chapter 8, Normal Modes, I will explain how to treat the seismic wavefield as a superposition of standing waves by viewing the entire Earth as a single finite system. Similar to the relationship between the frequency domain and the time domain, this is not a completely independent topic from what is discussed up to Chapter 7, but rather provides a **different perspective**.

Chapter 9 briefly discusses waves in fluids. While waves in fluids and solids are often studied separately, in reality, there are many phenomena that require treating the solid Earth, oceans, and atmosphere as a single coupled system. For example, the 2022 eruption of the Hunga Tonga-Hunga Ha'apai volcano is still fresh in our memories. This chapter will provide a simple conceptual guide for understanding such coupled phenomena.

In the final Chapter 10, we will learn about seismic interferometry as an application. Since this lecture emphasizes the fundamentals, the focus will mainly be on its theoretical background and necessary assumptions.

§1.2 Textbooks

Dahlen and Tromp (1998)[2] and Aki and Richards (2009)[1] are standard textbooks in the field of seismic wave propagation. Mathematical approaches in a more intuitive manner are given in Snieder and Wijk (2015).[4] Saito (2009)[3] is also an excellent textbook in this area, but it is written in Japanese.

§1.3 Bibliography

[1] K. Aki and P.G. Richards. *Quantitative Seismology*. Univ Science Books, 2nd edition, 2009.

[2] F.A. Dahlen and J. Tromp. *Theoretical Global Seismology*. Princeton University Press, Princeton, 1998.

[3] Saito Masanori. *Seismic Wave Theory*. University of Tokyo Press, 2009.

[4] Roel Snieder and Kasper van Wijk. *A Guided Tour of Mathematical Methods for the Physical Sciences*. Cambridge University Press, 3 edition, 2015.

Equations for the elastic Earth

Chapter 2

In this chapter, I summarize the governing equations of an elastic medium. For a deeper understanding, please refer to *Theoretical Global Seismology* by Dahlen and Tromp.[1]

§2.1 A microscopic model for Hooke's law

For a better understanding of P- and S-wave propagation in an elastic medium, let us consider a simple mass-spring model. In particular, for S-wave propagation, a **cross spring** is important.

2.1.1 1-D case

Restoring force (stress) against deformation in an elastic medium causes seismic wave propagation. First, let us consider a 1-D case for simplicity. Figure 2.1 shows an example where masses (with mass m) are connected by springs (with spring constant k).

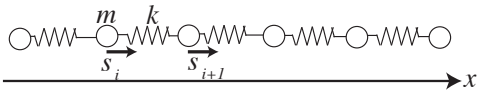

Figure 2.1: A 1-D mass-spring model.

The equations of motion can be written by

$$m\frac{\partial^2 s}{\partial t^2} = k(s_{i+1} - 2s_i + s_{i-1}). \tag{2.1}$$

The right-hand term is the second-order finite difference of s. If the spatial interval of mass Δx is small enough, in the limit of a continuum, the equation becomes a wave equation as,

$$\frac{m}{\Delta x}\frac{\partial^2 s}{\partial t^2} = (k\Delta x)\frac{\partial^2 s}{\partial x^2}, \tag{2.2}$$

where $m/\Delta x$ represents the density ρ, and $k\Delta x$ represents the elastic modulus κ. Here κ satisfies the relation $\kappa = \rho c^2$ between ρ and the wave speed c. The wave equation can be rewritten by

$$\rho \frac{\partial^2 s}{\partial t^2} = \kappa \frac{\partial^2 s}{\partial x^2}. \tag{2.3}$$

Since strain E is given by $E = \frac{\partial s}{\partial x}$, the stress T is written by $T = \kappa E$. Therefore, the wave equation

$$\rho \frac{\partial^2 s}{\partial t^2} = \frac{\partial T}{\partial x} \tag{2.4}$$

can be interpreted by the equations of motion of the elastic body. Because the direction of particle motions coincides with the propagation direction, in this case, the wave corresponds to a P wave. Details will be explained in the next chapter.

2.1.2 2-D case: P and S waves

The P wave propagates faster than the S wave. The travel time difference is crucial for locating the hypocenter of an earthquake (e.g., the Omori formula[note 1)]). An earthquake early warning system forecasts the arrival of the large S wave using the preceding P wave arrivals. Why is the P wave faster than the S wave?

First, to understand the properties of a P wave, let us consider a thought experiment as illustrated in Figure 2.2. Initially, imagine a thin uniform sheet where uniform pressure is applied from its surroundings, causing it to shrink uniformly. Since a P wave is a wave where compressed and expanded regions propagate alternately, let us align these compressed and decompressed thin sheets adjacent to each other. However, to make this a continuous deformation of a P wave, they must be welded together without any gaps at the boundaries. At these interfaces, additional forces perpendicular to the propagation direction must be applied to resolve the discontinuous deformation. This **boundary correction** is exactly the shear deformation that corresponds to an S wave. At first glance, **it might seem that a P wave is composed only of expansion and compression**, but it is crucial to note that it actually involves shear deformation in addition to fluid-like volumetric change. The reason a P wave shows a stiffer response and propagates faster than an S wave can be interpreted as this additional rigidity associated with the volumetric change.

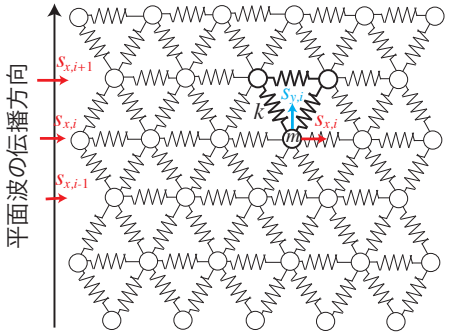

Figure 2.3: A 2-D mass-spring model.

Let us extend the 1-D mass-spring model to a 2-D one. "Cross-springs" are crucial for representing S-wave propagation in a 2-D case. Here we consider a simple model as shown in Figure 2.3.

First, let us consider a plane wave propagation of the S wave in the y direction. The displacement does not depend on x. The i-th mass is moved with displacement s_{xi} in the x direction.

note 1) You can find the paper[8] at http://hdl.handle.net/2261/32677.

(1) Apply pressure p from all sides

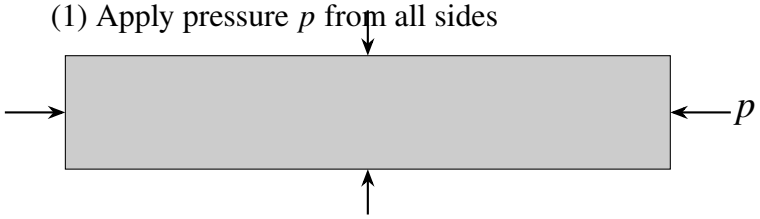

(2) Contracts due to pressure

(3) Arranged alternately with decompressed regions to model P-waves.
Displacement occurs between the layers.

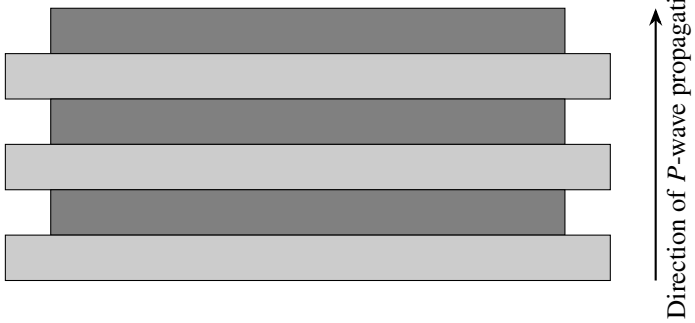

(4) Bonding the boundaries induces shear forces to counteract the displacement.
This makes the material stiffer.

Figure 2.2: Deformation of the medium associated with P-wave propagation.

The spring shown by the thick line in the Figure exerts restoring force T^S to the mass m. T^S can be written as,

$$T_i^S = \frac{1}{2}k(s_{x,i+1} - s_{x,i}). \tag{2.5}$$

Because the lower spring also exerts restoring force to the mass, the total restoring force is $T_i^S - T_{i-1}^S$. Then we obtain a discretized wave equation.

Next, let us consider P-wave propagation. The displacement does not depend on x. The ith mass is moved with displacement s_{yi} in the y direction. The spring shown by the thick line in the Figure exerts restoring force T^P to the mass m. T^P in the x direction can be written as,

$$T_i^P = \frac{3}{2}k(s_{y,i+1} - s_{y,i}). \tag{2.6}$$

The total restoring force is $T_i^P - T_{i-1}^P$. A comparison of equation 2.6 with equation 2.5 shows that the restoring force of the P wave is stronger than that of the S wave. This leads to faster P-wave propagation than S-wave one.

Last, the relation of the mass-spring model to the Lamé constant is clarified as follows. A model depicted in Figure 2.3 leads to $\lambda = \mu = \sqrt{3}/4k$. In the case, S-wave β speed is determined by rigidity μ and density ρ, whereas P-wave velocity Vp) is related to both λ and μ as,

$$\begin{aligned} \alpha &= \sqrt{\frac{\lambda + 2\mu}{\rho}} \\ \beta &= \sqrt{\frac{\mu}{\rho}}. \end{aligned} \tag{2.7}$$

For P-wave propagation, λ represents restoring force related to fluid pressure, whereas μ represents restoring force to suppress tangential motions.

Problem 2.1

Derive equation 2.5 and equation 2.6.

Hint: Because we consider a plane wave, relative motions depending on x are negligible. For a simple mode shown in the right Figure, calculate the restoring force to displacement s_x and s_y.

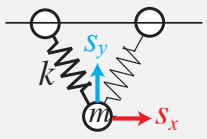

Figure 2.4: * [A simplified model.]A simplified model.

2.1.3 † Attenuation

Although most of this lecture note does not cover seismic attenuation, observed seismic waves decay with time. This is because elastic energy is gradually dissipated into thermal energy. This subsection briefly summarizes physical models of seismic attenuation in a spring–mass system. For simplicity, we will consider connecting a damper, which is responsible for viscous dissipation, to the spring–masssystem considered in the previous section.

Dashpot

If only the spring is considered, there is no energy dissipation (i.e., no seismic attenuation). In order to consider damping due to energy dissipation, a dashpot is considered in addition to the spring.

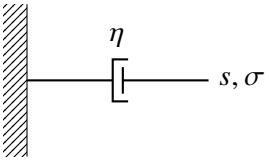

Figure 2.5: Dashpot

Here we consider a displacement $s(t)$ given at the lower right end. Since the dashpot is under viscous resistance η, the applied force $\sigma(t)$ is given by

$$\sigma = \eta \frac{ds}{dt}. \tag{2.8}$$

Kelvin–Voigt model

Here we consider a model of a spring–mass system with a dashpot.

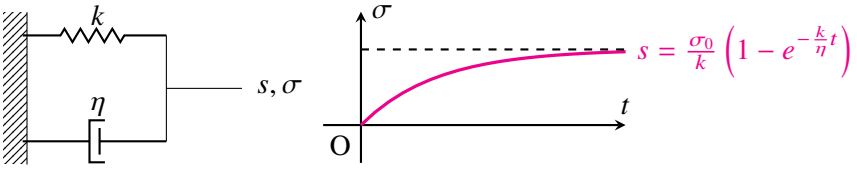

Figure 2.6: Kelvin–Voigt model and the response.

In this case, the relationship between the applied force σ at the lower right end and the displacement s can be written as:

$$\sigma = k\left(s + \frac{\eta}{k}\frac{ds}{dt}\right). \tag{2.9}$$

On the right-hand side, when a constant force σ_0 is applied at time t, the force σ is given by:

$$\begin{cases} 0, & t < 0, \\ \sigma_0, & t \geq 0. \end{cases} \tag{2.10}$$

The displacement (Creep response function $J(t)$) when a constant force σ_0 is applied at time t is:

$$s = \frac{\sigma_0}{k}\left(1 - e^{-\frac{k}{\eta}t}\right). \tag{2.11}$$

If only a spring is considered, the displacement would be σ_0/k instantaneously (black dashed line), but due to viscous relaxation, it can be observed that the displacement reaches the final value with a delay.

Zener model

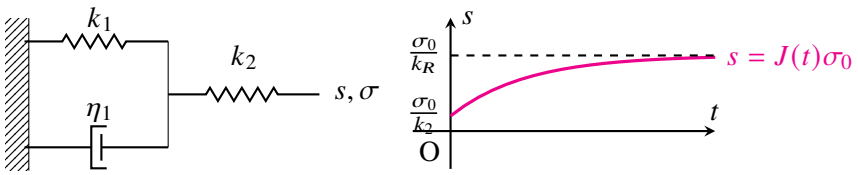

Figure 2.7: Zener model and the response.

Let us consider a more realistic model by adding one more spring.

The relationship between the force σ applied at the lower right edge and the displacement s is represented by

$$\sigma(t) + \tau_\epsilon \frac{d\sigma}{dt} = k_R\left(s + \tau_\sigma \frac{ds}{dt}\right), \tag{2.12}$$

where k_R, τ_ϵ, and τ_σ are defined as

$$k_R \equiv \frac{k_1 k_2}{k_1 + k_2}, \tau_\sigma \equiv \eta/k_1, \tau_\epsilon \equiv \eta/(k_1 + k_2). \tag{2.13}$$

Similarly, if we apply a force $\sigma = \sigma_0 H(t)$ ($H(t)$ is the Heaviside function) at the right end. If a force is applied, the response is $\sigma_0 J(t)$, where $J(t)$ is the creep response function given by

$$J(t) = \frac{1}{k_R}\frac{\tau_\epsilon}{\tau_\sigma} + \frac{1}{k_R}\frac{\tau_\sigma - \tau_\epsilon}{\tau_\sigma}\left[1 - e^{-\frac{t}{\tau_\sigma}}\right]. \tag{2.14}$$

Complex elastic constant

Here we consider a periodic input σ as $\sigma = \sigma_0 e^{-i\omega t}$, $s = s_0 e^{-i\omega t}$. After the sustitution, the Kelvin-Voight model is given by

$$\sigma_0 = k\left(1 - i\omega\frac{\eta}{k}\right)s_0, \tag{2.15}$$

and Zener model is given by

$$\sigma_0 = k_R\frac{1 - i\omega\tau_\sigma}{1 - i\omega\tau_\epsilon}s_0. \tag{2.16}$$

With complex elastic constant K, they can be rewritten by

$$K_v \equiv k\left(1 - i\omega\frac{\eta}{k}\right) \tag{2.17}$$

$$K_z \equiv k_R\frac{1 - i\omega\tau_\sigma}{1 - i\omega\tau_\epsilon}. \tag{2.18}$$

Thus, by extending the elastic constants to complex numbers, the attenuation can be described.

In the case of Zener model, Q^{-1} is given by

$$Q^{-1}(\omega) = \frac{\tau_\sigma - \tau_\epsilon}{\tau}\frac{\omega\tau}{1 + \omega^2\tau^2}, \tag{2.19}$$

where $\tau \equiv \sqrt{\tau_\sigma\tau_\epsilon}$.

Anelastic parameter Q

Let us consider displacement s

$$s(t) = s_2\cos(\omega t - \delta) \tag{2.20}$$

for a given input σ

$$\sigma(t) = \sigma_2\cos\omega t, \tag{2.21}$$

where σ_2, s_2 and ω are real constant.

When the energy E decreases by ΔE during one period of oscillation, the anelastic parameter Q is

$$\frac{2\pi}{Q} = \frac{\Delta E}{E} \tag{2.22}$$

This can be expressed as where ΔE, the amount of energy dissipated in one cycle, is

$$\Delta E = \int_0^{\frac{2\pi}{\omega}} \sigma\frac{ds}{dt}, \tag{2.23}$$

and E is

$$E = \frac{1}{2}\sigma(0)s(0) \tag{2.24}$$

can be evaluated as

Physical dispersion

To consider the dispersion of phase velocity caused by damping, we generalize the spring-mass model. Here, we consider the Zener model instead of the spring and similarly consider periodic oscillations characterized by the angular frequency ω. In this case, by taking Δx to be small, the wave equation with coefficients extended to complex numbers can be written as follows:

$$-\omega^2\rho s_0(x) = K_v\frac{\partial^2 s_0(x)}{\partial x^2}. \tag{2.25}$$

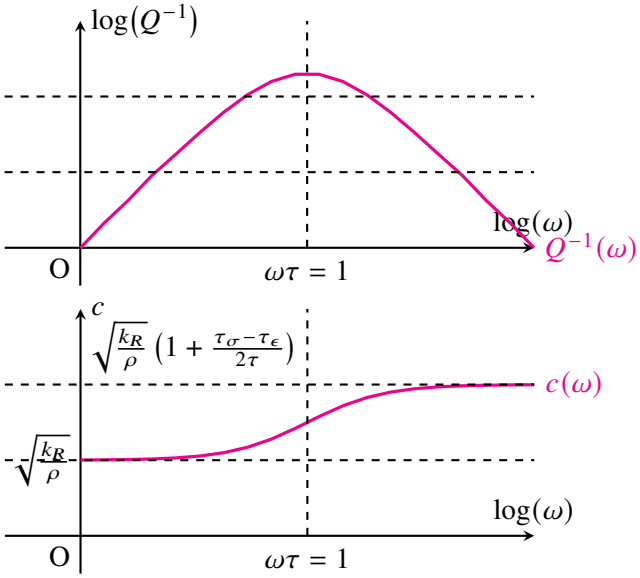

Figure 2.8: Physical dispersion

Let us consider displacement s_0, which describes wave propagation with phase velocity $c(\omega)$ as

$$s_0(x) = e^{-\frac{\omega x}{2c(\omega)Q(\omega)}} e^{i\omega\frac{x}{c(\omega)}}. \tag{2.26}$$

In this case $c(\omega)$ changes with frequencies (dispersion). The dispersion relation can be written by

$$c(\omega) = \sqrt{\frac{k_R}{\rho}}\left(1 + \frac{\tau_\sigma - \tau_\epsilon}{2\tau}\frac{\omega^2\tau^2}{1+\omega^2\tau^2}\right). \tag{2.27}$$

In the seismic frequency band (10^{-3}–10 Hz), Q is known to be frequency independent and approximately constant. Combining a spring-mass system with dashpot is known to explain the frequency independence of Q. Now in the Zener model, corresponding to a single relaxation time (τ_σ), there is a frequency band in which the damping works, but the phase speed changes with frequency significantly. In reality, the Earth has many different relaxation time scales corresponding to many physical processes. Therefore, by combining Zenner models with different relaxation times, we can extend the frequency range where Q^{-1} is constant.

https://www.eri.u-tokyo.ac.jp/people/knishida/eng/seismology.html

Problem 2.2

1. When a wave propagates through a medium, the medium loses the oscillation energy and converts it into heat, causing the wave to attenuate. The propagation of a wave s_0 oscillating at angular frequency ω can be expressed using the anelastic parameter Q as:

$$s_0(x,t) = e^{-\frac{|\omega|x}{2cQ}} e^{i\omega\left(\frac{x}{c}-t\right)} \tag{2.28}$$

   where Q is a positive real number. Consider the wave generated when an impulse is applied at $x = 0$ at $t = 0$. Since the impulse contains all frequency components equally, the wave packet propagating in the positive x direction for $t > 0$ and $x > 0$ can be written as:

$$s(x,t) = \frac{1}{\pi}\int_{-\infty}^{\infty} e^{-\frac{|\omega|x}{2cQ}} e^{i\omega\left(\frac{x}{c}-t\right)} d\omega \tag{2.29}$$

   Assuming c and Q are constant with respect to frequency, find the analytical solution for s. Also, illustrate the time evolution at position x.

2. The solution obtained in (1) is, strictly speaking, physically impossible. Discuss the reasons for this.

§2.2 Lagrangian and Eulerian variables

Here we consider a particle at $\boldsymbol{x}$ in a continuum at time 0. [note 2)] It moves with time as $\boldsymbol{r}(\boldsymbol{x}, t)$. A Lagrangian variable describes a quantity over time by its initial location $\boldsymbol{x}$, and an Eulerian variable describes a quantity over time in a fixed frame as $\boldsymbol{x}(\boldsymbol{r}, t)$. An Eulerian quantity q^E can be related to the Lagrangian quantity q^L as,

$$q^L(\boldsymbol{x}, t) = q^E(\boldsymbol{r}(\boldsymbol{x}, t), t). \tag{2.30}$$

Time derivatives of the equation lead to

$$\partial_t q^L = \partial_t q^E + \boldsymbol{u}^E \cdot \nabla_{\boldsymbol{r}} q^E \equiv D_t q^E, \tag{2.31}$$

where $\boldsymbol{u}^E$ is Euler velocity. Material derivative D_t represents the Lagrangian time derivative of a particle in the Eulerian form. Later, ∂_t is an abbreviation of $\frac{\partial}{\partial t}$. This relation holds for vector quantity as particle velocity $\boldsymbol{u}^L$ and $\boldsymbol{u}^E$. As a q^E, here we consider acceleration $\partial_t \boldsymbol{u}^L$ as

$$\partial_t \boldsymbol{u}^L = \partial_t \boldsymbol{u}^E + \boldsymbol{u}^E \cdot \nabla_{\boldsymbol{r}} \boldsymbol{u}^E \equiv D_t \boldsymbol{u}^E, \tag{2.32}$$

When we consider seismic records, the Lagrangian description is more natural because the seismometer is pinned at a surface point.

Later we consider an infinitesimal deformation in a framework of linear elasticity. Let us consider small deformation $\boldsymbol{s}$ as,

$$\boldsymbol{r}(\boldsymbol{x}, t) = \boldsymbol{x} + \boldsymbol{s}(\boldsymbol{x}, t). \tag{2.33}$$

$$\begin{aligned} q^E(\boldsymbol{r}, t) &= q_0(\boldsymbol{r}) + q^{E1}(\boldsymbol{r}, t), \\ q^L(\boldsymbol{x}, t) &= q_0(\boldsymbol{x}) + q^{L1}(\boldsymbol{x}, t). \end{aligned} \tag{2.34}$$

Because $\boldsymbol{s}$ is small, the perturbations e of Eulerian variable $q^{E1} and Lagrangian one q^{L1}$ can be written by,

$$q^{E1}(\boldsymbol{r}, t) = q^{E1}(\boldsymbol{x}, t), q^{L1}(\boldsymbol{x}, t) = q^{L1}(\boldsymbol{r}, t). \tag{2.35}$$

We note that the perturbations do not depend on $\boldsymbol{x}$, $\boldsymbol{r}$.

Next, let us consider the relationship between an Eulerian perturbation q^{E1} and a Lagrangian one q^{L1}. When we consider first-order perturbations, q^{L1} can be written as[note 3)]

$$q^{L1}(\boldsymbol{x}, t) = q^{E1}(\boldsymbol{r}, t) + \boldsymbol{s} \cdot \nabla_{\boldsymbol{r}} q_0. \tag{2.36}$$

note 2) A bold symbol like $\boldsymbol{x}$ denotes a vector in this textbook.
note 3) See §3.2 of Dahlen and Tromp (1998)(1) for details.

This equation is the integration of material derivatives. In a framework of linear elasticity, because we can neglect the second term of the right-hand side, we do not need to distinguish Eulerian from Lagrangian. However, because stress and density have initial values (∇q_0), the spatial derivatives cause the discrepancy between the Eulerian and Lagrangian. When we must consider initial stress (e.g. hydrostatic pressure owing to gravity), we must need attention to the difference between the descriptions. In §**??**, we will take such an example.

§2.3 Strain

In order to measure the deformation of an elastic body, let us trace two particles ($\boldsymbol{r}$,$\boldsymbol{r}+d\boldsymbol{r}$). At $t=0$, they are located at $\boldsymbol{x}$,$\boldsymbol{x}+d\boldsymbol{x}$. $d\boldsymbol{r}$ can be related to $d\boldsymbol{x}$ as,

$$d\boldsymbol{r} = \nabla_{\boldsymbol{x}}\boldsymbol{r}\cdot d\boldsymbol{x} = (\boldsymbol{I}+\nabla_{\boldsymbol{x}}\boldsymbol{s})\cdot d\boldsymbol{x}. \tag{2.37}$$

The change of the distance between the particles is estimated to be

$$|d\boldsymbol{r}|^2 - |d\boldsymbol{x}|^2 = 2(d\boldsymbol{x}\cdot\boldsymbol{E}^L\cdot d\boldsymbol{x}). \tag{2.38}$$

Here $\boldsymbol{E}^L$ is Green-Lagrange strain defined by

$$\boldsymbol{E}^L \equiv \frac{1}{2}[\nabla\boldsymbol{s}+(\nabla\boldsymbol{s})^T-(\nabla\boldsymbol{s})^T\nabla\boldsymbol{s}] = \frac{1}{2}\left(\frac{\partial s_j}{\partial x_i}+\frac{\partial s_i}{\partial x_j}+\frac{\partial s_l}{\partial x_i}\frac{\partial s_l}{\partial x_j}\right). \tag{2.39}$$

When $\boldsymbol{s}$ is small enough to neglect the second-order term, the strain can be simplified to

$$\boldsymbol{E}^L = \frac{1}{2}[\nabla\boldsymbol{s}+(\nabla\boldsymbol{s})^T] = \frac{1}{2}\left(\frac{\partial s_j}{\partial x_i}+\frac{\partial s_i}{\partial x_j}\right) \tag{2.40}$$

Here, following Einstein's summation convention, we calculate the summation of the term over all the values of the index. Although the strain tensor $\boldsymbol{E}^L$ is a Lagrangian variable, we do not need to distinguish it from its Eulerian counterpart for infinitesimal deformations. The strain tensor has 6 independent components because of the symmetry.

Problem 2.3

Calculate the strain tensor up to the first order when considering a rigid rotation with an infinitesimal angle in 2-D. You can find second-order terms, although rigid rotation should not cause strain from a physical point of view. Next, show Green-Lagrange strain of an infinitesimal rigid rotation vanishes completely.

2.3.1 Strain in an arbitrary coordinate

Here we consider linear strain in an arbitrary coordinate. A displacement vector $\boldsymbol{s}$ can be represented by orthogonal unit vectors as

$$\boldsymbol{s} = \sum_j s_j \hat{\boldsymbol{x}}_j. \tag{2.41}$$

The gradient of the vector is written by

$$\nabla \equiv \hat{\boldsymbol{x}}_i \frac{\partial}{\partial x_i}. \tag{2.42}$$

The insertion of the definition of $\boldsymbol{s}$ leads to the following equation:

$$\boldsymbol{\nabla s} = \sum_i \hat{\boldsymbol{x}}_i \frac{\partial \boldsymbol{s}}{\partial x_i} = \sum_i \hat{\boldsymbol{x}}_i \left[\sum_j \frac{\partial s_j}{\partial x_i} \hat{\boldsymbol{x}}_j + \sum_j s_j \frac{\partial \hat{\boldsymbol{x}}_j}{\partial x_i} \right]. \tag{2.43}$$

The second order tensor $\boldsymbol{E}$ can be represented by basis vectors and the corresponding components as

$$\boldsymbol{E} = \sum_{ij} E_{ij} \hat{\boldsymbol{x}}_i \hat{\boldsymbol{x}}_j. \tag{2.44}$$

The complication originates from the partial derivatives of the basis vectors.

Strain in a cylindrical coordinate (r, φ, z)

Here we consider strain in a cylindrical coordinate (r, φ, z). Partial derivatives of the unit vectors $\hat{\boldsymbol{r}}, \hat{\boldsymbol{\varphi}}, \hat{\boldsymbol{z}}$ are given by:

$$\begin{aligned}
&\frac{\partial \hat{\boldsymbol{r}}}{\partial r} = 0, && \frac{\partial \hat{\boldsymbol{r}}}{\partial \varphi} = \hat{\boldsymbol{\varphi}}, && \frac{\partial \hat{\boldsymbol{r}}}{\partial z} = 0 \\
&\frac{\partial \hat{\boldsymbol{\varphi}}}{\partial r} = 0, && \frac{\partial \hat{\boldsymbol{\varphi}}}{\partial \varphi} = -\hat{\boldsymbol{r}}, && \frac{\partial \hat{\boldsymbol{\varphi}}}{\partial z} = 0 \\
&\frac{\partial \hat{\boldsymbol{z}}}{\partial r} = 0, && \frac{\partial \hat{\boldsymbol{z}}}{\partial \varphi} = 0, && \frac{\partial \hat{\boldsymbol{z}}}{\partial z} = 0.
\end{aligned} \tag{2.45}$$

The definition of the strain with the above equations leads to the following representation of the corresponding components as:

$$\begin{aligned}
E_{rr} = &\quad \frac{\partial s_r}{\partial r}, E_{\varphi\varphi} = \frac{1}{r}\frac{\partial s_\varphi}{\partial \varphi} + \frac{s_r}{r}, E_{zz} = \frac{\partial s_z}{\partial z} \\
2E_{\varphi z} = &\quad \frac{\partial s_z}{\partial \varphi} + \frac{\partial s_\varphi}{\partial z}, E_{zr} = \frac{\partial s_r}{\partial z} + \frac{\partial s_z}{\partial r}, \\
2E_{r\varphi} = &\quad r\frac{\partial}{\partial r}\left(\frac{s_\varphi}{r}\right) + \frac{1}{r}\frac{\partial s_r}{\partial \varphi}.
\end{aligned} \tag{2.46}$$

Problem 2.4

Derive the strain in a cylindrical coordinate shown above.

Strain in a spherical coordinate (r, θ, φ)

Here only the results are shown as,

$$\begin{aligned} E_{rr} &= \frac{\partial s_r}{\partial r}, E_{\theta\theta} = \frac{1}{r}\frac{\partial s_\theta}{\partial \theta} + \frac{s_r}{r}, E_{\varphi\varphi} = \frac{1}{r\sin\theta}\left(\frac{\partial s_\varphi}{\partial \varphi} + s_\theta \cos\theta\right) + \frac{s_r}{r} \\ 2E_{\theta\varphi} &= \frac{1}{r}\frac{\partial s_\varphi}{\partial \theta} + \frac{1}{r\sin\theta}\left(\frac{\partial s_\theta}{\partial \varphi} - s_\varphi \cos\theta\right), 2E_{\varphi r} = \frac{1}{r\sin\theta}\frac{\partial s_r}{\partial \varphi} + r\frac{\partial}{\partial r}\left(\frac{s_\varphi}{r}\right) \\ 2E_{r\theta} &= r\frac{\partial}{\partial r}\left(\frac{s_\theta}{r}\right) + \frac{1}{r}\frac{\partial s_r}{\partial \theta}. \end{aligned} \tag{2.47}$$

§2.4 Stress and traction

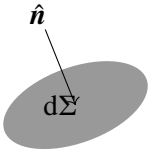

Let us consider a small surface $d\Sigma$ in a continuum with the normal vector $\hat{\boldsymbol{n}}$. Traction is defined by force $\boldsymbol{f}$ per unit area acting on $d\Sigma$. The traction is parallel to the normal vector $\hat{\boldsymbol{n}}$, and the positive sign is defined by force from the positive side according to the normal vector to the negative side. Stress $\boldsymbol{T}^E$[note 4)] is defined by

$$\boldsymbol{f} = d\Sigma \hat{\boldsymbol{n}} \cdot \boldsymbol{T}^E. \tag{2.48}$$

Traction $\boldsymbol{f}_{12}$ of medium 1 from medium 2 is $\boldsymbol{f}_{21}$.

§2.5 Conservation of angular momentum

Conservation of angular momentum requires that the stress tensor is symmetric as $T_{ij} = T_{ji}$.

[note 5)] as : $T_{ij} = T_{ji}$

This symmetry is held without microscopic spin interaction.(4)

[note 4)] This stress is Cauchy stress in a precise manner. There are two other definitions (see Dahlen and Tromp 1998 in details).

[note 5)] This symmetry is derived from the equilibrium of the moment of an infinitesimal volume.

Problem 2.5

Let us consider angular momentum along the z axis of an infinitesimal cube with a side of ϵ. Show $T_{xy} = T_{yx}$ from the conservation of angular momentum in cases:

1. T_{xy} and T_{yx} are constant, and other T_{ij} are zero.
2. (Optional)

$$T_{xy}(\boldsymbol{x}) = T_{xy}(\boldsymbol{x}_0) + T_{xy,x}(\boldsymbol{x}_0)\delta x + T_{xy,y}(\boldsymbol{x}_0)\delta y, \tag{2.49}$$
$$T_{yx}(\boldsymbol{x}) = T_{yx}(\boldsymbol{x}_0) + T_{yx,x}(\boldsymbol{x}_0)\delta x + T_{yx,y}(\boldsymbol{x}_0)\delta y, \tag{2.50}$$

and other $T_{ij} = 0$.

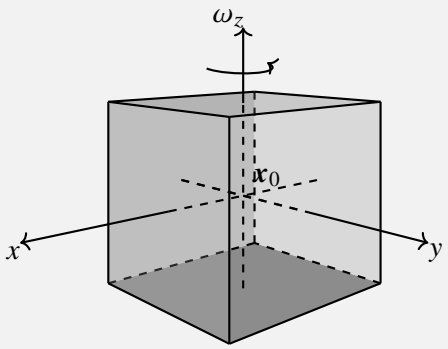

§2.6 Conservation of mass

Let us consider governing equations conservation of mass first. This equation becomes important for buoyancy force.

In general, conservation of mass can be written as,

$$\partial_t \rho^E = -\nabla \cdot (\rho^E \boldsymbol{u}^E), \tag{2.51}$$

where $\boldsymbol{u}^E$ is Eulerian particle velocity.

Here we consider the first-order perturbation of the density as

$$\rho^E = \rho_0 + \rho^{E1}. \tag{2.52}$$

Time integration of the first order perturbation leads to

$$\rho^{E1} = -\nabla \cdot (\rho_0 \boldsymbol{s}). \tag{2.53}$$

The right-hand term represents the divergence of the mass flux, whereas the left one does the change of the mass. On the other hand, the Lagrangian form can be written by

$$\rho^{L1} = -\rho_0 \nabla \cdot (\boldsymbol{s}). \tag{2.54}$$

Because we focused on a particle, the right-hand side shows corresponding expansion or deflation.

We note the discrepancy that the Lagrangian density perturbation ρ^{L1} is $\rho^{L1} = -\rho_0 \nabla \cdot \boldsymbol{s}$. If $\nabla\rho_0$ is 0, they are the same. However, they are different in general. When the wavelength of a seismic wave is much smaller than the typical scale of density change, we can neglect the difference.

§2.7 Equations of motion: conservation of momentum

Let us consider a temporal change a volume V^t.

$$\frac{d}{dt}\int_{V^t} \rho^E \boldsymbol{u}^E dV^t = \mathcal{F}, \tag{2.55}$$

The external force $\boldsymbol{F}$ can be written by surface force acting on ∂V^t and body force acting throughout the volume, such as gravity and electromagnetic force as

$$\mathcal{F} = \mathcal{F}_s + \mathcal{F}_b = \int_{\partial V^t} (\hat{\boldsymbol{n}}^t \cdot \boldsymbol{T}^E) d\Sigma^t + \int_{V^t} \rho^E \boldsymbol{g}^E dV^t. \tag{2.56}$$

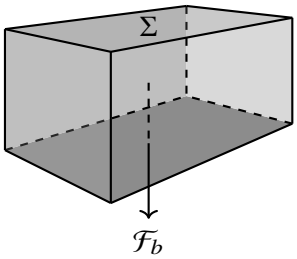

With a help of Gauss's divergence theorem, they can be written by

$$\rho^E D_t \boldsymbol{u}^E = \nabla_{\boldsymbol{r}} \cdot \boldsymbol{T}^E - \rho^E \nabla \phi^{E1}. \tag{2.57}$$

If we can neglect initial stress up to the first order, it can be simplified as

$$\rho_0 \partial_t^2 \boldsymbol{s} = \nabla \cdot \boldsymbol{T}^{E1}. \tag{2.58}$$

When we consider hydrostatic pressure, the equations of motion up to the first order can be written as

$$\rho_0 \partial_t^2 \boldsymbol{s} = \nabla \cdot \boldsymbol{T}^E - \rho^E \nabla \phi^E, \tag{2.59}$$

where ϕ^E is gravity potential [note 6)]. When we consider gravity, we must consider hydrostatic pressure, which sustains the gravity force. Deviatoric stress T^{E1} from the hydrostatic pressure

[note 6)] Here we consider gravity, but we neglect perturbation of gravity (an effect of self-gravitation). This approximation is known as the Cowling approximation in the field of astrophysics. In particular, this approximation is effective for a stratified atmosphere. The effect of self-gravitation becomes important in a period longer than 3000 s as described later.

can be written by,

$$T_{ij}^{E} = -p_0\delta_{ij} + T_{ij}^{E1}. \tag{2.60}$$

Because the hydrostatic pressure sustains the gravity force, the pressure p_0 should satisfy the relation as,

$$\nabla p_0 = -\rho_0 \nabla\phi_0 = \rho_0 \boldsymbol{g}. \tag{2.61}$$

They lead to

$$\rho_0\partial_t^2\boldsymbol{s} = \nabla\cdot\boldsymbol{T}^{E1} - \nabla[\rho_0\boldsymbol{s}\cdot\nabla\phi_0] - \rho_0\nabla\phi^{E1} - \rho^{E1}\nabla\phi_0. \tag{2.62}$$

Additionally, since the perturbation of the gravitational potential ϕ^{E1} is caused by the density perturbation ρ^{E1}, it must satisfy Poisson's equation:

$$\nabla^2\phi^{E1} = 4\pi G\rho^{E1}. \tag{2.63}$$

§2.8 Conservation of energy

Total energy (kinetic energy + elastic energy) U, and energy flux $\boldsymbol{K}$ can be written by

$$U = \frac{1}{2}\left[\rho_0\partial_t\boldsymbol{s}\cdot\partial_t\boldsymbol{s} + \sum_{ij}E_{ij}T_{ij}\right], \tag{2.64}$$

$$\boldsymbol{K} = -\boldsymbol{T}\cdot\partial_t\boldsymbol{s}. \tag{2.65}$$

Conservation of energy can be written as,

$$\partial_t U + \nabla\cdot\boldsymbol{K} = 0. \tag{2.66}$$

Elastic energy W can be defined by

$$W = \frac{1}{2}\sum_{ij}E_{ij}T_{ij}. \tag{2.67}$$

Stress can be represented by the spatial gradient of W as

$$T_{ij} = \frac{\partial W}{\partial E_{ij}}. \tag{2.68}$$

We will discuss the condition for the existence of elastic energy W as a potential energy below.

Work per unit volume δR done by the internal stress T_{ij} can be given[5] by

$$\delta R = -T_{ij}\delta E_{ij}. \tag{2.69}$$

For deformation from $\boldsymbol{E} = 0$ to $\boldsymbol{E} = \Delta\boldsymbol{E}$ of a given infinitesimal volume, the corresponding work ΔR by the internal stress is given by

$$\Delta R = -\int_0^{\Delta\boldsymbol{E}}\sum_{ij}T_{ij}dE_{ij}, \tag{2.70}$$

which depends on the history of the deformation. Then we deform it again from $\boldsymbol{E} = \Delta\boldsymbol{E}$ to $\boldsymbol{E} = 0$. Elastic deformation requires $\Delta R = 0$ because the internal stress should be conservative. The conservative property requires the following condition

$$\frac{\partial T_{ij}}{\partial E_{kl}} = \frac{\partial T_{kl}}{\partial E_{ij}}. \tag{2.71}$$

In the 2-D case (in this case, the number of the independent stress/strain components is 3), this condition can be interpreted as vortex-free (Problem 2.8). Consequently, the elastic energy W can be interpreted as a scalar potential.

Problem 2.6

Derive

$$dR = -T_{ij}dE_{ij}. \tag{2.72}$$

(Hint: Estimate work done by the internal force $F_j = \partial_i T_{ij}$.)

Problem 2.7

(1)

Let us consider works for two different deformation paths for a simple 2-D case. A rectangular area is deformed according to the strain of $E_{xx} = \Delta E_{xx}$, $E_{yy} = \Delta E_{yy}$ with two different paths: (i) first deform the area with ΔE_{yy}, then deform it with ΔE_{xx}. (ii) First deform it with ΔE_{xx}, then deform it with ΔE_{yy} as shown in Figure 2.9. Estimate works of $\Delta R^{(i)}$ and $\Delta R^{(ii)}$ for the cases (i) and (ii), respectively.

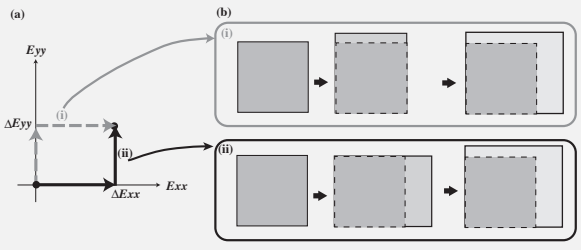

Figure 2.9:

When the stress satisfies the condition of a conservative force, $\Delta R^{(i)} = \Delta R^{(ii)}$ is required. Show the following condition of elastic modulus, which satisfies the above requirement.

$$C_{ijkl} = C_{klij}, \tag{2.73}$$

Problem 2.8

In order to understand the relation (equation 2.71):

$$\frac{\partial T_{ij}}{\partial E_{kl}} = \frac{\partial T_{kl}}{\partial E_{ij}}, \tag{2.74}$$

let us consider the 2-D case (3 independent variables of stress/strain components). Derive the condition for the case that works δR, which is work done by the internal stress, does not depend on deformation paths.
This condition guarantees that the spatial gradient of a scalar potential W can represent stress $\boldsymbol{T}$. Thus elastic energy W can be interpreted as the scalar potential for stress $\mathbf{T}$.

§2.9 Constitutive equation: Hooke's law

To determine elastic deformation, we must know the constitutional relation between stress $\boldsymbol{T}^{L1}$ and strain E_{L1}. For understanding the deformation of an arbitrary volume, Lagrangian description is essential. First, we do not take care of the difference between Lagrangian and Eulerian without considering initial stress. For a linear elastic medium, a relation between stress and strain can be represented by Hooke's law as

$$T_{ij} = C_{ijkl}E_{kl}, \tag{2.75}$$

where C_{ijkl} is elastic tensor with 81 components. The symmetry of stress and strain tensor leads to the symmetry of C_{ijkl} as $C_{ijkl} = C_{jikl}, C_{ijkl} = C_{ijlk}$. 1st law of thermodynamics requires $C_{ijkl} = C_{klij}$[note 7)]. As a result, the elastic tensor has 21 independent components.

2.9.1 Betti–Rayleigh reciprocity theorem

We introduce the Betti–Rayleigh reciprocity theorem for the representation theorem of an elastic medium explained later.

Let us consider a situation where forces $\boldsymbol{f}_1$ and $\boldsymbol{f}_2$ are applied. We assume that dynamic forces can be neglected. We evaluate the work done in two cases: applying $\boldsymbol{f}_1$ followed by $\boldsymbol{f}_2$, and applying $\boldsymbol{f}_2$ followed by $\boldsymbol{f}_1$ (Figure 2.10). Here, the forces are applied quasi-statically. First, $\boldsymbol{f}_1$ is gradually applied from 0 to $\boldsymbol{f}_1$. After reaching a steady state, $\boldsymbol{f}_2$ is gradually applied from 0 to $\boldsymbol{f}_2$. The other deformation path reverses the order of the applied forces. As considered in Problem 2.7, the work done by internal forces is independent of the deformation path (using Maxwell's reciprocity theorem). Therefore, only the work done by traction and body forces contributes.

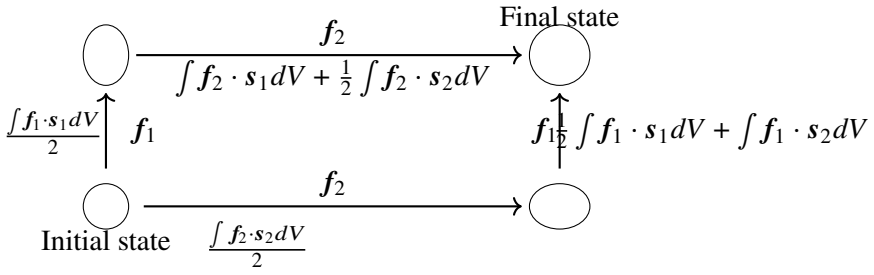

Figure 2.10: Two different deformation paths.

Since the work done in both deformation paths is equal, we can derive the following relation:

$$\int_V \boldsymbol{f}_1(\boldsymbol{x}) \cdot \boldsymbol{s}_2 dV - \int_V \boldsymbol{f}_2(\boldsymbol{x}) \cdot \boldsymbol{s}_1 dV = -\int_\Sigma [\boldsymbol{T}_1 \cdot \boldsymbol{s}_2(\boldsymbol{x})] \cdot \hat{\boldsymbol{n}} d\Sigma + \int_\Sigma [\boldsymbol{T}_2 \cdot \boldsymbol{s}_1(\boldsymbol{x})] \cdot \hat{\boldsymbol{n}} d\Sigma. \tag{2.76}$$

[note 7)] See a textbook of continuum mechanics in details.

This is known as the Betti–Rayleigh reciprocity theorem.

By substituting $\boldsymbol{f}_i = \sum_j f_j^i \boldsymbol{n}_j \delta(\boldsymbol{x} - \boldsymbol{x}_j)$ and defining the corresponding displacements at each point as $s_j \boldsymbol{n}_j$ (where $\boldsymbol{x}_j$ is a unit vector pointing in an arbitrary direction), and assuming no traction (the right-hand side is 0), we can derive Betti's theorem, well known in solid mechanics:

$$\sum_j f_j^1 s_j^2 = \sum_j f_j^2 s_j^1. \tag{2.77}$$

2.9.2 Isotropic medium

When an elastic medium is isotropic, the elastic tensor can be simplified using Lamé constants λ, μ as,

$$C_{ijkl} = \lambda \delta_{ij} \delta_{kl} + \mu(\delta_{ik}\delta_{jl} + \delta_{il}\delta_{jk}). \tag{2.78}$$

Here we derive Hooke's law for the isotropic medium explicitly for further sections.

$$\begin{aligned} T_{xx} &= (\lambda + 2\mu)E_{xx} + \lambda(E_{yy} + E_{zz}), & T_{xy} &= 2\mu E_{xy}, & T_{xz} &= 2\mu E_{xz} \\ T_{yy} &= (\lambda + 2\mu)E_{yy} + \lambda(E_{xx} + E_{zz}), & T_{yz} &= 2\mu E_{yz} \\ T_{zz} &= (\lambda + 2\mu)E_{zz} + \lambda(E_{xx} + E_{yy}). \end{aligned} \tag{2.79}$$

The are several different definitions of the elastic constant, although they are identical in theory. Young modulus E and Poisson's ratio ν are also major, and they can be related to Lamé's constant as

$$E = \frac{\mu(3\lambda + 2\mu)}{\lambda + \mu}, \nu = \frac{\lambda}{2(\lambda + \mu)}. \tag{2.80}$$

Here we consider the effects of hydrostatic pressure on elastic medium. In the deep Earth, the hydrostatic pressure reaches several hundred GPa, the initial pressure is not negligible in some cases. In order to trace the temporal change of an infinitesimal volume V^t, the variables are described by Lagrangian as,

$$p^L = p_0 + p^{L1}. \tag{2.81}$$

The constitutional relation can be written by

$$p^{L1} = -\lambda(\boldsymbol{x}) \nabla \cdot \boldsymbol{s}. \tag{2.82}$$

Eulerian equations of motion can be written by

$$p^{E1} = p^{L1} - \boldsymbol{s} \cdot \nabla p_0. \tag{2.83}$$

§2.10 Relation between density and seismic wave velocity

At a planetary scale, the possible values for seismic wave velocities are theoretically bounded. Counterintuitively, we can roughly estimate seismic wave velocities by assuming hydrostatic

equilibrium. This provides crucial knowledge for considering seismic wave propagation on other planets.

2.10.1 Sustaining hydrostatic equilibrium with elasticity

Let us estimate the typical seismic wave velocity when considering a global scale. We consider the elastic constant K. Letting the seismic wave velocity be c_s and the density be ρ, K is given by $k = \rho c_s^2$. Since K has the dimension of pressure, we consider the typical pressure. Letting the Earth's radius be R_e and the gravitational acceleration at the surface be g, the typical hydrostatic pressure is $\rho g R_e$. Therefore, from dimensional analysis:

$$\rho (c_s)^2 \sim \rho g R_e, \tag{2.84}$$

we can estimate the seismic wave velocity as $c_s \sim \sqrt{gR_e}$. Note that we can estimate the seismic wave velocity simply from the Earth's radius and gravitational acceleration. In this case, the seismic wave velocity comes out to around 8 km/s, which is a surprisingly good estimate.

Let us now consider a state where hydrostatic pressure is comparable to the bulk modulus K. Here, the bulk modulus K is defined as

$$K = \rho \left(\alpha^2 - \frac{4}{3}\beta^2 \right) = \rho c_s^2, \tag{2.85}$$

and c_s is called the bulk sound velocity[note 8)]. If the hydrostatic pressure matches K, the strain E becomes on the order of 1, and for a linear elastic medium, the volume would become 0. In other words, when hydrostatic pressure P is sustained by elasticity, the elastic constant K is required to be greater than or equal to P.

Since hydrostatic pressure is 0 in shallow regions, a naive application of dimensional analysis yields $c_s = 0$. In reality, this is not the case, meaning rocks have an intrinsic rigidity exceeding what is necessary to support the hydrostatic pressure. Consider isotropically compressing a rock on the surface. Microscopically, the interatomic distances gradually decrease. As a result, the density increases, and the interatomic forces strengthen, which is expected to correspond to increased seismic wave velocities.

Thinking in terms of a planetary average, this particular argument feels slightly contrived. Let us consider the balance between the gravitational potential and accumulated elastic energy[note 9)]. Assuming a uniform sphere for simplicity, letting U be the total elastic energy and Ω be the total gravitational potential, we obtain:

$$U = 3 \int P dV \sim 3M(c_s)^2 \tag{2.86}$$

$$\Omega = \frac{3}{5} g R_e, \tag{2.87}$$

[note 8)] $\phi \equiv c_s^2$ is also known as the seismic parameter.

[note 9)] To be precise, the virial theorem leads to the equipartition of gravitational potential and elastic energy under hydrostatic equilibrium.[(2)]

which leads to $(c_s)^2 = gR_e/5$ and halves the value of c_s[note 10]. This discrepancy arises because calculating the average includes the unrealistic condition that pressure is 0 near the surface ($c_s = 0$). As a result, heuristically taking R_e as the length scale empirically yielded an estimate closer to reality. A proper evaluation naturally yields consistent results. Below, we discuss this more quantitatively.

2.10.2 Adams–Williamson equation

Let us consider a situation where hydrostatic pressure P is sustained by adiabatic compression. The pressure gradient must balance gravity:

$$\frac{dP}{dr} = -\rho g(r). \tag{2.88}$$

For a spherically symmetric structure, the gravitational acceleration g is

$$g(r) = G\frac{M(r)}{r^2}, \tag{2.89}$$

where $M(r)$ is the mass enclosed within radius r.

Assuming hydrostatic pressure is sustained by elasticity. Here, the bulk modulus K represents the response of density against an infinitesimal change in pressure, satisfying $K = \rho\frac{dP}{d\rho}$. Thus, the pressure gradient becomes:

$$\frac{dP}{dr} = \frac{dP}{d\rho}\frac{d\rho}{dr} = \frac{K}{\rho}\frac{d\rho}{dr}. \tag{2.90}$$

[note 11] From these two equations, we obtain the Adams–Williamson equation:(6), (9), (11)

$$\frac{d\rho}{dr} = -\frac{\rho}{c_s^2}g(r). \tag{2.91}$$

Here, we define a density scale height H_ρ, a parameter frequently used to describe atmospheric structure, as:

$$H_\rho = \left(-\frac{1}{\rho}\frac{d\rho}{dr}\right)^{-1}. \tag{2.92}$$

It represents the thickness over which density decreases by a factor of $1/e$. Rearranging the equation yields:

$$c_s = \sqrt{H_\rho(r)g(r)}. \tag{2.93}$$

This formula corresponds directly to the earlier dimensional analysis. Our previous estimation using the Earth's radius R_e implicitly approximated the density scale height H_ρ with R_e. In the lower mantle, for instance, H_ρ is roughly 10^4 km, demonstrating this is not a bad approximation.

[note 10] $U = \int \boldsymbol{r}\cdot\nabla P dV$ takes $\nabla\cdot\boldsymbol{r} = 3$ and uses Green's theorem. Ω is evaluated by bringing thin spherical shells from infinity to form a sphere, leading to $\Omega = -\int_0^M GM(r)/r\, dM(R)$.

[note 11] Here, since the bulk modulus is estimated from seismic wave velocities, we assume macroscopic deformation is adiabatic due to being sufficiently fast. If the temperature structure deviates from the adiabatic gradient, thermal expansion must be considered to balance static pressure. Moreover, effects from phase transitions or chemical changes require separate consideration.

2.10.3 Equation of state: Estimation of Earth's seismic wave velocity structure

To estimate a planet's seismic wave velocity structure, we need the relationship between density ρ and seismic wave velocity c_s (equation of state). Given the equation of state, we can estimate these structures by solving a coupled system of hydrostatic equilibrium, gravity, and the equation of state. First, we consider Earth, then expand to general planets.

Earth: Birch's law

Imagine learning about Earth's mass distribution without any prior information on its seismic wave velocities. Determining elastic constants requires learning the pressure-density relationship. For gases, the ideal gas law is well known; for solids, it is more complicated. Empirically, the variation of Earth's rock seismic velocities can be described as a function of density. Known as Birch's law,[3), 9)] it states:

$$c_s \approx a + b\rho. \tag{2.94}$$

Thus, seismic wave velocities can be described as a linear function of density[note 12)]. Let us examine if this contradicts the Adams–Williamson equation for the real Earth.

Here, we assume $c_s = -2\times10^3 + \rho$ [kg/m^3] in the inner and outer core, and $c_s = -1.75\times10^3 + 2.36\rho$ [kg/m^3][9)] in the mantle. Furthermore, we assume a density jump of 4.1424×10^3 [kg/m^3] at the core–mantle boundary. Earth's total mass 5.972×10^{24} kg is assumed to be known. By coupling the Adams–Williamson equation and gravity formulation, we perform numerical integration from Earth's center toward the surface. By finding the distribution that results exactly in the total mass upon reaching the surface, we can estimate both density and bulk sound velocity.

The lower mantle reveals a remarkably accurate prediction, meaning it can be well represented by the adiabatic compression of a uniform material. On the other hand, estimations drastically diverge from actual PREM values in the upper mantle and crust. This occurs because the shallow regions deviate heavily from an adiabatic temperature gradient, and also because the compositional difference between the crust and upper mantle renders our assumed Birch's parameters invalid.

Because Earth's deep interior consists of much heavier material (the core being predominantly iron), $g(r)$ in the lower mantle stays roughly constant (around the surface value), a behavior beautifully reproduced by the computed model. Until seismic observations were made by the InSight mission, such density-based deductions[7)] were among the very few ways to estimate seismic wave velocity structures.

[note 12)] Strictly speaking, this approximates the equation of state using a first-order perturbation with respect to density around a certain reference value.

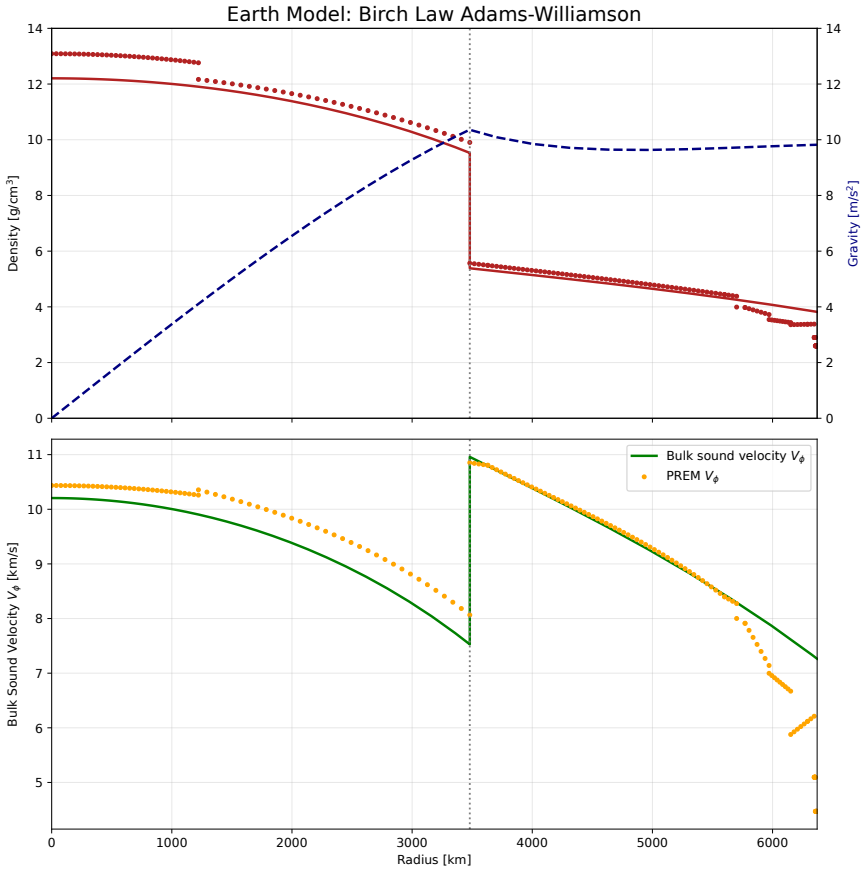

Figure 2.11: Estimated density structure and bulk sound velocity. PREM values are shown for reference. Birch's law was assumed, and the Adams–Williamson equation alongside the gravity profile was integrated outward from Earth's center.

2.10.4 Seismic velocities in other planets: Planetary free oscillations

In the case of Earth, the Adams–Williamson equation has historically been used to estimate density structures from seismic wave velocity structures, since the latter is far more constrained than the former. When performing seismology on other planets, the situation is reversed. For many planets, although gravity can be accurately restrained through remote sensing, no empirical seismic observations exist. Being able to estimate seismic wave velocity structures by positing density bounds is extremely critical when initiating seismology for a new planet.

Here, let us consider an elastic free oscillation of a planet. As estimated earlier, if the planet's radius is R_p, its aggregate seismic wave velocity is bounded by $c_s = \sqrt{gR_p}$. Letting the average density be $\bar{\rho}$, gravitational acceleration g is given by:

$$g = \frac{4\pi}{3} G\bar{\rho} R_p. \tag{2.95}$$

Substituting this yields:

$$c_s = \sqrt{\frac{4\pi}{3} G\bar{\rho}} R_p. \tag{2.96}$$

We can estimate the fundamental eigenperiod T of elastic free oscillation as:

$$T = \frac{2\pi R_p}{c_s} = \frac{2\pi}{\sqrt{\frac{4\pi}{3} G\bar{\rho}}} = \sqrt{\frac{3\pi}{G\bar{\rho}}}. \tag{2.97}$$

The average density is roughly 5×10^3 kg/m^3 for terrestrial solid planets, and 1×10^3 kg/m^3 for gas giants and the Sun. Thus, the fundamental period of elastic free oscillations spans approximately 1000–5000 seconds. From this, we realize that while planets might differ radically in size, their global elastic oscillations share roughly the same temporal scale.

Planet / Composition	Density
Mercury	5.43×10^3 kg/m^3
Earth	5.51×10^3 kg/m^3
Venus	5.24×10^3 kg/m^3
Mars	3.93×10^3 kg/m^3
Jupiter	1.33×10^3 kg/m^3
Saturn	0.69×10^3 kg/m^3
Sun	1.41×10^3 kg/m^3

Table 2.1: Average density of the Sun and the planets.

2.10.5 Power-law equation of state: Towards an understanding of generalized planets

In this subsection, we look into generalized equations of state to evaluate various types of planets, including gas giants.

A generalized equation of state relating pressure P and density ρ is posited via a power law:

$$P - P_0 \propto \left(\frac{\rho}{\rho_0}\right)^{\gamma} = \left(\frac{\rho}{\rho_0}\right)^{1+\frac{1}{n}} \tag{2.98}$$

$$\left(\frac{c_s}{c_0}\right)^2 \propto \left(\frac{\rho}{\rho_0}\right)^{\gamma-1} = \left(\frac{\rho}{\rho_0}\right)^{\frac{1}{n}}. \tag{2.99}$$

Here, n represents the polytropic index. Larger values of n imply a gaseous behavior, whereas lower values of n indicate solid behaviors. ρ_0, c_0, and P_0 correspond to surface reference values.

Isothermal atmosphere: $n = \infty$

For $\gamma = 1$ ($n = \infty$), the equation of state is:

$$(c_s)^2 \propto \rho^{\gamma-1} = \text{constant}. \tag{2.100}$$

Since the speed of sound is proportional to the square root of temperature, this configuration proves an isothermal atmospheric structure.

Stability limit: $n = 3$

Through dimensional analysis, overall mass M and radius R subject to zero-density bounds follow:

$$M \propto R^{\frac{3-n}{1-n}}. \tag{2.101}$$

For simplicity, we define the radius R at the shell where density extinguishes to 0. Under $n = 3$, M ceases to depend on R. The existence of equivalent total masses at assorted radii implies that infinitesimally smaller sizes become more gravitationally stable. This incites a sudden instability causing rapid planetary deflation once compression starts.

Monatomic ideal gas: $n = 1.5$

For the adiabatic expansion of a monatomic ideal gas, $\gamma = 5/3$ ($n = 1.5$), which gives the equation of state:

$$(c_s)^2 \propto \rho^{\frac{1}{3}}. \tag{2.102}$$

Bullen's density model: $n = 1$

This model was deployed by Bullen to approximate the Earth entirely in a single uniform shell. From $M \propto R^{\frac{3-n}{1-n}}$, setting $n = 1$ enforces that the radius loses density dependence limitlessly. For $n < 1$, heavier masses yield smaller radii, whereas for $n > 1$, heavier masses swell the target radius. Hence, $n = 1$ partitions gaseous and solid behaviors. The coupled equation of state reads:

$$(c_s)^2 \propto \rho. \tag{2.103}$$

In this scenario, an analytical solution exists, modeling the density configuration as:

$$\rho(r) = \rho_c \frac{\sin \xi_0 r}{\xi_0 r}, \tag{2.104}$$

where $\xi_0 = \sqrt{4\pi G\rho}/c_s$.

Solid (rock) planetary model: $n = 1/3$

The equation of state corresponds to:

$$(c_s)^2 \propto \rho^3. \tag{2.105}$$

As observable from $c_s = \sqrt{gH_\rho}$, a softened surface velocity parameter c_0 reduces the density scale height H_ρ, localizing lower velocities exclusively along outer surface layers.

§2.11 Boundary conditions

When we solve equations of motion, the boundary conditions are indispensable. Lagrangian description of the boundary conditions is natural. However, we do not take care of the difference when we do not consider initial stress.

2.11.1 Solid-solid boundaries such as Moho and 660 km discontinuity

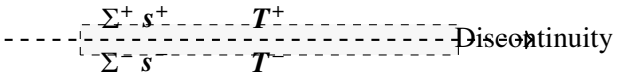

Figure 2.12: Schematic figure of a plane Σ^+ and Σ^-.

Let us consider a pair of closely placed planes Σ^+ and Σ^- encompassing the boundary. The equilibrium of forces and the continuity of displacement within this intermediate region yield the fundamental boundary conditions that must be satisfied across any internal discontinuity in an elastic body.

First, by requiring physical continuity, the continuity of displacement is imposed as $[\boldsymbol{s}]^+_- = \boldsymbol{0}$. This means that material particles across the boundary remain continuously attached without separating or interpenetrating each other after deformation. Next, regarding mechanical interaction, the continuity of total traction must hold, leading to $[\boldsymbol{T}^{L1} \cdot \hat{\boldsymbol{n}}]^+_- = \boldsymbol{0}$. Following the principle of action and reaction, the force per unit area transmitted through the normal vector $\hat{\boldsymbol{n}}$ must perfectly balance across the boundary. These conditions are the most fundamental constraints determining how elastic waves reflect and transmit at discontinuous boundaries.

2.11.2 Solid-fluid boundaries such as ocean floor and core-mantle boundary

At solid-fluid boundaries (such as the seafloor or the core-mantle boundary), the formulation of boundary conditions is of critical importance. In particular, when the fluid is treated as an ideal inviscid fluid, free slip along the solid wall is permitted, which fundamentally distinguishes it from a pure solid-solid boundary. At this interface, the continuity of displacement is first imposed as $[\boldsymbol{s} \cdot \hat{\boldsymbol{n}}]^+_- = 0$. This ensures that the normal component of displacement is identical on both sides, preventing any cavitation or overlap at the boundary. However, a discontinuity in the components parallel to the boundary, or **slip**, is permitted. This horizontal discontinuity allows the existence of special waves where energy is strictly localized near the boundary. The **Stoneley mode**, which will be detailed in the next chapter, is a prime example of this; its energy is concentrated at the seafloor and the CMB, making it notoriously difficult to detect from surface observation networks.

https://www.eri.u-tokyo.ac.jp/people/knishida/eng/seismology.html

Next, the mechanical balance is defined by the continuity of total traction, denoted as $[\boldsymbol{T}^{L1} \cdot \hat{\boldsymbol{n}}]^+_- = \hat{\boldsymbol{n}}[\hat{\boldsymbol{n}} \cdot \boldsymbol{T}^{L1} \cdot \hat{\boldsymbol{n}}]^+_- = \boldsymbol{0}$. Crucially, because shear stress is always zero in the fluid, the traction transmitted across the boundary is strictly limited to the pressure component in the normal direction. Note that when dealing with systems dominated by massive initial stress or hydrostatic pressure, such as deep inside the Earth, these contributions cannot be neglected and require extra care in formulation.(1)

2.11.3 Continuity of gravity potential for all boundaries

When addressing vibration problems in elastic bodies involving self-gravity, boundary conditions require meticulous formulation. Inherently, representing elastic deformations is most naturally handled using the Lagrangian description, which tracks material points. Contrarily, describing fields such as gravitational potentials naturally necessitates the Eulerian description, which is referenced to fixed spatial points. In typical problems where initial stress is negligible, differentiating between these two descriptions is rarely required. However, when accommodating self-gravitation involving the perturbation of the gravitational potential ϕ, the discrepancy between both definitions directly infuses into the structure of boundary conditions. Particularly at discontinuity surfaces, boundary conditions are consolidated utilizing the Eulerian perturbation of potential ϕ^{E1} as follows.

First, because the gravitational potential itself must remain smoothly continuous across the discontinuity surface, the continuity condition for the potential acts as $[\phi^{E1}]^+_- = 0$. Next, concerning the continuity condition for the vertical component of gravity, the alteration in mass geometry (the effect of the density discontinuity) accompanying boundary displacement must be evaluated. This manifests as a combination between the jump in the potential's gradient and terms dependent on both the displacement vector $\boldsymbol{s}$ and the background density ρ_0, formulated as $[\boldsymbol{n} \cdot \nabla\phi^{E1} + 4\pi G\rho_0 \boldsymbol{n} \cdot \boldsymbol{s}]^+_- = 0$. Detailed inspections corresponding to the rigorous separation of these descriptions are examined thoroughly later in subsequent chapters.

Let us estimate the order of each term of the equations of motion for a wave $s = e^{i(kx-\omega t)}$, where ω is the angular frequency and k is the wavenumber. The inertia term is $\rho\partial_t^2 s \approx -\rho\omega^2 s$. The elasticity term $\nabla \cdot \boldsymbol{T}$ is estimated as $k^2\kappa s$, where κ is a typical elastic constant. The gravity term corresponds to the second term on the right side of Eq. (2.62), which relates to buoyancy and is estimated as ρksg. Here, g is gravity acceleration. A comparison between the gravity term and the elasticity term is given by,

$$\frac{\text{Gravity}}{\text{Elasticity}} \sim \frac{\rho g}{k\kappa} = \frac{\rho g\lambda}{4\pi\kappa} = \frac{\rho g\lambda c^2}{4\pi\kappa c^2} = \frac{gT}{4\pi c}. \tag{2.106}$$

where we used wavelength λ, period T, and typical seismic wave velocity c. For the gravity term to be significant, the time scale must be $T \sim \frac{4\pi c}{g}$. As estimated earlier, a typical seismic wave velocity c can be approximated as $\sqrt{gR_e}$ using the Earth's radius R_e. From this relation[note 13)], the period T where gravity and elasticity become comparable is:

$$T \sim \frac{4\pi c}{g} = \frac{4\pi R_e}{c} \sim \frac{4\pi \times 6400 \times 10^3}{10 \times 10^3} \sim 8000 \text{ s}. \tag{2.107}$$

note 13) Using $g = c^2/R_e$.

This is consistent with the periods of the Earth's longest-period fundamental modes (free oscillations), demonstrating that we can safely neglect the gravity term for periods shorter than 100 s. For acoustic waves in the atmosphere (sound velocity ~ 340 m/s), the gravity term becomes comparable to the compressibility term at a period of about 200 s (acoustic-gravity waves).

Next, let us consider the effect of **self-gravity** (the perturbation of the gravitational potential ϕ^{E1}). This corresponds to the third term on the right side of Eq. (2.62). Its magnitude is on the order of $\rho\nabla\phi^{E1} \sim \rho k\phi^{E1} \sim \rho k\left(\frac{4\pi G\rho}{k^2}s\right) = 4\pi\frac{G\rho^2}{k}s$ (where we used Poisson's equation to convert ϕ^{E1}). Comparing this self-gravity term with the elasticity term yields:

$$\frac{\text{Self-gravity}}{\text{Elasticity}} \sim 4\pi\frac{\rho^2 G}{k^2\kappa} = \frac{4\pi G\rho}{k^2c^2} = \frac{3g}{R_e k^2 c^2}, \tag{2.108}$$

where we used the relation $4/3\pi\rho G R_e \sim g$. Using the typical velocity $c \sim \sqrt{gR_e}$, the period T where self-gravity and elasticity become comparable is:

$$T \sim \frac{2\pi R_e}{\sqrt{3}c} \approx \frac{2\pi R_e}{c}. \tag{2.109}$$

This also indicates an order of magnitude of several thousand seconds.

At periods longer than 1000 s, Coriolis force originating from Earth's rotation is not negligible. In such a case, seismic wave velocity depends on the propagation direction[note 14)]. Figure 2.13 shows the splitting of resonant peaks of ${}_0S_2$ due to Coriolis force during when 2004 Sumatra–Andaman earthquake. The directivity breaks the reciprocity of elastic Green's function, which is explained in the following chapter (see Dahlen and Tromp 1998 for details). Read Snieder *et al.* (2016)[10] for details of the Coriolis effects.

Problem 2.9

Based on a comparison of the Coriolis term and elastic restoration force, estimate the period at which the Coriolis force becomes significant.

[note 14)] An example of the 1960 great Chilean earthquake can be found in The Feynman lectures on physics http://www.feynmanlectures.caltech.edu/I_51.html. We can imagine the atmosphere of Caltech in 1960'

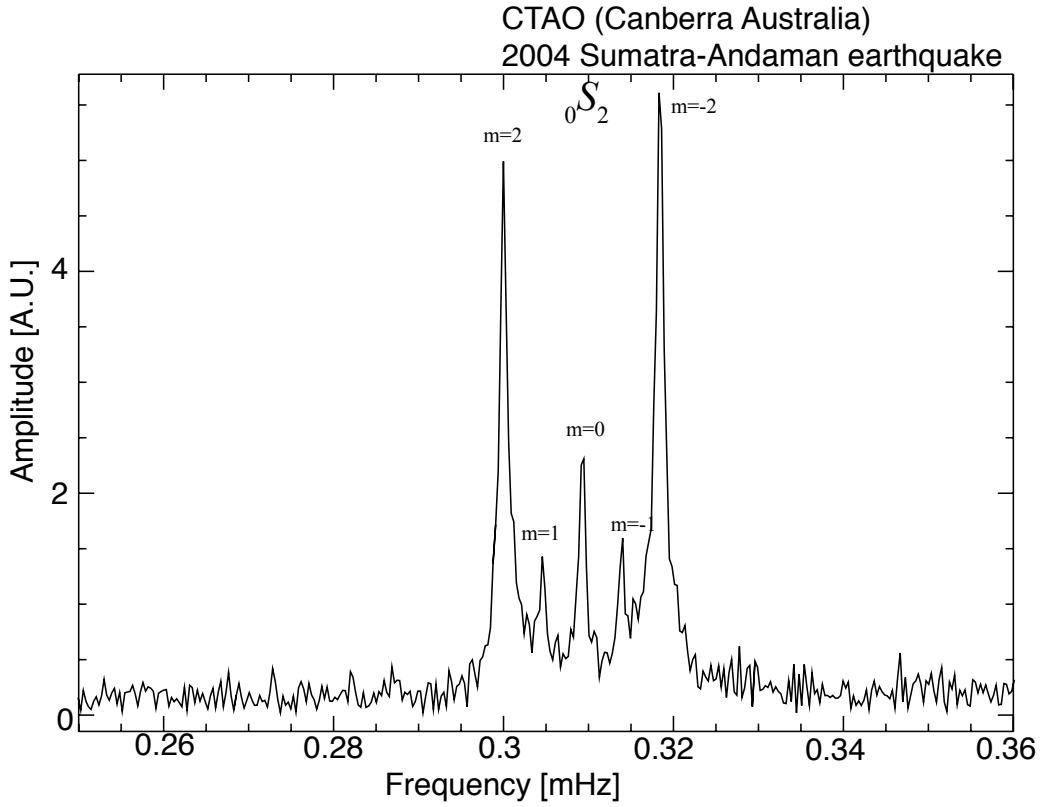

Figure 2.13: Coriolis splitting of the resonant peak of $_0S_2$ when the great Sumatra-Andaman earthquake in 2004.

§2.12 Bibliography

[1] F.A. Dahlen and J. Tromp. *Theoretical Global Seismology*. Princeton University Press, Princeton, 1998.

[2] Fukue, J., Wada, K., and Umemura, M. *Fundamentals of Cosmic Fluid Dynamics [Revised Edition]*. October 2022.

[3] Shun-Ichiro Karato. *Deformation of earth materials: An introduction to the rheology of solid earth*. Cambridge University Press, Cambridge, England, July 2012.

[4] D. Kobayashi, T. Yoshikawa, M. Matsuo, R. Iguchi, S. Maekawa, E. Saitoh, and Y. Nozaki. Spin current generation using a surface acoustic wave generated via spin-rotation coupling. *Phys. Rev. Lett.*, 119:077202, Aug 2017.

[5] L.D. Landau, E.M. Lifshitz, A.M. Kosevich, J.B. Sykes, L.P. Pitaevskii, and W.H. Reid. *Theory of Elasticity*. Course of theoretical physics. Elsevier Science, 1986.

[6] William Lowrie and Andreas Fichtner. *Fundamentals of geophysics*. Cambridge University Press (Virtual Publishing), Cambridge, England, 3 edition, January 2020.

[7] E A Okal and D L Anderson. Theoretical models for mars and their seismic properties. *Icarus*, 33(3):514–528, 1978.

[8] F. Omori. On the relation between the duration of the preliminary tremor and the epicentral distance for near earthquakes. *Bulletin of the Imperial Earthquake Investigation Committee*, 9(1):33–39, mar 1918.

[9] Jean-Paul Poirier. *Introduction to the physics of the earth's interior*. Cambridge University Press, Cambridge, England, 2 edition, January 2005.

[10] Roel Snieder, Christoph Sens-Schönfelder, Elmer Ruigrok, and Katsuhiko Shiomi. Seismic shear waves as Foucault pendulum. *Geophys. Res. Lett.*, 43(6):2576–2581, mar 2016.

[11] Frank D Stacey and Paul M Davis. *Physics of the earth*. Cambridge University Press, Cambridge, England, 4 edition, August 2008.

Green's function and representation theorem

Chapter 3

Green's function is useful when considering seismic wavefield excited by an event. This chapter explains a framework for interpreting seismic wavefields excited by various events, such as earthquakes and volcanic eruptions, using the representation theorem , which can be regarded as a natural extension of Huygens's principle . First, an acoustic (scalar) wave treatment is explained, then an elastic (vector) wave treatment is explained briefly.

§3.1 A solution of the wave equation in 1-D medium

First, let us consider the simplest case of a wave equation: 1-D wave equation. Here we consider acoustic wave propagations. The elastic constant κ and density ρ are homogeneous for simplicity. Pressure fluctuation p satisfies the following wave equation:

$$\frac{1}{\alpha^2}\frac{\partial^2 p(x,t)}{\partial t^2} - \frac{\partial^2 p}{\partial x^2} = 0, \tag{3.1}$$

where α is sound speed given by $\alpha = \sqrt{\kappa/\rho}$.

For understanding, the wave equation is mapped into the time-frequency domain by Fourier transform. The Fourier component $P(k,\omega)$ of the pressure fluctuation becomes a function of wavenumber k and the angular frequency ω as:

$$\left(\frac{\omega^2}{\alpha^2} - k^2\right) P(k,\omega) = 0. \tag{3.2}$$

Thus P must satisfy a dispersion relation $\omega^2/\alpha^2 - k^2 = 0$. Here we consider one Fourier component $P(k,\omega)e^{i(\omega t + kx)}$. Because the dispersion relation leads to $k = \pm\omega/\alpha$, the The Fourier component can be rewritten as $P(k,\omega)e^{i(\omega(t\pm x/\alpha))}$, which represents the propagation toward the positive and negative directions of the x axis, respectively.

d'Alembert solution

Let us evaluate the behaviors of the solution more mathematically. With changes of variables; $\xi = x - \alpha t$, $\eta = x + \alpha t$, the solution of the 1-D wave equation can be represented by the arbitrary function ϕ and ψ as,

$$p(x,t) = \phi(x - \alpha t) + \psi(x + \alpha t). \tag{3.3}$$

The first term of the right-hand side represents the propagation toward the positive direction along the x axis, whereas the second term represents that toward the negative one.

Initial value problem

Let us consider how to solve the problem for the initial value at $t = 0$ given by

$$p(x,0) = p_0(x), \tag{3.4}$$

$$\left.\frac{\partial p}{\partial t}\right|_{t=0} = q_0(x). \tag{3.5}$$

By comparing the initial value with the d'Alembert solution as

$$p_0 = \phi(x,0) + \psi(x,0) \tag{3.6}$$

$$q_0 = -\alpha\left(\frac{\partial \phi}{\partial x} - \frac{\partial \psi}{\partial x}\right). \tag{3.7}$$

Integrating equation 3.7 leads to the solutions for ϕ and ψ. By the insertion of ϕ and ψ, we obtain the solution $p(x,t)$ as,

$$p(x,t) = \frac{1}{2}\left[p_0(x - \alpha t) + p_0(x + \alpha t)\right] + \frac{1}{2\alpha}\int_{x-\alpha t}^{x+\alpha t} q_0(x')dx'. \tag{3.8}$$

Problem 3.1

1. Derive equation 3.3.
2. When p meets the initial condition at $t = 0$ given by

$$p(x, 0) = e^{-\frac{x^2}{\sigma^2}} \tag{3.9}$$

$$\frac{\partial p(x, 0)}{\partial x} = 0 \tag{3.10}$$

   solve and plot the solution.

3. When p meets the initial condition at $t = 0$ given by

$$p(x, 0) = 0, \tag{3.11}$$

$$\left.\frac{\partial p(x, t)}{\partial t}\right|_{t=0} = e^{-\frac{x^2}{\sigma^2}}, \tag{3.12}$$

   solve and plot the solution.

§3.2 Acoustic Green's function

An external force can represent the excited waves when considering seismic waves caused by geophysical phenomena such as earthquakes and volcanoes. In this case, we can evaluate the excited wave motion by considering the impulse response (Green's function) to the external force and by convolving the spatiotemporal distribution of the external force. This section first shows the features of Green's function.

First, let us consider acoustic wave propagation for essential understanding. Equation of motions and Hook's law ($\kappa \nabla \cdot \boldsymbol{s} = -p$) lead to a wave equation concerning pressure perturbation $p(\boldsymbol{x}, t)$ as,

$$-\nabla \cdot \frac{\nabla p(\boldsymbol{x}, t)}{\rho_0(\boldsymbol{x})} + \frac{1}{\kappa(\boldsymbol{x})} \frac{\partial^2 p(\boldsymbol{x}, t)}{\partial t^2} = -\nabla \cdot \left(\frac{\boldsymbol{f}(\boldsymbol{x}, t)}{\rho_0(\boldsymbol{x})} \right). \tag{3.13}$$

Here we consider a Green's function $g(\boldsymbol{x}, t; \xi, \tau)$, which is an impulse response for impulsive force $\delta(\boldsymbol{x} - \xi)\delta(t - \tau)$[note 1)] as

$$-\nabla \cdot \frac{\nabla g(\boldsymbol{x}, t; \xi, \tau)}{\rho_0(\boldsymbol{x})} + \frac{1}{\kappa(\boldsymbol{x})} \frac{\partial^2 g(\boldsymbol{x}, t; \xi, \tau)}{\partial t^2} = -\delta(\boldsymbol{x} - \xi)\delta(t - \tau). \tag{3.14}$$

Problem 3.2

Explain the physical meaning of the external force term $-\delta(\boldsymbol{x} - \boldsymbol{\xi})$ of equation 3.14 (divergence of the particle velocity $\nabla \cdot \boldsymbol{v}$).

If the boundary condition is time-independent, the Green's function exhibits time invariance as,

$$g(\boldsymbol{x}, t; \xi, \tau) = g(\boldsymbol{x}, t - \tau; \xi, 0). \tag{3.15}$$

Therefore, the time difference $t - \tau$ is enough variable to represent this problem.

Pressure field $p(\boldsymbol{x}, t)$ can be represented by superposition of Green's function ($g(\boldsymbol{x}, t - \tau; \xi, 0)$) as

$$p(\boldsymbol{x}, t) = \int_V g(\boldsymbol{x}, t; \xi, \tau) \nabla_\xi \cdot \left(\frac{\boldsymbol{f}}{\rho_0} \right) dV(\xi) d\tau. \tag{3.16}$$

note 1)

$$f(0) = \int f(\boldsymbol{x}) \delta(\boldsymbol{x}) dV.$$

Therefore note that the dimension of the delta function in 3D is $1/\mathrm{m}^3$.

https://www.eri.u-tokyo.ac.jp/people/knishida/eng/seismology.html

Next, the representation of the equation in the frequency domain is considered. $P(\omega, \boldsymbol{x})$ shows the Fourier transform of pressure p, and ω is the angular frequency[note 2)]

We do not consider hydrostatic pressure here.

$$\nabla \cdot \frac{\nabla P(\boldsymbol{x}, \omega)}{\rho_0(\boldsymbol{x})} + \frac{\omega^2}{\kappa(\boldsymbol{x})} P(\boldsymbol{x}, \omega) = F(\boldsymbol{x}, \omega), \tag{3.17}$$

where F is Fourier transform of external force term $\nabla \cdot \left(\frac{\boldsymbol{f}(\boldsymbol{x},t)}{\rho_0(\boldsymbol{x})} \right)$.

Green's function in frequency domain satisfies the following equation,

$$\nabla \cdot \frac{\nabla G(\boldsymbol{x}, \xi, \omega)}{\rho_0(\boldsymbol{x})} + \frac{\omega^2}{\kappa(\boldsymbol{x})} G(\boldsymbol{x}, \xi, \omega) = \delta(\boldsymbol{x} - \xi), \tag{3.18}$$

where $G(\boldsymbol{x}, \xi, \omega)$ is Green's function in frequency domain. Then, pressure field P excited by an arbitrary force distribution F can be represented by a convolution between Green's functions and the force distribution as,

$$P = \int_V G(\boldsymbol{x}, \xi, \omega) F(\xi, \omega) dV(\xi). \tag{3.19}$$

§3.3 Green's function in an infinite homogeneous medium

To understand the behaviors of Green's function, this section explains the explicit representation of Green's function. First, let us summarize the basics of the wave equation.

3.3.1 Derivations of Green's function in a 1-D medium

For an infinite homogeneous medium, equation 3.18 can be simplified as,

$$\frac{1}{\rho_0} \frac{\partial^2 G^{1D}}{\partial z^2} + \frac{\omega^2}{\kappa} G^{1D} = \delta(z). \tag{3.20}$$

[note 2)] Take care about definitions of the sign and the normalization of the Fourier transform because the definition depends on the field. Fourier transform $\mathcal{F}$ and inverse Fourier transform $\mathcal{F}^{-1}$ are defined as

$$U(\omega) = \mathcal{F}(u) \equiv \int_{-\infty}^{\infty} u(t) e^{-i\omega t} dt,$$

$$u(t) = \mathcal{F}^{-1}(U) \equiv \frac{1}{2\pi} \int_{-\infty}^{\infty} U(f) e^{i\omega t} d\omega.$$

Details of the definition in this text are shown in the appendix 3.E.

Problem 3.3

1. Solve the equation except for $z = 0$.

2. At $z = 0$, the equation is singular because of the delta function. Integrate equation 3.20 in a rage of $-\epsilon/2 <= z <= \epsilon/2)$. Then derive the following equation,

$$\left[\frac{\partial G^{1D}}{\partial z}\right]_{-\epsilon/2}^{+\epsilon/2} = \rho_0. \tag{3.21}$$

   Note that integration of Green's function in the infinitesimal range is negligible from equation 3.19.

3. By continuation of the two solutions at $z = 0$, derive the following result of 1-D Green's function as,

$$G^{1D}(z,\omega) = \frac{\rho_0 i}{2k} e^{-ik|z|}. \tag{3.22}$$

4. Inverse Fourier transform of G^{1D} show

$$g^{1D}(z,t) = \begin{cases} 0 & t < |z|/\alpha \\ -\frac{\alpha}{2}\rho_0 & t >= |z|/\alpha. \end{cases} \tag{3.23}$$

5. Problem 3.1 (3) gave the initial velocity at $t = 0$. Compare the solution to the above solution of this problem and interpret the physical relation.

Derivation of 1D Green's function using complex integration

Here, we calculate a Fourier transform in the spatial direction and use complex integration to find G^{1D}. For simplicity, we define k_0 as $k_0^2 \equiv \rho_0\omega^2/\kappa$.

Considering the Fourier transform of G^{1D} with respect to space (z), we denote its Fourier component as $\tilde{G}$. When we consider the Fourier transform of the wave equation, the spatial derivative becomes ik using the wavenumber k, thus:

$$\tilde{G} = \frac{\rho_0}{k_0^2 - k^2} \tag{3.24}$$

By considering the inverse Fourier transform, we can find G^{1D}:

$$G^{1D} = \frac{1}{2\pi}\int_{-\infty}^{\infty} \frac{\rho_0}{k_0^2 - k^2} e^{ikz}\, dk \tag{3.25}$$

We need to evaluate this integral using residues. However, as it stands, the first-order poles $(k = \pm k_0)$ lie on the real axis, making evaluation difficult. Therefore, we consider causality and shift the poles to $\pm k_0 \pm i\epsilon$, taking the limit as ϵ approaches zero. Physically, this represents a situation where the wave propagates from the origin to the future, with a slight attenuation in amplitude.

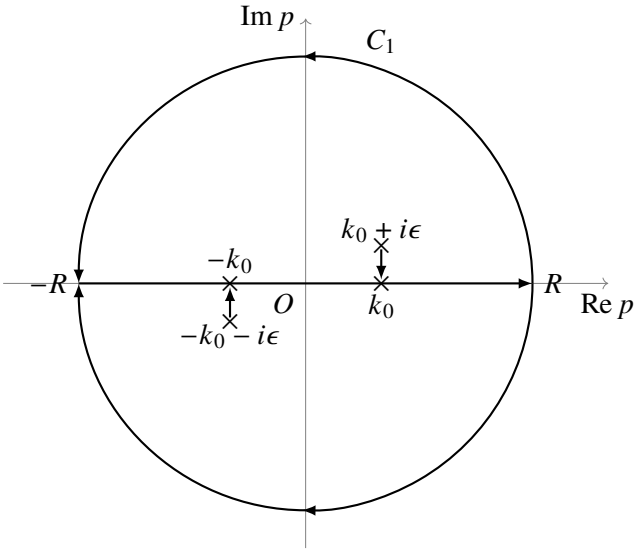

We can calculate G^{1D} as

$$G^{1D}(z,\omega) = \frac{\rho_0 i}{2k_0} e^{-ik_0|z|} \tag{3.26}$$

by evaluating the residue.

3.3.2 Derivations of Green's function in a 2-D medium

Here we consider a cylindrical coordinate (r, ϕ) with origin at $\boldsymbol{xi}$.

$$\frac{1}{\rho_0}\frac{1}{r}\frac{\partial}{\partial r}\left(r\frac{\partial G^{2D}}{\partial r}\right) + \frac{\omega^2}{\kappa}G^{2D} = \delta(\boldsymbol{x} - \boldsymbol{x}_0). \tag{3.27}$$

1. Except for $r = 0$, a solution of equation 3.27can be represented by superposition of 0th order Bessel function of the first kind $J_0(r)$ and 0th order Neumann function $N_0(r)$.

2. At $r = 0$, the equation is singular. Then integrate equation 3.27 at an infinitesimal circular area (C) at around the origin. Using Gauss's divergence theorem, show

$$\int_C \frac{\partial G^{2D}}{\partial r} dl = \rho_0. \tag{3.28}$$

3. By continuation of the two solutions at the origin $r = 0$ derive the following result of 2-D Green's function as

$$G^{2D} = -i\frac{\rho_0}{4} H_0^{(2)}(kr). \tag{3.29}$$

   Here $H_0^{(2)}$ is Hankel's function of the second kind.

4. In the time domain, the corresponding Green's function can be written by,

$$g^{2D}(r,t) = -\frac{\rho_0}{2\pi}\frac{H(t - r/\alpha)}{\sqrt{t^2 - r^2/\alpha^2}}, \tag{3.30}$$

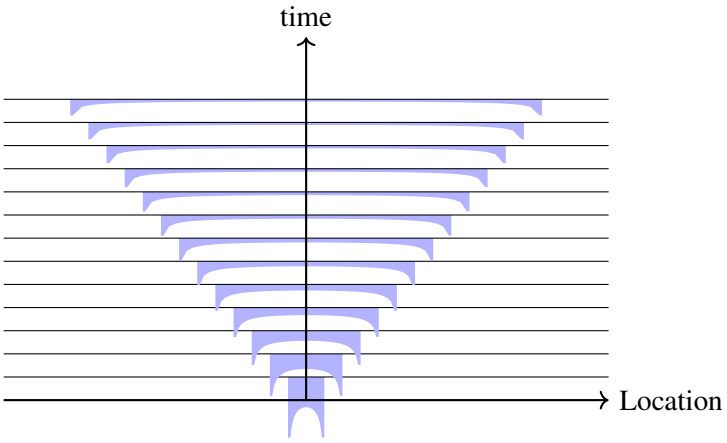

Figure 3.1: Propagation of 2-D Green's function.

where H is the Heaviside step function.

Problem 3.4

1. Show that Hankel function of the first kind can be approximated by a cylindrical wave in far field.
2. Interpret distance dependence of the amplitude based on the conservation of energy.
3. Show the amplitude of 2D Green's function in time domain (equation 3.30) is proportional to $1/\sqrt{r}$ if the distance r is enough long.

3.3.3 Green's function of a 3-D medium

This subsection explains Green's function in a 3-D medium, which describes 3-D wave propagation for the forcing $\delta(\boldsymbol{x})\delta(t)$.

$$-\frac{1}{\rho_0}\frac{1}{r^2}\frac{\partial}{\partial r}\left(r^2\frac{\partial g^{3D}}{\partial r}\right)+\frac{1}{\kappa}g^{3D}\frac{\partial^2}{\partial t^2}=-\delta(\boldsymbol{x})\delta(t) \tag{3.31}$$

To consider the amplitude, first, let us consider the d'Alembert solution[note 3)]. With a change of the variable as $p=\bar{p}/r$, the solution is given by,

$$p=\frac{p_0(t-r/\alpha)}{r}+\frac{p_1(t+r/\alpha)}{r}, \tag{3.32}$$

[note 3)] In general, behaviors of solution of wave equations in even dimensions are quite different from those in odd dimensions. The former is localized close to the wavefront and lasts for a long time.

https://www.eri.u-tokyo.ac.jp/people/knishida/eng/seismology.html

which represents spherical waves outward and inward. The amplitude decays with $1/r$. The distance-dependent is also given by energy conservation on the expanding (or shrinking) wavefront.

Green's function in a 3-D medium is given by

$$g^{3D}(r,t) = -\frac{\rho_0}{4\pi}\frac{\delta(t-r/\alpha)}{r}. \tag{3.33}$$

See Problem 3.5 for the derivation.

Problem 3.5

Here we consider a spherical coordinate (r,θ,ϕ) with origin at $\boldsymbol{\xi}$.

$$\frac{1}{\rho_0}\frac{1}{r^2}\frac{\partial}{\partial r}\left(r^2\frac{\partial G^{3D}}{\partial r}\right) + \frac{\omega^2}{\kappa}G^{3D} = \delta(\boldsymbol{x}-\boldsymbol{\xi}) \tag{3.34}$$

1. With a change of variable as $G^{3D} = \bar{G}/r$, rewrite the above equation.
2. Solve the equation except $r = 0$.
3. At $r = 0$, the solution is singular. Integrate equation 3.18 within an infinitesimal sphere. Then show the following equation

$$\int_\Sigma \frac{\partial G^{3D}}{\partial r} d\Sigma = \rho_0, \tag{3.35}$$

   using Gauss's divergence theorem.
4. By continuation of the two solutions at the origin $r = 0$ derive the following result of 3-D Green's function as,

$$G^{3D} = -\frac{\rho_0}{4\pi}\frac{e^{-ikr}}{r} \tag{3.36}$$

5. Calculate inverse Fourier transform the above equation.

3.3.4 †Green function in n-dimension space

The 2-D Green's function behaves quite differently from the 1-D and 3-D Green's functions. In this section, we will investigate these differences by examining the properties of the Green's function for the general n-dimensional wave equation. This section contains advanced material, so you may skip it.

Relationship between 3-D and 1-D Green's functions

In the 3-D case, we consider

$$\frac{1}{\rho_0}\frac{1}{r^2}\frac{\partial}{\partial r}\left(r^2\frac{\partial G^{3D}}{\partial r}\right)+\frac{\omega^2}{\kappa}G^{3D}=\frac{\delta^+(r)}{4\pi r^2}. \tag{3.37}$$

By defining $G^{3D}=\Psi/r$ and rearranging the equation, we obtain

$$\begin{aligned}\frac{1}{\rho_0}\frac{\partial^2\Psi}{\partial r^2}+\frac{\omega^2}{\kappa}\Psi&=\frac{\delta^+(r)}{4\pi r}\\&=-\frac{1}{4\pi}\frac{d\delta^+(r)}{dr}.\end{aligned} \tag{3.38}$$

Looking closely at this equation, the left-hand side is in the form of a 1-D wave equation. Therefore, we can see that Ψ can be written in the form of a convolution with respect to r between the 1-D Green's function and the derivative of the delta function:

$$\begin{aligned}\Psi&=-\frac{1}{4\pi}G^{1D}*\frac{d\delta^+}{dr}\\&=-\frac{2}{4\pi}\frac{\partial G^{1D}}{\partial r}\\&=-\frac{1}{2\pi}\frac{\partial G^{1D}}{\partial r}.\end{aligned} \tag{3.39}$$

Here, we multiplied by 2 at the end because the corresponding Green's function G^{1D} is defined on both sides of 0 with respect to the variable. Ultimately, the 3-D and 1-D Green's functions can be connected by the relation

$$G^{3D}=-\frac{1}{2\pi r}\frac{\partial G^{1D}}{\partial r}. \tag{3.40}$$

This can be confirmed from the Green's function derived previously using a different method.

Relationship between n-D and $(n+2)$-D Green's functions

For the n-D Green's function, we consider the n-D wave equation. Assuming the Green's function is symmetric about the origin, integrating over all directions other than r in polar coordinates yields

$$S_n\frac{1}{r^{n-1}}\frac{\partial}{\partial r}\left(r^{n-1}\frac{\partial G^n}{\partial r}\right)+k_0^2G^n=\frac{\delta^+(r)}{\rho_0 r^{n-1}}. \tag{3.41}$$

Here, S_n represents the surface area of the n-dimensional unit sphere, which appears because we fixed r and integrated over the other coordinates. Additionally, S_n satisfies the recurrence relation

$$S_n=\frac{2\pi^{n/2}r^{n-1}}{\Gamma\left(\frac{n}{2}\right)}, \tag{3.42}$$

and it also satisfies the relationship

$$S_{n+2} = \frac{2\pi}{n} S_n. \tag{3.43}$$

The 3-D wave equation could be connected to the 1-D solution by a simple relation. Can we connect the $(n+2)$-D solution and the n-D solution in general? In fact, it is possible. By a somewhat heuristic approach, if we define Ψ^n as

$$\Psi^n \equiv \frac{1}{r}\frac{\partial G^n}{\partial r} \tag{3.44}$$

and apply the $(n+2)$-D Laplacian, simple partial differentiation leads to

$$\frac{1}{r^{n+1}}\frac{\partial}{\partial r}\left(r^{n+1}\frac{\partial \Psi^n}{\partial r}\right) = \frac{1}{r}\frac{\partial}{\partial r}\left(\frac{1}{r^{n-1}}\frac{\partial}{\partial r}\left(r^{n-1}\frac{\partial \Psi^n}{\partial r}\right)\right). \tag{3.45}$$

In other words, if we take the partial derivative of both sides of the n-D wave equation (eq. 3.41) with respect to r and divide by r, we can write

$$\frac{1}{r^{n+1}}\frac{\partial}{\partial r}\left(r^{n+1}\frac{\partial \Psi^n}{\partial r}\right) + k_0^2 \Psi^n = \frac{1}{\rho_0 S_n}\frac{1}{r}\frac{d}{dr}\left(\frac{\delta^+}{r^{n-1}}\right). \tag{3.46}$$

Let us evaluate the right-hand side. Omitting the constants, we obtain

$$\frac{1}{r}\frac{d}{dr}\left(\frac{\delta^+}{r^{n-1}}\right) = -(n-1)\frac{\delta^+}{r^{n+1}} + \frac{d\delta^+}{dr}\frac{1}{r^n} = -n\frac{\delta^+}{r^{n+1}}. \tag{3.47}$$

Here we used the derivative formula for the delta function. Rearranging the equation using $S_{n+2} = 2\pi S_n/n$, we obtain

$$\frac{1}{r^{n+1}}\frac{\partial}{\partial r}\left(r^{n+1}\frac{\partial \Psi^n}{\partial r}\right) + k_0^2 \Psi^n = -2\pi\frac{\delta^+}{\rho_0 S_{n+2} r^{n+1}}. \tag{3.48}$$

From this, we can see that

$$G^{n+2} = -\frac{1}{2\pi}\frac{1}{r}\frac{\partial G^n}{\partial r} \tag{3.49}$$

satisfies the $(n+2)$-D wave equation. This means that for odd-dimensional Green's functions, the energy is concentrated at the wavefront, and Huygens' principle can be applied (secondary wave sources can be uniquely determined). In the case of odd dimensions, the Green's function can be written as

$$G^n = \left(-\frac{1}{2\pi}\frac{1}{r}\frac{\partial}{\partial r}\right)^{\frac{n-1}{2}} G^{1D}. \tag{3.50}$$

In the case of even dimensions, fractional derivatives formally appear, indicating that it cannot be simply connected to G^{1D}. In general, it can be written as

$$G^n = -\frac{i\rho_0}{4}\left(\frac{1}{2\pi}\frac{k}{r}\right)^{\frac{n}{2}-1} H^{(2)}_{\frac{n}{2}-1}(kr). \tag{3.51}$$

Here, $H_\nu^{(2)}$ is the Hankel function of the second kind[note 4)].

Problem 3.6

1. The pressure response for forcing $f(\boldsymbol{x}) = \delta(z)$ in a 3-D medium can be interpreted by 1-D Green's function. Based on this fact, show the relation between 1-D Green's function and 3-D Green's function.

2. Equation 3.30 shows 2-D Green's function does not go zero after the arrival of the wavefront. Derive 2-D Green's function from the 3-D Green's function based on 3-D Green's function with a line source given by $\delta(r)$.

[note 4)] It can be derived using the equations in Appendix 3.C.

§3.4 Green's function in a homogeneous elastic medium

Let us consider the equation of motions

$$\rho \frac{\partial^2}{\partial t^2} s_i = \frac{\partial}{\partial x_j} T_{ij} + f_i. \tag{3.52}$$

Here we neglect self-gravitation and initial stress.

For an **isotropic and homogeneous elastic body**, the equation can be simplified as,

$$\begin{aligned} \rho \partial_t^2 \boldsymbol{s} &= (\lambda+\mu)\nabla(\nabla\cdot\boldsymbol{s}) &&+\mu\nabla^2\boldsymbol{s} &&+\boldsymbol{f} \\ &= \underbrace{(\lambda+2\mu)\nabla(\nabla\cdot\boldsymbol{s})}_{Pwave} &&\underbrace{-\mu(\nabla\times\nabla\times\boldsymbol{s})}_{Swave} &&+\boldsymbol{f} \end{aligned} \tag{3.53}$$

The first term of the right-hand side represents the P wave with volumetric changes, whereas the second one represents the S wave with shear deformation. Later we consider a homogeneous and isotropic medium

3.4.1 Elastic potential: Separation between P save and S wave

In order to clarify the perspective, displacement $\boldsymbol{s}$ is written by scalar potential ϕ[note 5)] and vector potential $\boldsymbol{\psi}$ using Helmholtz's theorem as

$$\boldsymbol{s} = \nabla\phi + \nabla\times\boldsymbol{\psi}. \tag{3.54}$$

I note that vector potential $\boldsymbol{\psi}$ has ambiguity for the choice of the reference. Vector potential $\boldsymbol{\psi}' \equiv \boldsymbol{\psi} + \nabla\chi$ leads to $\nabla\times\boldsymbol{\psi}' = \nabla\times\boldsymbol{\psi}$. For static magnetic field, we choose a vector potential as $\nabla\cdot\boldsymbol{\psi}$ in general. In the case of an electromagnetic field, vector potential is related to the scalar potential for each other, whereas, in the case of elastic deformation, they are independent, as shown in later sections. In the case of an elastic wave field, we can separate the P wave and S wave without the choice of a reference of vector potential as $\nabla\times\psi = 0$. For example, for a stratified medium described in later chapters, a form of vector potential as $\nabla\times(\psi+\nabla\times\chi)$ becomes convenient because the two terms (ϕ and χ) represent horizontally polarized S waves (SH) and vertically polarized S waves (SV), respectively.(4)

Insertion of equation 3.54 into equation 3.53 leads to

$$\begin{cases} \nabla^2\left(\rho\dfrac{\partial^2\phi}{\partial t^2} - (\lambda+2\mu)\nabla^2\phi\right) = \nabla\cdot\boldsymbol{f} \\ \nabla\times\nabla\times\left(\rho\dfrac{\partial^2\boldsymbol{\psi}}{\partial t^2} + \mu\nabla\times\nabla\times\boldsymbol{\psi}\right) = \nabla\times\boldsymbol{f} \end{cases} \tag{3.55}$$

[note 5)] Based on the definition, the scalar potential ϕ can be related to pressure $p = -\rho\alpha^2\nabla^2\phi$.

where α is P-wave velocity and β is S-wave velocity ($\lambda + 2\mu = \rho\alpha^2$, $\mu = \rho\beta^2$).

A formula of vector analysis of

$$\nabla \times \nabla \times \boldsymbol{\psi} = \nabla(\nabla \cdot \boldsymbol{\psi}) - \nabla^2 \boldsymbol{\psi} \tag{3.56}$$

and $\nabla \times [\nabla(\nabla \cdot \boldsymbol{\psi})] = 0$ lead to

$$\nabla \times \nabla \times \left(\rho \frac{\partial^2 \boldsymbol{\psi}}{\partial t^2} - \mu \nabla^2 \boldsymbol{\psi} \right) = \nabla \times \boldsymbol{f}. \tag{3.57}$$

Similarly, the Helmholtz decomposition of $\boldsymbol{f}$ is given by

$$\boldsymbol{f} = \nabla \Phi + \nabla \times \boldsymbol{\Psi} \tag{3.58}$$

Thus, to satisfy the equation of motions,

$$\begin{cases} \rho \dfrac{\partial^2 \phi}{\partial t^2} - (\lambda + 2\mu) \nabla^2 \phi = \Phi \\ \rho \dfrac{\partial^2 \boldsymbol{\psi}}{\partial t^2} - \mu \nabla^2 \boldsymbol{\psi} = \boldsymbol{\Psi} \end{cases} \tag{3.59}$$

is sufficient [note 6)]. These equations correspond to wave equations of P-wave and S-wave, respectively.

[note 6)] There are also terms for translational motion and rigid body rotation (see Problem 3.7) as solutions, but they can be dropped because they violate the infinitesimal assumption.

Problem 3.7

Let us consider the equation:

$$\nabla^2 \left(\frac{1}{\alpha^2} \frac{\partial^2 \phi}{\partial t^2} - \nabla^2 \phi \right) = 0 \tag{3.60}$$

1. Estimate ϕ_0, which satisfies $\nabla^2 \phi_0(\boldsymbol{x}, t) = 0$.
2. Show that $\phi + \phi_0$ also satisfies equation 3.60.
3. Show that ϕ_0 represents a translational motion when ϕ_0 satisfies equation 3.53.
4. Let us consider the same discussion for the vector potential $\boldsymbol{\psi}_0$ given by

$$\boldsymbol{\psi}_0 = \begin{pmatrix} 0 & r_{xy} & r_{xz} \\ -r_{xy} & 0 & r_{yz} \\ -r_{xz} & -r_{yz} & 0 \end{pmatrix} \begin{pmatrix} x \\ y \\ z \end{pmatrix}, \tag{3.61}$$

which represents a rigid rotation. Based on the discussion for scalar potential, the vector potential satisfies the governing equation. In this text, we drop the effects because they are not first-order variables.

3.4.2 Green's function for an explosive source

In general, an excitation problem in an elastic medium by a force is complicated. In order to understand the important concept of "near field" and "far field", let us consider an excitation problem of elastic waves by an explosion source, which can be described by only a scalar potential. This simple example could be helpful for understanding elastic wave propagation.

First, let us consider Green's function G^{ϕ} for scalar potential ϕ. For an impulsive pressure $\delta(t)$, the Green's function is given by

$$\frac{\partial^2 G^{\phi}(\boldsymbol{x},t;\boldsymbol{\xi},\tau)}{\partial t^2} - \frac{1}{\alpha^2}\nabla^2 G^{\phi} = \delta(\boldsymbol{x}-\boldsymbol{\xi})\delta(t-\tau) \tag{3.62}$$

$$G^{\phi}(\boldsymbol{x},t;\boldsymbol{\xi},\tau) = \frac{1}{4\pi\rho\alpha^2 \mid \boldsymbol{x}-\boldsymbol{\xi} \mid}\delta\left(t-\tau-\frac{\mid \boldsymbol{x}-\boldsymbol{\xi} \mid}{\alpha}\right) \tag{3.63}$$

Near field term and far-field term for a point explosive source

First, let us consider a response for a point explosive source for simplicity. Within an infinitesimal sphere with radius Δr at the origin suddenly increase the pressure Δp at $t = 0$ as,

$$p^{\text{source}}(\boldsymbol{\xi},\tau) = \Delta p(1 - H(r_{\xi} - \Delta r))H(\tau), \tag{3.64}$$

where r_{ξ} is the distance between the origin and $\boldsymbol{\xi}$, and $H(t)$ is Heaviside function[note 7)]. The minus sign originated from the difference between pressure and stress tensor. Because an explosive source cannot cause shear deformation in a homogeneous medium, we consider only scalar potential ϕ here. ϕ can be given by convolution between the Green's function and the source term p^{source} as

$$\begin{aligned}\phi &= \int_{-\infty}^{\infty} G^{\phi}(\boldsymbol{x},t,\boldsymbol{\xi},\tau)p^{\text{source}}(\boldsymbol{\xi},\tau)dV(\boldsymbol{\xi})d\tau \\ &= -\frac{\Delta p\Delta r^3}{3\rho\alpha^2}\frac{H\left(t-\frac{r}{\alpha}\right)}{r}.\end{aligned} \tag{3.65}$$

The displacement $\boldsymbol{s}$ can be represented by gradient of the scalar potential ϕ as

$$s_r = \frac{\Delta p\Delta r^3}{3\rho\alpha^2}\Bigg(\underbrace{\frac{H(t-r/\alpha)}{r^2}}_{\text{Near field term}} + \underbrace{\frac{\delta(t-r/\alpha)}{\alpha r}}_{\text{far field term}}\Bigg). \tag{3.66}$$

The frequency component of the displacement $S(\omega)$ is

$$S_r(\omega) = \frac{\Delta p\Delta r^3}{3(\lambda+2\mu)}\frac{\omega}{\alpha^2}e^{-i\omega\frac{r}{\alpha}}\Bigg(\underbrace{-\frac{i}{(kr)^2}}_{\text{Near field term}} + \underbrace{\frac{1}{kr}}_{\text{far field term}}\Bigg), \tag{3.67}$$

[note 7)] $H(t) = 1, t \geq 0, H(t) = 0, t < 0$

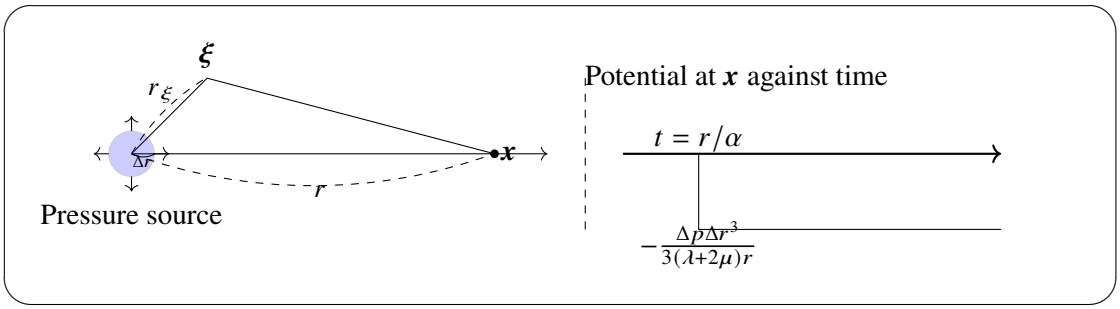

Figure 3.2: Schematic figure of the deformation by the explosive source.

This equation shows that the near-field term dominates at distances shorter than the wavelength.

The displacement of the near field term can be interpreted as static deformation by the incremental pressure at a point. For $t = \infty$ equation 3.62 can be simplified as,

$$\nabla^2 G^\phi = -\alpha^2 \delta(\boldsymbol{x} - \boldsymbol{\xi}). \tag{3.68}$$

The form of this equation is equivalent to a static electric field by a point charge.

The far-field term represents a propagation of the delta function. The amplitude decreases with distance $\sim 1/r$. This result means that net energy flux on a given sphere is constant ($4\pi r^2 (r^{-1})^2$ is constant) against the propagation distance. This result originated from energy conservation owing to the wave propagation.

vspace3cm

Problem 3.8

1. Derive equation 3.65.
2. Derive equation 3.66, and plot the near field term and the far field term.

3.4.3 Green's function of a homogeneous medium for impulsive force: a general case

Green's function is feasible for estimating an elastic response by a general forcing. Let us consider Green's function for an impulsive force $X_0(t)\delta(t)$ in the x direction,

$$\frac{\partial^2}{\partial t^2}\boldsymbol{G} = \alpha^2 \nabla(\nabla \cdot \boldsymbol{G}) - \beta^2 (\nabla \times \nabla \times \boldsymbol{G}) + [\delta(\boldsymbol{x}) X_0(t), 0, 0] \tag{3.69}$$

The external force can also be represented by scalar potentialΦ and vector potential $\boldsymbol{\Psi}$ based on Helmholtz theorem as,

$$[\delta(\boldsymbol{x}) X_0(t), 0, 0] = \nabla\Phi + \nabla \times \boldsymbol{\Psi}. \tag{3.70}$$

div of the both sides of the equation leads to

$$\nabla^2 \Phi = X_0(t) \frac{\partial \delta(\boldsymbol{x})}{\partial x}. \tag{3.71}$$

Here we consider the Green's function (equation 3.3.3) satisfies the following equation:

$$\nabla^2 \left(-\frac{1}{4\pi} \frac{1}{|\boldsymbol{x}|} \right) = \delta(\boldsymbol{x}). \tag{3.72}$$

The comparison leads to [note 8)],

$$\begin{aligned} \Phi &= -\frac{X_0(t)}{4\pi} \frac{\partial}{\partial x} \frac{1}{|\,\boldsymbol{x}\,|} \\ \boldsymbol{\Psi} &= \frac{X_0(t)}{4\pi} \left(0, \frac{\partial}{\partial z} \frac{1}{|\,\boldsymbol{x}\,|}, -\frac{\partial}{\partial y} \frac{1}{|\,\boldsymbol{x}\,|} \right). \end{aligned} \tag{3.73}$$

G can be also represented by a superposition of scalar potential ϕ and vector potential $\boldsymbol{\psi}$ based on Helmholtz theorem as,

$$G = \nabla \phi + \nabla \times \boldsymbol{\psi}. \tag{3.74}$$

Each potential satisfies the wave equation. For example, the scalar potential satisfies the following equation,

$$\frac{\partial^2 \phi}{\partial t^2} = \alpha^2 \nabla^2 \phi + \Phi. \tag{3.75}$$

ϕ can be given by convolution between the scalar Green's function in the 3-D medium and the forcing term Φ (see the first section of this chapter).

The scalar potential can be written by a convolution between the scalar Green's function and Φ as

$$\phi(\boldsymbol{x}, t) = -\frac{1}{(4\pi)^2 \rho \alpha^2} \int_V X_0 \left(t - \frac{|\boldsymbol{x} - \boldsymbol{x}_0|}{\alpha} \right) \frac{1}{|\boldsymbol{x} - \boldsymbol{x}_0|} \frac{\partial}{\partial x_0} \frac{1}{|\boldsymbol{x}_0|} dV_0. \tag{3.76}$$

A change of variables of $|\boldsymbol{x} - \boldsymbol{\xi}| = \alpha\tau$ leads to the following equation:

$$\phi(\boldsymbol{x}, t) = -\frac{1}{(4\pi)^2 \rho \alpha^2} \int_0^\infty \frac{X_0(t-\tau)}{\tau} \left(\iint_S \frac{\partial}{\partial \xi_0} \frac{1}{|\boldsymbol{\xi}|} dS \right) d\tau. \tag{3.77}$$

Here we focus on the integral $\iint dS$. The circle in Figure 3.3 represents a spherical shell with the radius $\alpha\tau$. The surface integral of a potential $1/r$ leads to an analogy to a problem of gravity potential. If the mass is the uniform distribution on a closed shell, the term represents the spatial gradient of the potential along x direction at the origin $\boldsymbol{O}$ (i.e., it corresponds to x component of gravity). Based on the analogy for a problem of gravity, when the point $\boldsymbol{O}$ is inside the shell, the gravity

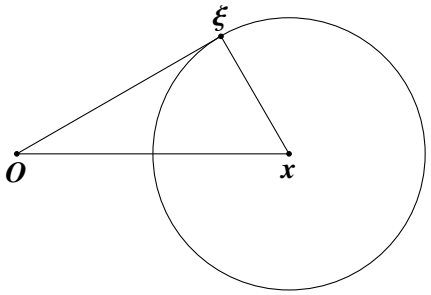

Figure 3.3: Coordinate for evaluation the potential ϕ.

[note 8)] see Aki and Richards[(1)] in details.

is 0. On the other hand, when it is outside the shell, the mass is concentrated at the center $\boldsymbol{x}$ virtually. This result leads to the following form:

$$\phi(\boldsymbol{x},t) = -\frac{1}{4\pi\rho}\left(\frac{\partial}{\partial x}\frac{1}{r}\right)\int_0^{r/\alpha} \tau X_0(t-\tau)d\tau. \tag{3.78}$$

The vector potential is also written similarly. With some calculations, we obtain the potentials as,

$$\begin{cases} \phi(\boldsymbol{x},t) = -\dfrac{1}{4\pi\rho}\left(\dfrac{\partial}{\partial x}\dfrac{1}{r}\right)\displaystyle\int_0^{r/\alpha} \tau X_0(t-\tau)d\tau \\ \boldsymbol{\psi}(\boldsymbol{x},t) = \dfrac{1}{4\pi\rho}\left(0, \dfrac{\partial}{\partial z}\dfrac{1}{r}, -\dfrac{\partial}{\partial y}\dfrac{1}{r}\right)\displaystyle\int_0^{r/\beta} \tau X_0(t-\tau)d\tau. \end{cases} \tag{3.79}$$

By substituting the scalar and vector potentials into $\boldsymbol{s} = \nabla\phi + \nabla\times\boldsymbol{\psi}$, we obtain the following expression:

$$\begin{aligned} s_i(\boldsymbol{x},t) = {} & \frac{1}{4\pi\rho}\left(\frac{\partial}{\partial x_i \partial x}\frac{1}{r}\right)\int_{r/\alpha}^{r/\beta} \tau X_0(t-\tau)d\tau \\ & + \frac{1}{4\pi\rho\alpha^2 r}\left(\frac{\partial r}{\partial x_i}\frac{\partial r}{\partial x}\right) X_0\left(t-\frac{r}{\alpha}\right) \\ & + \frac{1}{4\pi\rho\beta^2 r}\left(\delta_{i1} - \frac{\partial r}{\partial x_i}\frac{\partial r}{\partial x}\right) X_0\left(t-\frac{r}{\beta}\right). \end{aligned} \tag{3.80}$$

The first term represents a near field, the second represents a far field of the P wave, and the third represents a far field of the S wave.

Now let us consider the near and far field terms in more detail. We can determine whether we are near or far based on two timescales: the characteristic time of $X(t)$, and the P-S travel time difference $r/\beta - r/\alpha$. From a simple calculation (see Problem 3.9), when the characteristic time of $X(t)$ is sufficiently smaller than the P-S travel time difference, the second and third terms are proportional to $1/r$, and the first term is proportional to r^{-2}. The first term is negligible at an enough distant point, whereas it represents the static displacement corresponding to the crustal movement at a near-source point. On the other hand, if $X(t)$ is sufficiently longer than the P-S travel time difference, all terms are proportional to $1/r$, and all terms become important. The details will be explained in the next chapter. Still, the actual earthquake is a bit more complicated, and there are intermediate terms in addition to the far and near terms, which can be understood using Green's function derived in this section.

Problem 3.9

1. In a case of $X(t) = \delta(t)$, evaluate the near field term (the first term of the right-hand side of equation 3.80.

2. In a case of $X(t) = H(t)$, evaluate the near field term (the first term of the right-hand side of equation 3.80. Here H is the Heaviside step function.

Problem 3.10

1. When r is large enough, the far-field term of Green's function proportional to $1/r$ (the second term of equation 3.80) becomes dominant at the distant point. By evaluating the P-wave potential $\nabla\phi$ (equation 3.79), estimate the far field term of P-wave displacement.

2. Derive equation 3.80.

3. For $X(t) = \delta(t)$, evaluate the near field term (the first term of equation 3.80).

§3.5 Reciprocity of acoustic wave

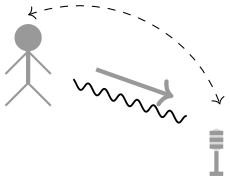

Reciprocity of acoustic wave states that an acoustic wave at point A excited by a source at B is the same as an acoustic wave at point B excited by a source at A. *"If I can hear you, you can hear me."*.[(5)] The theorem is valid under a certain condition. For example, the "wind" effect breaks the theorem. In this section, I try to explain the physical and mathematical background of the reciprocity theorem of the acoustic wave.

Here we consider that an external force $F(\boldsymbol{x},\omega)$ exerts on the system, and causes a pressure perturbation $P(\boldsymbol{x},\omega)$.

$$\nabla\cdot\frac{\nabla P(\boldsymbol{x},\omega)}{\rho_0(\boldsymbol{x})}+\frac{\omega^2}{\kappa(\boldsymbol{x})}P(\boldsymbol{x},\omega)=F(\boldsymbol{x},\omega)\equiv\mathcal{F}\left[\boldsymbol{\nabla}\cdot\left(\frac{\boldsymbol{f}}{\rho_0}\right)\right]. \tag{3.81}$$

Formally, we consider a quantity PF [note 9)].

Here we consider a pair of acoustic wave fields (P_1, F_1 and P_2, F_2) [note 10)].

$$\nabla\cdot\frac{\nabla P_1(\boldsymbol{x},\omega)}{\rho_0(\boldsymbol{x})}+\frac{\omega^2}{\kappa(\boldsymbol{x})}P_1(\boldsymbol{x},\omega)=F_1(\boldsymbol{x},\omega), \tag{3.82}$$

$$\nabla\cdot\frac{\nabla P_2(\boldsymbol{x},\omega)}{\rho_0(\boldsymbol{x})}+\frac{\omega^2}{\kappa(\boldsymbol{x})}P_2(\boldsymbol{x},\omega)=F_2(\boldsymbol{x},\omega). \tag{3.83}$$

Here we consider the difference between two quantities (i) F_1P_2 and (ii) F_2P_1. Multiple equation 3.82 with P_2, multiply equation 3.83 with P_1, and subtract the resulting expressions (we call this quantity the interaction quantity [(3)]). Integration over volume within Σ leads to [note 11)]

$$\int_V(P_2F_1-P_1F_2)dV=\int_\Sigma\frac{1}{\rho}(P_2\nabla P_1-P_1\nabla P_2)\cdot\hat{\boldsymbol{n}}d\Sigma. \tag{3.84}$$

Here we consider a problem under a homogeneous boundary condition (on the boundary Σ, $P=0$ or $\nabla P=0$). The left-hand side of equation 3.84 disappears. Green's function for $F_1=\delta(\boldsymbol{x}), F_2=\delta(\xi)$ exhibits the spatial symmetry as,

$$G(\boldsymbol{x},\boldsymbol{x}_1,\omega)=G(\boldsymbol{x}_1,\boldsymbol{x},\omega). \tag{3.85}$$

This equation is known as reciprocity, which is not crucial for theoretical consideration but also for numerical applications.

---

note 9) The multiplication of Fourier components $F(\omega)P(\omega)$ corresponds to the convolution integral of P and F in the time domain. Physically, this represents the time integral of a **work-related quantity** that the wave source and the wavefield mutually exert on each other in a time-reversed state.

note 10) In this case, because we neglect the advection term due to the smaller amplitude, the wavefield can be characterized by pressure perturbation.

note 11) de Hoop [1988][(3)] wrote "As far as acoustic wave fields are concerned, Lord Rayleigh is commonly credited as the first to derive a reciprocity theorem; it applies to harmonic sound vibrations in a homogeneous, ideal fluid. (He denotes it as Helmholtz's theorem but gives no reference to Helmholtz.)"

In the case of the Earth, the ground can be approximated by free surface ($p = 0$). I note that Coriolis force owing to Earth's rotation, breaks the reciprocity at very low frequency ($< 10^{-3}$ Hz). When we consider an advection term of the mean flow, such as infrasound propagation within a layer of a westerly jet, the reciprocity is also broken.

†Because the mathematical operations are a bit abstract, you may find it difficult to understand the physical meanings. Here we will try to explore the physical implications a little further. However, you may skip the following, as it anticipates the contents of the later further chapter (8 chapter).

First, the governing equations are abstracted as linear partial differential operators.

$$\mathcal{L} \equiv \nabla \cdot \frac{\nabla}{\rho_0(\boldsymbol{x})}. \tag{3.86}$$

Here we consider arbitrary functions u and v.

The operator $\bar{\mathcal{L}}$ that satisfies

$$\left(\int u^* \mathcal{L} v dV \right)^* = \int u^* \bar{\mathcal{L}} v dV. \tag{3.87}$$

is called the Hermitian conjugate operator with $\mathcal{L}$. If $\mathcal{L}$ satisfies

$$\mathcal{L} = \bar{\mathcal{L}}, \tag{3.88}$$

we call $\mathcal{L}$ the Hermite operator or self adjoint operator [note 12)].

The Hermitian operator has two important characteristics[note 13)]: (i) the eigenvalues are real, and (ii) the eigenfunctions are orthogonal and form a complete system. Therefore any function can be expanded in terms of eigenfunctions.

Here we consider eigenvalues λ_n and eigenfunctions u_n for an operator $\mathcal{L}$ as:

$$\mathcal{L} u_n = -\frac{\lambda_n}{\kappa(\boldsymbol{x})} u_n. \tag{3.89}$$

Expanding the Green's function in terms of eigenfunctions yields

$$G = \sum_n a_n u_n. \tag{3.90}$$

The insertion of the expansion into the wave equation leads to

$$\sum \left(\frac{\omega^2 - \lambda_n}{\kappa(\boldsymbol{x})} \right) a_n u_n = \delta(\boldsymbol{x} - \boldsymbol{x}_1). \tag{3.91}$$

From the orthonormality of the eigenfunctions:

$$\int \frac{u_n^*(\boldsymbol{x}) u_{n'}(\boldsymbol{x})}{\kappa(\boldsymbol{x})} dV = \delta_{nn'}, \tag{3.92}$$

note 12) In the case of one-dimensional problems, the equations can be reduced to ordinary differential equations of the Sturm-Liouville type. In the case of horizontally stratified structures, the equation can be rewritten in the Sturm-Liouville form by separating variables. Therefore, the various properties have been studied in detail and are easy to treat.

note 13) Remember the Hermitian matrix

the coefficients a_n are given by

$$a_n = \frac{u_n(\boldsymbol{x}_1)}{\omega^2 - \lambda_n}. \tag{3.93}$$

Accordingly, Green's function can be written by

$$G = \sum \frac{u_n(\boldsymbol{x}_1)u_n(\boldsymbol{x}_2)}{\omega^2 - \lambda_n}. \tag{3.94}$$

From this expression, Green's function satisfies the reciprocity property. This discussion also shows that, generally, when the eigenfunctions can be described as self-adjoint operators, the eigenfunctions satisfy orthogonality and completeness, and therefore, the reciprocity is satisfied. For example, in the case of sound waves with mean wind, when the sound wave propagates upwind or downwind, the travel time changes due to the effect of the mean wind, and thus, the reciprocity is not satisfied. In this case, the governing equations do not satisfy the self-associative property.

Also, the definition of the Hermite operator shows that checking the interaction quantity is checking whether the self-adjoint property is satisfied. When rewritten in matrix form, the Hermitian operator corresponds exactly to the Hermitian matrix, and the various properties become easier to understand [note 14)].

Problem 3.11

1. Using Green's theorem, Derive equation 3.84. Hint : Use $\nabla \cdot (F\boldsymbol{u}) = F(\nabla \cdot \boldsymbol{u}) + \boldsymbol{u} \cdot \nabla F$, and Gauss's divergence theorem.

[note 14)] For example, the Hermitian matrix corresponds to an orthogonal matrix that is diagonalizable and whose eigenvalues are real numbers

3.5.1 †Physical interpretation of interaction quantity

Evaluating the quantity of interaction, we can derive the reciprocity. However, it is not quite clear what it means in the physical sense. Let us consider the interaction quantity, focusing on how the order of deformation changes the work done by external forces.

Total amount of work done by external forces on the fluid

First, we evaluate the work done by external forces on the fluid per unit time. The work per unit time, $w(t)$, done by external forces in the region V is given by

$$w(t) = \int_V \boldsymbol{f} \cdot \boldsymbol{v} dV \tag{3.95}$$

where $\boldsymbol{v}$ is the particle velocity. In this chapter, we use pressure p as the variable, so we consider the expression in terms of p instead of $\boldsymbol{v}$. From the equation of motion,

$$\rho_0 \partial_t \boldsymbol{v}(\boldsymbol{x}, t) = -\nabla p(\boldsymbol{x}, t) \tag{3.96}$$

If we define $h(t)$ as the function obtained by integrating p once with respect to time, $\boldsymbol{v}$ can be written as

$$\boldsymbol{v}(\boldsymbol{x}, t) = -\frac{1}{\rho_0} \nabla h(t) \tag{3.97}$$

Using the relation $\nabla \cdot (F\boldsymbol{u}) = F(\nabla \cdot \boldsymbol{u}) + \boldsymbol{u} \cdot \nabla F$,

$$w(t) = \int_V \left(\nabla \cdot \left(\frac{\boldsymbol{f}}{\rho_0} \right) \right) h dV \tag{3.98}$$

We now consider the integral of $w(t)$ over all time. From the generalized Parseval's theorem[note 15)] we find that

$$\int_{-\infty}^{\infty} w(t) dt = \frac{1}{2\pi} \int_V \int_{-\infty}^{\infty} F^*(\boldsymbol{x}, \omega) \frac{P(\boldsymbol{x}, \omega)}{i\omega} d\omega dV$$

Here, F is the Fourier component of $\nabla \cdot \left(\frac{\boldsymbol{f}}{\rho_0} \right)$, and $P(\omega)$ is the Fourier component of p. In summary, by integrating the Fourier component $F^* P / (i\omega)$ over the frequency domain, we can estimate the total work done by external forces on the fluid.

[note 15)] The generalized Parseval's theorem states that for any functions f and g,

$$\int_{-\infty}^{\infty} f^*(t) g(t) dt = \frac{1}{2\pi} \int_{-\infty}^{\infty} F^*(\omega) G(\omega) d\omega \tag{3.99}$$

The left-hand side can be interpreted as the cross-correlation function at lag 0, and this equation can be derived by considering the inverse transform of the cross spectrum.

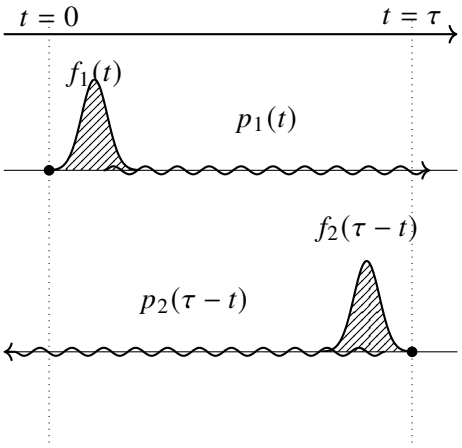

Figure 3.4: At $t = 0$, a force $f_1(\boldsymbol{x}, t)$ is applied, generating a sound field $p_1(\boldsymbol{x}, t)$. At $t = \tau$, a time-reversed force $f_2(\tau - t)$ is applied, and we consider the sound field $p(\tau - t)$ in the reverse time direction. We evaluate the total work done by the external forces. The order of applying the forces is then reversed, and the respective works are compared.

Why can we compare components at each frequency?

To compare work, we need to consider the time integral of $f(t)p(t)$ or the equivalent frequency integral of $F(\omega)P(\omega)$. However, the interaction quantity is evaluated at each frequency. Why is this? This is because there is a condition that the order in which forces f_1 and f_2 are applied does not matter.

Let us consider a situation like in Figure 3.4. Suppose a force $f_1(\boldsymbol{x}, t)$ is applied at $t = 0$, generating a sound wave $p_1(\boldsymbol{x}, t)$. At time $t = \tau$, a force $f_2(\boldsymbol{x}, \tau - t)$ is applied, and we consider the time-reversed sound field $p_2(\boldsymbol{x}, \tau - t)$. In this case, the work done by f_1 on p_2 can be written as

$$\int_v \int_0^\tau f_1(\boldsymbol{x}, t) p_2(\boldsymbol{x}, \tau - t) dV(\boldsymbol{x}) dt, \tag{3.100}$$

Since this equation holds for any time shift τ, the work is a function of τ. Considering the Fourier transform with respect to τ, we find that

$$\int_v F_1(\boldsymbol{x}, \omega) P_2(\boldsymbol{x}, \omega) dV(\boldsymbol{x}), \tag{3.101}$$

Thus, it can be decomposed into components at each frequency. Since it must hold for any time shift, we need to consider the balance of each Fourier component.

Changing the order of applying forces

(i) Applying f_1 first to generate a sound wave, and then applying the time-reversed f_2 after τ seconds. (ii) Applying f_2 first to generate a sound wave, and then applying the time-reversed f_1 after τ seconds. To compare these cases, we derive the condition $\mathrm{Im}\{F_1 P_2 - F_2 P_1\} = 0$, focusing only on the imaginary part of the interaction quantity. Here, causality becomes important.

When considering signals that satisfy causality, causal signals must satisfy the Kramers–Kronig relations. Considering the Fourier components of causal signals, the real and imaginary parts must satisfy the Hilbert transform relations. Therefore, satisfying $\mathrm{Im}\{F_1P_2 - F_2P_1\} = 0$ simultaneously satisfies $\mathrm{Re}\{F_1P_2 - F_2P_1\} = 0$[note 16)], and as a result, we find that the condition for the interaction quantity to be zero ($F_1P_2 - F_2P_1 = 0$) must be considered.

In the chapter on Hooke's law, we considered the symmetry of elastic constants, specifically the symmetry that does not depend on the path of deformation (this symmetry itself is known as reciprocity). When this symmetry is generalized to dynamic problems, it is shown that the reciprocity of the Green's function for sound waves can be derived.

[note 16)] Strictly speaking, the Fourier components of causal signals must also satisfy finiteness.

§3.6 Representation theorem: as a natural extension of Huygens's principle

The representation theorem is key for interpreting seismic wave propagation. In this section, I show the theorem is a natural extension of Huygens's principle, which does not predict the wavefront but also the amplitudes. For simplicity, we start a case of an acoustic (scalar) wave equation.

With an assumption that F_1 is 0 within a volume V ($P_1 = P$) and $F_2 = \delta(\boldsymbol{x} - \boldsymbol{x}_1)$, we obtain the equation,

$$P(\boldsymbol{x}_1, \omega) = \int_\Sigma \frac{1}{\rho}(P(\boldsymbol{x}, \omega)\nabla G(\boldsymbol{x}, \boldsymbol{x}_1, \omega) - G(\boldsymbol{x}, \boldsymbol{x}_1, \omega)\nabla P(\boldsymbol{x}, \omega)) \cdot \hat{\boldsymbol{n}}\Sigma. \tag{3.102}$$

For a better description of the boundary condition, we rewrite pressure gradient by displacement $\boldsymbol{S}(\boldsymbol{x}, \omega)$ as,

$$P(\boldsymbol{x}_1, \omega) = \int_\Sigma \frac{1}{\rho}\{P(\boldsymbol{x}, \omega)\nabla G(\boldsymbol{x}, \boldsymbol{x}_1, \omega) - \rho\omega^2 G(\boldsymbol{x}, \boldsymbol{x}_1, \omega)\boldsymbol{S}(\boldsymbol{x}, \omega)\} \cdot \hat{\boldsymbol{n}} d\Sigma. \tag{3.103}$$

For a given region surrounded by a boundary Σ, the displacement and the pressure distribution on the surface Σ give us a complete description of the acoustic wavefield within the surface.

To compare Huygens's principle we replace a source at $\boldsymbol{x}_1$ by receiver at $\boldsymbol{x}$ using the reciprocity as,

$$P(\boldsymbol{x}_1, \omega) = \int_\Sigma \frac{1}{\rho}\{P(\boldsymbol{x}, \omega)\nabla G(\boldsymbol{x}_1, \boldsymbol{x}, \omega) - \rho\omega^2 G(\boldsymbol{x}_1, \boldsymbol{x}, \omega)\boldsymbol{S}(\boldsymbol{x}, \omega)\} \cdot \hat{\boldsymbol{n}} d\Sigma. \tag{3.104}$$

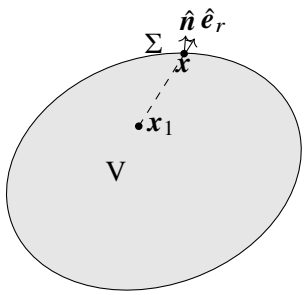

Figure 3.5: Geometry of the fluid body.

Problem 3.12

To understand the nature of the representation theorem, let us consider a one-dimensional problem for simplicity. As described in the chapter on the Green function, we consider a plate-like region $0 \leq x \leq L$ as the domain of Σ, corresponding to the case where P is the function of only x.

1. Derive the following form of the representation theorem:

$$P(x_1, \omega) = \left[\frac{1}{\rho(x)} \left\{ P(x, \omega) \left(\frac{\partial}{\partial x} G^{1D}(x_1, x, \omega) \right) - G^{1D}(x_1, x, \omega) \frac{\partial P(x, \omega)}{\partial x} \right\} \right]_{x=0}^{L} \tag{3.105}$$

2. In a case of a homogeneous medium ($\rho(x) = \rho_0$, $k = \omega/\alpha_0$), the 1-D Green's function is given by

$$G^{1D}(x_1, x, \omega) = \frac{\rho_0 i}{2k} e^{-ik|x_1 - x|}. \tag{3.106}$$

   Here we consider a propagation wave solution $P(x, \omega) = P_0(\omega) e^{-ik|x|}$. Show that the representation theorem holds in this case.

The representation theorem shows that the wave field inside the boundary can be completely reproduced by information on the boundaries describing the wave inward and outward.

For a better understanding of the equation, let us consider a simple situation the Green function $G(r)$ is a function of only r using a spherical coordinate at the origin $\boldsymbol{x}_1$. Because $\nabla G = \partial_r G \hat{\boldsymbol{e}}_r$, the equation can be rewritten by,

$$P(\boldsymbol{x}_1, \omega) = \int_\Sigma \left\{ \frac{1}{\rho} P \frac{\partial G(r)}{\partial r} (\hat{\boldsymbol{e}}_r \cdot \hat{\boldsymbol{n}}) - \omega^2 G(r) (\boldsymbol{S} \cdot \hat{\boldsymbol{n}}) \right\} d\Sigma, \tag{3.107}$$

The first term of the right-hand side corresponds to a dipole source, whereas the second one corresponds to a monopole. The combination of the radiation patterns gives us a prediction of amplitudes of refracted and reflected wave fields. This formulation is known as the Fresnel-Kirchhoff diffraction formula in optics.

If you interpret the representation theorem as an extension of Huygens' principle, you have understood the physical implications. However, a closer look at the formula raises many questions. For example, if the boundary conditions do not satisfy the homogeneous boundary condition in a supposed medium (e.g., if stress and displacement are given at the boundary, as in a speaker), does the condition break the reciprocity of Green's function? This is a typical example. Actually, this problem can be avoided. That is, the wavefield combination we are considering ((F_1, P_1) and (F_2, P_2)): they are same within the region V, but not necessarily outside it.

First, as a simple case, let us consider a spherical region as the region V. Suppose that at the sphere surface, we have a free surface (satisfying the homogeneous boundary condition). In this field, you would think of a Green's function that naturally satisfies the homogeneous boundary condition on the surface of V. However, it is not necessary to choose so, and there is no problem choosing a Green's function in full space (see section 3.3.3), considering the situation where the medium continues infinitely outside the domain as well.

Next, consider the case where the homogeneous boundary condition is broken on the sphere (for example, there is a source on the boundary, such as a speaker in part). In this case, we can still choose an infinite Green's function (also called the fundamental or principal solution), and the reciprocity can be applied without any problem. In other words, the representation theorem can be applied similarly.

3.6.1 Relation to Huygens' principle

First, let us consider the boundary on a plane parallel to the wavefront in a situation where a plane wave is propagating upwards (Figure 3.6). Similar to Huygens' principle, this can be interpreted as a situation where secondary wave sources are placed on the boundary surface. The difference is that the radiation from the secondary wave sources is not uniform, but rather directed upwards. This is due to the combination of dipoles and monopoles, resulting in the radiation pattern shown in the figure.

Next, let us consider the case where the wavefront of the propagating plane wave is perpendicular to the boundary (Figure 3.7). Although it is less intuitive compared to the parallel case, let us examine it step by step. The radiation pattern of each secondary wave source is identified as a dipole. The timing of wave excitation coincides with the passage of the wavefront. Therefore, the wavefronts emitted from all secondary wave sources overlap, forming a plane wave. Since the propagation speed of the wave in the medium matches the timing of wave emission from the

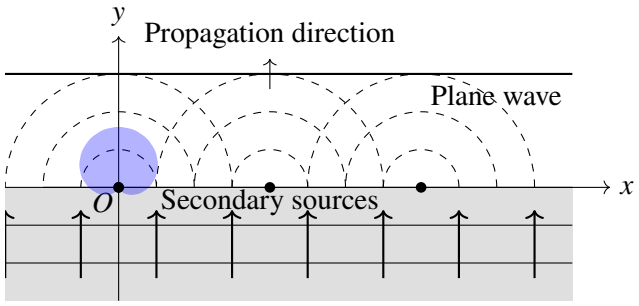

Figure 3.6: Considering the boundary parallel to the wavefront of a plane wave.

secondary sources, it can also be interpreted that the shock front is advancing perpendicular to the boundary.

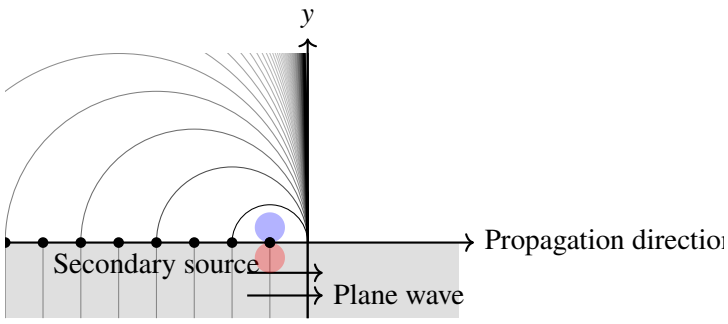

Figure 3.7: A case in which the wavefront of a plane wave is perpendicular to the boundary.

We can reconstruct all the seismic wavefields within the Earth's interior from the surface observations if we know Green's function of the medium. Based on the reconstructed seismic wavefield within the Earth, we can infer elastic constants at a given point from the ratio between the spatial gradient of pressure and the time derivative at the point. This is the basic principle of seismic imaging in seismic exploration. However, we must know the seismic structure in advance to calculate Green's function. At a glance, the logic seems to be a circular argument. From a practical point of view, we start **an initial model**, then we update it with a modification based on the surface observation and the initial Green's function. Updating the information based on the observed wavefield is essential for exploring Earth's interior using seismic exploration techniques.

https://www.eri.u-tokyo.ac.jp/people/knishida/eng/seismology.html

Problem 3.13

Let us consider the amplitude of the plane wave excited at the boundary surface in Figure 3.6.

1. Let us consider the conditions under which the wavefront of a cylindrical wave is emphasized in Figure 3.6. For a spherical wave with radius r excited at $x = 0$, approximate the wavefront near $x = 0$ to second-order accuracy.
2. Consider the interference with the wave excited by a secondary source located at $x = \delta x$. When δx is sufficiently small compared to r, find δx such that the phase difference between the two spherical waves at $x = 0$ is approximately $\pi/4$.
3. Since we are considering the 3D Green's function, the amplitude on the wavefront is proportional to $(kr)^{-1}$. Estimate the amplitude of the secondarily excited wavefront by considering the contributions of secondary sources within the circle with a radius of δx.

Problem 3.14

Let us consider the amplitude of the plane wave excited at the boundary surface in Figure 3.7 in the same manner as Problem 3.13. Note that (i) the secondary excitation source is moving with the wavefront and (ii) the radiation pattern must be considered because the excitation sources are dipoles.

§3.7 Reciprocity of elastic medium

The reciprocity of an acoustic medium can be extended to an elastic medium. First, we extend equation 3.84to that for an elastic medium, known as Betti's theorem. Here I show only the results [note 17)] as,

[note 17)] read Aki and Rechards[(1)] for details.

Betti's theorem

As in the case of the acoustic wave, we consider two types of wave fields as follows. Let us consider a pair of elastic wavefields: (i) elastic wavefield $\boldsymbol{s}_1$ excited by forcing $\boldsymbol{f}_1$ and (ii) elastic wavefield $\boldsymbol{s}_2$ excited by forcing $\boldsymbol{f}_2$. Then integrate the inner product between the equation of motions for (i) and $\boldsymbol{s}'$ for (ii), and vice versa.

$$\int_V \left\{\boldsymbol{s}_1(\boldsymbol{x},t)\cdot(\boldsymbol{f}_2(\boldsymbol{x},\tau)-\rho\partial_t^2\boldsymbol{s}_2)-\boldsymbol{s}_2(\boldsymbol{x},\tau)\cdot(\boldsymbol{f}_1(\boldsymbol{x},t)-\rho\partial_t^2\boldsymbol{s}_1)\right\}dV \tag{3.108}$$

$$=\int_\Sigma \{[\boldsymbol{s}_2(\boldsymbol{x},\tau)\cdot\boldsymbol{T}_1(\boldsymbol{s}_1(\boldsymbol{x},t))\cdot\hat{\boldsymbol{n}}]-[\boldsymbol{s}_1(\boldsymbol{x},t)\cdot\boldsymbol{T}_2(\boldsymbol{s}_2(\boldsymbol{x},\tau))\cdot\hat{\boldsymbol{n}}]\}\,d\Sigma \tag{3.109}$$

The derivation requires the following relation,

$$\sum_{ij}E_{ij}T'_{ij}=\sum_{ij}E'_{ij}T_{ij}, \tag{3.110}$$

according to the symmetry of elastic tensor as $C_{ijkl}=C_{klij}$[note 18)].

By time integration of the above equation with the change of variables $\tau=\tau-t$, we get the following relation:

$$\int_{-\infty}^{\infty}dt\int_V[\boldsymbol{s}_1(\boldsymbol{x},t)\cdot\boldsymbol{f}_2(\boldsymbol{x},\tau-t)-\boldsymbol{s}_2(\boldsymbol{x},\tau-t)\cdot\boldsymbol{f}_1(\boldsymbol{x},t)]dV \tag{3.111}$$

$$=\int_{-\infty}^{\infty}dt\int_\Sigma\{[\boldsymbol{s}_2(\boldsymbol{x},\tau-t)\cdot\boldsymbol{T}_1(\boldsymbol{s}_1(\boldsymbol{x},t))\cdot\hat{\boldsymbol{n}}]-[\boldsymbol{s}_1(\boldsymbol{x},t)\cdot\boldsymbol{T}_2(\boldsymbol{s}_2(\boldsymbol{x},\tau-t))\cdot\hat{\boldsymbol{n}}]\}\,d\Sigma. \tag{3.112}$$

Here we use the relation shown in problem 3.15.

Problem 3.15

Show the following relation:

$$\int_{-\infty}^{\infty}\left\{\boldsymbol{s}_1(\boldsymbol{x},t)\cdot\partial_t^2\boldsymbol{s}_2(\tau-t)-\boldsymbol{s}_2(\boldsymbol{x},\tau)\cdot\partial_t^2\boldsymbol{s}_1(\tau-t)\right\}dt=0, \tag{3.113}$$

for given a finite time τ by partial integration under the following condition $\boldsymbol{s}_1(\infty)=\boldsymbol{s}_1(-\infty)$ and $\boldsymbol{s}_2(\infty)=\boldsymbol{s}_2(-\infty)$.

Reciprocity of Green's function

When we consider homogeneous boundary conditions (on a boundary Σ, $\boldsymbol{s}=\boldsymbol{s}'=0$ or $\boldsymbol{T}_n[\boldsymbol{s})]=\boldsymbol{T}_n[\boldsymbol{s}')]=0$), the right-hand side vanishes. With the transnational symmetry of Green's function, we obtain reciprocity of elastic Green's function as,

$$G_{lm}(\boldsymbol{x}_2,\tau;\boldsymbol{x}_1,0)=G_{ml}(\boldsymbol{x}_1,\tau;\boldsymbol{x}_2,0) \tag{3.114}$$

$$G_{lm}(\boldsymbol{x}_2,\tau_2;\boldsymbol{x}_1,\tau_1)=G_{ml}(\boldsymbol{x}_1,-\tau_1;\boldsymbol{x}_2,-\tau_2). \tag{3.115}$$

[note 18)] this relation is based on the independence of elastic energy on deformation paths, as explained in the previous chapter.

§3.8 Representation theorem of an elastic medium

Let us insert $G_{pm}(\boldsymbol{x}, t; \boldsymbol{\eta}, 0)$, which represents the p component of displacement for an external force toward mth direction at $\boldsymbol{\eta}$ into s_2 of **Betti's theorem (equation3.7)**. Now, considering the translational symmetry with respect to time, Fourier transform with respect to τ leads to the following equation

$$\begin{aligned} s_m(\omega, \boldsymbol{x}) = &\int_V f_p(\omega, \boldsymbol{\eta}) \cdot G_{pm}(\omega, \boldsymbol{\eta}, \boldsymbol{x}) dV(\boldsymbol{\eta}) \\ &+ \int_\Sigma \{G_{pm}(\omega, \boldsymbol{\eta}, \boldsymbol{x}) T_{pq}(\boldsymbol{s}(\omega, \boldsymbol{\eta})) \hat{n}_q - s_q(\omega, \boldsymbol{\eta}) T_{pq}\left[(\boldsymbol{G}_m(\omega, \boldsymbol{\eta}, \boldsymbol{x})\right] \hat{n}_q\} d\Sigma(\boldsymbol{\eta}), \end{aligned} \tag{3.116}$$

In this equations To obtain displacement $\boldsymbol{s}$ at $\boldsymbol{x}$, the above equation evaluates the convolution between Green's function for an impulsive force applied at the observed point $\boldsymbol{x}$ and the distributed sources. The evaluation makes the equation difficult to understand. Assuming that Green's function satisfies a homogeneous boundary condition, reciprocity of Green's function can simplify the formulation [note 19)]. With the reciprocity, the representation theorem can be simplified as

$$\begin{aligned} s_m(\omega, \boldsymbol{x}) = &\int_V f_p(\omega, \boldsymbol{\eta}) G_{mp}(\omega, \boldsymbol{x}, \boldsymbol{\eta}) dV(\boldsymbol{\eta}) \\ &+ \int_\Sigma \{G_{mp}(\omega, \boldsymbol{x}, \boldsymbol{\eta}) T_p(\boldsymbol{\eta}) - s_p(\boldsymbol{\eta}) C_{pqkl} \partial_l G_{mk}(\omega, \boldsymbol{x}, \boldsymbol{\eta}) \hat{n}_q\} d\Sigma(\boldsymbol{\eta}), \end{aligned} \tag{3.117}$$

where $\hat{\boldsymbol{n}}$ is normal vector ont the boundary.

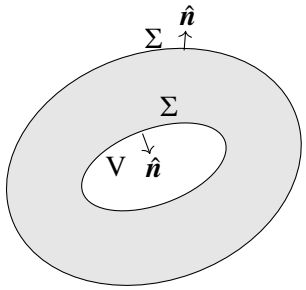

Figure 3.8: Geometry of the system we consider.

[note 19)] The confusion originates that the boundary conditions for the Green function can be independent of the boundary conditions for the displacement $\boldsymbol{s}$. This means that the choice of Green's function is arbitrary, which causes confusion. For example, when considering a homogeneous medium but complex boundaries, using the infinite medium Green's function (the fundamental solution) improves the outlook.

The Representation Theorem is very important when considering the excitation of seismic waves. The Representation Theorem assures us that cutting out a part of an elastic body has no effect on the motion of the elastic body outside it as long as the displacement and stress conditions at the boundary are known. Consider, for example, the phenomenon of earthquakes, which are caused by brittle fractures in a part of the Earth. The area near the fault cannot be represented by an elastic body. However, if we consider the operation of hypothetically replacing the brittle region with an elastic body through it, with a closed surface that surrounds it. Then, as long as the stresses and displacements on the boundary are identical to each other, we can completely describe the motion in the elastic body. We will see this in detail in the next chapter.

§3.A Delta function

3.A.1 Delta Function of a Composite Function

When $f(x)$ has the i-th zero point x_i,

$$\delta(f(x)) = \sum_i \frac{\delta(x - x_i)}{|f'(x_i)|}, \tag{3.118}$$

This indicates that the delta function takes values at $f(x) = 0$, and it becomes clearer when considering the Taylor expansion of $f(x)$.

3.A.2 Differentiation of the Delta Function

Since the delta function cannot be differentiated in the usual sense, it is defined by integration of parts.

$$\int_{-\infty}^{\infty} f(x) \frac{d\delta(x)}{dx} dx = -f'(0) \tag{3.119}$$

3.A.3 Polar Coordinate Representation

Consider the delta function in polar coordinates r. Since $r \geq 0$, it is defined on one side as

$$\int_0^{\epsilon} \delta^+(r) dr = 1. \tag{3.120}$$

There is also a definition where it is set to $1/2$.

In three dimensions, the polar coordinate representation of the delta function is

$$\delta(\boldsymbol{x}) = \frac{\delta^+(r)}{4\pi r^2}. \tag{3.121}$$

Here, the delta function located at the origin is considered to be a function of r only due to its symmetry about the origin. Additionally, since the delta function can be defined through integration with a test function, integrating both sides over the entire space shows that they are equivalent.

In this case, the differentiation of the delta function is

$$\frac{\delta^+(r)}{r} = -\frac{d\delta^+(r)}{dr}. \tag{3.122}$$

This can be easily derived by integrating with the test function $g(r)/r$.

§3.B Bessel function

$$\frac{1}{r}\frac{1}{dr}\left(r\frac{dR}{dr}\right)+\left(k^2-\frac{m^2}{r^2}\right)R=0, \tag{3.123}$$

is a differential equation of Bessel, and the solutions are known as Bessel function of the first kind $J_m(kr)$, and Neumann function $Y_m(kr)$. $J_0(0)=1$, $J_m(0)=0, m\neq 0$, whereas Neumann function diverges at $r=0$. Both functions converge to $1/\sqrt{r}$ for $r\to\infty$. Read Mathematical Methods for Physicists[2] for details.

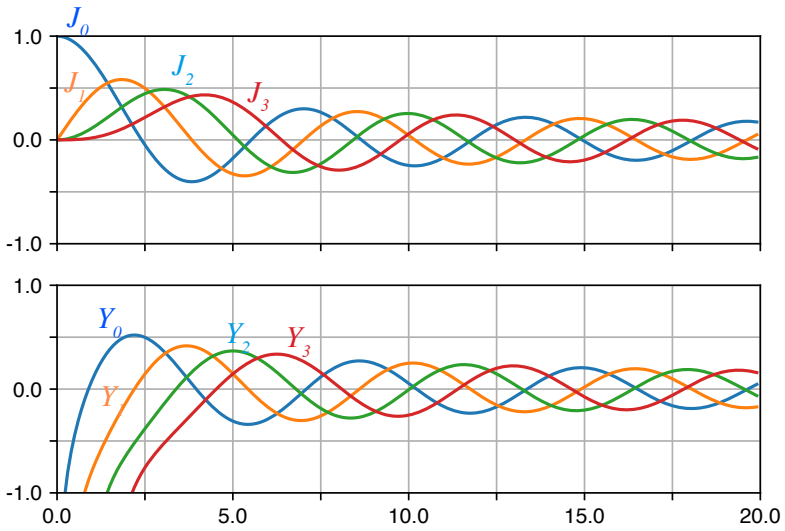

Figure 3.9: Plots of Bessel functions and Neumann functions.

3.B.1 Properties

$$J_{-m}(x)=(-1)^n J_m(x) \tag{3.124}$$

$$J_{m-1}(x)+J_{m+1}(x)=\frac{2m}{x}J_m(x) \tag{3.125}$$

$$J_{m-1}(x)-J_{m+1}(x)=2J'_m(x) \tag{3.126}$$

3.B.2 Asymptotic for $x\to 0$

$$J_m(x) \sim \frac{1}{m!}\left(\frac{x}{2}\right)^m \tag{3.127}$$

$$Y_0(x) \sim \frac{2}{\pi}\ln\frac{x}{2}, \tag{3.128}$$

$$Y_m(x) \sim -\frac{(m-1)!}{\pi}\left(\frac{2}{x}\right)^m, m \geq 0 \tag{3.129}$$

3.B.3 Asymptotic for $kr \gg 1$

$$J_m(kr) \sim \sqrt{\frac{2}{\pi kr}}\cos\left(kr - \frac{2m+1}{4}\pi\right) \tag{3.130}$$

$$Y_m(kr) \sim \sqrt{\frac{2}{\pi kr}}\sin\left(kr - \frac{2m+1}{4}\pi\right) \tag{3.131}$$

$$H_m^{(1)}(kr) \sim \sqrt{\frac{2}{\pi kr}}e^{i\left(kr - \frac{2m+1}{4}\pi\right)} \tag{3.132}$$

Here $H_m^{(2)}(kr) = H_m^{(1)*}(kr)$.

§3.C Hankel Functions

Here, we summarize the relations used in the main text regarding Hankel functions.

3.C.1 Recurrence Relations

$$\left(\frac{1}{z}\frac{d}{dz}\right)^k\left(z^{-\nu}H_\nu^{(2)}(z)\right) = (-1)^k z^{-\nu-k}H_{\nu+k}^{(2)}(z)$$

Refer to DLMF (https://dlmf.nist.gov/10.6).

3.C.2 Relation to 2-D Green's function

The 2-D Green's function in the frequency domain ($\omega > 0$) can be written as

$$G^{2D}(r,\omega) = -\frac{\rho_0 i}{4}H_0^{(2)}(\omega(r/c)) = -\frac{\rho_0}{4}\left(Y_0(\omega(r/c)) + J_0(\omega(r/c))i\right) \tag{3.133}$$

where $c \equiv \sqrt{\kappa/\rho_0}$. Since it must be real in the time domain, $G^{2D}(r,\omega) = (G^{2D}(r,-\omega))^*$ is required. Therefore,

$$G^{2D}(r,-\omega) = -\left(\frac{\rho_0 i}{4}H_0^{(2)}(\omega(r/c))\right)^* = -\frac{\rho_0}{4}\left(Y_0(\omega(r/c)) - J_0(\omega(r/c))i\right) \tag{3.134}$$

The real part of the Green's function is $Y_0(|\omega|(r/c))$, which is an even function of frequency, and the imaginary part is $J_0(|\omega|(r/c))\,\mathrm{sign}(\omega)$, which is an odd function. Note that intuitively we define $J_0(x) = J_0(-x)$ for negative values. Furthermore, since the Green's function must be causal, it must satisfy the Kramers–Kronig relations , and the Hilbert transform of $J_0(\omega(r/c))\,\mathrm{sign}(\omega)$ becomes $Y_0(|\omega|(r/c))$.

3.C.3 Relation to Spherical Hankel Functions

There is a relation between the spherical Hankel function $h_n^{(2)}$ and the Hankel function $H^{(2)}_{\frac{n}{2}-1}$:

$$h_n^{(2)}(r) = \sqrt{\frac{\pi}{2r}} H^{(2)}_{\frac{n}{2}-1}$$

Additionally,

$$h_0^{(2)}(kr) = -\frac{1}{kr} e^{-ikr}$$

§3.D Plane Wave Expansion

A plane wave can be expressed as a superposition of cylindrical waves.

$$e^{ikr\cos\phi} = \sum_{n=-\infty}^{\infty} i^n J_n(kr) e^{im\phi} \tag{3.135}$$

§3.E Fourier transform

For time series $u(t)$, the Fourier transform $\mathcal{F}$ and the inverse Fourier transform $\mathcal{F}^{-1}$ are defined as

Definitions of Fourier transform

$$U(f) \equiv \mathcal{F}(u) = \int_{-\infty}^{\infty} u(t) e^{-i2\pi ft}\, dt, \tag{3.136}$$

$$u(t) = \mathcal{F}^{-1}(U) \equiv \int_{-\infty}^{\infty} U(f) e^{i2\pi ft}\, df, \tag{3.137}$$

$$\tag{3.138}$$

where U represents Fourier components of u.

https://www.eri.u-tokyo.ac.jp/people/knishida/eng/seismology.html

Summary of Fourier transform

- If $u(t)$ is a real function, $U(f) = U^*(-f)$,
- Parseval's theorem : $\int_{-\infty}^{\infty} u(t)^2 dt = \int_{-\infty}^{\infty} U(f)^2 df$,
- Cross spectrum $C(u, v; f) = \mathcal{F}(\psi) = U^* \tilde{v}$
- Wiener-Khinchin theorem : $p(f) = \mathcal{F}(\phi) =\mid U \mid^2$.

§3.F Hilbert transform

Hilbert transform of $f(t)$ $\mathcal{H}f(t)$ is difined by

$$\mathcal{H}f(t) = \frac{1}{2\pi} \int_{-\infty}^{\infty} [-isign(\omega)] F(\omega) e^{-i\omega t} d\omega. \tag{3.139}$$

This can be interpreted as phase advance of 90° to the original signal in the frequency domain. In the time domain, it can be written as,

$$\mathcal{H}f(t) = \frac{1}{\pi} \mathcal{P} \int_{-\infty}^{\infty} \frac{f(\tau)}{\tau - t} d\tau. \tag{3.140}$$

Here $\mathcal{P}\int$ is Cauchy's principle integral

Additionally, applying the Hilbert transform twice results in

$$\mathcal{H}[\mathcal{H}f] = -f(t), \tag{3.141}$$

which inverts the sign.

For details. read textbooks of applied mathematics (e.g. Yomogida 2007,[6] Mathematical Methods for Physicists[2]).

§3.G Kramers–Kronig Relations

Now, let us consider a signal $f(t)$. Assuming this signal satisfies causality, we consider the signal $f(t)h(t)$, where $h(t)$ is the Heaviside step function

$$h(t) = \begin{cases} 0, & t < 0, \\ 1/2, & t = 0, \\ 1, & t > 0, \end{cases} \tag{3.142}$$

Let us consider the Fourier transform of $f(t)h(t)$. Denoting the Fourier transforms of $f(t)$ and $h(t)$ as $F(\omega)$ and $H(\omega)$ respectively, the Fourier transform of $f(t)h(t)$ can be expressed as the convolution

$$\mathcal{F}[fh] = \frac{1}{2\pi} \int_{-\infty}^{\infty} F(\omega') H(\omega - \omega') d\omega' \tag{3.143}$$

Here, $H(\omega)$ is given by

$$H(\omega) = \pi\delta(\omega) + \frac{1}{i\omega}. \tag{3.144}$$

The first term arises because the average value of the Heaviside function is not zero, thus it has a value at zero frequency to account for the average shift. The second term represents the integral in the frequency domain, as the Heaviside function can be roughly considered as the time integral of the delta function, resulting in $(i\omega)^{-1}$ in the frequency domain.

Substituting this into the equation, we get

$$\mathcal{F}[fh] = \frac{1}{2}F(\omega) - \frac{1}{2}i\mathcal{H}[F] \tag{3.145}$$

Denoting the real and imaginary parts of F as F_r and iF_i respectively, we have

$$\mathcal{F}fh = \frac{1}{2}\left(F_r(\omega) + \mathcal{H}F_i\right) + i\frac{1}{2}\left(F_i(\omega) - \mathcal{H}F_r\right) \tag{3.146}$$

Therefore, the imaginary part is the Hilbert transform of the real part.

In summary, causal signals have their real and imaginary parts linked by the Hilbert transform (known as the Kramers–Kronig relations). In the time domain, since the value is zero for $t < 0$, considering the degrees of freedom, there is a unique relationship between the real and imaginary parts, which is the Hilbert transform.

Problem 3.16

Let us consider the Fourier transform of the Heaviside function. Since it becomes 1 as $t \to \infty$, it cannot be Fourier transformed in the usual sense. Therefore, for sufficiently large T, we consider the function

$$h^T(t) = \begin{cases} 0, & t < 0, \\ 1/2, & t = 0, \\ 1, & 0 < t < T, \\ 1/2, & t = T, \\ 0, & t > T, \end{cases} \tag{3.147}$$

Calculate the Fourier transform of this function and then consider the limit as $T \to \infty$, showing that

$$H(\omega) = \pi\delta(\omega) + \frac{1}{i\omega} \tag{3.148}$$

§3.8 Bibliography

[1] K. Aki and P.G. Richards. *Quantitative Seismology*. Univ Science Books, 2nd edition, 2009.

[2] G.B. Arfken and H.J. Weber. *Mathematical Methods for Physicists*. Elsevier Science, 2013.

https://www.eri.u-tokyo.ac.jp/people/knishida/eng/seismology.html

[3] Adrianus T de Hoop. Time-domain reciprocity theorems for acoustic wave fields in fluids with relaxation. *J. Acoust. Soc. Am.*, 84(5):1877–1882, November 1988.

[4] Saito Masanori. *Seismic Wave Theory*. University of Tokyo Press, 2009.

[5] Roel Snieder and Kasper van Wijk. *A Guided Tour of Mathematical Methods for the Physical Sciences*. Cambridge University Press, 3 edition, 2015.

[6] K. Yomogida. *Introduction to Special Functions and Integral Transforms*. Kyoritsu Shuppan, 2007.

Excitation of Seismic Waves

Chapter 4

Various mechanisms can excite seismic waves, such as faulting and volcanic eruptions. These phenomena that excite seismic waves cannot be described within the framework of a linear elastic body. However, if the source region is localized, the representation theorem learned in the previous chapter shows that the problem of seismic wave excitation can be treated within the framework of a linear elastic theory. In this chapter, we will learn that these phenomena can generally be described by an **equivalent body force** within a linear elastic body. In other words, investigating an excitation source in seismology means estimating its **force system**.

Seismological methods are extremely powerful for discovering the characteristics of a seismic source, but it is important to note that wave propagation only provides information about the **force system**. In order to obtain a physical picture of the excitation source (e.g., amount of slip or volumetric change), it is necessary to reinterpret the **equivalent body force** in terms of physical phenomena. Depending on the situation, multiple interpretations may be possible, and the estimated picture of the source strongly depends on the assumed physical model. Thus, when trying to understand the excitation mechanism from seismological observations, it is important to be aware of this two-tiered logical structure.

The following sections will first explain the concept of an indigenous source to understand what an equivalent body force is. Then, we will discuss the moment tensor.

§4.1 Indigenous source

As long as an event that excites seismic waves does not occur, the Earth remains quiet without oscillating. When an external force (a force from outside the system, in this case, the Earth) acts at some point, seismic waves are excited. The easiest example of such an event is a meteorite impact. The ejection of mass associated with a volcanic eruption is another example that can be approximated by an impulse, provided the ejecta dissipates outside the Earth. In this way, when an external force is applied, the total momentum of the Earth changes by the amount of the impulse caused by the external force.

In most cases, however, the solid Earth can be approximated as a closed system. Even in such a case, phenomena inside the solid Earth can, of course, excite seismic waves. Earthquakes (faulting) are a typical example. Volcanic processes inside the solid Earth, such as the source of volcanic tremors, can also be cited as examples. Such an excitation source within an isolated solid Earth system is called an indigenous source. Specific physical processes of an indigenous source include thermal stress, phase transitions, faulting, and fluid movement (e.g., the source of volcanic tremors). Since the entire Earth can be regarded as an isolated system, the total momentum and angular momentum of the entire system must be conserved.

For an indigenous source to excite seismic waves, Hooke's law must break down in some part of the Earth's interior (otherwise, it will remain stationary). For example, faulting during an earthquake does not obey linear elasticity in the vicinity of the fault. If we consider an elastic body by analogy to weights and springs, this corresponds to a sudden change in the spring constant, such as a spring breaking. Fluid motion also plays an important role when considering the excitation of volcanic tremors. Let us consider a case where a region that does not obey the linear elastic theory is localized within a volume V. In this case, the phenomena can be roughly divided into two categories.

The first relates to cases in which the exchange of momentum and angular momentum between the region V and its exterior (the linear elastic region) can be ignored. Faulting is an example of this. In this case, momentum and angular momentum are conserved at all times even in the linear elastic region (outside V).

The second relates to cases in which momentum and angular momentum are exchanged between the region V and its exterior (the linear elastic region). A good example is a landslide, where a rigid block slides down a slope. At the beginning and end of the motion, the momentum of the sliding block is zero, but it poessesses momentum in between. For momentum to be conserved in the Earth as a whole, the region outside V must receive momentum from the sliding block. That is, an impulse acts on it[note 1)].

These properties become important when considering the equivalent body force described in the next section.

§4.2 Equivalent body force and stress glut

Let us now consider the occurrence of an earthquake. An earthquake is a phenomenon in which a discrepancy (slip) occurs on a fault plane. The rupture phenomenon itself cannot be described within the framework of elastic mechanics. Specifically, since Hooke's law is a physical law that should strictly hold elsewhere, we can say that a phenomenon is occurring whose constitutive law cannot be described by Hooke's law. Here, let us consider a volume V enclosed by Σ. Outside Σ, we assume that the phenomena can be completely described within the framework of a linear elastic body, and that Hooke's law breaks down only inside Σ.

note 1) For details, see Takei and Kumazawa [1994, 1995].(14), (15)

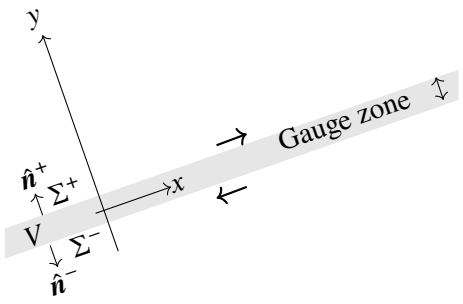

Figure 4.1: Schematic figure of a right-lateral vertical strike-slip fault.

The representation theorem guarantees that if the displacement and stress on Σ are known, the displacement and stress outside of it can be completely described. Information about the deformation inside Σ is not necessary for the deformation outside Σ. Therefore, let us consider virtually embedding a linear elastic body inside Σ as well, which satisfies the boundary conditions of displacement and stress on Σ. In the following, we will show that the entire system can be represented by a linear elastic body, and the effect of the breakdown of Hooke's law can be completely expressed by an equivalent force (**equivalent body force**)[note 2)].

Suppose an earthquake (faulting) occurs inside Σ. Inside Σ, brittle failure is occurring, and Hooke's law does not hold. Deformation due to brittle failure occurs in a thin layer known as fault gouge[note 3)]. Assume we can measure the actual stress and denote it by $\boldsymbol{T}_{\text{true}}$ (dashed line in the figure).

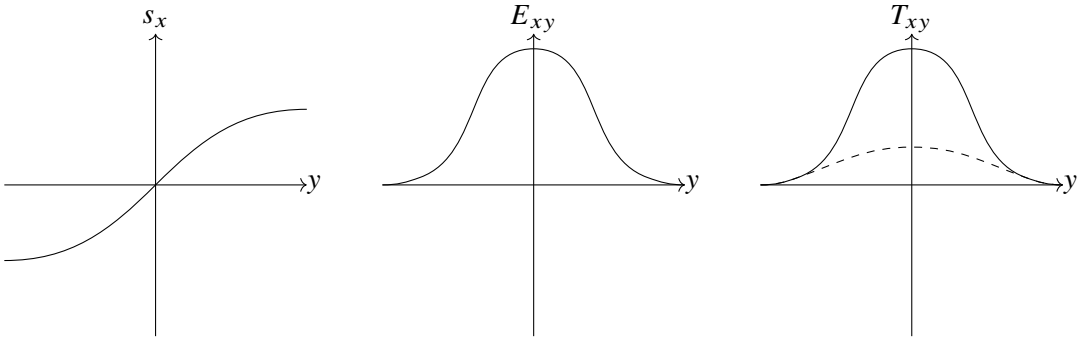

Figure 4.2: Schematic figure of the displacement, strain and stress.

Here, let us replace the interior of Σ virtually with an elastic body. Since Hooke's law holds inside Σ, we can calculate the stress from the strain. As shown in Figure 4.2, the stress obtained by modeling with a linear elastic body is larger than the actual stress. Let us denote this modeled stress by $\boldsymbol{T}_{\text{model}}$ (solid line in the figure). We now define the **stress glut** $\boldsymbol{\Gamma}$ as

note 2) For details, see Dahlen and Tromp (1998).(2)

note 3) Gouge consists of unconsolidated particles comminuted by brittle failure. See, for example, the website of Dr. Sakaguchi: http://www.arito.jp/LecEQ22.shtml.

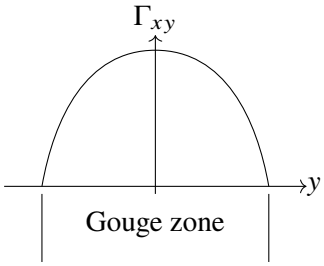

Figure 4.3: Schematic figure of the stress glut.

$\boldsymbol{\Gamma} = \boldsymbol{T}_{\text{model}} - \boldsymbol{T}_{\text{true}}$.[(1)] On Σ, we have $\boldsymbol{\Gamma} = 0$.

Let us consider an infinitesimal element within the region replaced by the elastic body. If we apply $-\Gamma$ inside Σ, the net stress applied to the perfectly elastic body becomes $\boldsymbol{T}_{\text{true}}$, and its equation of motion matches that before the replacement by the elastic body. In other words, by replacing the region inside Σ with an elastic body and applying $-\Gamma$ within the region, we can describe the deformation $\boldsymbol{s}$ within the entire volume V. Assuming the stress glut is distributed inside the elastic body, we can define the equivalent body force as $-\partial_j \Gamma_{ij}$. This allows us to completely describe the problem within the framework of linear elasticity, treating it as a problem where an equivalent body force acts on an elastic body.

Since the solid Earth is a closed system, the net force and torque on the system are zero. In the case of faulting, we can approximate that there is no exchange of angular momentum between the inside and outside of the region Σ, and the equivalent body force can be represented by two pairs of force couples.

When trying to understand a seismic source (the excitation source of seismic waves) from elastic waves, all we can do is determine the excitation region and the equivalent body force. The physical model that can explain the equivalent body force is not necessarily unique, and independent information is essential for considering its excitation mechanism.

§4.3 Multipole expansion

Using the stress glut $\boldsymbol{\Gamma}$, the equivalent body force can be written as

$$\boldsymbol{f} = -\nabla \cdot \boldsymbol{\Gamma}(\boldsymbol{x}, t). \tag{4.1}$$

The excitation of seismic waves by the equivalent body force can be written using Green's functions as

$$\boldsymbol{S}(\boldsymbol{x}, \omega) = \int_V \boldsymbol{G}(\boldsymbol{x}, \boldsymbol{\xi}, \omega) \boldsymbol{f}(\boldsymbol{\xi}, \omega) dV(\xi). \tag{4.2}$$

Let us Taylor expand the Green's function with respect to $\Delta\boldsymbol{\xi}$ in the vicinity of $\boldsymbol{\xi}_0$. Let k be a typical wavenumber of the Green's function. The n-th derivative of the Green's function G can be evaluated as $k^n G$. Therefore, the n-th order term of the Taylor expansion is approximately

$$\frac{1}{n!} k^n G \Delta\xi^n = \frac{1}{n!} G (k\Delta\xi)^n. \tag{4.3}$$

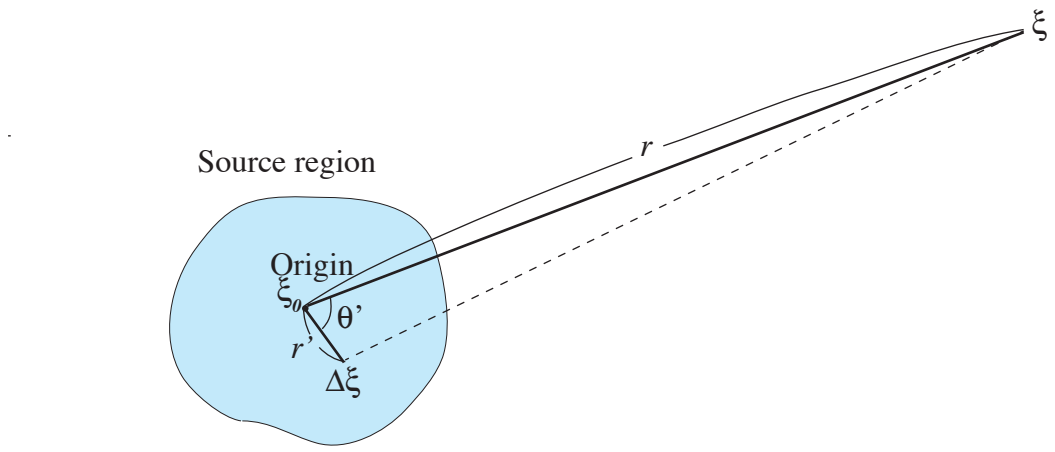

Figure 4.4: Schematic figure of the source-receiver geometry.

When $k\Delta\xi$ is sufficiently small, that is, when the dimension of the region Σ is sufficiently small compared to the wavelength of the seismic wave (Figure 4.4), we can apply a Taylor expansion. So, let's substitute the Taylor expansion up to the second-order term with respect to $\Delta\boldsymbol{\xi}$:

$$\boldsymbol{G}(\boldsymbol{x},\boldsymbol{\xi},\omega) \approx \boldsymbol{G}(\boldsymbol{x},\boldsymbol{\xi}_0,\omega) + \nabla_{\boldsymbol{\xi}}\boldsymbol{G}(\boldsymbol{x},\boldsymbol{\xi}_0,\omega)\Delta\boldsymbol{\xi} + \frac{1}{2}\Delta\boldsymbol{\xi}^T\mathcal{H}_{\boldsymbol{\xi}}\boldsymbol{G}(\boldsymbol{x},\boldsymbol{\xi}_0,\omega)\Delta\boldsymbol{\xi} + O(\Delta\boldsymbol{\xi}^3). \tag{4.4}$$

Substituting this expression into equation 4.2, we obtain

$$\begin{aligned} S_i(\boldsymbol{x},\omega) \approx\ & G_{ij}(\boldsymbol{x},\boldsymbol{\xi}_0,\omega)\int_V f_j(\boldsymbol{\xi},\omega)dV(\xi) \\ & + \partial_k G_{ij}(\boldsymbol{x},\boldsymbol{\xi}_0,\omega)\int_V f_j\Delta\xi_k dV(\boldsymbol{\xi}) \\ & + \partial_k\partial_l G_{ij}(\boldsymbol{x},\boldsymbol{\xi}_0,\omega)\int_V f_j\Delta\xi_k\Delta\xi_l dV(\boldsymbol{\xi}). \end{aligned} \tag{4.5}$$

The first term represents the resultant force (single force), and the second term represents the moment tensor. If the change in momentum and angular momentum within Σ can be ignored, the first term becomes zero. In addition, if angular momentum is conserved, the total torque is zero, so the anti-symmetric component of the moment tensor becomes zero. When it is necessary to consider the finite size of the source, the third and higher-order terms also become important. On the other hand, since the 3D Green's function has an r^{-1} dependence far from the source, the n-th term has an r^{-n-1} distance dependence. Thus, higher-order terms attenuate more rapidly.

Therefore, at long distances, the equivalent body force can be described by the third term (a quantity called the moment tensor)[note 4].

Let us consider a situation where the excitation source and the other elastic regions do not exchange momentum and angular momentum. The 0th-order term of the multipole expansion corresponds to the impulse, and the 1st-order term corresponds to the torque. Therefore, only the second and higher-order terms have values. Let us look at the second-order term in detail in the next section.

§4.4 Excitation of seismic waves by moment tensor

When the spatial scale of the source region is sufficiently shorter than the wavelength, it can be regarded as a point source, and the stress glut can be written as

$$\Gamma_{ij}(\boldsymbol{x}, t) = M_{ij}(t)\delta(\boldsymbol{x} - \boldsymbol{x}_0). \tag{4.7}$$

Here, $\boldsymbol{M}$ is the moment tensor. The trace of the moment tensor M_{ij} represents the volume change. Also, as shown in the previous section, we are considering a situation where there is no exchange of angular momentum inside and outside the source region. Therefore, it is sufficient to define the moment tensor as a symmetric matrix. Since the moment tensor is a symmetric matrix, it can be diagonalized with three eigenvalues and mutually orthogonal eigenvectors. In the case of ordinary earthquakes, the magnitude of two eigenvalues of M_{ij} is much larger than the other one (it can be represented by two pairs of force couples) [note 5]. When the time variation of each moment tensor component is similar, we can write

$$\Gamma_{ij} = \hat{M}_{ij}\delta(\boldsymbol{x} - \boldsymbol{x}_0)m(t). \tag{4.8}$$

$m(t)$ is an increasing function normalized such that $\int m(t)dt = 1$. Here, the magnitude of the moment tensor, $\mathcal{M}_0$, is defined as

$$\mathcal{M}_0 = \sqrt{\frac{1}{2}\sum_{i,j}\hat{M}_{ij}^2}, \tag{4.9}$$

[note 4] Here we considered the case where the source size is sufficiently small compared to the wavelength. What if the source region is wider? Let us consider a horizontally stratified structure. In this case, the Green's function can be expressed by a sum of Legendre functions (a spherical version of the Fourier series expansion). In this case, the following relation known as the addition theorem holds:

$$\frac{2l+1}{4\pi}P_l(\cos\Theta) = \sum_{m=-l}^{l} Y_{lm}(\boldsymbol{x})Y_{lm}(\boldsymbol{\xi})^*, \tag{4.6}$$

where Θ is the angle between $\boldsymbol{x}$ and $\boldsymbol{\xi}$. If the excitation source is distributed on the Earth's surface, one only needs to evaluate $\int Y_{lm}(\boldsymbol{\xi})f(\boldsymbol{\xi})dV$. When the source region is small compared to the wavelength, it corresponds to the Taylor expansion.

[note 5] For example, explosive sources can also be represented by a moment tensor. For details on non-double couple components, see, for example, Julian et al. [1998].(5)

and it can be expressed using the unit moment tensor $\hat{\boldsymbol{M}}$ as

$$\boldsymbol{M} = \sqrt{2}\mathcal{M}_0\hat{\boldsymbol{M}}. \tag{4.10}$$

At sufficiently low frequencies, the moment tensor can be simplified using the Heaviside function $H(t)$ as

$$\Gamma_{ij} = \sqrt{2}\mathcal{M}_0\hat{M}_{ij}\delta(\boldsymbol{x} - \boldsymbol{x}_0)H(t). \tag{4.11}$$

At a sufficiently distant observation point, the displacement of body waves (U) in an infinite homogeneous medium can be written as

$$U \sim \frac{\mathcal{M}_0}{r}\dot{m}(t - r/c), \tag{4.12}$$

where r is the distance from the source. This shows that the displacement waveform of a teleseismic body wave represents the moment rate function $\mathcal{M}_0\dot{m}(t)$.

Problem 4.1

1. In section 3.4.2, we considered an explosive source, and in this case, the source can be represented by a moment tensor. Derive the expression for the corresponding moment tensor when Δr is sufficiently small.
2. Compute the P-wave radiation pattern when the moment tensor has a value only for $M_{xx} = 1$.
3. Compute the P-wave radiation pattern when the moment tensor has values $M_{xx} = 1, M_{yy} = -1$ (see Figure 4.6).

§4.5 Work done by the moment tensor

In this section, let us consider the work done by the moment tensor on an elastic body. First, consider the stress glut $\boldsymbol{\Gamma}$, and assume that the corresponding equivalent body force $\boldsymbol{f}$,

$$\boldsymbol{f} = -\nabla \cdot \boldsymbol{\Gamma}(\boldsymbol{x}, t), \tag{4.13}$$

acts on the elastic body. Let $\boldsymbol{s}$ be the displacement of the elastic body. The work W done by the equivalent body force on the elastic body is

$$W = \int_V \boldsymbol{f} \cdot \boldsymbol{s} dV. \tag{4.14}$$

Using integration by parts (Problem 4.2), this equation can be rewritten as

$$W = \int_V \boldsymbol{f} \cdot \boldsymbol{s} dV = \sum_{ij} \int_V E_{ij}\Gamma_{ij} dV. \tag{4.15}$$

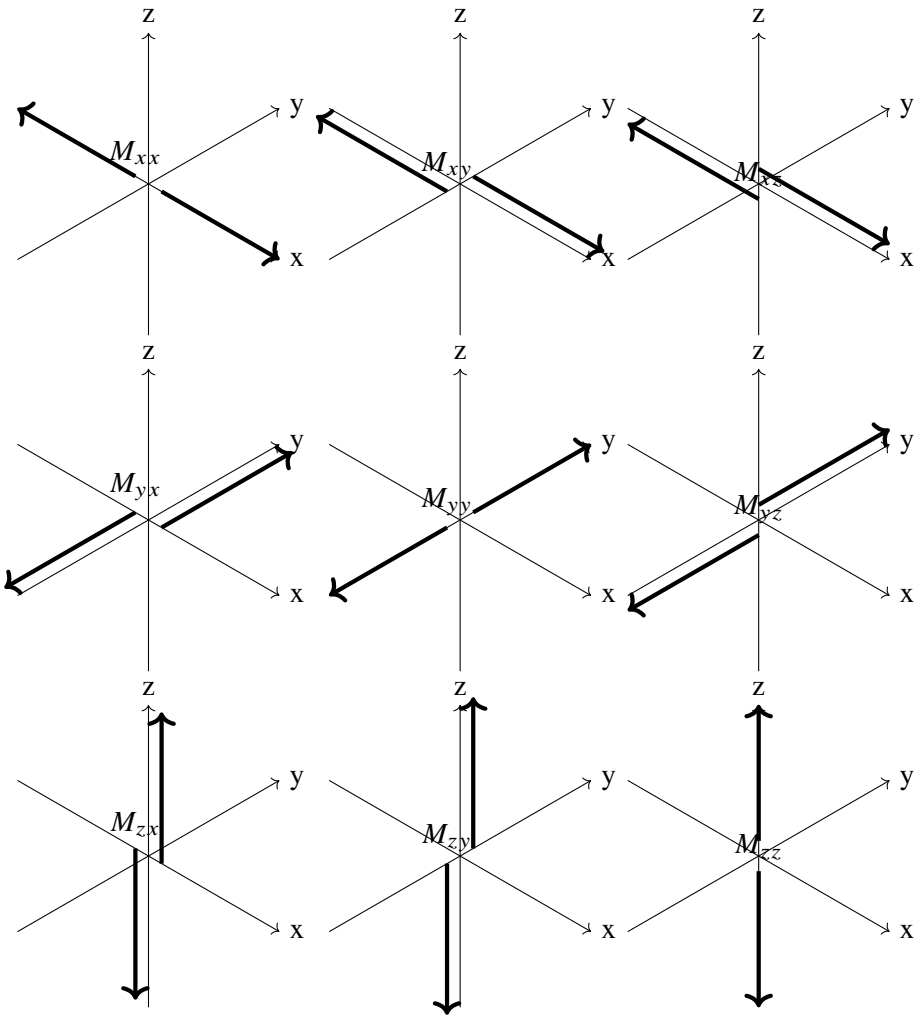

Figure 4.5: Each component of the moment tensor.

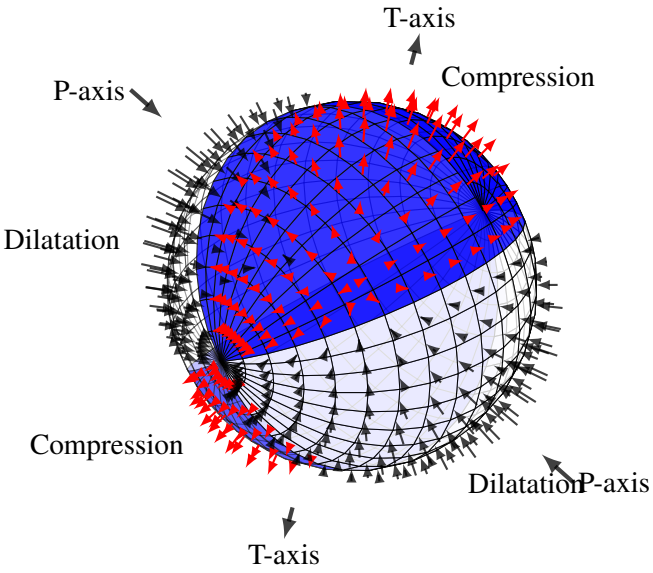

Figure 4.6: Radiation pattern of P-waves by a double couple source. Cyril Langlois (2010)/ CC BY 2.5.

Here, for simplicity, we assumed that the stress glut is 0 on the surface Σ of the elastic body. When the stress glut can be expressed by a moment tensor as in equation (4.7), it can be simplified to

$$W = \sum_{ij} E_{ij} M_{ij}(t). \tag{4.16}$$

In other words, the work can be expressed as the product of the strain E_{ij} caused by the earthquake at the source and the moment tensor M_{ij}. Considering the law of conservation of energy, the work W done by the stress glut Γ transforms into kinetic energy and elastic energy.

Problem 4.2

Derive equation (4.15) assuming the following conditions:

- Consider an elastic body within a volume V, and assume that the stress glut Γ exists only within a region enclosed by Σ.
- On the surface Σ, $\Gamma_{ij} = 0$.
- Assume the elastic body is an isolated system, and use the condition that the torque acting on the elastic body is zero ($\Gamma_{ij} = \Gamma_{ji}$).
- Hint: Use integration by parts and Gauss's divergence theorem.

§4.6 Effect of free surface on seismic wave excitation

In this section, let us consider how a free surface affects the excitation of seismic waves(6)note 6). To conclude beforehand, an initially puzzling result is obtained: shallow earthquakes do not excite seismic waves through their M_{xz} and M_{yz} components.

For simplicity, let us consider a semi-infinite medium. Assuming the Earth's surface is at $z = 0$, the free boundary condition is $T_{xz} = T_{yz} = T_{zz} = 0$ at $z = 0$. Rewriting the first two conditions in terms of strain yields

$$E_{xz}|_{z=0} = \left.\frac{T_{xz}}{\mu}\right|_{z=0} = 0 \tag{4.17}$$

$$E_{yz}|_{z=0} = \left.\frac{T_{yz}}{\mu}\right|_{z=0} = 0. \tag{4.18}$$

We established that the work W done by the moment tensor is $\sum_{ij} E_{ij}T_{ij}$. Since $E_{xz} = E_{yz} = 0$ at $z = 0$, it is clear that the corresponding moment tensor components M_{xz} and M_{yz} do not contribute to excitation. In other words, near a free surface (where the depth is sufficiently shallow compared to the wavelength of seismic waves), if the hypocenter depth can be considered sufficiently shallow compared to the wavelegnth, the boundary conditions at the free surface approximately hold for the strain field near the source. Thus, M_{xz} and M_{yz} cannot excite seismic waves. What does this mean in terms of actual physical phenomena?

For instance, shallow earthquakes near trenches often involve massive low-angle thrust faulting. In such cases, the M_{xz} and M_{yz} components do little to excite seismic waves, making it notoriously difficult to determine these components from seismic data. This problem is especially pronounced when estimating the moment tensor using long-period seismic waves. When attempting to find the moment of a shallow, low-angle thrust earthquake, a trade-off arises between the fault dip angle and the seismic moment, resulting in significant uncertainty in the estimated moment.

§4.7 Excitation of seismic waves by single force

When the excitation source (the region that deviates from linear elasticity) is sufficiently large and its change in momentum cannot be neglected, the term corresponding to the dipole in the multipole expansion cannot be ignored. This term, called a single force, is generated by the exchange of momentum (impulse) between the source region and the surrounding regions. This concept is easier to visualize when considering a landslide (Figure 4.7), for example. Naturally, the total momentum of the entire system must be conserved in such processes.

note 6)See, for example, Kawakatsu [1991].

Examples where a single force becomes important include: (i) landslides, (ii) glacial earthquakes,[3], [11] and (iii) excitation of seismic waves by ocean waves. In all these cases, the motion of a source with a sufficiently large volume corresponds to the excitation of seismic waves.

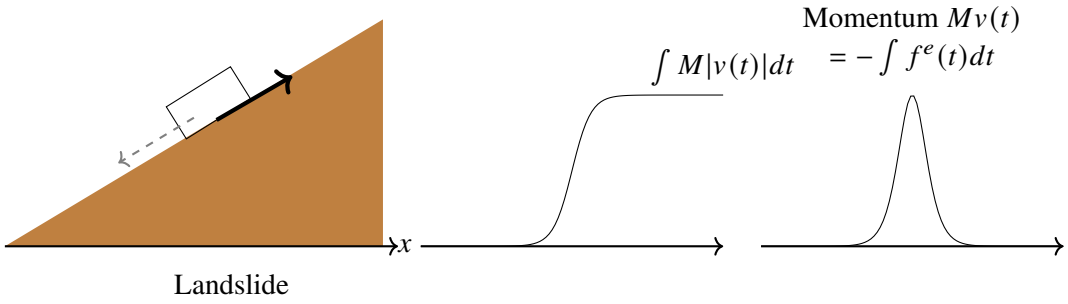

Figure 4.7: Schematic figure of the single force.[7]

Next, let's look at microseisms in more detail.

§4.8 Microseisms: ocean waves shake the Earth

The Earth is constantly shaking, even when earthquakes are not occurring. In the short period band (around 1 second), human activity is the primarily excitation source. At periods longer than 1 second, the vibration originating from human activities diminishes. This is because as the period increases, the wavelength of the seismic waves becomes longer, which means the excitation source needs to shake a deeper (scale on the order of km) region. In the period band longer than 5 seconds, ocean waves are constantly shaking the solid Earth, exciting surface waves (Rayleigh waves and Love waves). This phenomenon is called microseisms.

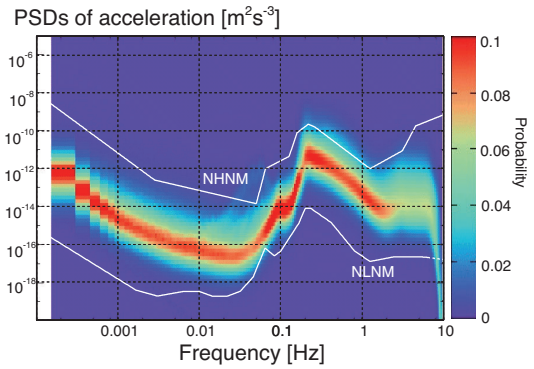

Figure 4.8: Probability density of power spectrum of horizontal acceleration at a Hi-net station in Japan.[12] A reddish color means more probable. The thick red line represents the power spectral densities of ambient noise.

Let us take a look at Figure 4.8. We can see a peak around the period of 10-20 seconds and a larger peak around the 8-second period. The lower frequency one is called primary microseisms, and the higher one is called secondary microseisms. Primary microseisms corresponds to the frequency of the ocean waves themselves,

while secondary microseisms corresponds to double the frequency. Although it seems counter-intuitive that the amplitude of the secondary microseisms is larger, this is due to the dominance of nonlinear effects as an excitation mechanism, making harmonics prominent (known as the Longuet-Higgins mechanism: Longuet-Higgins, 1950[9]). The amplitude of secondary microseisms is orders of magnitude larger, and microseisms are clearly observed even in the middle of a continent far from the ocean.

A ripple pattern by raindrops is analogous to those of microseisms. Please run an application at the website. An impulsive force at a point generates an outgoing concentric wave. On the other hand, we can trace wavefront generated by many random sources at first. Gradually, inside the circle, the wave field becomes quite random. We cannot identify any specific direction.

It is observed particularly clearly when a typhoon passes, as the wave height increases. Figure 4.9 shows an example during the passage of Typhoon No. 18 in 2004. A running spectrum[note 7] was calculated from approximately one and a half days of records at Minamidaito Island. As the typhoon weakens and moves away from the observation point, the amplitude can be seen to decrease. Also, the dominant period becomes shorter as the strength weakens. Because the arrival time is delayed in proportion to the frequency, the effect of deep-water wave dispersion (see Section 9.1.2) can also be observed.

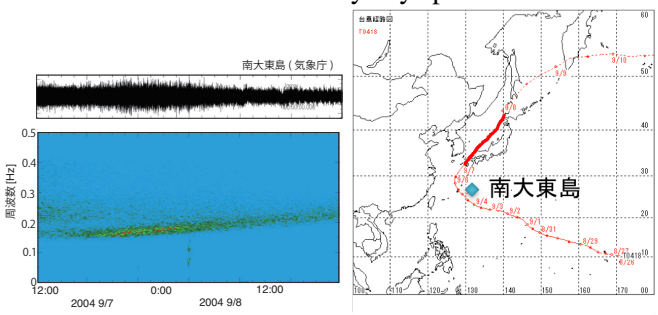

Figure 4.9: Left: Running spectrum from Sept. 7th to Sept. 8th in 2004. The vertical axis shows frequency, and the horizontal one shows time. Right: Track information about the typhoon. The red line shows the track. The thick red line corresponds to the time period of the running spectrum.

A faint vertical streak can be seen in Figure 4.9. This is a seismic wave from a distant earthquake. In this way, microseisms hide seismic wave signals. For seismic observation, microseisms constitute a major source of noise.

4.8.1 Excitation mechanism of microseisms: Longuet-Higgins mechanism

In this section, we will explain the excitation mechanism of microseisms based on Longuet-Higgins [1950][9][note 8] [note 9]. See Section 9.1.2 for more on water surface waves.

[note 7] A running spectrum is a figure showing the temporal variation of a power spectrum. It is used to investigate changes in frequency over time. To calculate it practically: (1) cut out data from the original data while shifting the time window, (2) calculate the power spectrum for each segment of cut-out data, and (3) arrange the calculated power spectra in order along the time axis.

[note 8] Longuet-Higgins was an applied mathematician and physical oceanographer who actively conducted various studies on the statistical theory of ocean waves and ocean waves in general.

[note 9] Although the handling of the nonlinear term here is somewhat ad hoc, it has been simplified. For details, refer to Longuet-Higgins (1950), Hasselmann (1963)[4][note 10], and Kedar *et al.* (2008).[8]

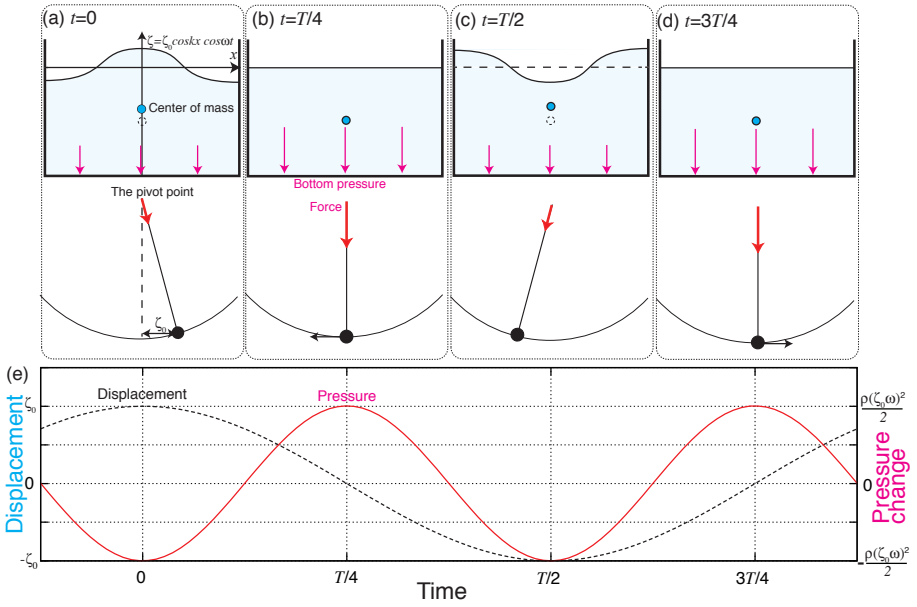

Figure 4.10: Top: Simplified model (a-d) and pendulum analogy. In the top left figure, waves do not propagate because a standing wave is considered. Taken from Nishida (2017).[13]

Let us consider a pendulum as an analogy, as shown on the right of Figure 4.10 (Longuet-Higgins, 1953[10]). In the left figure, since a standing wave is considered, the wave does not propagate but moves vertically. Therefore, considering the position of the center of gravity at each instant, it is higher in (a) and (c) than in (b) and (d). To cause an up-and-down movement of the center of gravity, a pressure fluctuation with a frequency of 2ω is necessary. This is easy to understand if we think based on the pendulum on the right side of the figure. The position of the pendulum represents the position of the center of gravity, the force at the fulcrum corresponds to the pressure at the ocean floor, and the horizontal displacement of the pendulum corresponds to the depth of the center of gravity of the seawater. The swinging of the pendulum corresponds to the movement of water (see also the streamlines at the bottom of Figure 4.10). Considering the fluctuation of the force at the fulcrum, one can see that the pressure fluctuates at 2ω. From a simple calculation, it can also be seen that the pressure fluctuation is proportional to the square of the wave amplitude. In other words, this pressure fluctuation is a second-order term (nonlinear effect).

Next, let's consider a traveling wave instead of a standing wave. In the case of a traveling wave, it simply moves at a constant speed while preserving its shape, so the center of gravity does not change. That is, no pressure fluctuation occurs. We can see that the Longuet-Higgins mechanism is valid only for standing waves and not for traveling waves. In other words, to excite microseisms by the Longuet-Higgins mechanism, at least one pair of ocean waves traveling in opposite directions is necessary. It is inferred that the reflection of waves at the coast and the existence of multiple wave sources are essential for the excitation of microseisms.

Parametric speaker

§4.9 Bibliography

[1] George Backus and Marjorie Mulcahy. Moment tensors and other phenomenological Discontinuous descriptions of seismic sources - I. displacements. *Geophys. J. R. Astron. Soc.*, 46(2):341–361, 1976.

[2] F.A. Dahlen and J. Tromp. *Theoretical Global Seismology*. Princeton University Press, Princeton, 1998.

[3] Göran Ekström, Meredith Nettles, and Geoffrey A Abers. Glacial earthquakes. *Science*, 302(5645):622–624, October 2003.

[4] K. Hasselmann. A statistical analysis of the generation of miceoseisms. *Rev. Geophys.*, 1:177–210, 1963.

[5] Bruce R. Julian, Angus D. Miller, and G. R. Foulger. Non-double-couple earthquakes 1. Theory. *Rev. Geophys.*, 36(4):525, 1998.

[6] H. Kawakatsu. Earthquake size and diversity. *Zisin 2nd ser.*, 44(Supplement):265–277, 1991.

[7] Hitoshi Kawakatsu. Centroid single force inversion of seismic waves generated by landslides. *J. Geophys. Res.*, 94(B9):12363, 1989.

[8] S. Kedar, M. Longuet-Higgins, F. Webb, N. Graham, R. Clayton, and C. Jones. The origin of deep ocean microseisms in the northern atlantic ocean. *Proc. R. Soc. A*, 464:777–793, 2008.

[9] M. Longuet-Higgens. A theory of the origin of microseisms. *Phil. Trans. of the Roy. Soc. of London*, 243:1–35, 1950.

[10] M. S. Longuet-Higgins. Can sea waves cause microseisms? *Proc. Symposium on Microseisms, Harriman 1952*, (306):74–93, 1953.

[11] Meredith Nettles and Göran Ekström. Glacial earthquakes in greenland and antarctica. *Annu. Rev. Earth Planet. Sci.*, 38(1):467–491, April 2010.

[12] K Nishida, H Kawakatsu, and K Obara. Three-dimensional crustal S wave velocity structure in japan using microseismic data recorded by hi-net tiltmeters. *J. Geophys. Res.*, 113(B10):B10302, October 2008.

[13] Kiwamu Nishida. Ambient seismic wave field. *Proc. Jpn. Acad. Ser. B Phys. Biol. Sci.*, 93(7):423–448, 2017.

[14] Yasuko Takei and Mineo Kumazawa. Why have the single force and torque been excluded from seismic source models? *Geophys. J. Int.*, 118(1):20–30, jul 1994.

[15] Yasuko Takei and Mineo Kumazawa. Phenomenological representation and kinematics of general seismic sources including the seismic vector modes. *Geophys. J. Int.*, 121(3):641–662, jun 1995.

Elastic wave propagation in a half space

Chapter 5

The previous chapter explained Green's function in an infinite medium. However, the structure of the real Earth is not so simple. Lateral heterogeneity causes the complexity of seismic wave propagation. This figure shows SH wave propagation from an earthquake. At frequencies below a few Hz, a stratified Earth structure (a seismic wave velocity structure depending only on depth) is a good approximation. Even the simple Earth structure still exhibits complexities, but we can trace the wavefront. The figure shows the waves can be approximated by plane waves.

In this figure, we can see reflections and conversions on the discontinuities (at the surface, 410 km, 660 km, and core-mantle boundary (CMB)). Because the free surface is the biggest boundary, we introduce the free surface first in this chapter.

First, we introduce the concept of a plane wave. Then, we will show that we can separate the wavefield into P-SV and SH waves according to the wave type and the polarization direction. This chapter describes the effects of a free surface: the reflection and the P-S conversion at a free surface.

§5.1 Review of seismic wave propagation: body waves and surface and boundary waves

Nature is full of waves. For example, if we look at the water's surface, we can see ripples spreading as the wind blows. When some restoring force acts on the medium, they propagate at a certain speed while maintaining their shape ($f(x-ct)$ (x is position, c is propagation speed, t is time)). Let us consider sound waves specifically.

1. Gas moves and density changes

2. Density change produces pressure change

3. A pressure gradient moves the gas

Sound waves propagate by repeating this cycle. Seismic waves propagate in solids in a similar cycle (see the next chapter for details). If the wave's amplitude is sufficiently small, its behavior is linear, and the principle of superposition holds. In other words, if individual wave components can be isolated and understood, the entire wavefield can be understood as a superposition of these components.

§5.2 Plane wave

To be revised Elastic wave propagation becomes more complex when considering free surfaces compared to a homogeneous infinite medium. For example, when trying to evaluate the Green's function for a half-space with a free surface, it can only be expressed analytically in limited cases, such as when the source is located on the ground surface (e.g., chapter 5.8). Even in the case of the Green's function for a homogeneous infinite elastic medium, the analytical form of the near-field term becomes complex. When considering Green's function for the infinite medium, the near-field term changes shape depending on the distance from the epicenter, while the far-field term maintains its shape. On the other hand, the far-field term propagates while keeping its shape[note 1)]. Therefore, this chapter will focus only on the far-field term.

Let us first consider the 3-dimensional scalar case for simplicity. Consider the case of an external force $\delta(\boldsymbol{x})$ acting at the epicenter. As we learned previously, the Green's function, in this case, is given [note 2)] by

$$G^{\phi}(r,\omega) = -\frac{1}{4\pi\kappa}\frac{e^{-ikr}}{r}. \tag{5.1}$$

We can define an isosurface where the phase of e^{-ikr} is constant and is generally referred to as a "wavefront". The trajectory orthogonal to the wavefront is called the ray (see Chapter **??** for details). In regions where r is sufficiently distant, the wavefront curvature can be neglected. [note 3)]. The wave can be treated as a plane wave when $r > 1/k$, where r is the radius of curvature.

Let us go back to the wave equation for once: the Green's function G^{ϕ} in the frequency domain satisfies

$$-rho_0\omega^2 G^{\phi} - \kappa\nabla^2 G^{\phi} = -\delta(\boldsymbol{x}). \tag{5.2}$$

[note 1)] As explained in the section on Ray Theory, the far-field term maintains its shape when the typical spatial scale of the velocity structure is longer than the wavelength of interest.

[note 2)] In the 2-dimensional case as well as in the 3-dimensional case, the far-field of the Green's function can be approximated as e^{-ikr} 3.130.

[note 3)] More exact conditions are required for the approximation of plane waves: (i) the curvature of the wavefront can be neglected when focusing on wave propagation on spatial scales sufficiently short compared to the radius of curvature of the wavefront. (ii) Near the epicenter, the radius of curvature becomes so small that a plane wave cannot approximate it. From a simple estimation, it can be seen that the wave can be treated as a plane wave in the region of approximately $r > 1/k$

The Fourier transform in the space, and Fourier inverse transform again gives

$$G^{\phi} = -\frac{1}{\kappa} \iiint \frac{\alpha^2 e^{i(k_x x + k_y y + k_z z)}}{\alpha^2(k_x^2 + k_y^2 + k_z^2) - \omega^2} dk_x dk_y dk_z \tag{5.3}$$

We can write that this equation shows that the Green's function can be represented by a superposition of plane waves.

When considering the Green's function of a semi-infinite medium, if we understand the behavior of the plane wave element $e^{-i\boldsymbol{k}\cdot\boldsymbol{x}}$ at the free boundary surface, we can understand the overall behavior by superposition (inverse Fourier transform in the frequency domain). In other words, understanding the behavior of the plane wave $e^{-i\boldsymbol{k}\cdot\boldsymbol{x}}$ on the free surface is the key to understanding elastic wave propagation in a semi-infinite medium.

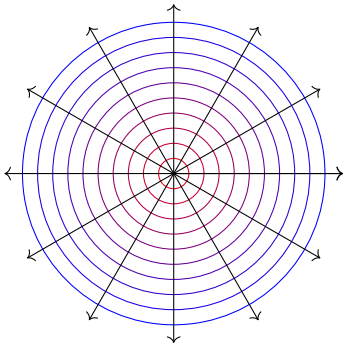

Figure 5.1: Wavefront and ray for Green's function for a 3-D in an infinite medium.

Summary of plane wave

When the source is enough far away from the source, the curvature of the wavefront becomes small. In this case, the waveform can be approximated by a plane wave:

1. Plane wave is preserving its shape,
2. Plane wave has a plane wavefront,
3. Plane wave propagates perpendicular to the wavefront[a].

In this case, the scalar variable $\phi(t - \boldsymbol{p}\cdot\boldsymbol{x})$ can be represented as a function of $t - \boldsymbol{k}\cdot\boldsymbol{x}$. $\boldsymbol{p}$ is a quantity called slowness defined as $\boldsymbol{p} = \boldsymbol{k}/\alpha$ (acoustic wave).

[a] Exactly speaking, here we neglect the dispersion for simplicity.

Here we consider a propagating wave into the x axis ($p_y = 0$). When $p_x > 1/\alpha$, p_z has real

value. Then it propagates into the z direction (plane wave). with P-wave speed α along the slowness vector. On the ground ($z = 0$), at $t = 0$ the wavefront is at the point of $x = z = 0$. At $t = \tau$ it is at the point of $(\tau/p_x, 0, \tau/p_z)$. When we observed the waveform on the ground using seismometers, it propagates in the x direction with "apparent velocity" with $1/p_x$. Thus we can estimate the horizontal apparent velocity from the surface seismic observations.

5.2.1 Plane wave in an elastic medium

Next, Let us consider an elastic wave with a sinusoidal shape at angular frequency ω[note 4], and slowness vector $\boldsymbol{p}$. Scalar potential ϕ and vector potential $\boldsymbol{\psi}$ can be written by [note 5]

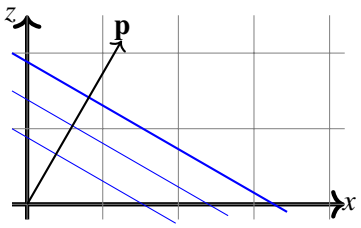

$$\phi = A_\alpha e^{i(\boldsymbol{k}_\alpha \cdot \boldsymbol{x} - \omega t)} = A_\alpha e^{i\omega(\boldsymbol{p}_\alpha \cdot \boldsymbol{x} - t)} \tag{5.4}$$

$$\boldsymbol{\psi} = \boldsymbol{A}_\beta e^{i(\boldsymbol{k}_\beta \cdot \boldsymbol{x} - \omega t)} = \boldsymbol{A}_\beta e^{i\omega(\boldsymbol{p}_\beta \cdot \boldsymbol{x} - t)}. \tag{5.5}$$

The corresponding displacement is given by,

$$\boldsymbol{s}_\alpha(\boldsymbol{x}, t) = A_\alpha \boldsymbol{k}_\alpha e^{i(\boldsymbol{k}_\alpha \cdot \boldsymbol{x} - \omega t)} = \omega A_\alpha \boldsymbol{p}_\alpha e^{i\omega(\boldsymbol{p}_\alpha \cdot \boldsymbol{x} - t)} \tag{5.6}$$

$$\boldsymbol{s}_\beta(\boldsymbol{x}, t) = \boldsymbol{k}_\beta \times \boldsymbol{A}_\beta e^{i(\boldsymbol{k}_\beta \cdot \boldsymbol{x} - \omega t)} = \boldsymbol{p}_\beta \times \boldsymbol{A}_\beta \omega e^{i\omega(\boldsymbol{p}_\beta \cdot \boldsymbol{x} - t)}. \tag{5.7}$$

The polarization vector of the P wave is parallel to the propagation direction $\boldsymbol{p}_\alpha$, whereas that of the S wave is perpendicular to the propagation direction, with an ambiguity in its orientation. Although we use the form $e^{i\boldsymbol{k}\cdot\boldsymbol{x} - \omega t}$ here to represent wave propagation, we note that only the real part of a physical quantity has physical meaning.

$\boldsymbol{p}$ is called **slowness**, defined as $\boldsymbol{p} = \boldsymbol{k}/\omega$. Its dimension is the inverse of speed, and it is parallel to the propagation direction. For example, the squared norm can be written as

$$p_x^2 + p_y^2 + p_z^2 = \frac{1}{\alpha^2}. \tag{5.8}$$

Inverse Fourier transform of $e^{i\omega(\boldsymbol{p}\cdot\boldsymbol{x} - t)}$ gives us formula of general waveform. A P-wave propagates while maintaining its shape as $\boldsymbol{s}_\alpha(\boldsymbol{x}, t) = \boldsymbol{p}_\alpha f(t - \boldsymbol{p}_\alpha \cdot \boldsymbol{x})$, whereas an S-wave propagates as $\boldsymbol{s}_\beta(\boldsymbol{x}, t) = \boldsymbol{p}_\beta \times \boldsymbol{A}_\beta f(t - \boldsymbol{p}_\beta \cdot \boldsymbol{x})$.

5.2.2 Body wave and inhomogeneous wave

When $p^2 > 1/\alpha^2$, p_z becomes imaginary. Using an definition of $p_z = \xi i$, the corresponding potential is given by

$$\phi = A_\alpha e^{i\omega(p_x x - \omega t)} e^{-\xi z}. \tag{5.9}$$

[note 4] When we consider seismic wave propagation, the sign of the Fourier convention is different from other physical cases, including the appendix of the previous chapter. To keep consistency a propagation in positive $\boldsymbol{x}$ direction as $e^{i(\boldsymbol{k}\cdot\boldsymbol{x} - \omega t)}$. Read the box of Aki and Richards for details. Please take care of the Fourier convention when you read a paper of a textbook.

[note 5] In seismology, when considering wave propagation, the sign on ω is often taken to be negative. The definition of the Fourier transform is also often changed. This is to treat traveling waves as positive, and this is the sign taken by Aki and Richards (2002) and Saito (2009). In seismology, too, Dahlen and Tromp (1998) use the opposite sign, so it is important to be careful about which definition you are following.

This equation shows that it decreases exponentially in the z direction. The wave is called an inhomogeneous wave[note 6)] In an infinite medium, it diverges at infinity, making it physically impossible as a standalone wave. However, when boundaries exist, it can exist while satisfying the boundary conditions. Section 5.6 explains Rayleigh waves as a kind of inhomogeneous wave in a semi-infinite medium with a free boundary.

Let us review the global propagation of seismic waves. We can categorize it into body wave, which propagates in the Earth's interior, and boundary/surface wave, which propagates along a boundary including the Earth's surface (Figure 5.2left). Figure 5.2 shows such an example of Green's functions using seismic interferometry. The Horizontal axis shows the epicentral distance, whereas the vertical one shows the travel time[note 7)]. The figures show global propagations of seismic surface waves and body waves. This section describes a brief summary of seismic wave types.

In general, we can categorize seismic waves into body waves and boundary waves. Body waves propagate in an internal body, whereas boundary waves travel along a boundary. A surface wave is a kind of boundary wave trapped close to the free surface.

note 6)This wave is also known as an evanescent wave or external wave in physics or meteorology.
note 7)travel time is defined as the time from the origin time to the arrival time

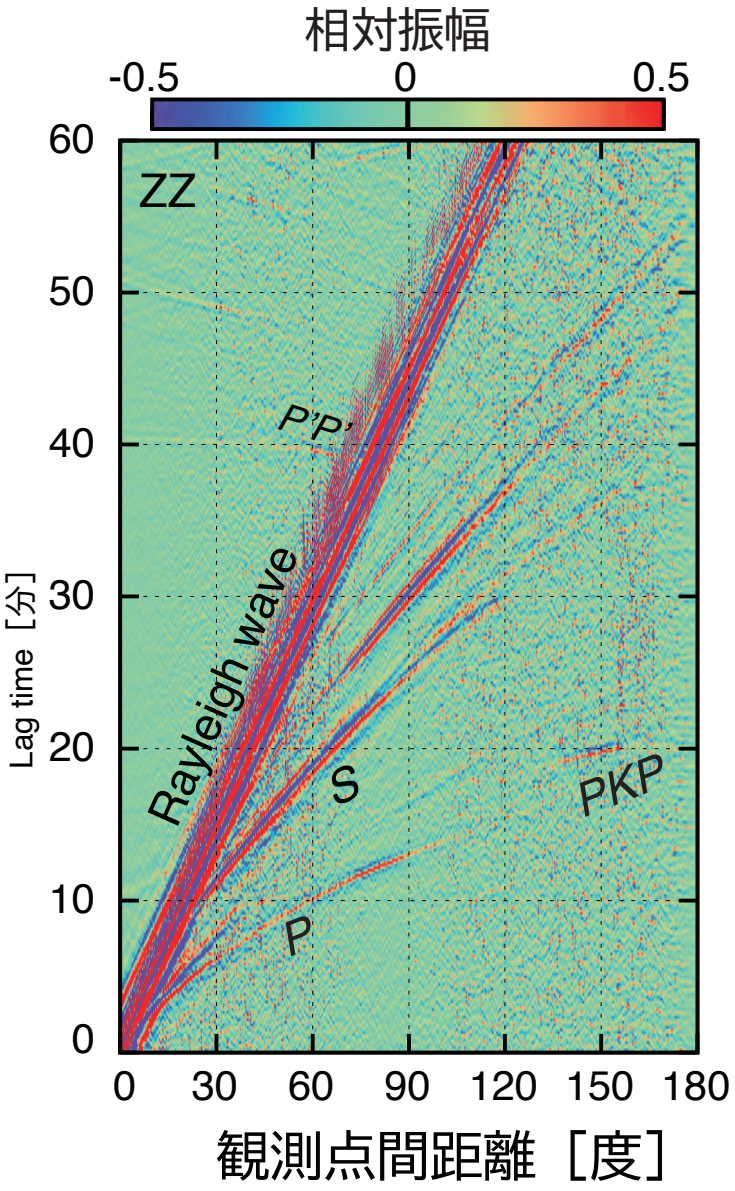

Figure 5.2: Global propagation of body and surface waves. The waveforms are virtual Green's functions retrieved by cross-correlating ambient seismic wave field, also known as microseisms[4] (see chapter 10 for details of seismic interferometry.)

Body wave

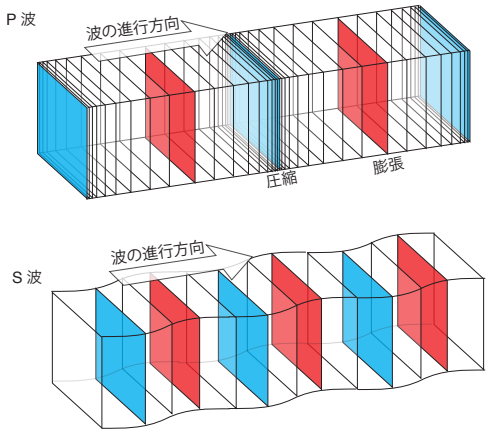

Figure 5.3: A schematic figure of P and S wave propagation.

We can categorize body waves into P and S waves; the polarization of the P wave is parallel to the propagation direction, whereas that of the S wave is perpendicular to the propagation direction (Figure 5.3). "P" originated from the Primary wave, and "S" originated from the Secondary wave. The deformation of the P wave is volumetric, whereas that of the S wave is shear. note 8).In general, with the decreasing temperature of the material, the stiffness increases, which causes an increase in the P wave and S wave velocities.

We all know well that P-waves propagate faster than S-waves, and the Omori formula for determining the distance to the epicenter from the difference in the arrival times of P-waves and S-waves note 9). You may have also heard of the Earthquake Early Warning, which estimates the hypocenter from the fast-moving P-waves and predicts the arrival of large tremors (S-waves).

Inhomogeneous waves: surface waves and boundary wave

Surface waves in an elastic medium can be categorized into Rayleigh waves, associated with volumetric changes, and Love waves associated with multiple reflections of SH waves in a surface low-velocity layer.

5.2.3 Energy flux

The total energy of an elastic medium per unit volume $\mathcal{U}$ can be written as the sum of the kinetic energy $\mathcal{U}^k$ and the strain energy $\mathcal{U}^p$ as

$$\mathcal{U} = \mathcal{U}^k + \mathcal{U}^p. \tag{5.10}$$

Energy flux $\boldsymbol{K}$ perpendicular to a unit area is given by(1)

$$\boldsymbol{K} = -\boldsymbol{T} \cdot \partial_t \boldsymbol{s}. \tag{5.11}$$

note 8)A Web site of demonstration of body wave propagation.http://www.eri.u-tokyo.ac.jp/knishida/Seismology/body_wave.html

note 9)(5) is available at http://hdl.handle.net/2261/32677

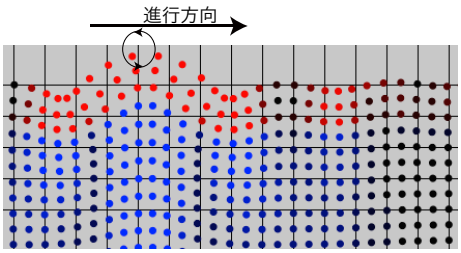

Figure 5.4: Rayleigh wave propagation. The red color shows particle motions in retrograde, and the blue color shows those in prograde.

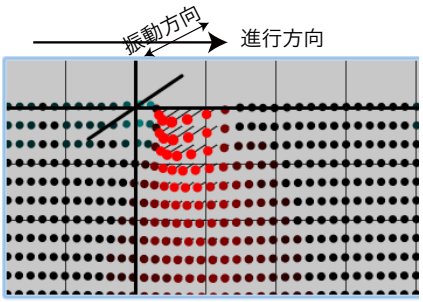

Figure 5.5: Love wave propagation.

By equipartition between the kinetic energy and the strain energy, the total energy $\mathcal{U}$ can be written by,

$$\mathcal{U} = \rho \left| \frac{\partial \boldsymbol{s}}{\partial t} \right| \tag{5.12}$$

where A is the displacement.

In particular, the energy flux of the P wave and that of the S wave are given by

$$\boldsymbol{K} = \begin{cases} \alpha \hat{\boldsymbol{n}} \mathcal{U} & \text{P wave} \\ \beta \hat{\boldsymbol{n}} \mathcal{U} & \text{S wave,} \end{cases} \tag{5.13}$$

where $\hat{\boldsymbol{n}}$ is a unit vector of the propagation direction. Conservation of energy is represented by

$$\frac{\partial \mathcal{U}}{\partial t} + \nabla \cdot \boldsymbol{K} = 0. \tag{5.14}$$

Problem 5.1

1. For a plane wave (P wave), show that the kinetic energy is equal to the strain energy as,

$$\frac{1}{2}T_{ij}E_{ij} = \frac{1}{2}\rho\left|\frac{\partial \boldsymbol{s}}{\partial t}\right|^2 . \tag{5.15}$$

2. Here we consider a wave form of P wave $\boldsymbol{s} = \boldsymbol{p}\, f(t - \boldsymbol{p}\cdot\boldsymbol{x})$. Calculate the energy flux from equation 5.11.

3. For the inhomogeneous wave (P wave) with propagation in $z < 0$ given by P wave potential $\phi = \sin(\omega t - kx)\exp(\xi z)$. Then the displacement is written by

$$s_x = -k\cos(\omega t - kx)\exp(\xi z) \tag{5.16}$$
$$s_z = \xi\sin(\omega t - kx)\exp(\xi z). \tag{5.17}$$

Calculate the energy flux.

§5.3 SH wave and P-SV wave

Free surface condition on the ground is crucial for seismic wave propagations. For simplicity, let us consider semi-infinite homogeneous medium in $z < 0$ with free surface condition on $z = 0$ (T_{iz}=0) (Figure 5.7). By introducing the free surface, we can categorize S wave into two. Figure 5.6 shows (1) vertically polarized S wave in xz plane (SV wave) and (2) horizontally polarized S wave (SH wave). This category is also crucial for stratified Earth, which is a good approximation at frequencies lower than several Hz.

In this chapter, the first section explains reflections and refraction of SH wave, and then we will explain reflection, refraction, and conversion of SV waves.

5.3.1 Equations of motion and Hooke's law

As shown in Figure 5.6, we take the y axis along the wave front,

$$\frac{\partial}{\partial y} = 0. \tag{5.18}$$

Then, the equations of motion are given by

$$\rho \frac{\partial^2 s_x}{\partial t^2} = \frac{\partial T_{xx}}{\partial x} + \frac{\partial T_{xz}}{\partial z} \tag{5.19}$$

$$\rho \frac{\partial^2 s_y}{\partial t^2} = \frac{\partial T_{yx}}{\partial x} + \frac{\partial T_{yz}}{\partial z} \tag{5.20}$$

$$\rho \frac{\partial^2 s_z}{\partial t^2} = \frac{\partial T_{zx}}{\partial x} + \frac{\partial T_{zz}}{\partial z}, \tag{5.21}$$

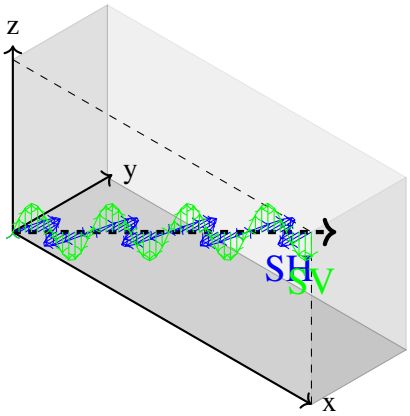

Figure 5.6: Propagations of SH wave and SV waves and the polarization.

and Hooke's law is given by

$$T_{xx} = (\lambda + 2\mu)\frac{\partial s_x}{\partial x} + \lambda\cancel{\frac{\partial s_y}{\partial y}} + \lambda\frac{\partial s_z}{\partial z} \tag{5.22}$$

$$T_{xz} = \mu\left(\frac{\partial s_x}{\partial z} + \frac{\partial s_z}{\partial x}\right) \tag{5.23}$$

$$T_{yx} = \mu\left(\frac{\partial s_y}{\partial x} + \cancel{\frac{\partial s_x}{\partial y}}\right) \tag{5.24}$$

$$T_{yz} = \mu\left(\frac{\partial s_y}{\partial z} + \cancel{\frac{\partial s_z}{\partial y}}\right) \tag{5.25}$$

$$T_{zz} = \lambda\frac{\partial s_x}{\partial x} + \lambda\cancel{\frac{\partial s_y}{\partial y}} + (\lambda + 2\mu)\frac{\partial s_z}{\partial z}. \tag{5.26}$$

Let us drop the stress term and rearrange the equations as,

$$\rho\partial_t^2 s_x = (\lambda+\mu)\partial_x(\partial_x s_x + \partial_z s_z) \qquad +\mu(\partial_x^2 s_x + \partial_z^2 s_x) \tag{5.27}$$

$$\rho\partial_t^2 s_y = \qquad +\mu(\partial_x^2 s_y + \partial_{z^2} s_y) \tag{5.28}$$

$$\rho\partial_t^2 s_z = (\lambda+\mu)\partial_z(\partial_x s_x + \partial_z s_z) \qquad +\mu(\partial_x^2 s_z + \partial_z^2 s_z) \tag{5.29}$$

s_x and s_y are coupled with each other, whereas, s_y is decoupled with the others. Because s_y is polarized in a horizontal plane, the wave is called an SH wave. On the other hand, because s_x and s_z are composed of the P wave and vertical polarized S wave. the wave is called as P-SV wave. As described in later sections, the separation of the SH wave field and P-SV wave field is possible for a stratified Earth mode. Therefore, when we analyze seismic waveforms, rotations of horizontal components from north-south component and east-west component to transverse component (perpendicular to the great circle path between the source and the receiver) and radial component (parallel to the path). The transverse component represents the SH wave, and the radial component represents P-SV wave[note 10)].

5.3.2 Plane waves in the case of P-SV and SH waves: how to take the vector potential

When considering seismic wavefields, in particular, plane waves in the P-SV case (see next section for details), it is useful to introduce a potential as explained in the 3.4.1section. As already mentioned, there is one degree of freedom in the vector potential. When considering wave propagation in a horizontal multilayer structure in Cartesian coordinates

$$\boldsymbol{A} = \begin{pmatrix} 0 \\ 0 \\ \chi \end{pmatrix} \qquad +\nabla\times\begin{pmatrix} 0 \\ 0 \\ \psi \end{pmatrix} \tag{5.30}$$

$$SH \qquad\qquad SV$$

SV and SH can be separated,[(3)] and the outlook improves if we use the following formula. Because of the arbitrary property of the vector potential, we can choose a convenient way to take the vector potential for our problem. For future calculations, we will write down the case of propagation along a two-dimensional xz plane. Assuming that the potential does not depend on y, the partial derivative with respect to y disappears, and we have a simple form. Below unexplained components are set to zero.

note 10)Exactly speaking, this separation valid for the far field.

P wave

$$s_x = \frac{\partial \phi}{\partial x}, \qquad s_y = 0, \qquad s_z = \frac{\partial \phi}{\partial z} \tag{5.31}$$

$$E_{xx} = \frac{\partial^2 \phi}{\partial x^2}, \qquad E_{xz} = \frac{\partial^2 \phi}{\partial x \partial z}, \qquad E_{zz} = \frac{\partial^2 \phi}{\partial z^2} \tag{5.32}$$

$$T_{xx} = E\frac{(1-\nu)\frac{\partial^2 \phi}{\partial x^2} + \nu \frac{\partial^2 \phi}{\partial z^2}}{(1+\nu)(1-2\nu)}, \qquad T_{xz} = \frac{E}{1+\nu}\frac{\partial^2 \phi}{\partial x \partial z}, \qquad T_{zz} = E\frac{(1-\nu)\frac{\partial^2 \phi}{\partial z^2} + \nu \frac{\partial^2 \phi}{\partial x^2}}{(1+\nu)(1-2\nu)} \tag{5.33}$$

SV wave

$$s_x = \frac{\partial^2 \psi}{\partial x \partial z}, \qquad s_y = 0, \qquad s_z = \frac{\partial^2 \psi}{\partial x^2} \tag{5.34}$$

$$E_{xx} = \frac{\partial^3 \psi}{\partial x^2 \partial z}, \qquad E_{xz} = \frac{1}{2}\left(\frac{\partial^3 \psi}{\partial x \partial z^2} - \frac{\partial^3 \psi}{\partial x^3}\right), \qquad E_{zz} = -E_{xx} \tag{5.35}$$

$$T_{xx} = -E\frac{(2\nu-1)\frac{\partial^3 \psi}{\partial x^2 \partial z}}{(1+\nu)(1-2\nu)}, \qquad T_{xz} = \frac{E}{1+\nu}\frac{1}{2}\left(\frac{\partial^3 \psi}{\partial x \partial z^2} - \frac{\partial^3 \psi}{\partial x^3}\right), \qquad T_{zz} = -T_{xx} \tag{5.36}$$

SH wave

$$s_x = 0, \qquad s_y = -\frac{\partial \chi}{\partial x}, \qquad s_z = 0 \tag{5.37}$$

$$E_{xx} = 0, \qquad E_{xy} = -\frac{1}{2}\frac{\partial^2 \chi}{\partial x^2}, \qquad E_{yz} = -\frac{1}{2}\frac{\partial^2 \chi}{\partial x \partial z}, \tag{5.38}$$

$$T_{xx} = 0, \qquad T_{xz} = -\frac{E}{1+\nu}\frac{1}{2}\frac{\partial^2 \chi}{\partial x^2}, \qquad T_{yz} = -\frac{E}{1+\nu}\frac{1}{2}\frac{\partial^2 \chi}{\partial x \partial z} \tag{5.39}$$

In the following, the plane wave amplitudes are treated as variables (e.g., A, B, C). In the next section, we will consider the potentials

$$\phi = \frac{A}{\omega i} e^{i(\boldsymbol{k}\cdot\boldsymbol{x} - \omega t)} \tag{5.40}$$

$$\psi = -\frac{B}{p_x \omega^2} e^{i(\boldsymbol{k}\cdot\boldsymbol{x} - \omega t)} \tag{5.41}$$

$$\chi = \frac{C}{\omega i} e^{i(\boldsymbol{k}\cdot\boldsymbol{x} - \omega t)} \tag{5.42}$$

and discuss the corresponding amplitudes.

§5.4 Reflection of SH-wave at a free surface

Let us consider the reflection and refraction of an SH wave in a semi-infinite elastic medium $z \leq 0$ with a free surface on $z = 0$. An incident SH wave entering with incident angle φ can be represented by a general solution of equation 5.28 as

$$s_y = Ae^{-i\omega(t-p_x x-p_z z)} + Be^{-i\omega(t-p_x x+p_z z)}, \quad (5.43)$$

where A and B are integral constants. The first term shows incident waves, and the second term shows the reflected wave. The free surface condition is written by

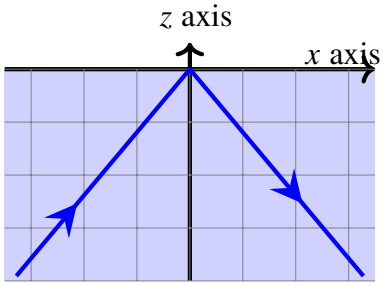

Figure 5.7:

$$T_{zy} = -\mu \frac{\partial s_y}{\partial z} = 0. \quad (5.44)$$

Then the result $A = B$ indicates that the phase of the reflected wave is the same as that of the incident wave. Displacement on the free surface is given by,

$$s_y = 2Ae^{-i\omega(t-px)}, \quad (5.45)$$

which is twice as large as the incident wave.

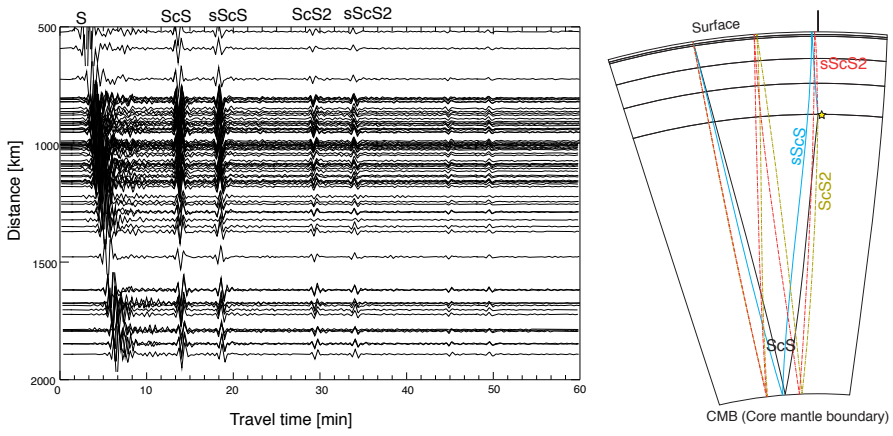

Figure 5.8: Left: An example of seismograms of ScS reverberations from the deep Ogasawara earthquake on 2015/5/30. They are vertical components of broadband seismometers of F-net band-pass-filtered from 30 s to 200 s. Right: Ray paths of ScS, sScS, ScS2, sScS2.

https://www.eri.u-tokyo.ac.jp/people/knishida/eng/seismology.html

This reflected wave can be interpreted as a "mirror image" of the incident wave to satisfy the boundary condition. When we consider an incident wave $Ae^{-i\omega(t-p_x x-p_z z)}$, superposition between a mirror described by $Ae^{-i\omega(t-p_x x+p_z z)}$ and the incident wave satisfy the boundary condition.

The governing equation for an SH wave is the same as the acoustic wave equation. However, their boundary conditions are different. For the SH wave, stress components T_{zx} and T_{zy} act as vector components, whereas the pressure for an acoustic wave is a scalar. To meet the free surface condition of an acoustic wave at $z = 0$, a mirror of $-Ae^{-i\omega(t-p_x x+p_z z)}$ is needed. The sign is different from the SH wave.

Figure 5.8 shows an example of reverberations of SH waves between the surface and the core-mantle boundary (CMB). Because the outer core is liquid, the CMB acts as a free surface for S waves. The figure shows many wave packets with fast apparent velocities, which correspond to multiple reflections of vertically propagating SH waves between the surface and the CMB[note 11)]. The figure also shows that the phase of ScS (reflected once at the CMB) is the same as that of ScS2 (reflected twice).

[note 11)] The amplitudes attenuate with distance due to intrinsic attenuation of the material.

§5.5 Reflection and conversion of P-SV wave at a free surface

For a given angular frequency ω, let us consider an incident P wave ($\boldsymbol{p}_\alpha^{in}$), and an incident SV wave ($\boldsymbol{p}_\beta^{in}$). The reflected P wave ($\boldsymbol{p}_\alpha^{refl}$), and the reflected SV wave ($\boldsymbol{p}_\beta^{refl}$) can be related by,

$$\boldsymbol{s} = \boldsymbol{A}_\alpha^{in} e^{i\omega(\boldsymbol{p}_\alpha^{in}\cdot\boldsymbol{x}-t)} + \boldsymbol{A}_\alpha^{refl} e^{i\omega(\boldsymbol{p}_\alpha^{refl}\cdot\boldsymbol{x}-t)} + \boldsymbol{A}_\beta^{in} e^{i\omega(\boldsymbol{p}_\beta^{in}\cdot\boldsymbol{x}-t)} + \boldsymbol{A}_\beta^{refl} e^{i\omega(\boldsymbol{p}_\beta^{refl}\cdot\boldsymbol{x}-t)}, \quad (5.46)$$

where $\boldsymbol{s}$ is displacement, and $\boldsymbol{A}$ represents polarization vector with the amplitudes. For simplicity, we solve a problem in the xz plane for propagating wave into y direction. The slowness vectors and the polarization vectors are given by,

$$\boldsymbol{p}_\alpha^{in} = \begin{pmatrix} p \\ \xi \end{pmatrix}, \quad \boldsymbol{p}_\alpha^{refl} = \begin{pmatrix} p \\ -\xi \end{pmatrix}, \quad \boldsymbol{p}_\beta^{in} = \begin{pmatrix} p \\ \eta \end{pmatrix}, \quad \boldsymbol{p}_\beta^{refl} = \begin{pmatrix} p \\ -\eta \end{pmatrix}, \quad (5.47)$$

$$\boldsymbol{A}_\alpha^{in} = A\begin{pmatrix} p \\ \xi \end{pmatrix}, \quad \boldsymbol{A}_\alpha^{refl} = B\begin{pmatrix} p \\ -\xi \end{pmatrix}, \quad \boldsymbol{A}_\beta^{in} = C\begin{pmatrix} \eta \\ -p \end{pmatrix}, \quad \boldsymbol{A}_\beta^{refl} = D\begin{pmatrix} \eta \\ p \end{pmatrix}, \quad (5.48)$$

Then we can simplify the equations as,

$$s_x(x,z)e^{i\omega(t-px)} = p(Ae^{i\omega\xi z} + Be^{-i\omega\xi z}) + \eta(Ce^{i\omega\eta z} + De^{-i\omega\eta z}) \quad (5.49)$$

$$s_z(x.z)e^{i\omega(t-px)} = \xi(Ae^{i\omega\xi z} - Be^{-i\omega\xi z}) + p(-Ce^{i\omega\eta z} + De^{-i\omega\eta z}). \quad (5.50)$$

Later in this chapter, we will explain the reflection and conversion coefficients of two cases: (1) incident SV wave ($A = 0$), and (2) incident P wave ($C = 0$) with boundary conditions of $T_{zx}(0) = 0$, and $T_{zz}(0) = 0$ as

$$2p\xi(A - B) + (\eta^2 + p^2)(C + D) = 0, \quad (5.51)$$

$$(\eta^2 - p^2)(A + B) - 2p\eta(C + D) = 0. \quad (5.52)$$

Here we define polarization vectors as

$$\hat{\boldsymbol{n}}_\alpha^{in} = \begin{pmatrix} p \\ \xi \end{pmatrix}\alpha, \quad \hat{\boldsymbol{n}}_\alpha^{refl} = \begin{pmatrix} p \\ -\xi \end{pmatrix}\alpha, \quad (5.53)$$

$$\hat{\boldsymbol{n}}_\beta^{in} = \begin{pmatrix} \eta \\ -p \end{pmatrix}\beta, \quad \hat{\boldsymbol{n}}_\beta^{refl} = \begin{pmatrix} \eta \\ p \end{pmatrix}\beta \quad (5.54)$$

In order to estimate the coefficients, we calculate the inner product between the polarization vectors and displacement $\boldsymbol{s}$.

5.5.1 P-wave incidence

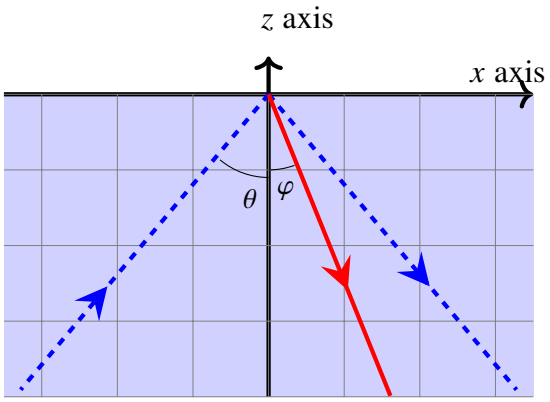

Figure 5.9: P-wave incidence

The reflection coefficient from P wave to P wave $R_{PP} = (B/\alpha)/(A/\alpha)$ is given by,

$$R_{PP} = -\frac{(\eta^2 - p^2)^2 - 4p^2\xi\eta}{(\eta^2 - p^2)^2 + 4p^2\xi\eta}. \tag{5.55}$$

The reflection coefficient from P wave to S wave $R_{PS} = (D/\beta)/(A/\alpha)$ is given by

$$R_{PS} = \frac{4p\xi(\eta^2 - p^2)}{(\eta^2 - p^2)^2 + 4p^2\xi\eta}\frac{\alpha}{\beta}. \tag{5.56}$$

Snell's Law

As already explained, both incident and reflected waves must have a dependence of $e^{-i\omega px}$ to satisfy the boundary condition. [note 12)]. In order for p to be a conserved quantity, the incident and reflected angles must satisfy the following relation: i.e., Snell's law,

$$\frac{\sin\varphi}{\beta} = \frac{\sin\theta}{\alpha}. \tag{5.57}$$

Conservation of energy

Consider the energy balance in a region on a thin region that includes the ground surface. The vertical energy flux must be balanced between the incident and reflected waves. The energy conservation law is given by

$$\alpha\cos\theta = \beta\cos\varphi|R_{PS}|^2 + \alpha\cos\theta|R_{PP}|^2. \tag{5.58}$$

note 12) As explained in the ray theory chapter (**??**), p is a conserved quantity related to momentum.

Problem 5.2

1. Derive equation 5.55.
2. Derive equation 5.56.

5.5.2 SV-wave incidence

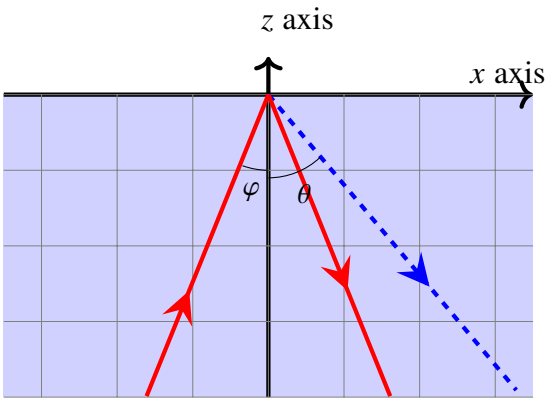

Figure 5.10: SV-wave incidence

Consider the case of an SV wave with unit amplitude ($C = 1$) incident at an angle of 25° (φ in Figure 5.10). For this, both the reflected SV wave and the reflected P wave take non-zero values. To satisfy the boundary condition, the total stress must be zero after superposition. In fact, the resultant wavefield in the figure shows that the stress T_{zz} is zero at the surface. We search the values of B and D to meet the boundary condition: $T_{zz} = T_{xz} = 0$. Since the sum of the unknowns and the number of boundary conditions are equal, we can find B and D.

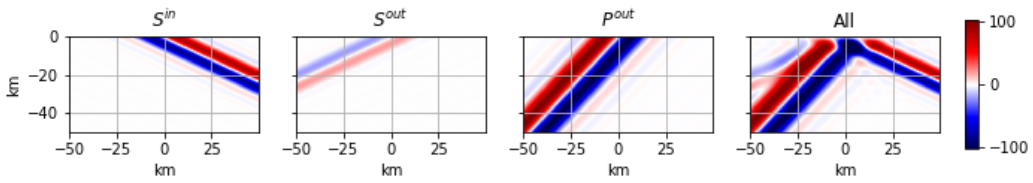

Figure 5.11: The stresses T_{zz} for reflected SV and reflected P waves when the SV wave is incident at an angle of incidence (φ) of 25°. This figure shows that the stress for the superposed wave field is zero at the ground surface.

https://www.eri.u-tokyo.ac.jp/people/knishida/eng/seismology.html

Reflection coefficient from S wave to S wave $R_{SS} = (D/\beta)/(C/\beta)$ is written by

$$R_{SS} = \frac{(\eta^2 - p^2)^2 - 4p^2\xi\eta}{(\eta^2 - p^2)^2 + 4p^2\xi\eta}. \tag{5.59}$$

Here slowness and the incidental angles are related as, $p = \frac{\sin\theta}{\alpha} = \frac{\sin\varphi}{\beta}$, $\xi = \frac{\cos\theta}{\alpha}$, $\eta = \frac{\cos\varphi}{\beta}$.

Reflection coefficient from S wave to P wave $R_{SP} = (B/\alpha)/(C/\beta)$ is given by,

$$R_{SP} = \frac{4p\eta(\eta^2 - p^2)}{(\eta^2 - p^2)^2 + 4p^2\xi\eta}\frac{\beta}{\alpha}. \tag{5.60}$$

Corresponding conservation of energy is represented by

$$\beta\cos\varphi = \beta\cos\varphi|R_{SS}|^2 + \alpha\cos\theta|R_{sp}|^2. \tag{5.61}$$

Figure 5.12 shows the reflection coefficients.

Snell's law

Similarly, the continuity of displacement and stress at the boundary leads to Snell's law. The conservation of p and Snell's law hold as well as P-wave:

$$\frac{\sin\varphi}{\beta} = \frac{\sin\theta}{\alpha}. \tag{5.62}$$

Critical angle

After the critical angle φ_c

$$\varphi_c = \sin^{-1}\frac{\beta}{\alpha}, \tag{5.63}$$

total reflection occurs. In this case, the z component of the slowness of the converted P wave becomes imaginary and cannot carry net energy in the vertical direction (known as an inhomogeneous wave). The S-wave will be out of phase due to the inhomogeneous P-wave sticking near the ground surface. [note 13)].

Inhomogeneous P wave

Let us consider the stress T_{zz} for the case where the SV wave is incident at an angle of 75° (φ) beyond the critical angle. Figure 5.13 shows the incident SV wave and the reflected SV wave. The figure also shows that the phase of the reflected SV wave is out of phase by about 90 degrees (the incident SV wave is shaped like a half period of the sin function, while the reflected SV wave is

[note 13)] As calculated in Problem 5.1, the inhomogeneous waves carry energy up and down at a local scale but zero on a larger scale. When the wave incidents after the critical angle, the inhomogeneous P-wave accompanies the S-wave at the surface. The inhomogeneous P wave receives energy vertically from the S-wave and returns the energy with a slight time delay. The S wave is out of phase because of the temporary energy transfer by the inhomogeneous P wave

shaped like one period of the cos function). The figure also shows that there are inhomogeneous P waves to meet the boundary conditions because of the phase shift of the reflected SV. The inhomogeneous P-wave is localized at the reflection point, and we can see that it is consistent with $Tzz = 0$.

Conservation of energy

Let us consider the energy balance in a thin region along the Earth's surface. The vertical energy flux must be balanced between the incident and reflected energy flux. Before the critical angle, the energy conservation law is given by

$$\beta \cos\varphi = \beta \cos\varphi |R_{SS}|^2 + \alpha \cos\theta |R_{SP}|^2. \tag{5.64}$$

Since the reflected wave becomes evanescent after the critical angle, the net energy flux becomes 0, which leads to the following relation,

$$1 = |R_{SS}|^2. \tag{5.65}$$

Problem 5.3

1. Derive equation 5.59.
2. Derive equation 5.60.

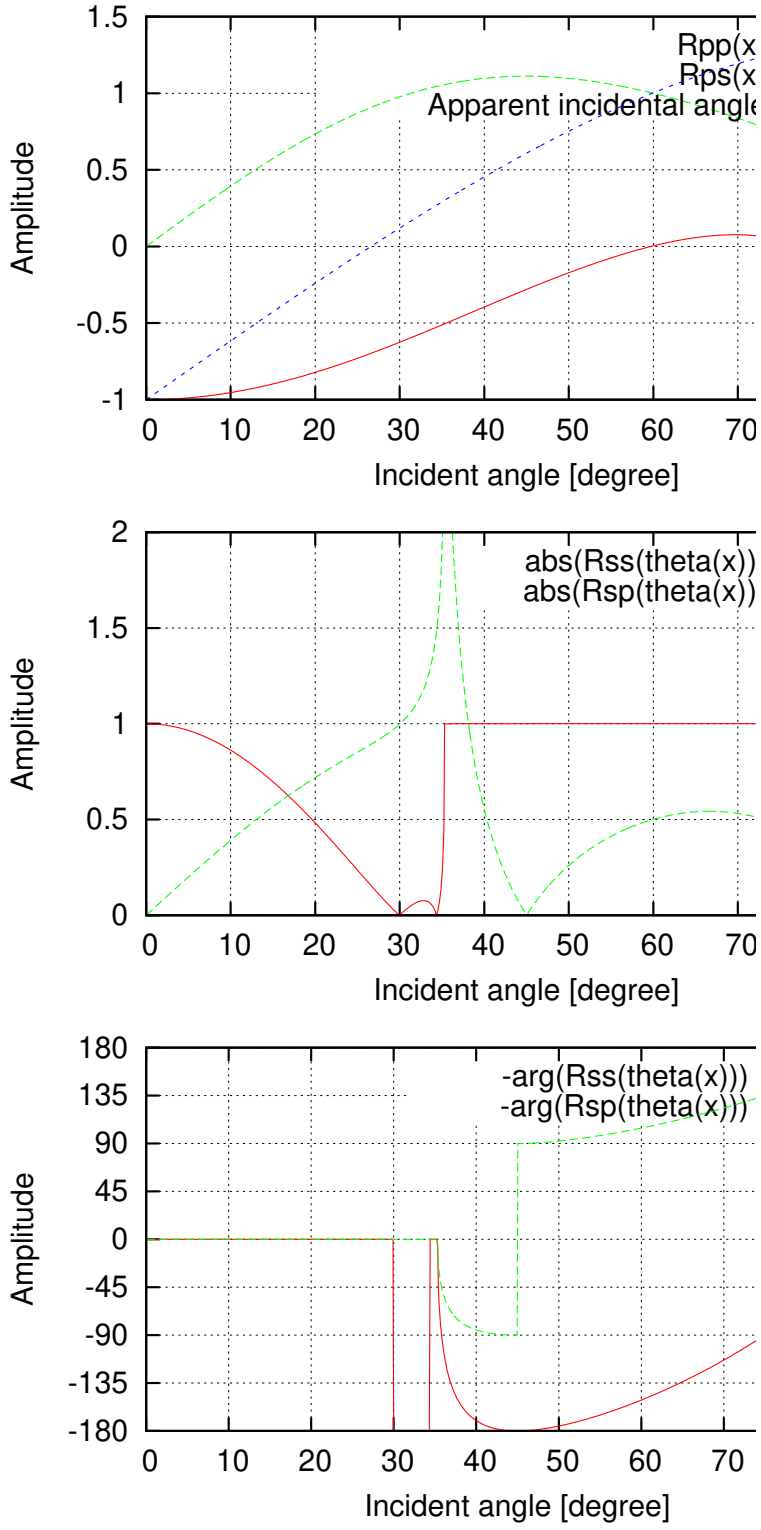

Figure 5.12: R_{sp} has the finite value at its critical angle.

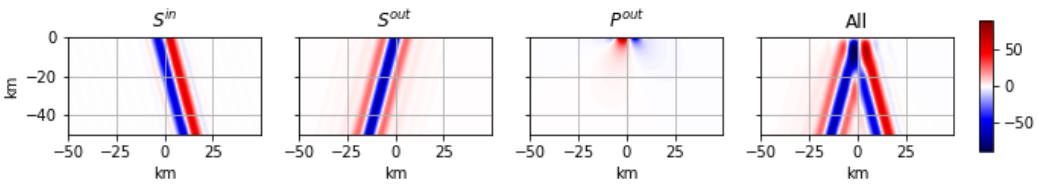

Figure 5.13: Stress T_{zz} for SV wave incident with angle φ of 75°, the reflected SV wave and the reflected P wave. wave. The superimposed stress field satisfies the boundary condition of the free surface.

Similarities and differences between SH and P waves

Both SH and P waves can be described by a single variable and behave very similarly because they satisfy the scalar wave equation. However, the reflection coefficient changes because the boundary conditions appear differently. Let us focus on this point here.

Here we consider an acoustic and an SH wave propagated in a xz plane. The governing equations are given by

$$\rho \frac{\partial^2 p}{\partial t^2} = \kappa \left(\frac{\partial^2 p}{\partial x^2} + \frac{\partial^2 p}{\partial y^2} \right) \tag{5.66}$$

$$\rho \frac{\partial^2 s_y}{\partial t^2} = \mu \left(\frac{\partial^2 s_y}{\partial x^2} + \frac{\partial^2 s_y}{\partial y^2} \right). \tag{5.67}$$

The equations show that both can be described by a two-dimensional scalar wave equation. For example, if the speed of sound and SH wave velocity is the same, p and s_y have the same solution.

One point should be noted, however. The acoustic wave takes pressure as a variable, while the SH wave takes displacement as a variable. There is a big difference when considering free surface. When considering acoustic waves, $p = 0$ is the boundary condition at the free surface. On the other hand, when we consider a free surface at $z = 0$, the boundary condition at the free surface for SH waves is given by

$$-\rho \frac{\partial s_y}{\partial z} = 0. \tag{5.68}$$

This corresponds to the boundary condition of a rigid wall for acoustic waves. The reflection coefficient at the surface with respect to pressure for acoustic waves is -1, while for SH waves (with respect to displacement), the reflection coefficient at the surface is 1. The difference is whether stress or displacement is taken as the variable; in both cases, the stress at the surface is zero. The analogy with acoustic waves is valid, but be careful how you choose the variables.

Problem 5.4

Let us consider P wave propagation in a 3-D half space of fluid.

1. As in the case of SH wave, estimate reflection coefficients for an incident plane wave (P-wave) as a function of incident angle.
2. Compare the above result with P-wave reflection coefficients for the P-SV problem. In particular, discuss it for the incidental angles of about 0° and 90°.
3. As in the case of full space (see subsection 3.4.2), estimate the Green's function for an explosion source in a half-space of fluid. Discuss the behavior as the source depth approach the free surface.

5.5.3 Apparent incident angle of a P-SV wave

When analyzing seismic waveforms, particle motion is informative. For example, Figure 5.5.3 shows the particle motion of P wave against radial and vertical components when the deep earthquake at Ogasawara was recorded by the F-net station at Fukue. The figure shows an inclined linear polarization. The inclination shows the approximate incident angle. This subsection describes this relation.

First, let us consider that the P wave enters the free surface. The ratio between the vertical displacement s_x and the horizontal one s_y is given by

$$\frac{s_x}{s_z} = \frac{p(A+B)+\eta D}{\xi(A-B)+pD} = \frac{2p\eta}{\eta^2-p^2} = \tan 2\varphi. \quad (5.69)$$

The inclination of P wave polarization (or apparent incident angle) θ' is twice as large as the S-wave reflected angle as (Figure 5.12),

$$\theta' = 2\varphi. \quad (5.70)$$

When the incident angle is sufficiently small for a Poisson medium ($\alpha = \sqrt{3}\beta$), the relation between the apparent incident angle and the P-wave incident angle can be simplified as

$$\theta' = 2\varphi \sim \frac{2\beta}{\alpha}\theta \sim 1.15\theta. \quad (5.71)$$

This result shows that the P-wave incident angle can be approximated by the apparent incident angle.

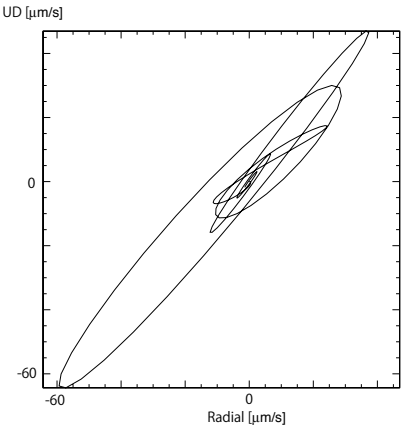

Figure 5.14: An example of particle motion of P-wave against radial and vertical components of F-net station at Fukue.

In the same manner, the incident angle of the S wave can be related to the apparent incident angle as:

$$\frac{s_x}{s_z} = \frac{pB+\eta(C+D)}{-\xi B+p(-C+D)} = -\frac{\eta^2-p^2}{2p\xi} \quad (5.72)$$

When the incident angle is small (this assumption is valid for teleseismic events), the apparent incident angle can be related to the incident angle by

$$\varphi' = 2\frac{\beta^2}{\alpha^2}\varphi = 2\frac{\beta}{\alpha}\varphi. \quad (5.73)$$

Here we assumed that the incident angle is smaller than the critical angle.

It may seem somewhat intuitive that the direction of oscillation of the P wave coincides with the direction of incidence, but it is by no means obvious. For example, consider the limit $\beta \to 0$, assuming a medium similar to a fluid. In this case, the direction of oscillation is 0 degrees. Let us consider the case of a fluid. In Fig 5.15, we consider a pressure source in the ground. To satisfy the boundary conditions at the water surface, we consider a pressure source with the

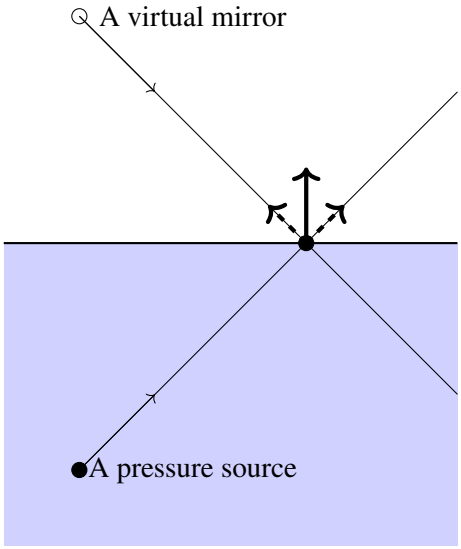

Figure 5.15: Particle motion near the surface in fluid.

opposite sign at the mirror-symmetric location. In this case, considering the particle trajectory at the ground surface, it will move up and down. Since this relationship holds at any time, the particle trajectory at the water surface is always vertical, regardless of the angle of incidence.

Problem 5.5

1. Derive equation 5.69.
2. Derive equation 5.72.

§5.6 Rayleigh wave

In the previous sections, this chapter explained body waves that can propagate freely in the vertical direction. Inhomogeneous waves accompany incoming SV waves beyond the critical angle. Can inhomogeneous waves exist on their own without body waves? Rayleigh waves have energy concentrated near the surface and are known to propagate horizontally. Figure 5.16 shows the observation record during the 2014 Chilean earthquake. The waves labeled R1 and R2 are Rayleigh waves, which propagate at an approximately constant speed. The Chilean earthquake excited Rayleigh waves efficiently because the depth of the epicenter is 35 km, which is much shorter than the wavelength of the waves. First, let us consider qualitatively the nature of Rayleigh waves.

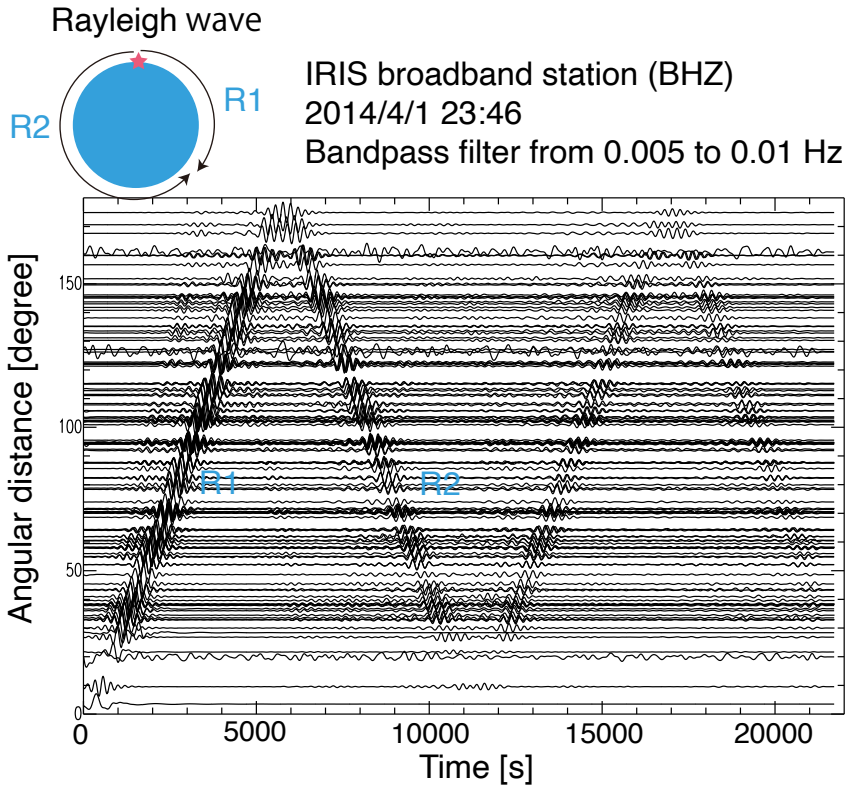

Figure 5.16: Waveforms in vertical components recorded by broadband seismometers when the 2014 Chilean earthquake.

When considering acoustic or SH wave propagation in a half-space, inhomogeneous waves cannot exist alone because they cannot satisfy the boundary conditions at the free surface. On the other hand, they can exist for P-SV propagations: these are known as Rayleigh waves.(6) Rayleigh waves satisfy the free surface condition because P-wave-like and S-wave-like deformations can exist simultaneously, balancing each other at the surface. Rayleigh waves have energy concentrated near the surface so that we can observe global propagation (Fig. 5.17). We will first consider its properties qualitatively. First, let us consider the Rayleigh wave note 14).

Let us consider a situation where an S-wave propagates to the right while oscillating vertically through an infinite medium. We then cut out an infinite medium in the middle. Then, to satisfy the boundary condition of zero stress at the free surface, the regions with large stress will bulge out (the parts with large volumetric strain). The free surface causes a large deformation, and the effective elastic constant decreases. As a result, the Rayleigh wave propagates slower than the S-wave (about 90% of the S-wave velocity). The particle motion becomes elliptical because the phase of the volume deformation is shifted by 90 degrees compared to that of the S-wave. Because the horizontal propagation velocity is slower than the S-wave and P-wave velocities, they can only exist as inhomogeneous waves. The amplitude decreases exponentially in the depth direction. At the surface, the particle motion is in the opposite direction of the rotation of a bicycle wheel (retrograde). On the other hand, in deeper regions (blue in the figure), the direction is the same as the rotation of a bicycle wheel (prograde).

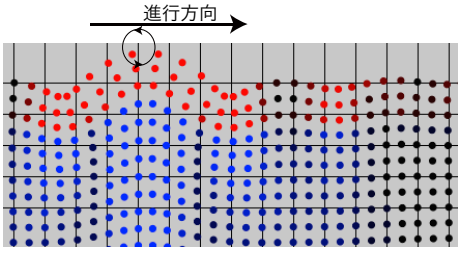

Figure 5.17: Schematic figure of Rayleigh wave propagation. Red circles show retrograde particle motions, whereas blue ones show prograde motions.

5.6.1 Can elastic waves along a free surface exist?

To consider this a little more quantitatively, let us now clarify the problem. Let us consider the propagation in the xz plane and assume that it does not change in the y direction, just as we would consider the reflection and conversion of a P-SV wave at the free surface. The boundary condition is given by $T_{zz} = T_{zx} = 0$ at the surface. To begin with, let us simply consider if acoustic waves and SH waves can propagate horizontally in half space.

As you may recall from Figure 5.15, the reflection coefficient of an acoustic wave at a free surface is -1. Because the incident and reflected waves cancel each other out, the acoustic wave is not excited when an excitation source is near the free surface. Since the sign of the mirror image is reversed in Figure 5.15, it can be interpreted that in the case of a very shallow pressure source, the waves are not excited because the source pressure cancels out with the mirror image pressure, which has the opposite sign. The fact that acoustic waves cannot be excited by an explosive source near the water surface may, at first glance, seem inconsistent with physical intuition. However, it makes physical sense when one considers that the elastic energy is zero due to the free boundary surface (see also the section 4.6).

note 14) see demo http://www.eri.u-tokyo.ac.jp/knishida/Seismology/Rayleigh_wave.html

On the other hand, in the case of SH waves, the amplitude doubles at the surface and is amplified since the reflection coefficient is 1 in the case of SH waves. In other words, horizontally propagating waves do exist in the case of SH waves. This difference is due to the difference in boundary conditions. As mentioned before, the difference between displacement and stress comes into play because the pressure satisfies the scalar wave equation for acoustic waves, while s_y satisfies it in the SH case. If so, is this possible for SV waves? It is impossible because SV waves do not satisfy the boundary conditions when horizontally propagating.

5.6.2 A case of the reflection coefficient of zero

Let us now reconsider the number of boundary conditions. For the $P-SV$ problem, we need two boundary conditions, $T_{zz}=0, T_{zx}=0$. If we now consider arbitrary incident waves, we will need to add together two independent solutions to eliminate these two. This situation corresponds exactly to the reflection/transformation wave for the incident wave at the free surface in the previous section. The similarity means that a combination of the three waves is required. So let us look at the SV incidence in Figure 5.12. R_{SS} in the figure shows two points where the amplitude of the S reflection is zero. R_{SP} in the figure shows one point where the P reflection is zero. The zeros show the possibility of combining the two waves to satisfy the boundary condition if one looks for the appropriate frequency. Let us consider the possibility of this kind of solution.

In the following, let us consider T^p_{zx}, T^p_{zz} caused by an inhomogeneous P wave and T^S_{zx}, T^S_{zz} caused by an inhomogeneous SV wave. If we can find a phase velocity or slowness p that gives the same stress ratio T_{zx}/T_{zz} for both waves, the difference between the two normalized solutions will satisfy the boundary conditions. Now, let us look at the stress ratio for each wave.

Inhomogeneous P wave

Here, the scalar potential for an inhomogeneous P wave is defined by

$$\phi = e^{i\omega p x} e^{-\omega \xi z} e^{-i\omega t}. \tag{5.74}$$

P-wave velocity α satisfies the relation $\alpha^{-2} = p^2 - \xi^2$. The result in section **??** leads to the ratio between T_{zz} and T_{zx}:

$$\frac{T_{zx}}{T_{zz}} = -i\frac{(1-2\nu)\xi p}{(1-\nu)\xi^2 - \nu p^2}. \tag{5.75}$$

For a Poisson solid ($\nu = 1/4$), we can simplify the relations by eliminating ξ:

$$\frac{T_{zx}}{T_{zz}} = -i\frac{2\sqrt{p^2-\alpha^{-2}}\,p}{2p^2 - 3\alpha^{-2}}. \tag{5.76}$$

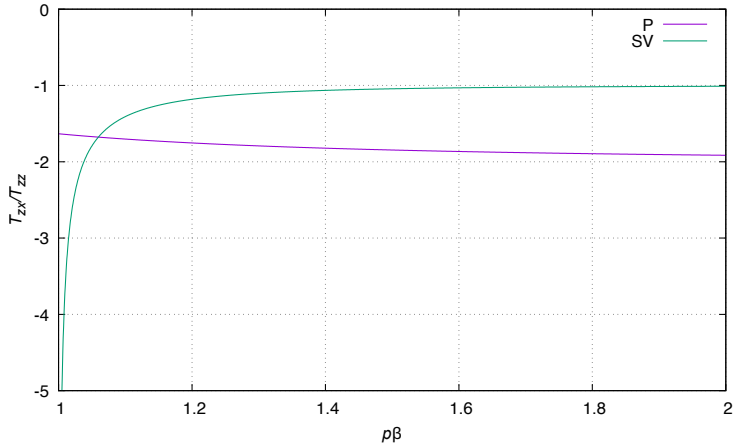

Figure 5.18: Stress ratio T_{zx}/T_{zz} at the surface for slowness p. Here we consider a Poisson material, and the slowness is normalized by the S-wave velocity. We plot them for $p\beta > 1$ because the vertical wavenumber becomes pure imaginary (which can propagate in the vertical direction as body waves) for $p\beta < 1$.

Inhomogeneous SV wave

Here, the component of vector potential for an inhomogeneous SV wave is defined by

$$\frac{\partial \psi}{\partial x} = e^{i\omega p x} e^{-\omega \eta z} e^{-i\omega t}. \tag{5.77}$$

The S-wave velocity β satisfies the relation $\beta^{-2} = p^2 - \eta^2$. The result in section **??** leads to the stress ratio between T_{zz} and T_{zx} as:

$$\frac{T_{zx}}{T_{zz}} = -i\frac{(\eta^2 - p^2)}{2p\eta}, \tag{5.78}$$

For a Poisson solid ($\alpha = \sqrt{3}\beta$), elimination of η leads to

$$\frac{T_{zx}}{T_{zz}} = -i\frac{2p^2 - \beta^{-2}}{2p\sqrt{p^2 - \beta^{-2}}}. \tag{5.79}$$

Let us compare the two stress ratios. Figure 5.18 shows that the two curves intersect when p is slightly greater than β^{-1}, which would represent the condition under which inhomogeneous waves can exist alone. This corresponds to Rayleigh waves. Let us consider in more detail the conditions under which the stress ratio at the surface is constant. The condition of equal stress ratio leads to the following relation;

$$(\eta^2 - p^2)^2 + 4p^2\xi\eta = 0. \tag{5.80}$$

For the better understandings of the equation, we define $X \equiv p^2\beta^2$ and $\gamma^2 \equiv \alpha^{-2}/\beta^{-2}$. With the squared stress ratios of the inhomogeneous P wave and the inhomogeneous SV wave, we can

rearrange the equation is as follows:

$$16(1-\gamma^2)X^3 - (24-16\gamma^2)X^2 + 8X - 1 = 0. \tag{5.81}$$

In the case of Poisson material, the equation can be simplified as,

$$32X^3 - 56X^2 - 24X - 3 = 0, \tag{5.82}$$

and the analytic solutions are given by

$$X = \frac{1}{4}, \frac{3}{4} \pm \frac{\sqrt{3}}{4}. \tag{5.83}$$

Only the last one satisfies the condition $p > \beta^{-1}$, and the solution corresponds to the solution shown by Figure 5.18. What are the physical meanings of the other two solutions? The incident angles estimated from p are 30° and 34.3° for Poisson material. These two angles correspond exactly to the zero crossing of the R_{SS} in Figure 5.12: i.e., the case where all incident S waves are converted to reflected P waves. Thus, the three solutions make physical sense. In other words, the problem of finding a condition where the incident S-wave reflected at the free surface is extended to the problem of finding a condition where the inhomogeneous P-wave converted only the inhomogeneous SV-wave wave. We summarize the displacement of the Rayleigh wave:

$$s_x(x,z,t) = ipB\left[e^{\omega\xi z} + \frac{1-2p\beta}{2p\beta}e^{\omega\eta z}\right]e^{i\omega(t-px)} \tag{5.84}$$

$$s_z(x,z,t) = \xi B\left[e^{\omega\xi z} + \frac{2p\beta}{1-2p\beta}e^{\omega\eta z}\right]e^{i\omega(t-px)}, \tag{5.85}$$

where $\xi = \sqrt{p^2-\alpha^{-2}}$, $\eta = \sqrt{p^2-\beta^{-2}}$, and B is an integral constant. Also, in order to choose a physically meaningful solution (no divergence at $z = -\infty$), the signs are chosen so that $\mathrm{Im}\,\eta < 0$ and $\mathrm{Im}\,\xi < 0$.

Figure 5.19(a) shows the depth profile of Rayleigh wave amplitudes (s_x and s_z). It can be seen that the amplitude decreases exponentially with depth. The major difference from a body wave is the phase shift between horizontal and vertical motion. The motion of particles at the surface is plotted in Fig 5.19(b). Taking the real parts of s_x and s_z, we see that they rotate in the direction of the arrows in the figure since $s_x \propto -\sin\omega t$, $s_z \propto \cos\omega t$. Since the Rayleigh wave is now traveling from left to right in the figure, we call it retrograde. [note 15)] Also, the sign of s_x reverses around $z = -0.25$ (normalized depth), so the direction of rotation is reversed at deeper points. This direction is called the forward direction (prograde).

To better visualize this, a demo page for Rayleigh waves is available on the web.[note 16)]. Please refer to it as needed.

Rayleigh waves are two-dimensional because they have energy only near the surface. The behavior is, therefore, similar to that of a two-dimensional Green's function. Specifically, the

note 15) It is easy to understand if you think of the direction of rotation of a bicycle wheel.

note 16) https://www.eri.u-tokyo.ac.jp/people/knishida/Seismology/Rayleigh_wave.html

https://www.eri.u-tokyo.ac.jp/people/knishida/eng/seismology.html

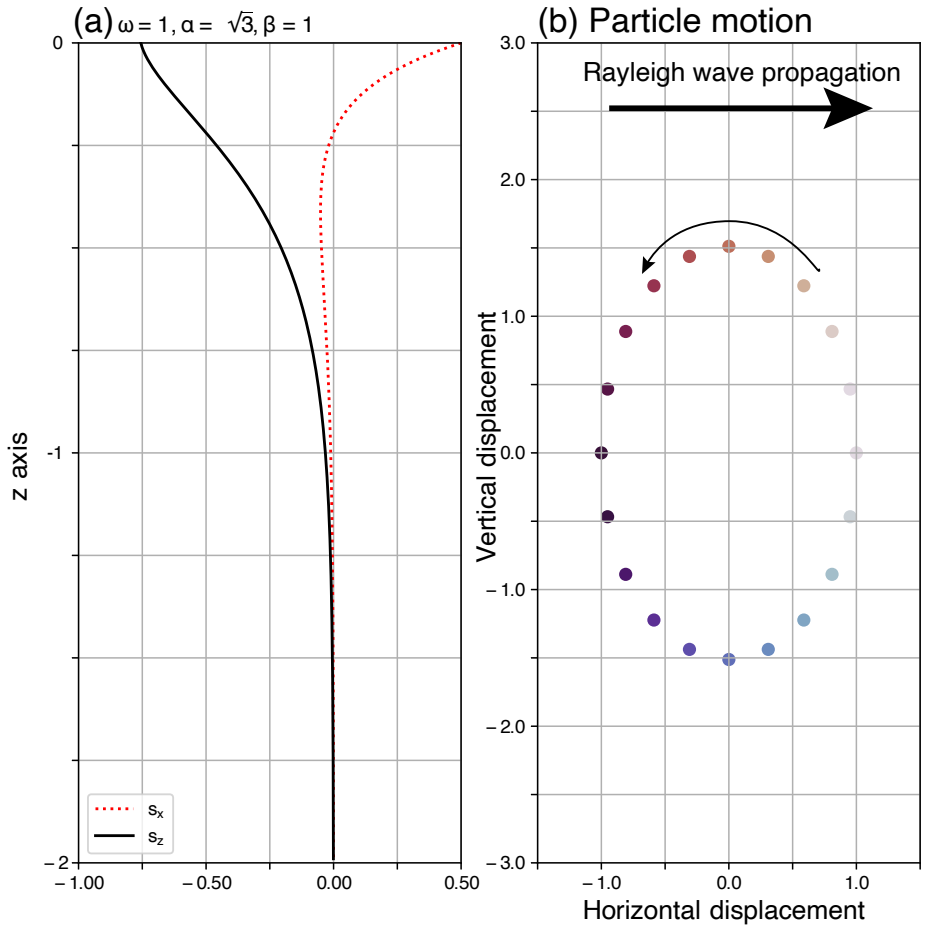

Figure 5.19: (a) Depth profile of Rayleigh wave amplitudes. (b) Particle motion at the surface.

amplitude is proportional to $r^{-1/2}$. [note 17)] When the epicentral distance is far, the surface waves are larger than the body waves. [note 18)] Also, surface waves are not efficiently excited when the hypocenter is deeper than the wavelength (because they decay exponentially in the depth direction).

§5.7 Excitation of Rayleigh waves

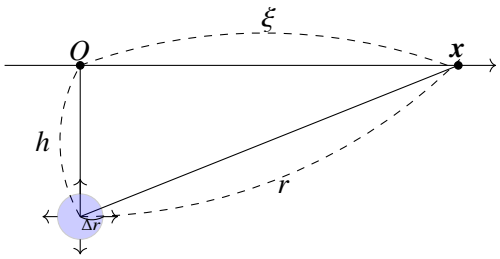

Figure 5.20: Configuration and coordinate system of an explosive source (pressure source) in a semi-infinite medium.

When considering the excitation of Rayleigh waves, it is difficult to intuitively understand how they are excited. As long as we think in terms of the superposition of plane waves, considering reflected and converted waves does not seem to lead to the generation of Rayleigh waves just to satisfy boundary conditions. What becomes important here is the near-field term introduced in the section on Green's function for elastic bodies. We can physically explain this by considering that the near-field term creates a secondary excitation source to satisfy the boundary conditions, and this secondary excitation source excites the Rayleigh wave. Here, let us consider an explosive source as an example. In the following, we first separate the stress field generated by the explosive source into the near-field and far-field terms. Next, we reduce it to a problem of inhomogeneous wave incidence using Weyl's integral representation, and consider the Rayleigh wave as a problem of incidence and reflection of inhomogeneous waves.

[note 17)] Roughly speaking, for epicentral distance r, amplitude A, and propagation velocity c_R, the energy flux can be written as $c_R \rho \omega A^2$, and energy conservation yields

$$\nabla \cdot \boldsymbol{K} = \frac{1}{r} \frac{\partial}{\partial r}(Kr) = 0, \tag{5.86}$$

which leads to $A \sim r^{-1/2}$.

[note 18)] Recalling the far-field term of Green's function, we can see that the body waves are proportional to r^{-1}. This can be derived from considering the conservation of energy as well as surface waves.

5.7.1 Wavefield and stress field produced by an explosive source

The frequency component of displacement $S(\omega)$ can be written as

$$S_r(\omega) = \frac{\Delta p \Delta r^3}{3(\lambda+2\mu)} \frac{\omega}{\alpha^2} e^{i\omega\frac{r}{\alpha}} \underbrace{\left(-\frac{i}{(kr)^2}\right)}_{\text{Near-field}} + \underbrace{\left(\frac{1}{kr}\right)}_{\text{Far-field}}, \tag{5.87}$$

The stresses T_{zz} and T_{zx} at the surface are respectively given by

$$T_{zz} = \frac{\Delta p \Delta r^3}{3(\lambda+2\mu)} e^{i\omega\frac{r}{\alpha}} \left(\frac{2\mu(\xi^2-2h^2)}{r^5}\frac{1}{i\omega} - \frac{\lambda r^2 + 2\mu h^2}{\alpha r^4}\right) \tag{5.88}$$

and

$$T_{zx} = -\frac{\Delta p \Delta r^3}{3(\lambda+2\mu)} e^{i\omega\frac{r}{\alpha}} \left(\frac{6\mu\xi h}{r^5 i\omega} - \frac{2\mu\xi h}{r^4}\right). \tag{5.89}$$

5.7.2 Contribution of the near-field term

For the far-field term, we have seen that reflected and converted waves are generated to satisfy boundary conditions. How does the near-field term behave? Here, let us look at the behavior of the near-field term of T_{zz}.

$$T_{zz} \propto \frac{e^{i\omega\frac{r}{\alpha}}}{i\omega}\left(\frac{\xi^2-2h^2}{r^5}\right) \tag{5.90}$$

In this case, the near-field term has sufficient amplitude. From the ξ dependence of T_{zz}, we can see that the secondary source is localized near the origin and has a short-wavelength spatial structure compared to the wavelength of interest. For such a short-wavelength structure to propagate horizontally, it must be an inhomogeneous wave that decays exponentially in the depth direction. This can be viewed as a problem where an inhomogeneous P-wave (or S-wave) is emitted horizontally from directly above the source and converted into an inhomogeneous S-wave (or P-wave) to satisfy the boundary conditions. Since $T_{zz} = 0$ must hold at the free boundary surface, we consider $-T_{zz}$, which cancels this out, as a secondary excitation source. Regarding this term, let us consider its contribution by comparing h with the wavelength.

$h > \lambda$

When h is sufficiently longer than the wavelength, this term can be ignored compared to the far-field term. In the first place, the near-field term plays a minor role in the wavefield.

$h < \lambda$

Let us consider the case where the depth of the explosive source is shallower than the wavelength. In this case, the near-field term has sufficient amplitude. From the ξ dependence of T_{zz}, we can

see that it is localized near the origin. Therefore, when considering a certain frequency ω, the secondary source has a shorter wavelength spatial structure compared to the corresponding wavelength. To propagate horizontally, it must be an inhomogeneous wave that decays exponentially in the depth direction. Moreover, it can be viewed as a problem where an inhomogeneous P-wave (or S-wave) is excited horizontally from directly above the source and converted into an inhomogeneous S-wave (or P-wave) to satisfy the boundary conditions. When the source is shallow compared to the wavelength, both the near-field and far-field terms become important, and it becomes difficult to distinguish their contributions. Qualitatively, the contribution of the inhomogeneous wave becomes larger in the near-field term and plays an important role[note 19)]. As can be seen from the fact that an inhomogeneous wave cannot propagate in the vertical direction, it is generally understood as a deformation in response to a forced variation. You can probably imagine that when it exceeds the critical angle, it cannot propagate vertically and is forced to vibrate to satisfy the boundary conditions. Rayleigh waves can also be interpreted as a pair of inhomogeneous waves that can exceptionally become **self-sustaining** without being forced. Therefore, let us consider it as an incidence problem of an inhomogeneous P-wave.

5.7.3 As a problem of inhomogeneous P-wave incidence

Here, let us interpret the Rayleigh wave as a problem of reflection and transmission of P-SV inhomogeneous waves. To consider the explosive source, let us consider the 3-D Green's function in a homogeneous infinite medium corresponding to the P-wave potential. The Green's function G^{3D} in the frequency domain satisfies

$$\frac{\omega^2}{\kappa}G^{3D} + \frac{1}{\rho_0}\nabla^2 G^{3D} = \delta(\boldsymbol{x}). \tag{5.91}$$

By performing a spatial Fourier transform and then an inverse Fourier transform again, we can see that it can be written as

$$G^{3D} = -\frac{1}{\kappa}\iiint \frac{\kappa e^{i(k_x x + k_y y + k_z z)}}{\alpha^2(k_x^2 + k_y^2 + k_z^2) - \omega^2} dk_x dk_y dk_z. \tag{5.92}$$

Here, we used the relation $\kappa = \rho_0\alpha^2$. This equation indicates that the Green's function can be expressed by the superposition of plane waves.

If we assume that the z-component of the wavenumber is real, we cannot account for inhomogeneous waves. Therefore, let us consider an equation that does not Fourier-transform only in z:

$$\left(-\frac{1}{\rho_0}(k_x^2 + k_y^2) + \frac{\omega^2}{\kappa}\right)G^{3D} + \frac{1}{\rho_0}\frac{\partial^2 G^{3D}}{\partial z^2} = \delta(z). \tag{5.93}$$

This can be written as above. Regard k_x, k_y as constants, and define k_z as

$$k_z \equiv \sqrt{\left(\frac{\omega}{\alpha}\right)^2 - k_x^2 - k_y^2}. \tag{5.94}$$

note 19) Strictly speaking, the far-field term also includes an inhomogeneous wave, but its effect is relatively small.

With this definition, it takes the same form as the Green's function for the 1-D wave equation with respect to z (equation (**??**)). We can write it as

$$G^{3D}(k_x, k_y, \omega) = \frac{\rho_0 i}{2k_z} e^{-ik_z|z|}. \tag{5.95}$$

Applying a 2-D inverse Fourier transform with respect to k_x and k_y, we get

$$G^{3D}(x, y, z, \omega) = \frac{\rho_0 i}{8\pi^2} \iint_{-\infty}^{\infty} dk_x dk_y \frac{e^{i(k_x x + k_y y - k_z|z|)}}{k_z}. \tag{5.96}$$

Comparing this with the 3-D Green's function for an infinite medium (equation (**??**)),

$$-\frac{\rho_0 i}{4\pi} \frac{e^{-ikr}}{r} = \frac{\rho_0}{8\pi^2} \iint_{-\infty}^{\infty} dk_x dk_y \frac{e^{i(k_x x + k_y y - k_z|z|)}}{k_z}. \tag{5.97}$$

This equation is also called Weyl's integral representation, which indicates that the 3-D infinite Green's function can be represented by the superposition of plane waves. Furthermore, although it implicitly assumes that k_x and k_y are real numbers, by separating z, it can be naturally extended to inhomogeneous waves in the z-axis direction. Therefore, by considering the reflection and transmission of plane waves at boundaries, it can naturally be extended to wave propagation in a two-layer medium.

Looking at Weyl's integral representation, you will see that it is represented by an inhomogeneous P-wave that attenuates upward from the source. Since the amplitude of this inhomogeneous P-wave diverges with depth, it seems physically impossible at first glance. Let us recall the representation theorem here. It can be realized by considering a boundary surface for the incident inhomogeneous P-wave and providing the boundary conditions of stress and displacement at the boundary surface[note 20)]. In other words, we will consider it as a problem of incidence of an upwardly decaying inhomogeneous P-wave emitted from the source.

Let us take the horizontal slowness on the horizontal axis and calculate the reflection and conversion coefficients even for values larger than the S-wave slowness (Figure 5.21). When $p\beta$ is smaller than $1/\sqrt{3}$, the incident P-wave is a body wave, so it is equivalent to the problem of reflection and conversion of a P-wave at a free boundary surface. When $p\beta$ is greater than $1/\sqrt{3}$ and smaller than 1, the incident P-wave is an inhomogeneous wave, but the converted S-wave is a body wave. The inhomogeneous P-wave appearing as a reflection corresponds to a wave whose amplitude decreases vertically downward.

At the point where $p\beta$ is slightly larger than 1, R_{ps} and R_{pp} diverge[note 21)]. You can see that the wavenumber corresponding to the Rayleigh wave is emphasized. What is happening?

Since it becomes difficult to grasp the physical meaning when it diverges, let us consider an inhomogeneous P-wave that decreases vertically downward[note 22)]. Looking at Figure 5.22, you

note 20) The representation theorem is powerful as it allows us to easily consider such virtual operations

note 21) They diverge in the wavenumber domain, but for physically realizable excitations, they do not diverge in the spatiotemporal domain.

note 22) When considering the incidence of an inhomogeneous P-wave descending vertically upward, we considered an inhomogeneous P-wave decreasing vertically downward as the reflected wave, and its conversion coefficient diverged at the Rayleigh wave velocity. Therefore, you can consider it as re-normalized by the amplitude of the converted inhomogeneous P-wave.

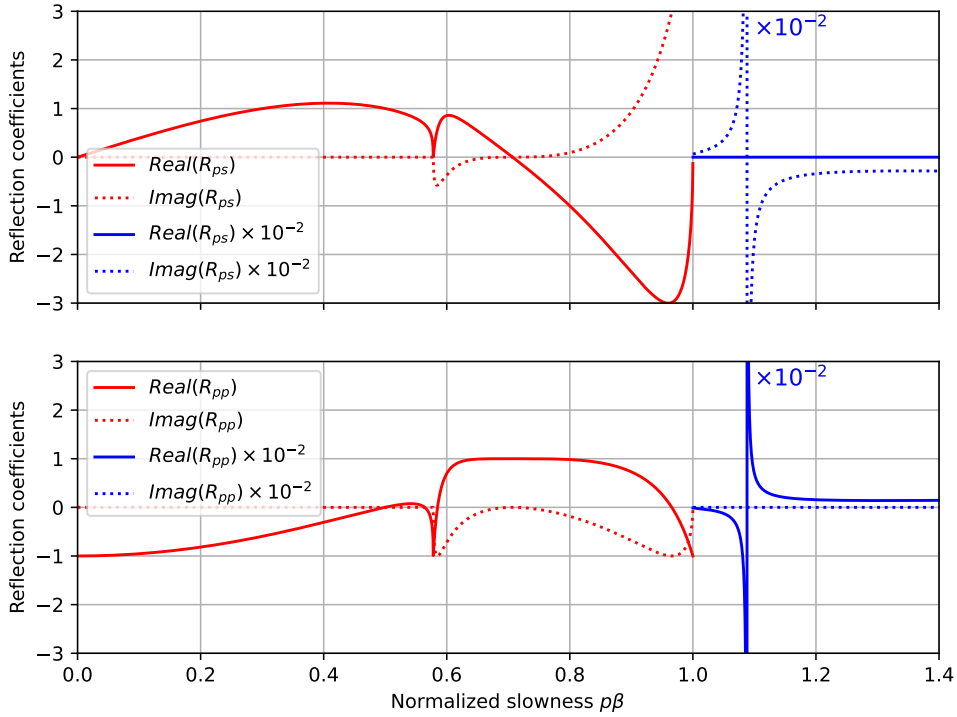

Figure 5.21: Reflection and transmission coefficients for inhomogeneous P-wave incidence. A wave decaying vertically upward is taken as the incident inhomogeneous P-wave. For plotting purposes, the reflection and conversion coefficients are multiplied by $1/100$ for $p\beta > 1$. It can be seen that they diverge at the velocity corresponding to the Rayleigh wave velocity.

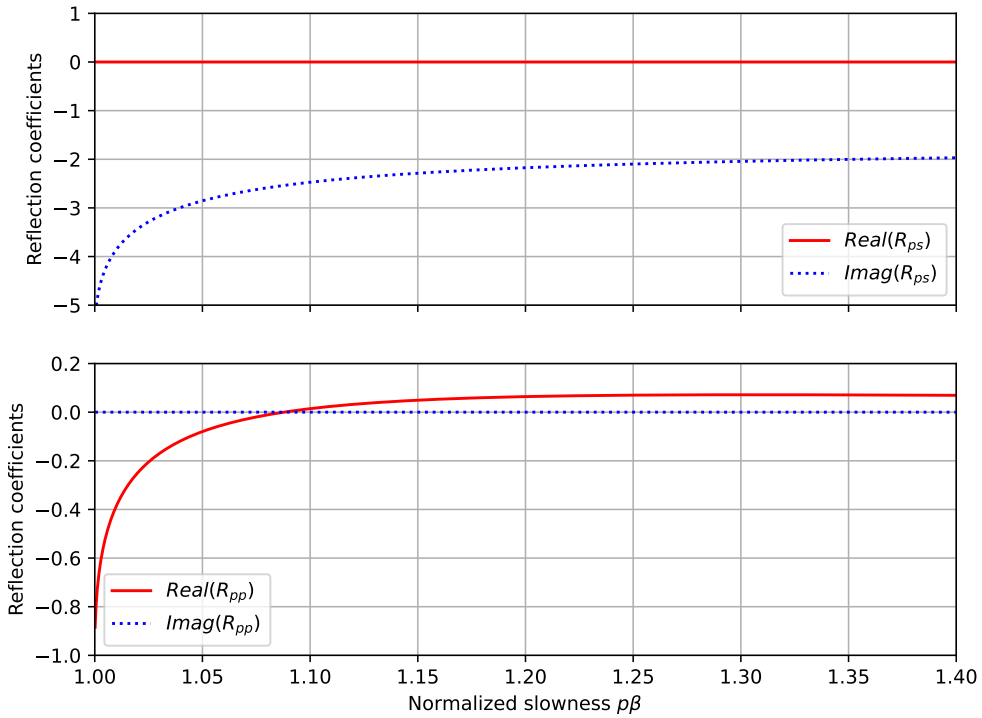

Figure 5.22: Reflection and transmission coefficients for inhomogeneous P-wave incidence. A wave decaying vertically downward is taken as the incident inhomogeneous P-wave. It can be seen that R_{pp} becomes zero at a point where the slowness is slightly greater than $1/\beta$.

will notice that R_{pp} becomes 0 at the slowness corresponding to the Rayleigh wave velocity. Now, an inhomogeneous wave decreasing vertically upward can only exist if supported by an external force at the excitation source (which can also be rephrased as the near-field term), so if this component exists, it cannot exist far from the source. At the slowness corresponding to the Rayleigh wave velocity, it is possible to exist even without an excitation source because an inhomogeneous P-wave and an inhomogeneous S-wave decreasing vertically downward support each other. In this way, it can be viewed as a generalized problem of the reflection and conversion of inhomogeneous P-waves.

Let us consider what is happening physically. When the incident inhomogeneous P-wave reaches the surface, secondary waves are excited to satisfy the free boundary surface. From the representation theorem, consider placing a secondary pressure source that cancels out the stress of the incident inhomogeneous P-wave. To satisfy the boundary conditions, inhomogeneous P-waves and inhomogeneous S-waves are excited. Due to physical constraints, secondary waves can exist only as vertically downward decreasing waves. Therefore, except under the condition

$R_{pp} = 0$, the incident inhomogeneous P-wave is required to support the secondarily excited inhomogeneous P-waves and S-waves. Thus, the near-field term is used to cause the surface to bulge, thereby satisfying the boundary conditions.

On the other hand, when the condition $R_{pp} = 0$ is satisfied, there is no need to support the reflected inhomogeneous P-wave and the converted inhomogeneous S-wave with the incident inhomogeneous P-wave. Therefore, a cycle is established where the inhomogeneous P-wave excites the inhomogeneous S-wave, and the inhomogeneous S-wave excites the inhomogeneous P-wave. Because it propagates maintaining its amplitude over long distances, it diverges at the wavenumber corresponding to the Rayleigh wave velocity, which has an amplitude when Fourier transformed[note 23)]. In this way, the generation of Rayleigh waves can be understood by considering that the loop of inhomogeneous P-waves and inhomogeneous S-waves, whose phases are shifted by 90 degrees relative to each other, closes only at the Rayleigh wave velocity.

Problem 5.6

1. Show that the equation 5.81 has a solution with slowness greater than $p = 1/\beta$ for any elastic constant.
2. Illustrate the Rayleigh wave velocity versus Poisson's ratio when $\beta = 1$. Also, discuss the physical meanings.
3. Calculate the ellipticity of the particle motion at the earth's surface in the same way and discuss it physically.

[note 23)] Due to physical requirements, it will have a finite value if converted back to the time domain

§5.8 Lamb's solution

We present the analytical form of Lamb's problem for a 3-D elastic half-space, as given by Kausel (2014).[2] r is the radial distance, θ is the azimuth, μ is the shear modulus, ρ is the density, ν is Poisson's ratio, C_R is the Rayleigh wave velocity, C_S is the S-wave velocity, C_P is the P-wave velocity, t is time, a is C_S/C_P. Here, κ_j are the three dimensionless roots to the Rayleigh characteristic equation (= C_S/C_j), $\gamma \equiv \kappa_1 = C_S/C_R$ is the true Rayleigh root, and τ is the dimensionless time tC_S/r.

The Rayleigh characteristic equation is given by

$$16(1-a^2)\kappa^6 - 8(3-2a^2)\kappa^4 + 8\kappa^2 - 1 = 0. \tag{5.98}$$

$$\begin{gathered} A_j = \frac{\left(\kappa_j^2 - \frac{1}{2}\right)^2 \sqrt{a^2 - \kappa_j^2}}{D_j}, \quad B_j = \frac{\left(1-2\kappa_j^2\right)\left(1-\kappa_j^2\right)}{D_j}, \quad C_j = \frac{\left(1-\kappa_j^2\right)\sqrt{a^2-\kappa_j^2}}{D_j} \\ D_j = \left(\kappa_j^2 - \kappa_i^2\right)\left(\kappa_j^2 - \kappa_k^2\right), \quad i \neq j \neq k \end{gathered} \tag{5.99}$$

$$u_{zz}(r,\tau) = \frac{(1-\nu)}{2\pi\mu r} \begin{cases} \dfrac{1}{2}\left(1 - \displaystyle\sum_{j=1}^{3} \frac{A_j}{\sqrt{\tau^2 - \kappa_j^2}}\right), & a < \tau < 1 \\ 1 - \dfrac{A_1}{\sqrt{\tau^2 - \gamma^2}}, & 1 \le \tau < \gamma \\ 1, & \tau \ge \gamma \end{cases} \tag{5.100}$$

$$u_{rx} = \frac{(\cos\theta)}{2\pi\mu r} \begin{cases} \dfrac{1}{2}(1-\nu)\tau^2 \displaystyle\sum_{j=1}^{3} \frac{C_j}{\sqrt{\tau^2 - \kappa_j^2}}, & a < \tau < 1 \\ 1 + (1-\nu)\tau^2 \dfrac{C_1}{\sqrt{\tau^2 - r^2}}, & 1 \le \tau < \gamma \\ 1, & \tau \ge \gamma \end{cases} \tag{5.101}$$

$$u_{\theta x} = \frac{(1-\nu)(-\sin\theta)}{2\pi\mu r} \begin{cases} \dfrac{1}{2}\left[1 - \displaystyle\sum_{j=1}^{3} C_j \sqrt{\tau^2 - \kappa_j^2}\right], & a < \tau < 1 \\ 1 - C_1\sqrt{\tau^2 - \gamma^2}, & 1 \le \tau < \gamma \\ 1, & \tau \ge \gamma \end{cases} \tag{5.102}$$

§5.9 Bibliography

[1] F.A. Dahlen and J. Tromp. *Theoretical Global Seismology*. Princeton University Press, Princeton, 1998.

[2] Eduardo Kausel. Lamb's problem at its simplest. *Proc. R. Soc. A Math. Phys. Eng. Sci.*, 469(2149):20120462–20120462, nov 2012.

[3] Saito Masanori. *Seismic Wave Theory*. University of Tokyo Press, 2009.

[4] K Nishida. Global propagation of body waves revealed by cross-correlation analysis of seismic hum. *Geophys. Res. Lett.*, 40(9):1691–1696, May 2013.

[5] F. Omori. Note on the preliminary tremor of earthquake motion. *Journal of the College of Science, Imperial University of Tokyo*, 11(3):147–159, 1899.

[6] John William Strutt Rayleigh. On waves propagated along the plane surface of an elastic solid. *Proc. Lond. Math. Soc.*, s1-17(1):4–11, November 1885.

SH-wave propagation from a point source in a medium with two layers

Chapter 6

On October 8, 1909, a massive earthquake occurred in the Kulpa Valley, causing severe damage. A Croatian meteorologist and seismologist, Andrija Mohorovičić, collected seismograms across Europe and plotted the travel-time curve, as shown in Figure 6.1. Based on these observations, he discovered a structural discontinuity at a depth of 54 km. He estimated the P-wave velocity of the crust to be 5.68 km/s, whereas that of the underlying mantle was 7.75 km/s. This boundary is now known as the Mohorovičić discontinuity, or Moho discontinuity for short.(2) In this chapter, we will learn how to infer such discontinuities based on the behavior of reflected and refracted waves originating from a point source. For simplicity, we focus on SH wave propagations.

§6.1 Plane wave decomposition

In the previous chapter, we learned the reflection and refraction of plane waves. They are fundamental to interpreting seismic wave propagation because a seismic wave field can be represented by a superposition of plane waves as,

$$\phi(\boldsymbol{x},t) = \int_{-\infty}^{\infty} d\omega \int_{-\infty}^{\infty} dk_x dk_y A(k_x,k_y,\omega) e^{i\left[k_x x + k_y y + \left(\frac{\omega^2}{\alpha^2} - k_x^2 - k_y^2\right)^{1/2} z - \omega t\right]}. \tag{6.1}$$

Based on these results, we will consider seismic wave propagation in a two-layered medium, alongside the features of Green's functions in an infinite medium. For simplicity, we will focus on SH waves (which are mathematically equivalent to acoustic waves) in this chapter.

Let us review the Weyl integral representation explained in Section 5.6.

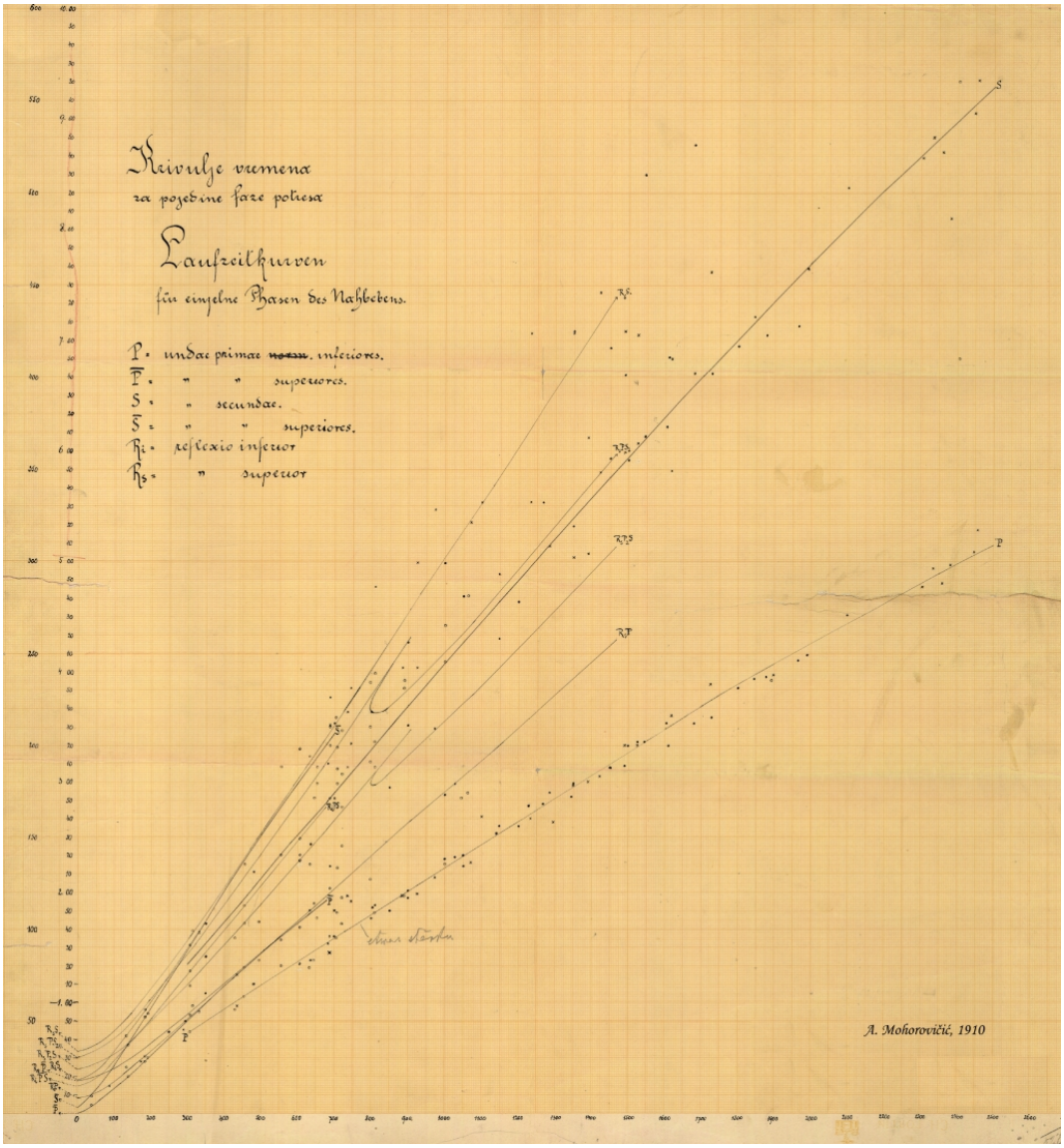

Figure 6.1: Observed travel-time curves for the 1909 earthquake, taken from a paper translated into English (4) from Croatian[5] by Mohorovičić (1910).

§6.2 Reflection and refraction on an internal boundary

6.2.1 SH wave

Next, we consider reflection and refraction on a boundary inside an infinite elastic medium (Figure 6.2). A semi-infinite medium 2 $z < 0$ is welded to the medium 1 $z > 0$. The incident SH wave enters downward in medium 1, then it is reflected in medium 1 and refracted to medium 2. Corresponding plane wave solutions are given by

$$z > 0 : s_y = A_1 e^{-i\omega(t - p_{1x}x - p_{1z}z)} + B_1 e^{-i\omega(t - p_{1x}x + p_{1z}z)} \tag{6.2}$$

$$z < 0 : s_y = A_2 e^{-i\omega(t - p_{2x}x - p_{2z}z)}. \tag{6.3}$$

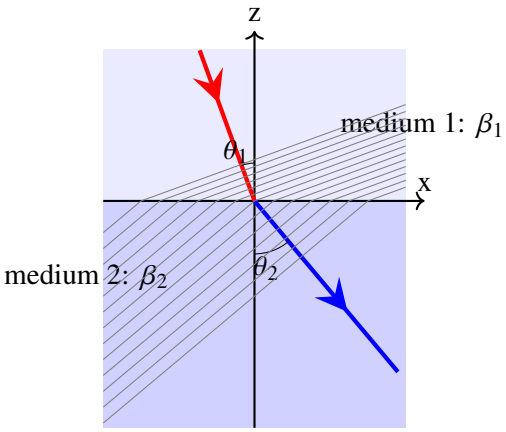

Figure 6.2:

The first term of s_y for $z > 0$ represents the incident wave, the second term represents the reflected wave, and s_y for $z < 0$ represents the refracted (transmitted) wave in medium 2. To satisfy the boundary condition for the continuity of displacement, the horizontal slowness must be continuous across the boundary, meaning $p_{1x} = p_{2x}$. This condition is mathematically identical to Snell's law:

$$\frac{\sin\theta_1}{\beta_1} = \frac{\sin\theta_2}{\beta_2}. \tag{6.4}$$

To satisfy the condition of continuity of displacement at $z = 0$, the relation $A_1 + B_1 = A_2$ is required. Furthermore, to satisfy the boundary condition for the continuity of stress, $\mu_1 p_{1z}(A_1 - B_1) = \mu_2 p_{2z} A_2$ is also required. Consequently, the corresponding reflection coefficient R_{12} and transmission coefficient T_{12} are given by:

$$R_{12} = \frac{B_1}{A_1} = \frac{\mu_1 p_{1z} - \mu_2 p_{2z}}{\mu_1 p_{1z} + \mu_2 p_{2z}} = \frac{\rho_1\beta_1\cos\theta_1 - \rho_2\beta_2\cos\theta_2}{\rho_1\beta_1\cos\theta_1 + \rho_2\beta_2\cos\theta_2} \tag{6.5}$$

$$T_{12} = \frac{A_2}{A_1} = \frac{2\mu_1 p_{1z}}{\mu_1 p_{1z} + \mu_2 p_{2z}} = \frac{2\rho_1\beta_1\cos\theta_1}{\rho_1\beta_1\cos\theta_1 + \rho_2\beta_2\cos\theta_2}. \tag{6.6}$$

The continuity of displacement at the boundary leads to the relation $1 + R_{12} = T_{12}$. You can explore a playful web application demonstrating reflection and transmission phenomena at: https://www.eri.u-tokyo.ac.jp/people/knishida/eng/Seismology/wave_coe.html.

Conservation of energy

The total energy flux entering a unit area at $z = 0$, given by $K_{in}\cos\theta_1$, must equal the sum of the outgoing energy fluxes from the reflected wave ($K_{refl}\cos\theta_1$) and the refracted wave

($K_{trans} \cos\theta_2$). In the case of SH waves, the conservation of energy is expressed as:

$$\rho_1\beta_1 \cos\theta_1 = \rho_1\beta_1 \cos\theta_1 |R_{12}|^2 + \rho_2\beta_2 \cos\theta_2 |T_{12}|^2. \tag{6.7}$$

Total reflection

When $\theta_2 > \theta_1$, total reflection occurs for an incident angle θ_1 that is larger than the critical angle θ_c, which is defined by:

$$\theta_c = \sin^{-1}\frac{\beta_1}{\beta_2}. \tag{6.8}$$

In this case, since p_{2z} becomes purely imaginary, the amplitude of the refracted wave in medium 2 decreases exponentially with depth z. Consequently, the refracted wave does not transfer energy downward into medium 2.

On the other hand, although the reflection coefficient R_{12} is a complex number, its absolute value is exactly 1 (since the numerator is the complex conjugate of the denominator). Considering the conservation of energy in Eq. 6.7, $|R_{12}|^2 = 1$ and $|T_{12}|^2 = 0$. This also indicates that the phase of the reflected wave is advanced during total reflection. The phase shift of R_{12} is given by:

$$arg R_{12} = -2\tan^{-1}\frac{\mu_2 i p_{2z}}{\mu_1 p_{1z}} = -2\tan^{-1}\frac{\mu_2\sqrt{p^2 - \beta_2^{-2}}}{\mu_1\sqrt{\beta_1^{-2} - p^2}} \tag{6.9}$$

When μ_2 goes infinity, the reflection coefficient $R_{12} = -1$ represents reflection at a rigid wall.

Acoustic impedance

For simplicity, here we consider Eq. **??** for vertically propagating wave ($\theta = 0$). The reflection and transmission coefficients are give by

$$R_{12} = \frac{\rho_1\beta_1 - \rho_2\beta_2}{\rho_1\beta_1 + \rho_2\beta_2} \tag{6.10}$$

$$T_{12} = \frac{2\rho_1\beta_1}{\rho_1\beta_1 + \rho_2\beta_2}. \tag{6.11}$$

$\rho\beta$ is called acoustic impedance, which shows resistance of entering wave. The equation shows the impedance contrast determines the reflection and transmission coefficients. The acoustic impedance is defined as the ratio between stress and particle velocity as an analogy of resistance of the electric circuit.

With increasing $\rho_2\beta_2$, the transmitted wave is harder to enter. When the two acoustic impedances match with each other as $\rho_1\beta_1 = \rho_2\beta_2$, no reflection occurs. Even if seismic velocities of two media are the same, a reflected wave occurs owing to the density contrast. In summary, the reflection and transmission coefficients do not contain information on seismic velocity contrast but also on density contrast. The coefficients are crucial for exploring density contrast at discontinuities of the Earth.

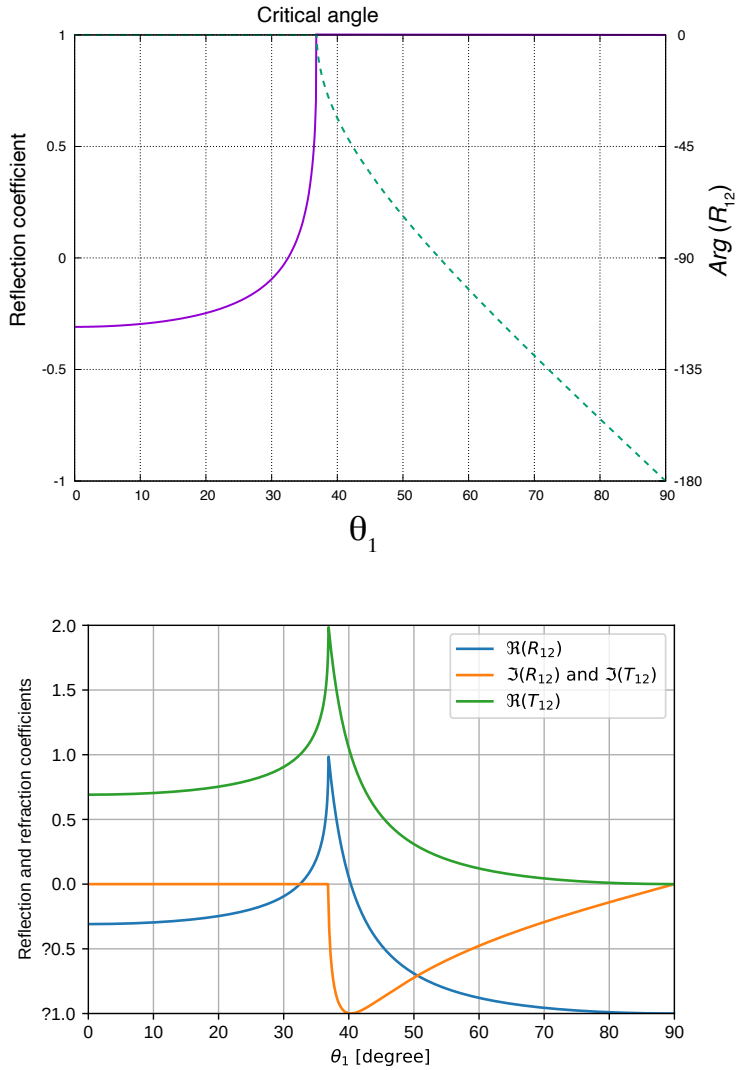

Figure 6.3: (Upper) Reflection coefficient R_{12} of SH wave on the internal boundary. The coefficient is real before the critical angle, and it becomes complex after the angle. The solid line shows the reflection coefficient, and the broken line shows the phase. (Lower) Reflection and Reflection coefficients R_{12} and T_1. This plot shows the real and imaginary parts. $\rho_1 = 2.2 \times 10^3$ [kg/m^3], $\rho_2 = 2.5 \times 10^3$ [kg/m^3], $\beta_1 = 3$ [km/s], $\beta_2 = 5$ [km/s].

6.2.2 Reflection, refraction, and conversion of P-SV at an internal boundary

Because the derivation is somewhat complex, we only show the final results here[note 1)]:

$$a = \rho_2 - 2(\mu_2 - \mu_1)p^2 \qquad K = a\xi_1 + b\xi_2 \qquad N = a\eta_1 + b\eta_2 \tag{6.12}$$

$$b = \rho_1 + 2(\mu_2 - \mu_1)p^2 \qquad L = d - 2(\mu_2 - \mu_1)\xi_1\eta_2 \qquad M = d - 2(\mu_2 - \mu_1)\xi_2\eta_1 \tag{6.13}$$

$$d = \rho_2 - \rho_1 - 2(\mu_2 - \mu_1)p^2 \qquad D = KN + p^2LM \tag{6.14}$$

SV wave incidence

$$R_{SS} = \frac{1}{\Delta}\{-(a\eta_1 - b\eta_2)K + p^2[d + 2(\mu_2 - \mu_1)\xi_2\eta_1]L\} \tag{6.15}$$

$$R_{SP} = -\frac{\beta_1}{\alpha_1}\frac{2p\eta_1}{\Delta}[ad + 2(\mu_2 - \mu_1)b\xi_2\eta_2] \tag{6.16}$$

$$T_{SS} = \frac{\beta_1}{\beta_2}\frac{2\rho_1\eta_1 K}{\Delta} \tag{6.17}$$

$$T_{SP} = \frac{\beta_1}{\beta_2}\frac{2\rho_1 p\eta_1 L}{\Delta} \tag{6.18}$$

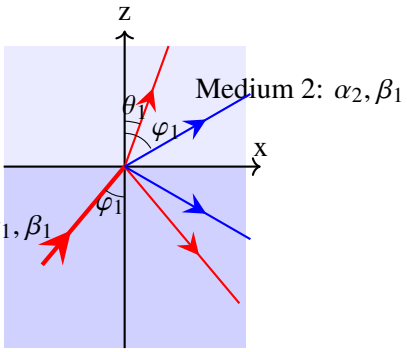

Figure 6.4:

Here,

$$p = \frac{\sin\theta_1}{\alpha_1} = \frac{\sin\theta_2}{\alpha_2} = \frac{\sin\varphi_1}{\beta_1} = \frac{\sin\varphi_2}{\beta_2} \tag{6.19}$$

$$\xi_i^2 = \frac{1}{\alpha_i^2} - p^2, \eta_i^2 = \frac{1}{\beta_i^2} - p^2, \gamma_i^2 = 2\beta_i^2 p^2. \tag{6.20}$$

P wave incidence

$$R_{PP} = \frac{1}{\Delta}\{(a\xi_1 - b\xi_2)N - p^2[d + 2(\mu_2 - \mu_1)\xi_1\eta_2]M\} \tag{6.21}$$

$$R_{PS} = -\frac{\alpha_1}{\beta_1}\frac{2p\xi_1}{\Delta}[ad + 2(\mu_2 - \mu_1)b\xi_2\eta_2] \tag{6.22}$$

$$T_{PP} = \frac{\alpha_1}{\alpha_2}\frac{2\rho_1\xi_1 N}{\Delta} \tag{6.23}$$

$$T_{PS} = \frac{\alpha_1}{\alpha_2}\frac{2\rho_1 p\xi_1 M}{\Delta} \tag{6.24}$$

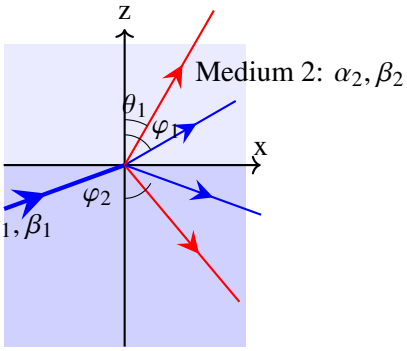

Figure 6.5:

[note 1)] For a more detailed derivation, please refer to Aki and Richards (2002) or Saito (2009).

$$R_{PP} = \frac{1}{\Delta}\{(a\xi_1 - b\xi_2)N - p^2[d + 2(\mu_2 - \mu_1)\xi_1\eta_2]M\} \tag{6.25}$$

$$R_{PS} = -\frac{\alpha_1}{\beta_1}\frac{2p\xi_1}{\Delta}[ad + 2(\mu_2 - \mu_1)b\xi_2\eta_2] \tag{6.26}$$

$$T_{PP} = \frac{\alpha_1}{\alpha_2}\frac{2\rho_1\xi_1 N}{\Delta} \tag{6.27}$$

$$T_{PS} = \frac{\alpha_1}{\alpha_2}\frac{2\rho_1 p\xi_1 M}{\Delta} \tag{6.28}$$

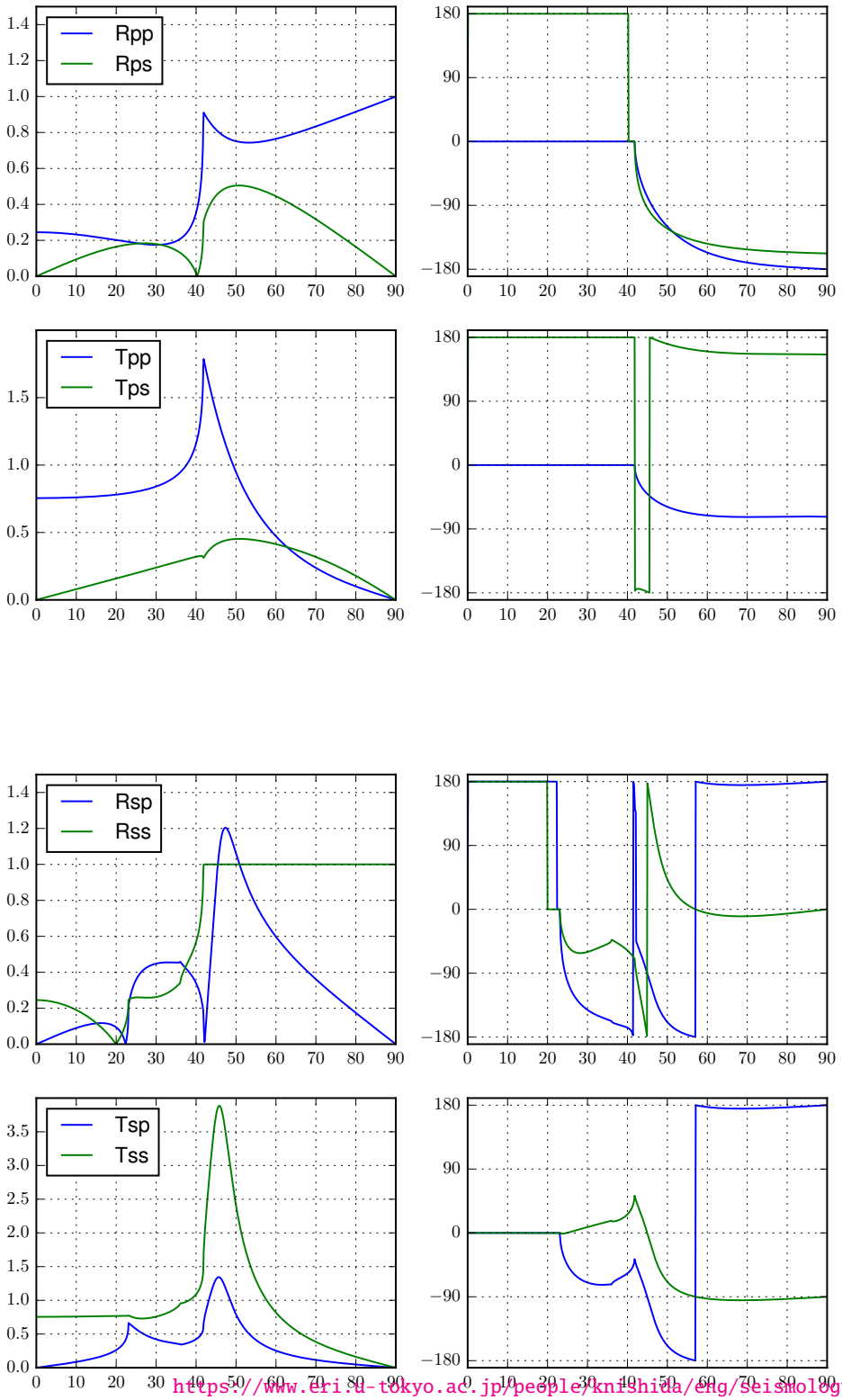

Figure 6.6: Reflection, transmission and conversion coefficients at a boundary taken from Saito (2009).[4]

6.2.3 Asymptotics for near vertical incident

This section describes the asymptotics of the coefficients for the near-vertical incident (p is enough small). Here we neglect higher-order terms of p than 2.

P wave incident

$$R_{PP} = \frac{\rho_2\alpha_2 - \rho_1\alpha_1}{\rho_2\alpha_2 + \rho_1\alpha_1} \tag{6.29}$$

$$R_{PS} = -\frac{2\alpha_1 p[\rho_2(\rho_2 - \rho_1)\alpha_2\beta_2 + 2\rho_1(\mu_2 - \mu_1)]}{(\rho_2\alpha_2 + \rho_1\alpha_1)(\rho_2\beta_2 + \rho_1\beta_1)} \tag{6.30}$$

$$T_{PP} = \frac{2\rho_1\alpha_1}{\rho_2\alpha_2 + \rho_1\alpha_1} \tag{6.31}$$

$$T_{PS} = \frac{2\rho_1\alpha_1 p[(\rho_2 - \rho_1)\alpha_2\beta_1 - 2(\mu_2 - \mu_1)]}{(\rho_2\alpha_2 + \rho_1\alpha_1)(\rho_2\beta_2 + \rho_1\beta_1)}. \tag{6.32}$$

S wave incident

$$R_{SS} = \frac{\rho_2\beta_2 - \rho_1\beta_1}{\rho_2\beta_2 + \rho_1\beta_1} \tag{6.33}$$

$$R_{SP} = -\frac{2\beta_1 p[\rho_2(\rho_2 - \rho_1)\alpha_2\beta_2 + 2\rho_1(\mu_2 - \mu_1)]}{(\rho_2\alpha_2 + \rho_1\alpha_1)(\rho_2\beta_2 + \rho_1\beta_1)} \tag{6.34}$$

$$T_{SS} = \frac{2\rho_1\beta_1}{\rho_2\beta_2 + \rho_1\beta_1} \tag{6.35}$$

$$T_{SP} = \frac{2\rho_1\beta_1 p[(\rho_2 - \rho_1)\alpha_2\beta_1 - 2(\mu_2 - \mu_1)]}{(\rho_2\alpha_2 + \rho_1\alpha_1)(\rho_2\beta_2 + \rho_1\beta_1)}. \tag{6.36}$$

Here, R_{PP} and R_{SS} can be represented by impedance, similarly to SH waves. Surprisingly, the conversion coefficients (e.g., T_{PS} and R_{PS}) are explicitly sensitive to both density contrast and S-wave velocity contrast. Figure 6.6 shows that this first-order approximation remains valid over a large range of slowness values p.

§6.3 Radiation of seismic wave from a point source: wavefront and ray path

here we consider propagations of a wave packet $f(t)$. Amplitude in y component s_y is given by

$$s_y(\boldsymbol{x}, t) = A(\boldsymbol{x}) f(t - T(\boldsymbol{x})), \tag{6.37}$$

where $T(\boldsymbol{x})$ is the arrival time at a location $\boldsymbol{x}$, and $A(\boldsymbol{x})$ is the amplitude. The isocontour for the same arrival time of $T(\boldsymbol{x})$ is known as the "wavefront". The ray is perpendicular to the wavefront. The direction of the ray is represented by $\hat{\boldsymbol{n}} \equiv \beta \nabla T$, where β is the S-wave velocity. The comparison with a plane wave shows that ∇T corresponds to the slowness vector.

Figure 6.7 shows a typical example of wavefronts for two-layer medium. The wavefronts are associated with ripples spread out when a single pebble is dropped into water.

For understanding ray paths, the physical interpretation is feasible. Here we consider that the spatial variation of A is enough loner than the wavelength. Because the spatial derivative of A is negligible, the displacement is written as,

$$\nabla s_y = -A \nabla f = -A \frac{df}{dt} \nabla T \tag{6.38}$$

The energy flux $\boldsymbol{K}$ is given by

$$\boldsymbol{K} = \beta \hat{\boldsymbol{n}} \rho \dot{f}^2 A^2. \tag{6.39}$$

Conservation of energy along the ray path gives us the information of the amplitude. Figure 6.8 shows a typical example of ray paths.

A comparison of ray paths for reflection before the critical angle with the corresponding wavefronts in Figure 6.7 is easy to interpret. On the other hand, the behavior after the critical angle is complex. Total reflection after the critical angle causes the split between the transited and reflected wave packets. The following section explains the behavior.

§6.4 Wave behavior at a seismic discontinuity

In the previous chapter, we learned about the reflection and transmission of plane waves at a material boundary. Building on those results, let us consider the physical behavior of seismic waves excited by a point source (i.e., a Green's function) located above a discontinuity. The resulting wave modes are generally categorized into four types: direct waves, reflected waves, transmitted waves, and head waves.

6.4.1 Direct wave

First, let us consider the direct wave. For simplicity, we neglect free surfaces on the ground. The green line in Figure 6.8 shows the direct wave. The SH-wave propagation can be represented by a Green's function in an infinite homogeneous medium. Of course, the travel time T is proportional to the epicentral distance between the source and the station as

$$T(r) = r/\beta_1, \tag{6.40}$$

where r is the epicentral distance for the station and source in the xy plane. For a point source in the 3-D medium, the amplitude decreases with $1/r$, which is given by the conservation of energy

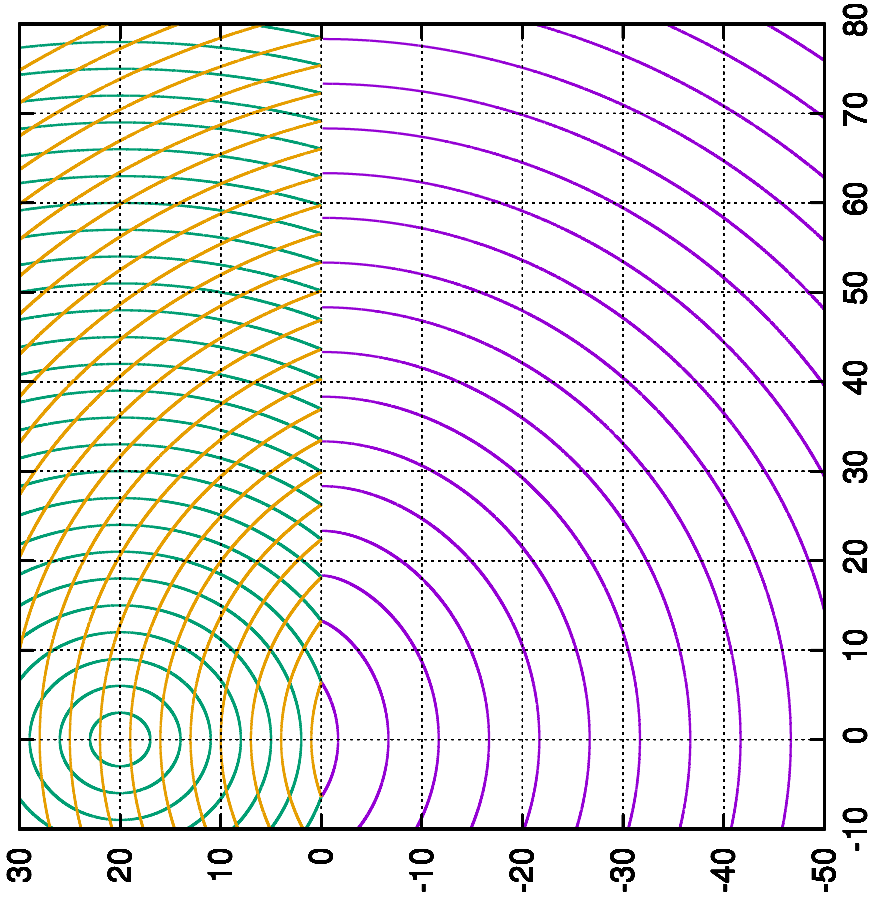

Figure 6.7:

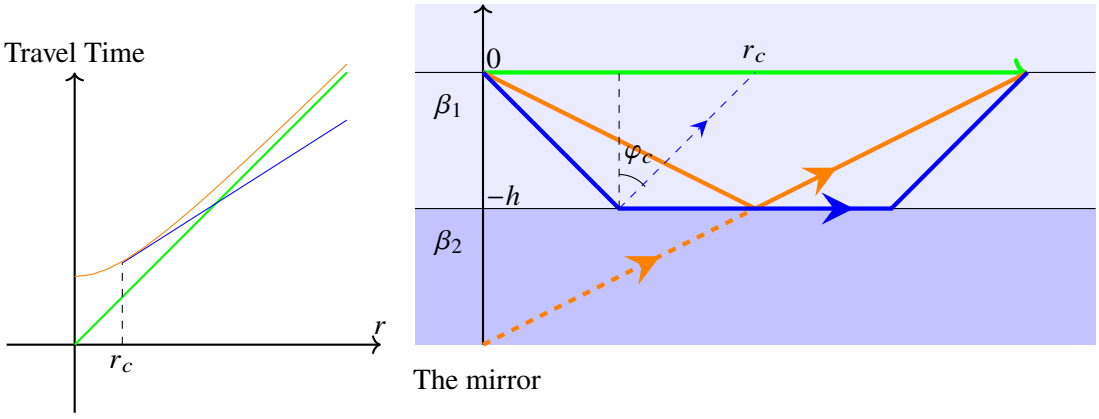

Figure 6.8:

along the path as,

$$A_d \sim \frac{1}{4\pi r} e^{ik_{\beta_1} r \mu_1 \beta_1} \tag{6.41}$$

6.4.2 Reflected wave

Next, let us consider the reflected wave. The orange line shows the reflected wave. The mirror-symmetric source for the discontinuity (at $z = -h$) helps us intuitively understand its ray path. The travel time is given by:

$$T = 2\sqrt{h^2 + (r/2)^2}/\beta_1, \tag{6.42}$$

and the amplitude is given by:

$$A_r \sim \frac{1}{4\pi R_0 \mu_1 \beta_1} R_{12}(\boldsymbol{p}) e^{ik_{\alpha_1} R_0}, \tag{6.43}$$

where R_{12} is the reflection coefficient. Because R_{12} is real before the critical angle, the reflection does not induce a phase shift. However, total reflection beyond the critical angle causes a phase shift, and its amplitude becomes 1. These are also known as post-critical reflections or wide-angle reflections.

Beyond the critical angle, the behavior becomes more complex, featuring the splitting of wavefronts and significant phase shifts. The properties of head waves are key to understanding this complexity, as will be explained in the next subsection.

6.4.3 Transmitted wave

Last, let us consider the transmitted wave. Because this wave does not return to the surface, of course, we cannot measure the travel

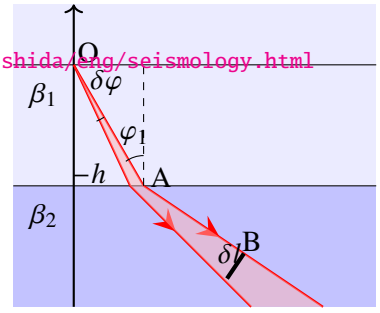

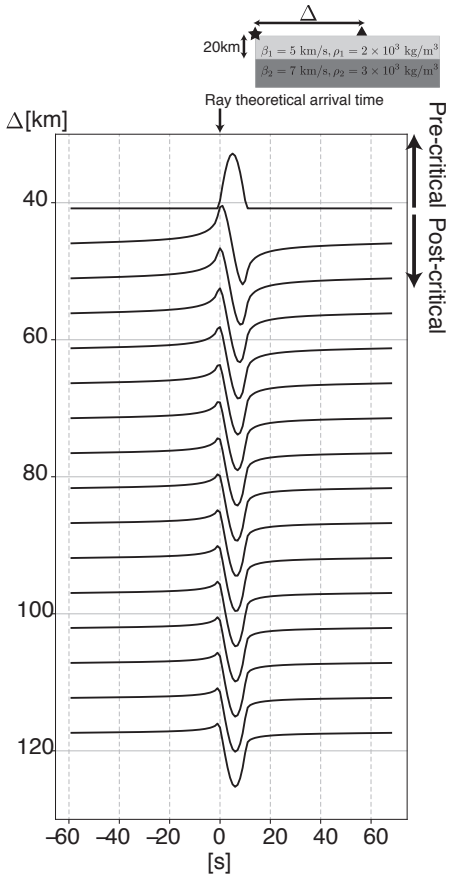

Figure 6.9: Example of wide-angle reflection. After the critical angle, we can see the reflected wave arrives before the ray theoretical value because of the phase shift due to the inhomogeneous wave.

time at a surface station.

$$A_t \sim \frac{1}{4\pi\sqrt{r}} T_{12}(\boldsymbol{p}) \left(r_1 + r_2 \frac{\beta_2 \cos^2 \varphi_1}{\beta_1 \cos^2 \varphi_2} \right)^{-1/2} , e^{i(k_{\alpha_1} r_1 + k_{\alpha_2} r_2)} \quad (6.44)$$

where r_1 is the length of segment OA, r_2 is the length of segment AB, and r is the length of segment OB. A wavefront interacts with the discontinuity at an incident angle φ_1, and it is transmitted at an emergence angle φ_2. Let us estimate the amplitude at point B based on energy conservation. Figure 6.10 illustrates a cross-section of the 3-D medium along the line OB. Here, δl represents the interception length at point B, perpendicular to the ray path. A straightforward

geometrical estimation yields:

$$\delta l = \frac{\cos\varphi_2}{\cos\varphi_1}\left(r_1 + r_2\frac{\beta_2\cos^2\varphi_1}{\beta_1\cos^2\varphi_2}\right)\delta\varphi. \tag{6.45}$$

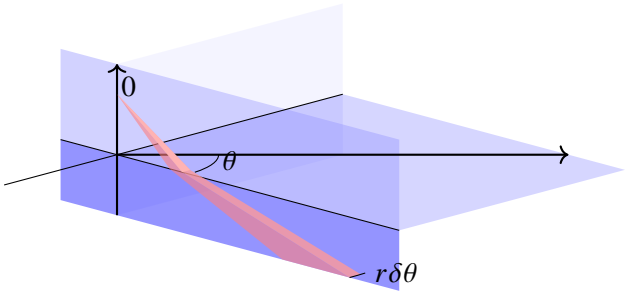

Figure 6.11: Enter of a ray path toward the discontinuity. The ray path is refracted to the radial direction, whereas it is not toward the tangential direction.

Figure 6.11 shows a bird's view of the ray path. The ray path is refracted to the radial direction (on rz plane), whereas it is not toward the tangential direction (θ). Therefore, a cross-section area at point r_0 away from the origin is given by $\delta r_0^2\delta\theta\delta\varphi$, and a cross-section area at point B is given by $r\delta\theta\delta l$. Here we define amplitude A_i on a unit sphere in medium 1. The conservation of energy along the ray leads to

$$\left(\frac{\rho_2\beta_2\cos\varphi_2}{\rho_1\beta_1\cos\varphi_1}|T_{12}|^2\right)\rho_1 A_1^2\omega^2\beta_1\delta\varphi r_0^2\delta\theta = \rho_2 A_t^2\omega^2\beta_2\delta l r\delta\theta. \tag{6.46}$$

Note that the transmission coefficient is multiplied by $\frac{\rho_2\beta_2\cos\varphi_2}{\rho_1\beta_1\cos\varphi_1}$.

Energy normalization of reflection and transmission coefficients

In the previous chapter, we introduced the reflection and transmission coefficients. They are traditionally defined by the amplitude ratio between the scattered wave and the incident wave. However, when considering energy conservation, an energy-normalized definition of these coefficients makes their physical meaning more explicit.

Conservation of energy (Eq. 6.47) for the reflection and transmission is given by

$$\rho_1\beta_1\cos\varphi_1 = \rho_1\beta_1\cos\varphi_1|R_{12}|^2 + \rho_2\beta_2\cos\varphi_2|T_{12}|^2. \tag{6.47}$$

Both sides divided by $\rho_1\beta_1\cos\varphi_1$ leads to

$$1 = |R_{12}|^2 + \frac{\rho_2\beta_2\cos\varphi_2}{\rho_1\beta_1\cos\varphi_1}|T_{12}|^2. \tag{6.48}$$

Here we define a energy normalized transmission coefficient T_{12}^{norm}as,

$$T_{12}^{norm} = \sqrt{\frac{\rho_2\beta_2\cos\varphi_2}{\rho_1\beta_1\cos\varphi_1}}T_{12}\ ^{\text{note 2)}}. \tag{6.49}$$

note 2) See a textbook by Shearer[8] for details. Sections of ray theory are easy-to-grasp.

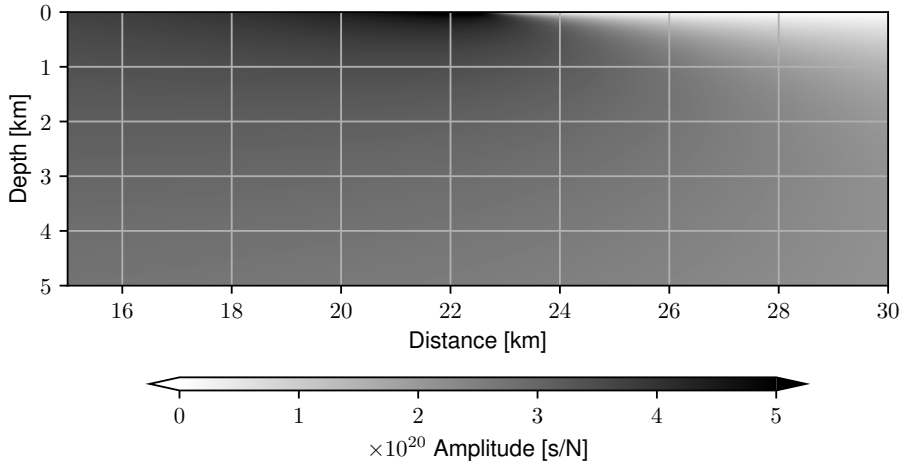

Figure 6.12: Spatial distribution of the Fourier amplitudes of the transmitted wave. The direct wave with the critical angle enters at the point of 2.25 km. $\rho_1 = 2$ [kg/m^2], $\rho_2 = 2.2$ [kg/m^2], $\beta_1 = 3.0$ [km/s], $\beta_2 = 5$ [km/s].

The behavior near the critical angle

Let us consider the behavior of the transmission wave near the critical angle.

First, let us examine the amplitude of the transmitted wave. Figure 6.12 shows its amplitude as a function of the horizontal position and depth below the boundary. The critical angle corresponds to a horizontal distance of 22.5 km. Beyond the critical angle, the amplitude of the transmitted wave diminishes sharply. This sudden drop in amplitude can be understood as a diffraction phenomenon occurring in that region.

Next, we consider the behavior of the transmission wave amplitude near the critical angle. Before the critical angle, because $r_2 = 0$ at the surface, the amplitude of the transmitted wave is given by

$$At \sim \frac{1}{4\pi\sqrt{r}\mu_1\beta_1} T_{12}(\boldsymbol{p}) r_1^{-1/2}. \tag{6.50}$$

After the critical angle, the finite length of r_2 and $\cos\varphi_2 = 0$ lead to $A_t \sim 0$ (Figure6.13). Without considering T_{12}, A_t is proportional to $1/r$ approximately. The amplitude changes with distance gently (Figure 6.13). However, the transmission coefficient changes drastically near the

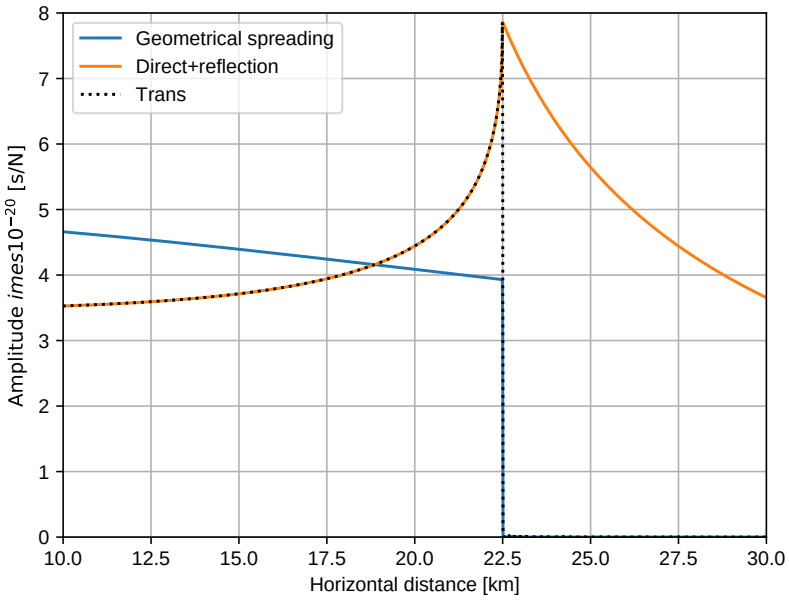

Figure 6.13: Amplitudes of transmitted wave (black) and the direct + reflection (red). The blue line shows the transmitted wave amplitude without the transmission coefficient. $\rho_1 = 2$ [kg/m^2], $\rho_2 = 2.2$ [kg/m^2], $\beta_1 = 3.0$ [km/s], $\beta_2 = 5$ [km/s].

critical angle. Accordingly, A_t has a peak near the critical angle ($r_c/2 = 22.5$ km).

Next, let us evaluate this sharpness. Let l be the horizontal distance from $r_c/2$. Consider the case where the incident angle is smaller than the critical angle by a small angle $\delta\varphi_2$. If we set the refraction angle $\varphi_2 = \pi/2 - \delta\varphi_2$, from Snell's law, we have

$$\frac{\tan\varphi_2 \delta\varphi_2^2}{2} \sim \delta\varphi_1, \tag{6.51}$$

This relationship is obtained. Additionally, from geometric properties,

$$l \sim \frac{h}{\cos^2\varphi_c}\delta\varphi_1, \tag{6.52}$$

This relationship is obtained. Using these relational expressions,

$$T_{12} \sim \frac{2}{1 + \frac{\rho_2\beta_2}{\rho_1\beta_1}\sqrt{\frac{2l}{h}\frac{\cos\varphi_c}{\sin\varphi_c}}} \tag{6.53}$$

Using these approximations, the characteristic width of the peak, defining the spatial extent of the diffraction effect l_d, becomes:

$$l_d \sim \frac{(\rho_1\beta_1)^2}{(\rho_2\beta_2)^2}\frac{\sin\varphi_c}{\cos\varphi_c}\frac{h}{2} = \frac{\rho_1^2\beta_1^3}{\rho_2^2\beta_2^3\cos\varphi_c}\frac{h}{2}. \tag{6.54}$$

We can expect the amplitude of the head wave to scale proportionally with the length l_d.

6.4.4 Head wave

The third type is a head wave (also known as a refracted wave). The wave enters the second layer with a critical angle, and it propagates in the horizontal direction along the uppermost part of the second layer (Figure 6.8). The travel time T_H is given by

$$T_H(r) = \frac{r - r_c}{\beta_2} + \frac{r_c}{\cos\varphi_c \beta_1}. \tag{6.55}$$

The amplitude A is written by

$$A_{head} \sim \frac{i}{2\pi\omega\mu_1\beta_1} \frac{\rho_1\beta_1^2}{\rho_2\beta_2(1-\beta_1^2/\beta_2^2)} \frac{1}{\sqrt{r}D^{3/2}} e^{i\omega t_h} \tag{6.56}$$

Although the frequency- and distance- dependencies are difficult to understand, I try to explain in an intuitive manner[note 3)].

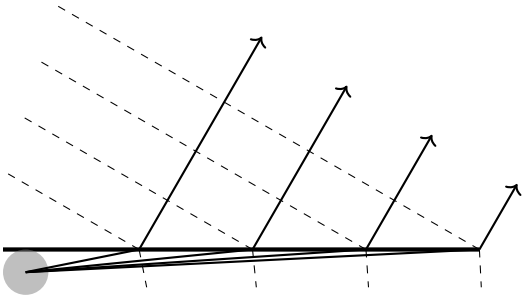

Figure 6.14: A schematic figure of head wave based on Huygens' principle.

Figure 6.7 shows wavefronts of the direct and the reflected and refracted wave share a point on the boundary before reaching the critical angle. After the critical reflection, they are split into two groups: one is a direct and reflected wave, and the other is a head wave and transmitted wave. Exactly speaking, inhomogeneous waves along the boundary also exists.

Let us consider the details of the split. A major difference between the two groups originated from the fact that the direct wave cannot enter the second layer into the second medium. When the transition from the transmitted wave to the inhomogeneous wave in the second layer, let us consider a secondary point source with a spatial scale of about the wavelength at r_c (finite frequency effect) based on the representation theorem, which is a natural extension of Huygens principle. As in the case of diffraction at a narrow slit, an SH wave is radiated in the right direction. Although the ray path of the head wave seems to be parallel to the boundary in layer 2, the path is slightly inclined to owe the source depth of an about wavelength. Thus SH wave is transmitted toward layer 1, as predicted by the Huygens principle. The incident angle can be estimated to be $90°\varphi_1 \sim D/\lambda$ The corresponding transmission coefficient T_{12} can be approximated by

$$T_{21} = \frac{2\rho_2\beta_2\cos\varphi_2}{\rho_1\beta_1\cos\varphi_1 + \rho_2\beta_2\cos\varphi_2} \sim \frac{2\rho_2\beta_2\lambda/D}{\rho_1\beta_1\cos\varphi_c} = \frac{4\pi\rho_2\beta_2^2}{\rho_1\beta_1} \frac{1}{D\omega\cos\varphi_c} \tag{6.57}$$

The amplitude decreases as $r^{-1/2}D^{-1}D^{-1/2}$, where (1) $r^{-1/2}$ represents geometrical spreading of the wavefront in xy plane, (2) $D^{-1/2}$ represents geometrical spreading of the wavefront in

[note 3)] Looking at Eq. 5.92, we see that $k_z = 0$ is a singular point. The singular point is the region where $k = \omega/\beta_2$, which corresponds to where the head wave occurs.

xz plane, and (3) D^{-1} represents contribution by the transmission coefficient. The frequency dependence of ω can be explained by the frequency dependence of the incident angle φ_1, which is proportional to the inverse of the wavelength. This is why the low-frequency component of the head wave is emphasized.

The phase is shifted by 90 degrees. This is because the phase shifts when the wavepacket splits. Because we are considering a 3-D problem, the split of the wavepacket occurs in a ring shape. For this reason, we can understand it by analogy to the 2-D Green's function, where the phase shifts by $\pi/4$ at the origin (hence the Bessel function appeared). When the wave diverges, the phase shifts by $\pi/4$, but this time both convergence and divergence happen, so the phase shifts by $2 \times \pi/4$, resulting in a $\pi/2$ phase shift[note 4)]. This equation exhibits that the head wave can be represented by the integration of the direct wave in time domain[note 5)]. An example of observation in Figure 6.19 shows the dominance of low-frequency components in the head wave.

By considering the head wave as a type of diffracted wave, its amplitude can be estimated. As evaluated in Eq. 6.54, let us assume that the head wave is a wave leaking from a length l_d. In this case, the amplitude should be proportional to l_d, and thus the amplitude should be proportional to $T_{12} l_d$. In this case,

$$A_t \propto \frac{\rho_1 \beta_1^2}{\rho_2 \beta_2 \cos^2 \varphi_c} = \frac{\rho_1 \beta_1^2}{\rho_2 \beta_2 (1 - \beta_1^2/\beta_2^2)}. \tag{6.58}$$

This dependence explains the amplitude dependence on density and seismic velocity.

Because a realistic Earth structure is more complex, the ray path is not so simple. For example, the Pn wave (head wave for Moho discontinuity) is refracted in the uppermost mantle: the behavior may be easy to understand. The next section explains such a case. [note 6)].

Thus, this section explains the behaviors of Green's function for a two-layer medium. In the next section, I will introduce ray theory for discussions of seismic wave propagations in a multi-layer structure.

[note 4)] This is strongly related to the Caustic explained in Section **??**. Intuitively, when a wave converges or diverges at a certain point, it becomes a singular point. Considering the connection of solutions, it can be interpreted that the coordinate system flips.

[note 5)] A more exact discussion mathematically is given by Aki and Richards[(1)] or Saito[(4)] (Chapters 8, 10). In the textbooks, the complex integrals are evaluated. On the other hand, we sacrifice some mathematical rigor to explain the shape of the equations with physical intuition in this chapter.

[note 6)] See Stein and Wysession[(9)] §3.2.3 for details.

Problem 6.1

Derive Eq. 6.45. This is a simple geometrical problem.

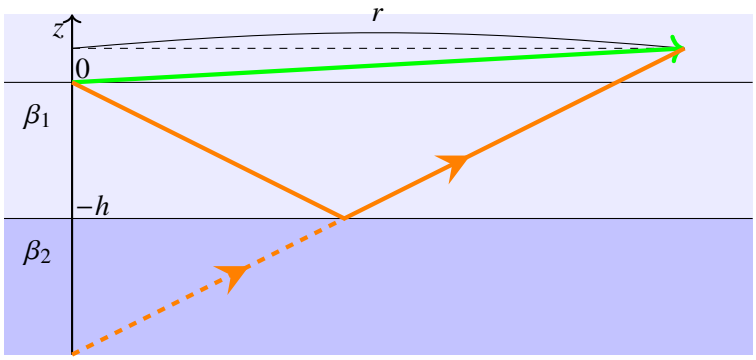

The mirror

Figure 6.15:

6.4.5 Evaluation of integral: stationary phase approximation

The previous sub-section physically interpreted direct, reflected, transmitted, and head waves. Now let us consider them more quantitatively using the stationary phase method.

As mentioned at the beginning of this chapter, wave propagation in a two-layer medium can be exactly evaluated by decomposing it into plane waves and multiplying each plane wave by the reflection-transmission coefficient and integrating it in the wavenumber domain. This expression can be naturally extended to cylindrical waves (Hankel function) and is expressed as The potential χ_d representing a direct wave is given by the integration of slowness as

$$\chi_d = \frac{\omega}{4\pi\mu_1}\int_{-\infty}^{\infty} H_0^{(1)}(\omega pr)\frac{e^{-i\omega\xi_1|z|}}{-2i\xi_1}pdp. \tag{6.59}$$

Here, let us consider a case of ξ_1 becomes imaginary. As χ_d is physically meaningful (not diverging) for $p \longrightarrow \infty$, we define the sign as

$$\xi_1 = \begin{cases} \sqrt{\beta_1^{-2} - p^2} & |p| \le 1/\beta_1, \\ \sqrt{p^2 - \beta_1^{-2}}i & |p| > 1/\beta_1. \end{cases} \tag{6.60}$$

Potentials χ_r and χ_t for reflected and transmitted waves are analogously given by:

$$\chi_r = \frac{\omega}{4\pi\mu_1}\int_{-\infty}^{\infty} R_{12}(p)H_0^{(1)}(\omega pr)\frac{e^{i\omega\xi_1|z+2h|}}{-2i\xi_1}pdp, \tag{6.61}$$

$$\chi_t = \frac{\omega}{4\pi\mu_1}\int_{-\infty}^{\infty} T_{12}(p)H_0^{(1)}(\omega pr)\frac{e^{i\omega(\xi_1 h - \xi_2(z+h))}}{-2i\xi_1}pdp. \tag{6.62}$$

It should be noted that the reflection potential χ_r contains the contributions of both the reflected and head waves.

This integral is numerically evaluated in Figure 6.16. [note 7)]. The direct wave is impulsive, showing that it propagates without changing its shape. The head wave is clearly visible from around 60 km, and it is also evident that it is predominantly long-period. The reflected waves are pulse-like at stations close to the epicenter (up to about 20 km), but when it exceeds the critical angle (wide-angle reflection), the reflected waves gradually shift in phase.

The numerical integration results show that, indeed, this integral (Weyl's table expression) seems to be correct. To grasp this integral roughly, let us consider its approximate behavior. Here we will consider direct-directed wave as the simplest case.

First, assuming that the propagation distance is sufficiently large compared to the wavelength, the Hankel function is approximated by

$$H_0^{(1)}(z) \sim \sqrt{\frac{2}{\pi z}} e^{i(z-\pi/4)}. \tag{6.63}$$

Then, χ_d can be approximated by

$$\chi_d \sim \frac{1}{4\pi\mu_1}\sqrt{\frac{2\omega}{\pi r}} e^{-i\pi/4} \int_{-\infty}^{\infty} \frac{e^{i\omega(pr-\xi_1|z|)}}{-2i\xi_1}\sqrt{p}dp. \tag{6.64}$$

Here we consider a case for z=20 km, r = 30 km, f = 2π5 [Hz], and β = 3 km/s, Figure 6.17 plot the integrand

$$\frac{e^{i\omega(pr-\xi_1|z|)}}{-2i\xi_1}\sqrt{p}. \tag{6.65}$$

The figure shows the oscillatory shape in most locations, but the oscillation stops near $p\beta_1 = 0.8$. When integrated, the contribution near this point becomes large.

Let us now evaluate the integral using stationary phase method. Because the part of the gentle oscillation shows a location where the phase change is small,

$$\frac{d\omega(pr-\xi_1|z|)}{dp} = 0. \tag{6.66}$$

Then,

$$\frac{d(pr-\xi_1|z|)}{dp} = r - |z|\frac{d\xi_1}{dp} = r - \frac{|z|p}{\xi_1} = 0. \tag{6.67}$$

Therefore, the contribution of the integral near p (called the stationary point) which satisfy

$$p_0 = \sqrt{\frac{r^2}{\beta_1^2 d^2}} \tag{6.68}$$

becomes large, where d is the distance $\sqrt{r^2+z^2}$.

Although the calculations are a little complicated [note 8)], the integrand can be evaluated by Tayler expansion up to the second order. Because the first-order term disappears from the

[note 7)] ξ_1 has a singularity. In order to avoid the singularity in the numerical integration, we gave a very small imaginary part to the elastic constants. This physically corresponds to giving a weak damping

[note 8)] This subsection plant to explain stationary phase method. The following is a simple calculation policy, but since the calculations are complicated. You can skip over the evaluations below.

condition to be the stationary point, we can evaluate the correpsonding phase up to the second order as

$$\omega(pr - \xi_1|z|) = \omega\left(\frac{d}{\beta_1} - \frac{d^3\beta_1}{|z|^2}\frac{(p-p_0)^2}{2}\right). \tag{6.69}$$

With an assumption that ξ_1 and p are small enough near the stationary point, the inegrand χ_d can be evaluated up to the second order terms of the Tayler expansion as

$$\chi_d \sim \frac{1}{4\pi\mu_1}\sqrt{\frac{2\omega}{\pi r}}e^{-i\pi/4}\int_{-\infty}^{\infty}\frac{e^{i\omega\left(\frac{d}{\beta_1}-\frac{d^3\beta_1}{|z|^2}\frac{(p-p_0)^2}{2}\right)}}{-2i\frac{|z|}{d\beta_1}}\sqrt{p_0}dp, \tag{6.70}$$

where

$$\xi_1|_{p=p_0} = \frac{|z|}{d\beta_1}. \tag{6.71}$$

This integral can be calculated by using the Fresnel integral

$$\int_{-\infty}^{\infty} e^{-ia^2x^2}dx = \frac{1}{|a|}\sqrt{\pi}e^{-i\pi/4}. \tag{6.72}$$

Although the calculation is complicated, the potential χ_d can be calculated as

$$\chi_d \sim \frac{1}{4\pi\mu_1}\sqrt{\frac{2\omega}{\pi r}}e^{i\left(\omega\frac{d}{\beta_1}+\frac{\pi}{4}\right)}\frac{d\beta_1\sqrt{p_0}}{2|z|}\int_{-\infty}^{\infty}e^{-i\omega\left(\frac{d^3\beta_1}{2|z|^2}p^2\right)}dp \tag{6.73}$$

$$= \frac{1}{4\pi\mu_1}\sqrt{\frac{2\omega}{\pi r}}e^{i\left(\omega\frac{d}{\beta_1}+\frac{\pi}{4}\right)}\frac{d\beta_1\sqrt{p_0}}{2|z|}\int_{-\infty}^{\infty}e^{-i\omega\left(\frac{d^3\beta_1}{2|z|^2}p^2\right)}dp \tag{6.74}$$

$$= \frac{1}{4\pi\mu_1}\sqrt{\frac{2\omega}{\pi r}}e^{i\left(\omega\frac{d}{\beta_1}\right)}\frac{\sqrt{r\pi}}{2d\sqrt{\omega}} \tag{6.75}$$

$$= \frac{1}{4\pi\mu_1 d}e^{i\omega\frac{d}{\beta_1}}. \tag{6.76}$$

For an external force

$$H(t)\nabla\times(0,0,\delta(\boldsymbol{x})), \tag{6.77}$$

we can evaluate displacement A_d from the potential χ_d as

$$A_d = \frac{1}{4\pi\mu_1\beta_1 d}e^{i\omega\frac{d}{\beta_1}}, \tag{6.78}$$

which is identical to the exact solution by chance.

Next, let's consider reflected and head waves (χ_r and χ_t). The reflected wave is similar to the direct wave, with a larger contribution from the stationary phase method. Next, let's consider the envelope. You can see that the shape of the envelope changes dramatically at around $p\beta_2 = 1$. This is because the reflection coefficient changes significantly at around the critical angle. At the point, the condition of stationary phase approximation, which is required to apply the stationary phase method, does not hold. Therefore, even when oscillating rapidly outside the stationary point, the integral contribution near $p\beta_1$ does not cancel each other out. This contribution corresponds to the head wave.

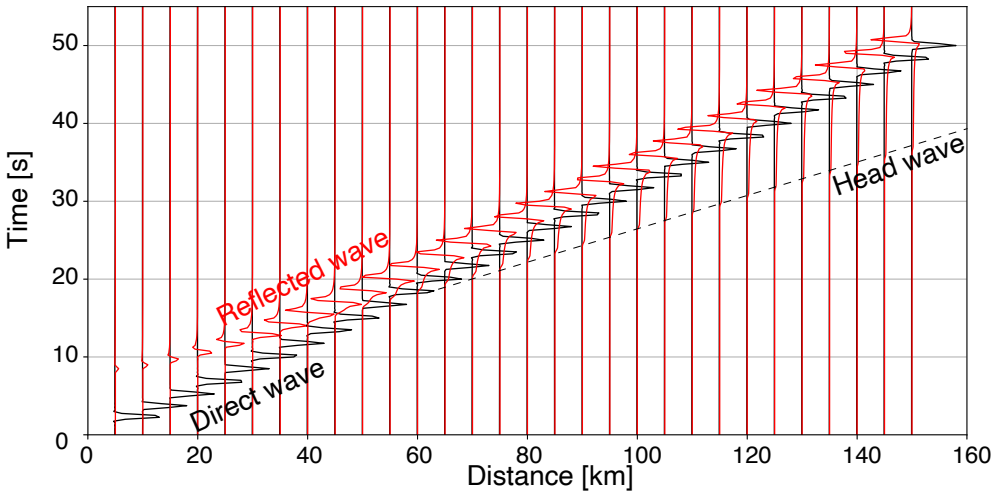

Figure 6.16: An example of numerical evaluation of the integrated for $\beta_1 = 3$ [km/s], $\beta_2 = 5$ km/s and $\rho_1 = \rho_2$. The hypocenter is located at $z = 10$ km and the observed station is located at $z = 15$ km.

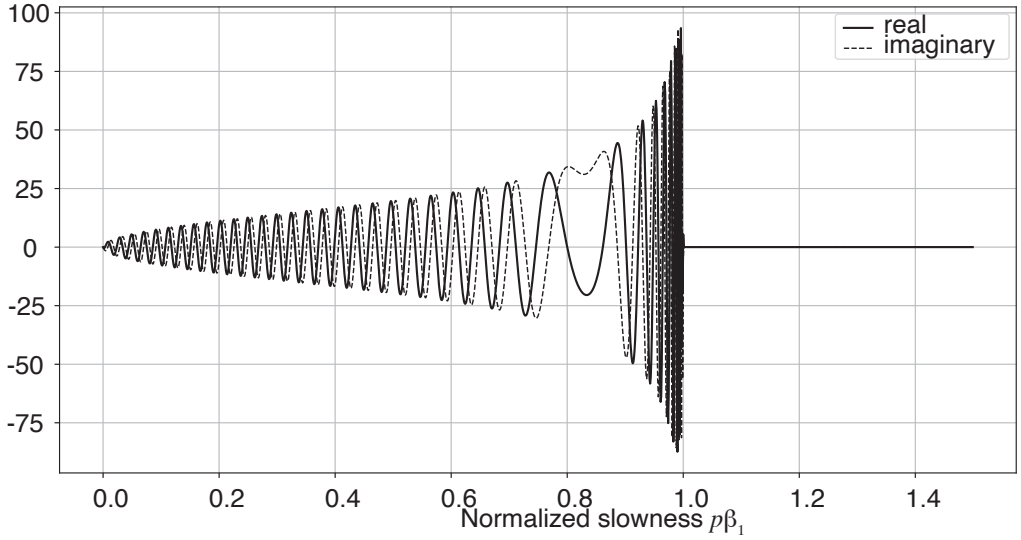

Figure 6.17: The integrand of the direct wave for z=20 km, $r = 30$ km, $f = 2\pi 5$ [Hz], $\beta = 3$ km/s. This figure shows rapid oscillations.

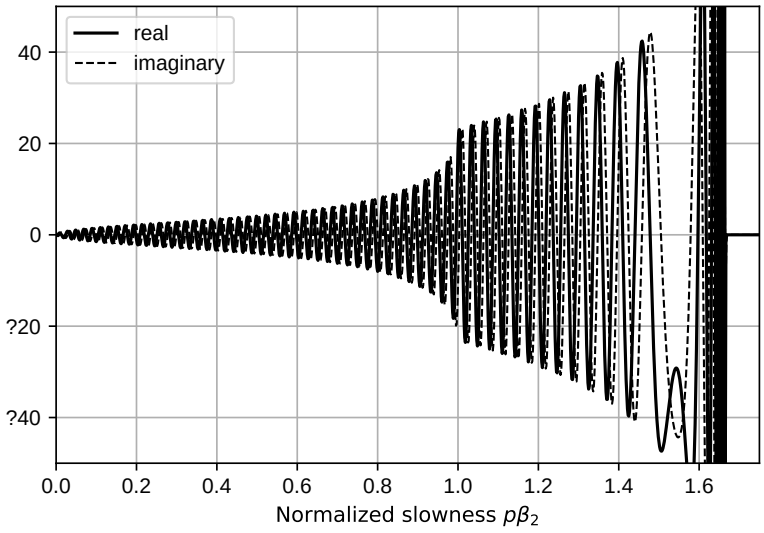

Figure 6.18: The integrand of the reflection wave and the head wave for z=20 km, $r = 30$ km, $f = 2\pi 5$ [Hz] and $\beta = 3$ km/s. This figure shows rapid oscillations.

6.4.6 An example of actual records

Figure 6.19 shows a record section when an earthquake with Mw 6.2 at Tottori prefecture on Oct. 21st 2016. The figure shows the first arrivals of Pg (direct wave, which propagates in the crust) up to an epicentral distance of about 170 km. Farther than the distance, the first arrivals are Pn wave arrivals (head wave for Moho discontinuity). The dominant frequency of the Pn wave is longer than the direct wave (Pg wave). In contrast, reflection phases (PmP) exhibit complex wave propagations. The complexity originated from scattering owing to lateral heterogeneities in the crust. At higher frequencies, the travel times of the first arrivals give us robust information because they are not disturbed by the scattering.

The apparent slopes of the Pg and Pn arrivals indicate that $\beta_1 \approx 6$ km/s and $\beta_2 \approx 8$ km/s, respectively. The crossover distance x_d between the Pg and Pn arrivals is given analytically by $x_d = 2h\sqrt{(\beta_1 + \beta_2)/(\beta_2 - \beta_2)}$. Using the observed intersection at roughly 170 km, we can estimate the crustal thickness h to be approximately 30 km. Although this estimation is clearly an oversimplification, a rough calculation like this gives an intuitive grasp of the structural properties. For modeling realistic situations with continuously varying profiles, the ray theory frameworks introduced in the next chapter are much more practical.

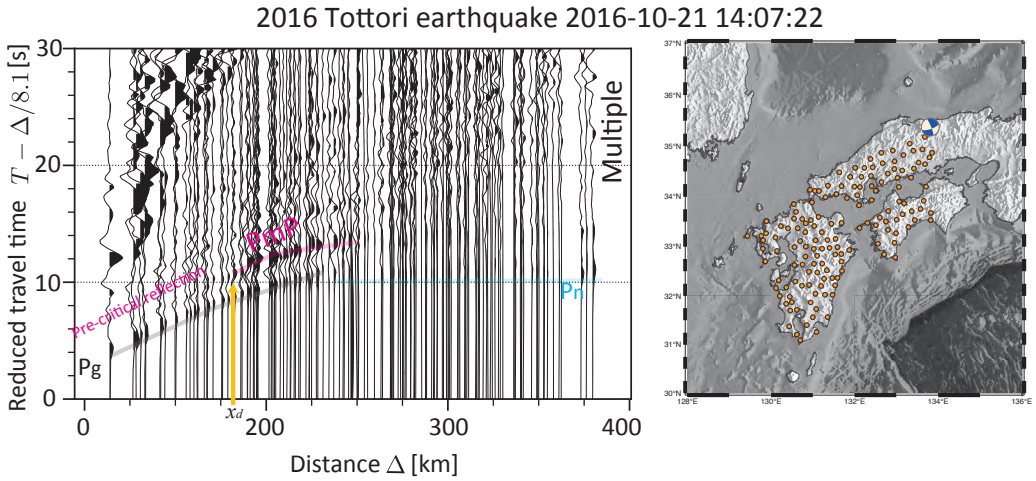

Figure 6.19: Seismograms recorded by Hi-net station against the epicentral distances when an earthquake with Mw 6.2 at Tottori prefecture on Oct. 21st in 2016. Although the first arrivals are easy to pick, the later phases show complex propagation properties. The complex features originated from lateral heterogeneities in the crust, although the lateral heterogeneities in the Chugoku region are weakest in Japan islands

Problem 6.2

The website demonstrates SH-wave propagation in a two-layer medium (2-D). Based on the seismograms, we can estimate (1) the S-wave ratio between the 1st layer and the 2nd layers and (2) the density ratio between the 1st layer and the 2nd layers.

1. Using the whole wave field (depth section in the upper panel), estimate the S-wave ratio between the layer and the density ratio.

2. Using only surface records (seismograms shown in the lower panel) estimate the S-wave ratio between the layer and the density ratio.

To derive an approximation around the critical angle, we can use the expansion detailed in Section 6.4.4 for head waves. Because the travel-time difference $r - T/V$ is smaller, a lower-frequency assumption is necessary, restricting the applicability of the plane wave composition method. Actually, near the antipode of an earthquake, the amplitude of seismic waves becomes exceptionally large due to the focusing of seismic rays. This phenomenon corresponds mathematically to a caustic. This will be explained more thoroughly in the subsequent chapter.
The website demonstrates SH-wave propagation in a two-layer medium (2-D) without the ground (free surface).

1. Run this demo and compare the amplitude of the reflected wave with the results of the reflection coefficient. Pay particular attention to the sign.

2. Discuss the relationship between the head wave and the wide angle reflected wave, which leads near the critical angle.

§6.5 Inhomogeneous wave: Love wave and Scholte wave

In the case of a semi-infinite medium, only a Rayleigh wave can exist as an inhomogeneous wave; what about the two-layer case? Let us consider a scenario where a layer of thickness h is welded to a semi-infinite medium below it (Figure 6.20). An inhomogeneous wave can exist because the wave energy is trapped within the upper, low-velocity layer. First, for the SH-wave case, we will explore a wave known as the Love wave.[3] Next, for a situation where the first layer is fluid and the second layer is solid, we encounter the Scholte wave.[7] We will discuss both types of waves in this section.

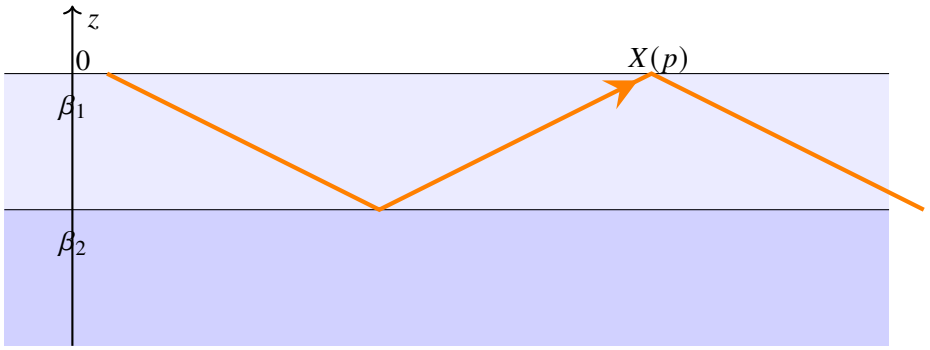

Figure 6.20:

6.5.1 Love wave

First, let us consider how the Love wave propagates (Figure6.21). ∘ in the figure shows a marker for the ground displacement. You can see in the figure how the ground is deformed horizontally. Move the cursor over the figure and press the s key on the keyboard; the Love wave starts to propagate to the right. The circle moving in the font of the page is shown in red and the circle moving in the back of the page is shown in light blue.

Love waves occur when a soft layer overlies a hard layer. For example, a soft crust overlying a stiff mantle. In this figure, circles are placed every 10 km along the vertical axis (depth) and every 6.25 km along the horizontal axis (horizontal). The fourth ∘ in the depth

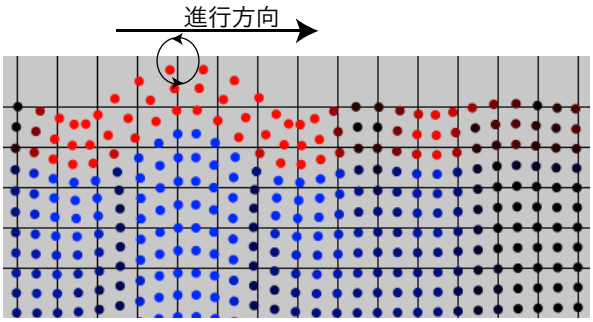

Figure 6.21: A snapshot of a demonstration of Love wave propagation. Sea the following web application: https://www.eri.u-tokyo.ac.jp/people/knishida/Seismology/Love_wave.html. Play the application for the understandings.

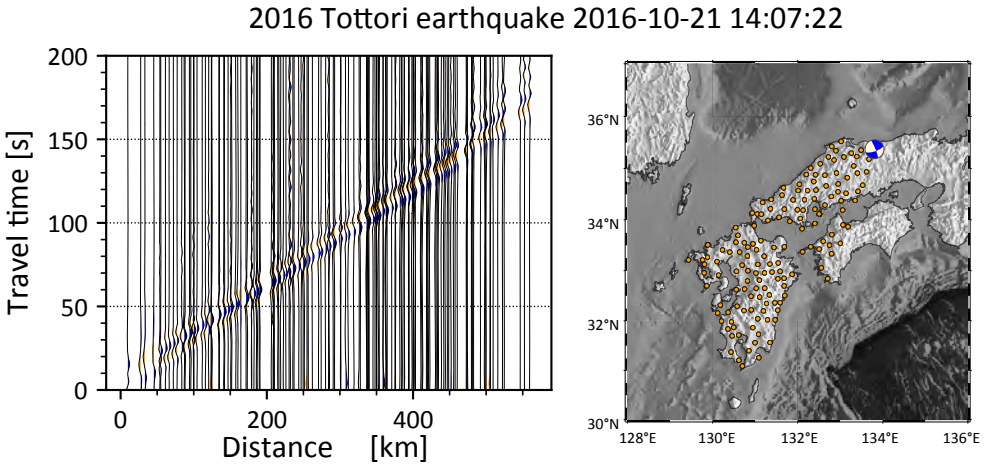

Figure 6.22: Left panel: Example of waveform recorded during the Mj 6.2 earthquake that occurred at a depth of 10 km on October 21, 2016 in Tottori, Japan. The transverse components of Hi-net data are plotted after correcting for the instrumental responses and applying a bandpass filter of 0.02-0.1 Hz. It shows the propagation of Love waves with dispersion. Right panel: The mechanism of the earthquake and the station distribution used in the analysis. Roughly speaking, we chose the stations where the polarities of the Love wave are expected to be the same.

direction is at the boundary between the crust and the mantle (the Moho discontinuity). You can see how the waves are efficiently propagating horizontally through the crust.

You can see how the shape of the wave has changed compared to the beginning of the wave and its propagation. The red areas extend both horizontally and vertically. On the other hand, the green part is concentrated near the surface. You can see the delayed propagation of the green part. The speed of wave propagation changes depending on the wavelength and the shape of the wave changes. This phenomenon is called dispersion. In this case, waves with longer wavelengths travel faster, and waves with shorter wavelengths travel slower. This is because long waves are strongly affected by the stiff layer (deep layer: mantle).

Next, let us look at the observed waveforms. Figure6.22 shows the waveforms recorded during the 2016 Tottori earthquake. The wave propagates with dispersion (Love wave propagates with a shape change; see Figure6.25 for details).

Standing wave

While the previous subsection described the properties of the Love wave qualitatively, physically it can be understood as a standing wave whose energy is trapped in the first layer. Let us consider the extreme case where β_2 approaches infinity (meaning the bottom is a rigid wall). This is analogous to the oscillation of an air column. Assuming the wave propagates vertically, the

stress is zero at the free surface, meaning $s_y \propto \cos(kz - \omega t)$. At depth h, the phase shifts by π due to the fixed boundary. However, at the ground surface, the phase does not shift upon reflection because it is an open boundary. Therefore, considering that the phase difference with the wave reflected there is 2π,

$$k_z \cdot 0 - \omega t = k(2h) - \omega t - \pi - 2n\pi. \tag{6.79}$$

Because $\lambda = 2\pi/k$ and $k_z = k$ in vertical incident case, we obtain the following relation for $n = 0, 1, 2...$:

$$\lambda = \frac{2h}{n + \frac{1}{2}}. \tag{6.80}$$

The wave front reflects off the surface, reflects off the rigid wall, and must shift in phase by 2π before returning to the surface, hence the $n + 1/2$[note 9)]. Let us make a similar estimate for the Love wave below.

Since we are now considering a situation where energy is trapped within the first layer, we assume that the incident wave is totally reflected beyond the critical angle (see Section 6.2.1). The phase of the reflection at the boundary between the first and second layers is shifted by:

$$argR_{12} = -2\tan^{-1}\frac{\mu_2 i p_{2z}}{\mu_1 p_{1z}} = -2\tan^{-1}\frac{\mu_2\sqrt{p^2 - \beta_2^{-2}}}{\mu_1\sqrt{\beta_1^{-2} - p^2}}. \tag{6.81}$$

The difference from the air column case is that once the wave is reflected, it returns to the surface point X (Figure6.20). This means that the phase of the incident SH wave at $(X, 0)$ must be the same as that of the reflected wave. The two-way travel time T can be written by

$$T = \frac{\sqrt{X^2 + (2h)^2}}{\beta_1}. \tag{6.82}$$

During the propagation, the incident wave advances in phase by Xp. The condition requires the following relation:

$$\omega T + argR_{12} = \omega p X + 2n\pi. \tag{6.83}$$

Because

$$X = \frac{2ph}{\sqrt{\beta_1^{-2} - p^2}} \tag{6.84}$$

in summary, we obtain the following relation:

$$\tan\left[h\omega\sqrt{\beta_1^{-2} - p^2}\right] = \frac{\mu_2\sqrt{p^2 - \beta_2^{-2}}}{\mu_1\sqrt{\beta_1^{-2} - p^2}}. \tag{6.85}$$

[note 9)] As described in Chapter **??**, $T - px$ is a quantity known as the interception time τ. Similar arguments can be made using τ not only for two-layer structures but also for general layered structures.

Rearranging this, we obtain Eq. **??**, known as the characteristic equation for Love waves. While we adopted a more intuitive explanation here, the formal derivation evaluates the roots of the denominator of the total reflection coefficient (referred to as the secular equation). For further details, please consult Aki and Richards (2002). To improve the perspective of the equation, we can rewrite the relation as

$$\tan\left(\frac{h\omega}{\beta_1}\beta_1\eta_1\right) = \frac{\mu_2}{\mu_1}\frac{\sqrt{1-(\beta_1/\beta_2)^2-(\beta_1\eta_1)^2}}{\beta_1\eta_1}, \tag{6.86}$$

where we define $\eta_1 \equiv \sqrt{\beta_1^{-2} - p^2}$, and we choose $\beta_1\eta_1$ as a variable. Figure 6.23 shows the left and right sides of the equation are plotted as functions of $\beta_1\eta_1$, respectively. When the two lines cross each other, the condition is satisfied and a Love wave can exist.

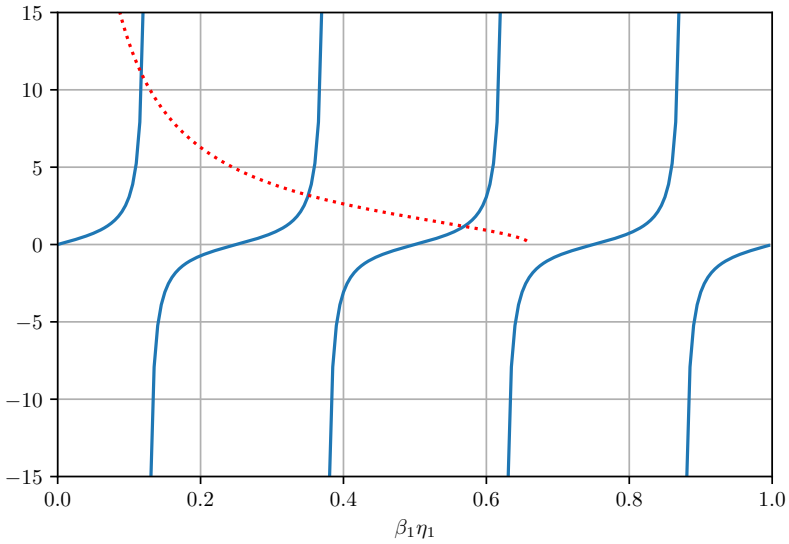

Figure 6.23: Root of the characteristic equation of a Love wave for h = 30 km, 0.2 Hz, β_1 = 3 km/s, β_2 = 4 km/s, ρ_1 = 2.5 g/cm^3 and ρ_2 = 2.8 g/cm^3.

The right side can exist if $\beta_1\eta_1$ is smaller than $\sqrt{1-(\beta_1/\beta_2)^2}$. Since the left side is tan, we know that at least one solution can exist. This solution is called the fundamental mode. In the current situation (0.2~ Hz), we can see that three solutions exist. They are called the fundamental mode (zeroth-order mode), first higher mode, and second higher mode, respectively, starting from the one with smaller $\beta_1\eta_1$ (i.e., longer wavelength).

Consider the conditions for the existence of a first higher mode. As the frequency decreases, the dashed line moves to the left. It cannot exist when the phase of tan is left of $3\pi/2$. This requires

$$\pi\frac{\beta_1}{h\omega} \leq \sqrt{1-(\beta_1/\beta_2)^2}. \tag{6.87}$$

The cut-off frequency of an nth higher mode f_n^{cut} is given by

$$f_n^{cut} = \frac{n\beta_1}{2h}\frac{1}{\sqrt{1-(\beta_1/\beta_2)^2}}. \tag{6.88}$$

Let us examine the displacement distribution as a function of depth for each mode. Figure 6.24 illustrates the depth distribution of displacement for the different modes. As shown, the energy is confined to the low-velocity layer (layer 1) and decays exponentially with depth in layer 2. Much like the oscillation of an air column, these correspond to the fundamental mode, the first-order mode, and the second-order mode, ordered by the number of nodes.

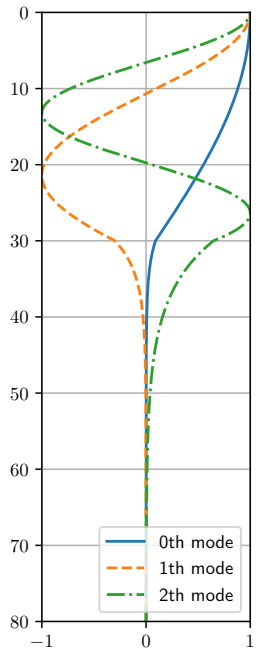

Figure 6.24: Depth distribution of Love wave amplitudes. Amplitudes of each mode are normalized at the surface.

Phase velocity and group velocity

The phase velocity (p^{-1}) of the Love wave for each frequency is plotted in Figure6.25. For each mode, the phase speed (solid line) is β_2 on the long-period side and monotonically decreases as the frequency increases, approaching β_1. The fundamental mode exists from frequency 0, while a higher-order mode has a cutoff frequency on the low-frequency side.

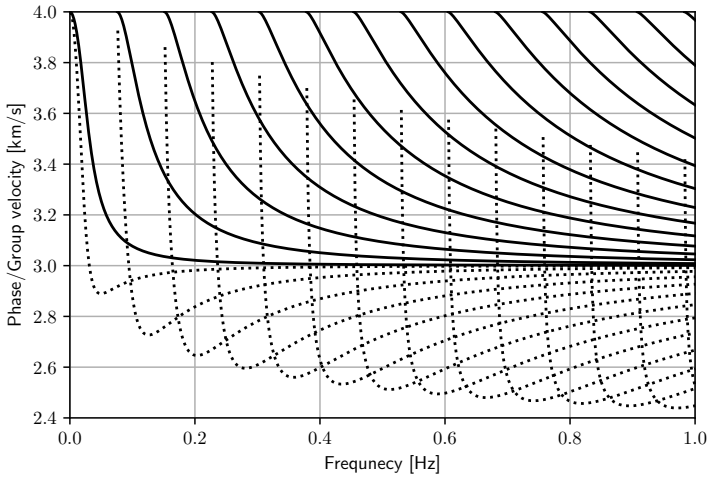

Figure 6.25: Dispersion curves for the Love wave. Phase velocity is shown as a solid line and group velocity as a dashed line. Here we assumed that $h = 30$ km, 0.2 Hz, $\beta_1 = 3$ km/s, $\beta_2 = 4$ km/s, $\rho_1 = 2.5$ g/cm^3 and $\rho_2 = 2.8$ g/cm^3.

Here is an example of observed dispersion of Love waves. Figure 6.26 shows the dispersion curve of Love waves recorded by Hi-net tiltmeters. It displays the fundamental mode alongside the first, second, and third higher modes, representing the average velocity structure beneath the Japanese Islands. A clear cutoff is visible around 4.5 km/s, indicating that the mantle's S-wave velocity is approximately 4.5 km/s. Furthermore, the phase velocity of the fundamental mode decreases at shorter periods. This happens because the crust cannot be perfectly modeled as a single homogeneous layer; the presence of shallower, slower layers reduces the phase velocity for high-frequency waves.

Surface waves have different propagation speeds at different frequencies. This phenomenon is called dispersion. Here, for simplicity, we consider the following wave propagation:

$$\int_{\omega_0-\Delta\omega}^{\omega_0+\Delta\omega} e^{i(k(\omega)x-\omega t)}\,d\omega, \tag{6.89}$$

where ω is angular frequency, $k(\omega)$ is wavenumber and x represents the location.

The Taylor expansion of $k(\omega)$ around the center frequency ω_0 leads to

$$k(\omega) \approx k_0 + \frac{dk}{d\omega}(\omega - \omega_0) + O(2). \tag{6.90}$$

If $\Delta\omega$ is enough small, we can simplify the equation as

$$\int_{\omega_0-\Delta\omega}^{\omega_0+\Delta\omega} e^{i(k(\omega)x-\omega t)}\,d\omega \approx e^{i(k_0x-\omega_0t)} \int_{-\Delta\omega}^{\Delta\omega} e^{i\omega'\left(\frac{dk}{d\omega}x-t\right)}\,d\omega' = e^{i(k_0x-\omega_0t)}\frac{2\sin\left(\frac{x}{c_g}-t\right)}{\frac{x}{c_g}-t}, \tag{6.91}$$

https://www.eri.u-tokyo.ac.jp/people/knishida/eng/seismology.html

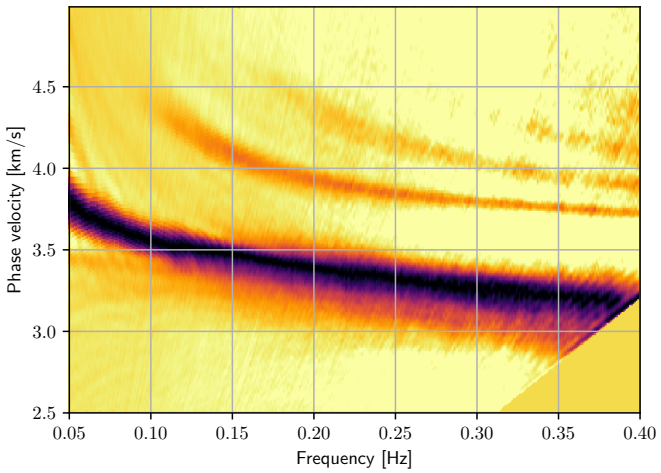

Figure 6.26: Dispersion curves of Love waves propagating through the Japanese Islands observed by Hi-net tiltmeters. See(6) for details of the analysis.

where group velocity c_g is defined by $d\omega/dk$. The phase propagates with ω_0/k_0, and the envelope (sinc function $\sin x/x$) propagates with the group velocity c_g.

The results of this numerical integration are displayed in Figure 6.27. Unlike simpler cases without dispersion, we can see that the waveform changes its shape as it propagates. Curves representing the same phase (or amplitude) propagate at the phase velocity ω/k. Conversely, the wave packet as a whole propagates at the group velocity $d\omega/dk$. By approximating the integral above as a sum of discrete frequencies, the equation for the group velocity can be derived using the sum-to-product trigonometric identities.

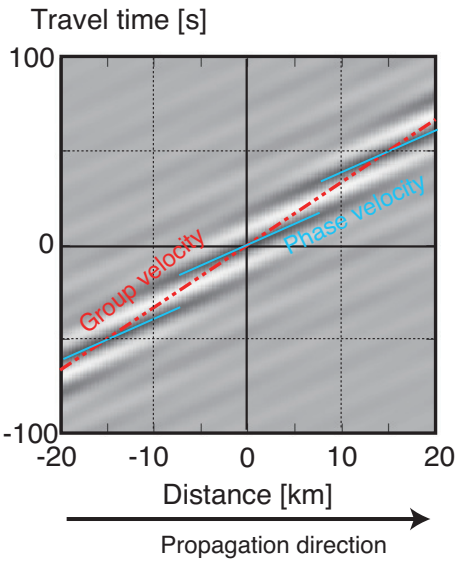

Figure 6.27: Wave Dispersion.

Let us return to Figure 6.25, where the group velocity is plotted as a dotted line. While phase velocities decrease monotonically with frequency, group velocities exhibit local minima. What happens near these minima? In those ranges, the group velocity changes very little. If we consider a narrow frequency band (e.g., of width $2\Delta\omega$) around a minimum, wave packets from different frequencies within that band travel at nearly the same velocity. Consequently, they arrive simultaneously, resulting in a large combined amplitude. This concentration of energy near a minimum in group velocity is known as the Airy phase[note 10)]. For instance, Figure 6.28 shows

[note 10)] For a more detailed treatment, see Saito (2009).

an example of the first higher mode of a Love wave. There, it is evident that the wave packets traveling at 2.7 km/s—the minimum group velocity—dominate the seismogram.

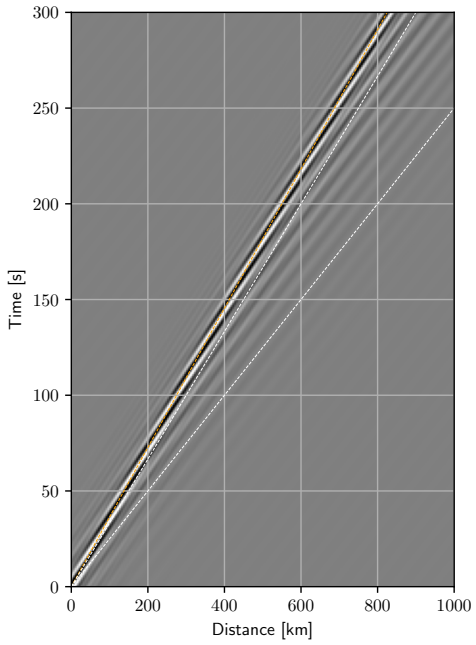

Figure 6.28: First-order higher mode of the Love wave plotted against distance and time. The white dashed lines correspond to phase speeds of 3 km/s and 4 km/s, and the orange dashed line corresponds to 2.7 km/s (the minimum value of group velocity). You can see the dominant wave packet where the group velocity takes a minimum value.

Superposition of Love modes

Finally, let us superimpose all the Love modes. As we first discussed in this section, we can see the wave with wide-angle multiple reflections (at a time shortly before the blue dotted line). The blue dotted line corresponds to the travel time $T(x) = x\beta_2/(\beta_1^2)$ and represents the travel time of the wide-angle multiple reflections. The fact that the wave is not visible at times later than this line indicates that it cannot represent a wave incident at a steep angle that would transmit to the layer below. It should be noted that the superposition of modes also reproduces head wave (red dashed line in the figure). While the reflected wave is impulsive, the head wave is bordered. This is because the head wave can be estimated by an integral of the direct waveform (see chapter 6.4.4). This is due to the contribution of higher-order modes near the cutoff frequency. The wave that is parallel to the head wave and visible 20 seconds later is the wave propagating as a head wave after once being reflected wide angle.

https://www.eri.u-tokyo.ac.jp/people/knishida/eng/seismology.html

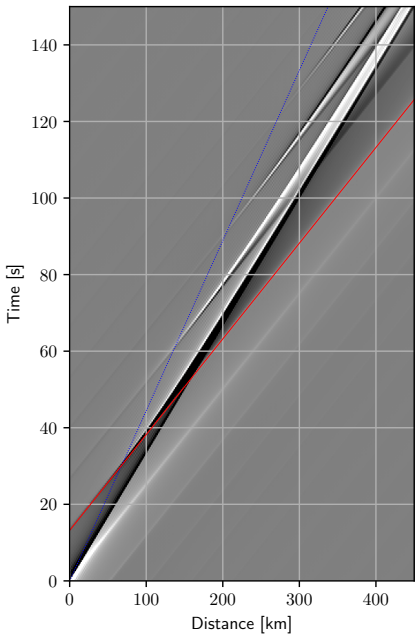

Figure 6.29: The figure shows the superposition of Love modes up to the 14th higher-order modes. The highest frequency is 1 Hz and the structure is the same as in the previous example. The blue dotted line corresponds to the travel time $T(x) = x\beta_2/(\beta_1^2)$ and represents the wide-angle multiple reflection travel time. The red line represents the travel time of the head wave.

One point to note is that we can see wave groups that are clearly physically incorrect (not satisfying the causality) before the head wave. These waves have a phase velocity of approximately 4 km/s (S-wave velocity in the second layer). This is because Love waves cannot represent waves propagating in the second layer. [note 11)]. What waves cannot be represented as a sum of modes can be interpreted physically. More strict treatment will be given in the chapter on normal mode theory.

[note 11)] Strictly speaking, it is the term expressed by the branch integral contribution. See Saito (2009) chapter 9.4

Problem 6.4

Let us evaluate the dispersive wave using the stationary phase approximation.

$$\frac{1}{\pi} Re \int_0^\infty e^{i(k(\omega)x-\omega t)} d\omega \tag{6.92}$$

Here we define the phase $\Psi = k(\omega)x/t - \omega$, we can rewrite the equation

$$\frac{1}{\pi} Re \int_0^\infty e^{it\Psi(\omega)} d\omega. \tag{6.93}$$

Because $e^{it\Psi}$ oscillates rapidly, the contribution near

$$\left.\frac{d\Psi(\omega)}{d\omega}\right|_{\omega=\omega_0} = 0 \tag{6.94}$$

became dominant. In this case,

1. Evaluate the integral by expanding ω to the second order term of ω_0.
2. Consider the group velocity.
3. Also, consider the case where the group velocity takes extreme values.

§6.6 Bibliography

[1] K. Aki and P.G. Richards. *Quantitative Seismology*. Univ Science Books, 2nd edition, 2009.

[2] Craig M Jarchow and George A Thompson. The nature of the mohorovicic discontinuity. *Annual Reviews of Earth and Planetary Sciences*, 17:475–506, 1989.

[3] A E H Love. *Some Problems of Geodynamics*. Cambridge University Press. Reprinted in 2015 by Dover Publications, Cambridge, England, December 1911.

[4] Saito Masanori. *Seismic Wave Theory*. University of Tokyo Press, 2009.

[5] Andrija Mohorovičić. Earthquake of 8 october 1909. *Geofizika*, 9(1):3–55, 1992.

[6] K Nishida, H Kawakatsu, and K Obara. Three-dimensional crustal S wave velocity structure in japan using microseismic data recorded by hi-net tiltmeters. *J. Geophys. Res.*, 113(B10):B10302, October 2008.

[7] J G J Scholte. RAYLEIGH WAVES. IN ISOTROPIC AND ANISOTROPIC. ELASTIC MEDIA. *Meded. en Verhand. KNMI*, 72:9–43, 1958.

[8] P.M. Shearer. *Introduction to Seismology*. Cambridge University Press, third edition, 2009.
https://www.eri.u-tokyo.ac.jp/people/knishida/eng/seismology.html

[9] S. Stein and M. Wysession. *An Introduction to Seismology, Earthquakes, and Earth Structure*. Wiley, 1991.

Ray theory

Chapter 7

The previous chapter explained SH wave propagation in a two-layer medium. Although it gives us insight into the seismic wave propagation of a realistic Earth, the real Earth's structure is more complex. To address seismic wave propagation for a more realistic Earth model, the next is the multi-layer approximation of the Earth's structure.

A typical dominant frequency of teleseismic events recorded by seismometers is on the order of 1 Hz. In this case, the spatial scale of the Earth's structure is approximated to be sufficiently longer than the wavelength of the seismic wave [note 1)]. Figure 7.1 shows observed seismograms when the 2015 earthquake off the western coast of the Ogasawara Islands (the focal depth is deeper than 660 km) on the global scale. This figure exhibits many phases, which are classified in terms of the ray path and wave type. To interpret the seismic wave propagations, an approximation of geometrical optics is feasible. Exactly speaking, although this approximation is valid only for high-frequency limits, this approach is feasible for seismic exploration of Earth's structure in many cases practically.

Figure 7.2 shows the arrival times of seismic phases visually picked from the onset times of observed seismograms, plotted against the epicentral distance. Black represents the P-wave, and red represents the S-wave. Numerous phases (classified according to the path taken and the combination of wave types) can be seen. Since the entire waveforms are too complicated to model directly, it is easier to grasp the dominant features through simplified information: arrival times. This figure also shows that the Earth's internal structure can be approximated as one-dimensional because the measured travel time is a simple function of the epicentral distance. In addition, for P waves (at an angular distance of 100 degrees and travel time of about 13 minutes), the travel times are highly scattered, which can be interpreted as a large velocity heterogeneity at the core-mantle boundary.

A theory of wave propagation based on geometrical optics is known as Ray theory. This theory has played an important role in seismology for a long time. In particular, the ray theory for a stratified medium (multi-layer medium) is a basic theory for seismic wave propagations. This chapter gives the outline of ray theory in a stratified medium for interpreting seismic wave propagations in a realistic Earth.

[note 1)] A wavenumber spectrum of Earth's heterogeneities shows that the long wavelength components are dominant (referred to as a "red spectrum").

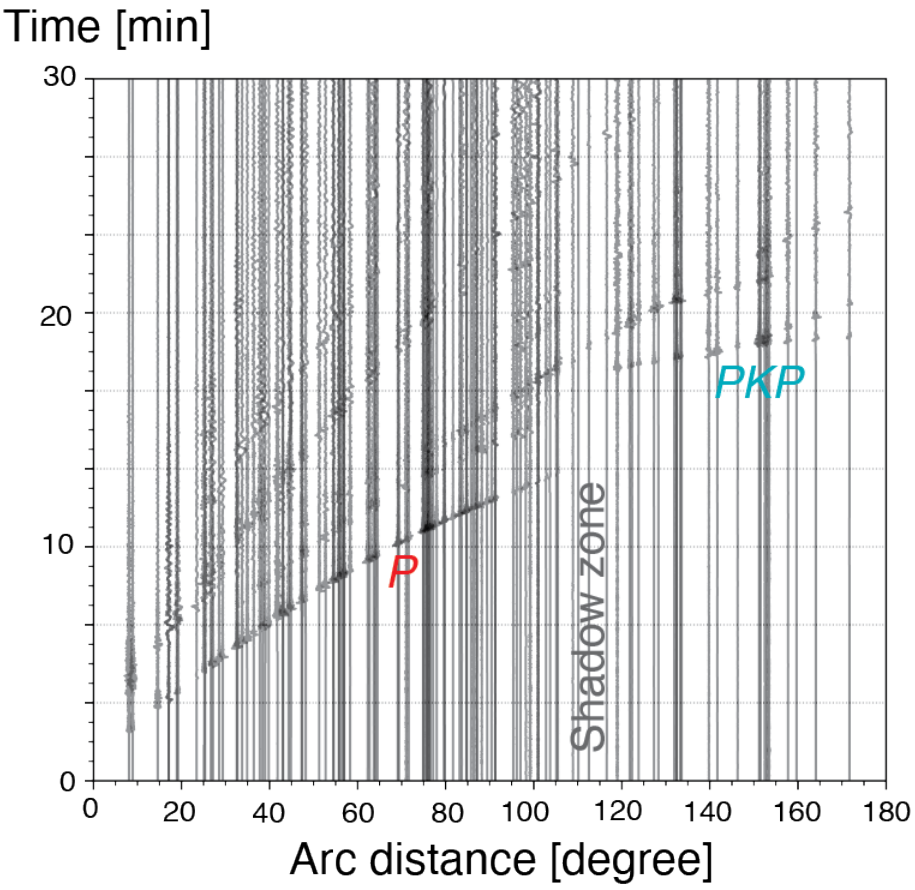

Figure 7.1: Observed records of the 2015 earthquake off the western coast of the Ogasawara Islands. The P-wave and S-wave are clear, but the waveforms are not so simple. The figure shows the shadow zone of the P-wave by the outer core, where the P-wave does not reach the surface (around the arc distance of 110 degrees).

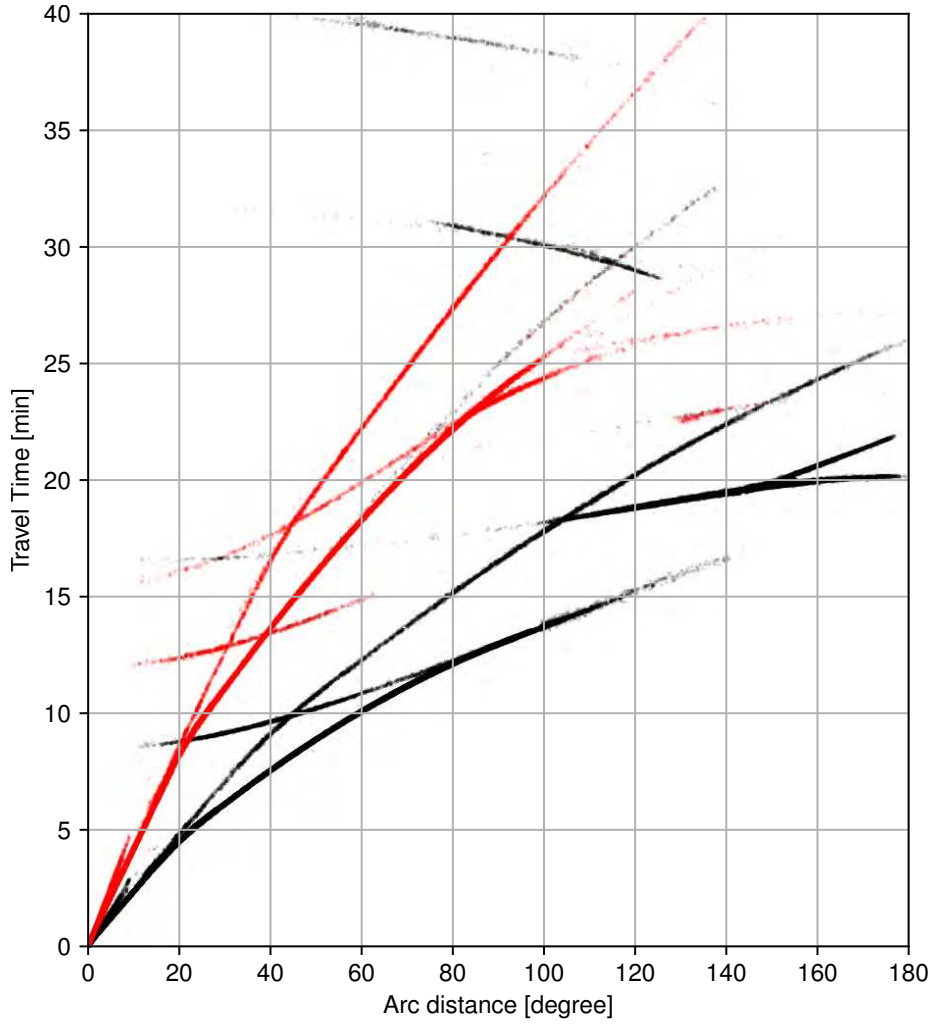

Figure 7.2: Travel-time plots of various seismic phases. Black represents P-waves, and red represents S-waves. Events shallower than 20 km that occurred in 2018 were selected. Data are from International Seismological Centre (2021), On-line Bulletin, https://doi.org/10.31905/D808B830.

§7.1 High frequency approximation

First, let us consider P-wave potential. With an assumption that typical spatial scales of physical properties (density and elastic constants) are enough longer than the wavelength of the P wave, the wave equation of P-wave can be simplified as

$$\ddot{\phi} = \alpha^2 \nabla^2 \phi. \tag{7.1}$$

Here we assume that a wave packet f propagates with the shape $\phi(\boldsymbol{x}, t) = A(\boldsymbol{x}) f(t - T(\boldsymbol{x}))$. Because the potential is represented by an isosurface (wavefront), the spatial derivative is given by the gradient as $\nabla f = -\nabla T \dot{f}$. Insertion of the relation into the wave equation yields the following equation:

$$\frac{1}{\alpha^2}\ddot{\phi} = \nabla^2 A f(t - T) - 2\nabla A \cdot \nabla T \dot{f}(t - T) + A\ddot{f}(t - T)(\nabla T)^2 - A\dot{f}(t - T)\nabla^2 T. \tag{7.2}$$

Fourier transform of both sides with respect to time is written as

$$-\frac{\omega^2}{\alpha^2} AF(\omega) = \nabla^2 AF(\omega) - 2i\omega \nabla A \cdot \nabla T F(\omega) - A\omega^2 F(\omega)(\nabla T)^2 - i\omega AF(\omega)\nabla^2 T. \tag{7.3}$$

Assuming the angular frequency ω is sufficiently large, the real part of the equation yields the Eikonal equation:

$$|\nabla T|^2 = \frac{1}{\alpha^2}. \tag{7.4}$$

Here we define slowness vector $\boldsymbol{p}$ by ∇T.

On the other hand, the imaginary part in the high-frequency limit leads to the transport equation.

$$2\nabla A \cdot \nabla T + A\nabla^2 T = 0. \tag{7.5}$$

This equation is called a transport equation. This equation can be rewritten as $\nabla \cdot (A^2 \boldsymbol{p}) = 0$, which represents the conservation of energy. By solving the Eikonal equation, we get travel time T. Then we can estimate A from the transport equation with the estimated T.

§7.2 Ray tracing: Hamiltonian formalism

Based on ray theory, integration of the Eikonal equation gives travel time T. Ray tracing is one of the solving methods. Ray can be defined by successions of slowness vectors as already introduced. The wavefront expands with a speed of the seismic velocity in a direction of slowness vector. Below, the physical meaning of ray tracing is explained: ray tracing can be interpreted as tracing the motion of a particle beneath a potential. This physical system can be described more simply by using a generating parameter σ instead of time, as explained later. Although the discussion is based on analytical mechanics, the formulation is highly helpful for physical interpretation.

https://www.eri.u-tokyo.ac.jp/people/knishida/eng/seismology.html

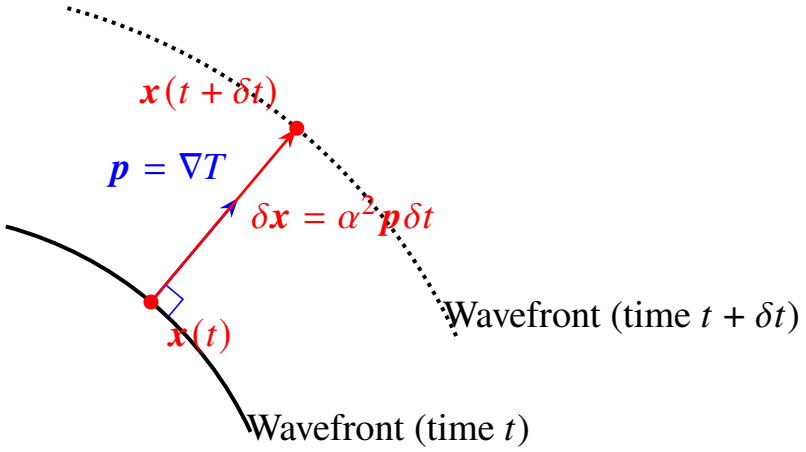

Figure 7.3: Schematic diagram of ray tracing.

7.2.1 Ray tracing

Let us consider a wavefront $T(\boldsymbol{x}) = t$ at time t (Figure 7.3). We trace the path of a ray from a point $\boldsymbol{x}(t)$ on this wavefront to the wavefront at a short time δt later, $T(\boldsymbol{x}) = t + \delta t$. In an isotropic medium, the ray travels perpendicular to the wavefront, along the slowness vector $\boldsymbol{p}$. Therefore, we have

$$\boldsymbol{x}(t + \delta t) = \boldsymbol{x}(t) + \alpha(\boldsymbol{x}(t))^2 \boldsymbol{p}(\boldsymbol{x}(t))\delta t. \tag{7.6}$$

The slowness vector advances slightly to time $t + \delta t$ and changes its propagation direction. Since Snell's law holds along the ray, the change over an infinitesimal time can be written as

$$\boldsymbol{p}(t + \delta t) = \boldsymbol{p}(t) - \frac{\nabla \alpha}{\alpha} \delta t. \tag{7.7}$$

Summarizing these, we obtain a set of ordinary differential equations with respect to t:

$$\frac{d\boldsymbol{x}}{dt} = \alpha^2 \boldsymbol{p} \tag{7.8}$$

$$\frac{d\boldsymbol{p}}{dt} = -\frac{\nabla \alpha}{\alpha}. \tag{7.9}$$

If the slowness vector $\boldsymbol{p}$ is regarded as a momentum, this can be seen as describing a particle moving under a potential. However, a problem arises here. As seen from the equations, the coefficient of $\boldsymbol{p}$ for $\dot{\boldsymbol{x}}$ (which corresponds to mass) is α^{-2}, meaning it depends on the location. When viewed as a dynamical system, the mass changes with position (and thus with t). Therefore, we want to introduce a parameter equivalent to time such that the mass becomes a constant (time-invariant). We introduce the generating parameter σ as such a parameter.

7.2.2 What is a generating parameter?

This dynamical system can be described more naturally by using a generating parameter σ instead of time. We define a parameter σ (the generating parameter), which determines the particle's position corresponding to time, as a function of t. If we can define σ such that

$$\frac{d\boldsymbol{x}}{d\sigma} = \boldsymbol{p}, \tag{7.10}$$

the mass can be considered constant. That is, we consider

$$\frac{d\sigma}{dt} = \alpha^2 \tag{7.11}$$

note 2). By introducing the generating parameter σ, ray tracing can be associated with the problem of tracing the motion of a particle moving under a potential $-\frac{1}{2}\alpha^{-2}$.

Hereafter, unless otherwise stated, $\dot{\boldsymbol{x}}$ means $\frac{d\boldsymbol{x}}{d\sigma}$. Given deductively, the Lagrangian L of the system is considered as

$$L(\boldsymbol{x}, \dot{\boldsymbol{x}}) = \frac{1}{2}\left[\dot{\boldsymbol{x}} \cdot \dot{\boldsymbol{x}} + \alpha^{-2}(\boldsymbol{x})\right], \tag{7.12}$$

which satisfies $\boldsymbol{p} = \partial_{\dot{\boldsymbol{x}}} L$ (definition of generalized momentum)note 3).

The Eikonal equation can be interpreted as a condition of the constraint of this system. The Eikonal equation can be rewritten as $H(\boldsymbol{x}, \boldsymbol{p}) = 0$ using Hamiltonian. Hamilton equations are written by

$$\frac{d\boldsymbol{x}}{d\sigma} = \frac{\partial H}{\partial \boldsymbol{p}} = \boldsymbol{p} \tag{7.13}$$

$$\frac{d\boldsymbol{p}}{d\sigma} = -\frac{\partial H}{\partial \boldsymbol{x}} = \frac{1}{2}\nabla\alpha^{-2}. \tag{7.14}$$

These equations can be interpreted as

1. Let us consider a problem of tracing a particle motion under a potential $-\frac{1}{2}\alpha^{-2}$.
2. The initial condition is given by $\boldsymbol{p}$. Note that $\boldsymbol{p}$ is constrained by the equation $H(\boldsymbol{p}, \boldsymbol{x}) = 0$. (This condition is equivalent that the absolute value of $\boldsymbol{p}$ at the initial injection point is $1/\alpha$).
3. According to Hamilton equations, $dH = \partial_{\boldsymbol{x}} H d\boldsymbol{x} + \partial_{\boldsymbol{p}} H d\boldsymbol{p} = 0$. This means that at any point along the ray path, $H = 0$ if the initial value $H = 0$ at the injection point.
4. The particle motion can be traced by integrating the Hamilton equations. Physically, σ represents time.

note 2) In principle, it is possible to construct the dynamical system with s or travel time T as the parameter determining position, but we proceed with σ in this chapter because it yields the clearest equations. Although the generating parameter is less intuitive due to its analytical mechanics abstraction, it has the advantage of making the underlying theory clearer.

note 3) For details, read chapter 15 of Dahlen and Tromp [1998](4)

The two first-order differential equations can be simplified as a single equation:

$$\frac{d^2\boldsymbol{x}}{d\sigma^2} - \frac{1}{2}\nabla\alpha^{-2} = \boldsymbol{0}. \tag{7.15}$$

This equation represents the equation of motion. The corresponding Lagrangian can be defined as,

$$L = \frac{1}{2}\left[\dot{\boldsymbol{x}}\cdot\dot{\boldsymbol{x}} + \alpha^{-2}(\boldsymbol{x})\right], \tag{7.16}$$

which satisfy the relation of $\boldsymbol{p} = \partial_{\dot{\boldsymbol{x}}} L$ (definition of generalized momentum)[note 4].

Here we consider a stratified medium. In this case, because α depends only on depth z[note 5], the x component of equation **??** leads to:

$$\frac{dp_x}{d\sigma} = 0 \tag{7.17}$$

showing that p_x becomes a conserved quantity. p_x is also known as the ray parameter.

It should be emphasized here that care must be taken when handling discontinuous interfaces in the seismic velocity structure. The fact that the seismic velocity is discontinuous means that the high-frequency approximation does not hold when crossing the discontinuity. Therefore, a large error occurs if the Hamilton formalism is used for integration across a discontinuity. Consequently, when a ray crosses a discontinuity, it is necessary to consider refraction (bending the slowness vector $\boldsymbol{p}$) that satisfies Snell's law at the interface.

7.2.3 †Ray tracing in anisotropic media

Although details are omitted, ray tracing in anisotropic media becomes more complicated. The difficulty arises because the direction of the ray path is not perpendicular to the wavefront. Rays travel in the direction of the energy flux, but in anisotropic media, the direction of wave propagation (perpendicular to the wavefront) does not align with the direction of the energy flux. $\frac{d\boldsymbol{x}}{dt}$ corresponds to the energy flux, i.e., group velocity, which is no longer orthogonal to the wavefront. For details, refer to Červený's textbook.(9)

7.2.4 For spherical Earth

When we consider global seismic wave propagation, a spherical coordinate system is more convenient. With an assumption that P-wave velocity $\alpha(r)$ depend only on radius r (spherical symmetry), the Lagrangian L is written by,

$$L = \frac{1}{2}(\dot{r}^2 + (r\dot{\theta})^2 + (r\sin\theta\dot{\phi})^2 - \alpha(r)^{-2}). \tag{7.18}$$

[note 4] We often use symbol $\boldsymbol{p}$ for slowness vector, because the slowness vector can be interpreted as generalized momentum based on ray theory. When we use time as a variable for determining the location, the generalized momentum is not proportional to the particle velocity. On the other hand, generalized momentum using generating parameter is proportional to the particle velocity. Generating parameter gives us a more simple physical analogy.

[note 5] In the context of analytical mechanics, such x is called a cyclic coordinate.

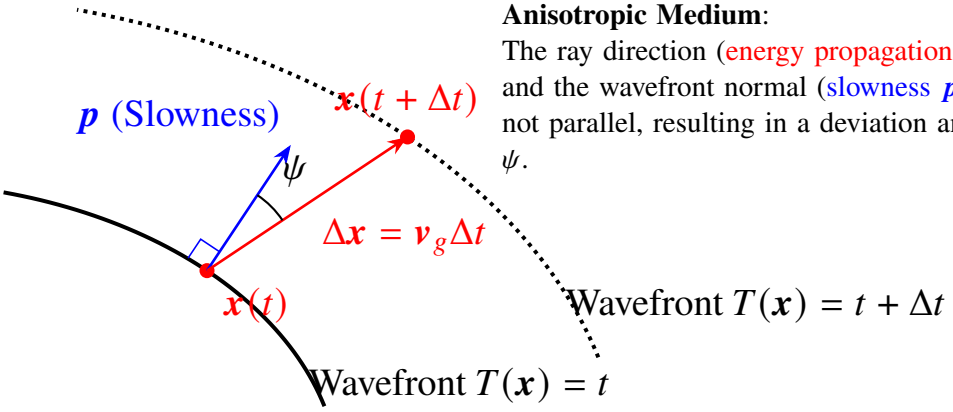

Anisotropic Medium:
The ray direction (energy propagation $\boldsymbol{v}_g$) and the wavefront normal (slowness $\boldsymbol{p}$) are not parallel, resulting in a deviation angle ψ.

Figure 7.4: Schematic diagram of ray tracing in anisotropic media.

By the appropriate choice of the spherical coordinate, we can drop ϕ. Angular distance Δ along the θ direction can describe the propagation. For a spherical structure, the slowness vector $\boldsymbol{p} = (p_r, p_\theta, p_\phi)$ in the spherical coordinate system is given by

$$\begin{aligned} p_r &= \frac{\partial L}{\partial \dot{r}} = \frac{dr}{d\sigma} \\ p_\theta &= \frac{\partial L}{\partial \dot{\theta}} = r^2 \frac{d\theta}{d\sigma} \\ p_\phi &= \frac{\partial L}{\partial \dot{\phi}} = (r \sin\theta)^2 \frac{d\phi}{d\sigma}. \end{aligned} \tag{7.19}$$

Similarly, the Hamiltonian H is

$$H = \frac{1}{2}(p_r^2 + r^{-2} p_\theta^2 + (r \sin\theta)^{-2} p_\phi^2 - \alpha(r)^{-2}) \tag{7.20}$$

and the Hamilton equation can be written as

$$\begin{aligned} \frac{dr}{d\sigma} &= \frac{\partial H}{\partial p_r} = p_r, \\ \frac{d\theta}{d\sigma} &= \frac{\partial H}{\partial p_\theta} = \frac{p_\theta}{r^2}, \\ \frac{d\phi}{d\sigma} &= \frac{\partial H}{\partial p_\phi} = \frac{p_\phi}{(r \sin\theta)^2}, \end{aligned} \tag{7.21}$$

$$\begin{aligned} \frac{dp_r}{d\sigma} &= -\frac{\partial H}{\partial r} = \frac{1}{2}\frac{\partial \alpha^{-2}}{\partial r} + \frac{1}{r^3}\left[p_\theta^2 + \frac{p_\phi^2}{(\sin\theta)^2}\right], \\ \frac{dp_\theta}{d\sigma} &= -\frac{\partial H}{\partial \theta} = \frac{1}{2}\frac{\partial \alpha^{-2}}{\partial \theta} + \frac{1}{r^2}\frac{\cot\theta}{(\sin\theta)^2} p_\phi^2, \\ \frac{dp_\phi}{d\sigma} &= -\frac{\partial H}{\partial \phi} = \frac{1}{2}\frac{\partial \alpha^{-2}}{\partial \phi}, \end{aligned} \tag{7.22}$$

https://www.eri.u-tokyo.ac.jp/people/knishida/eng/seismology.html

The result is as follows. In the case of a horizontally stratified structure, placing the emergence point at the pole does not lose generality. Also, since α does not depend on θ and ϕ, its partial derivative is 0. Assuming propagation in the direction $\phi = 0$, $p_\phi = 0$ from the definition of general momentum. Consequently, $\dot{p_\theta} = 0$. Therefore, as in the Cartesian coordinate case, p_θ is conserved along the ray path, and it is also called the ray parameter.

7.2.5 Earth flattening transform

When considering ray theory, there is a simple correspondence between horizontally stratified structures ($\alpha(z)$ is a z-only function) and spherically symmetric structures. Once one problem is solved, the other can be solved by variable transformation (Earth flattening transform). Let us consider this variable transformation below.

Let us consider the problem in the θ direction for isotropic seismic wave radiation from a point. The Eikonal equation in spherical coordinates leads to the following equation.

$$\left(\frac{\partial T}{\partial r}\right)^2 + \frac{1}{r^2}\left(\frac{\partial T}{\partial \theta}\right)^2 = \frac{1}{\alpha(r)^2} \tag{7.23}$$

Using the Earth radius R_e, we can rewrite the equation as

$$\frac{1}{R_e^2}\left(\frac{\partial T}{\partial \theta}\right)^2 + \frac{r^2}{R_e^2}\left(\frac{\partial T}{\partial r}\right)^2 = \frac{r^2}{R_e^2}\frac{1}{\alpha(r)^2}. \tag{7.24}$$

We can transform the equitation in spherical coordinates to an equation in Cartesian coordinates with the change of variable by $x = R_e\theta$, $r = R_e e^{-z/R_e}$, $\alpha(z) = R_e\alpha(r)/r$. The Earth flattening transform is strictly valid within ray theory. It also holds for SH wave propagation, but only approximately for SV wave. Footnotesee Aki and Richards Box 9.9 for details[(1)].

Problem 7.1

Consider a sphere with uniform velocity and find the corresponding horizontal stratification structure using the Earth flattening transform. Also, consider a wavy line in the Cartesian coordinate system and consider its correspondence with the case of a uniform sphere.

7.2.6 Fermat's principle (principle of least action)

Fermat's principle (principle of least action) states that the ray path is the path which minimizes the integration of Lagrangian among the possible paths. This leads to the following relation:

$$\delta \int_{\sigma_1}^{\sigma_2} L(\boldsymbol{x}, \dot{\boldsymbol{x}}) d\sigma = \delta \int_{\sigma_1}^{\sigma_2} \left[\boldsymbol{p} \cdot \dot{\boldsymbol{x}} - H(\boldsymbol{x}, \boldsymbol{p}) \right] d\sigma. \tag{7.25}$$

This relation is equivalent to minimizing the corresponding travel time.

$$\delta \int_{\boldsymbol{x}_1}^{\boldsymbol{x}_2} \boldsymbol{p} \cdot d\boldsymbol{x} = \delta \int_{T_1}^{T_2} dT = 0 \tag{7.26}$$

This indicates that the ray chooses the path that minimizes the travel time. In the problem we are considering, since it physically chooses the path with the shortest travel time, the action integral turns out to be structurally equal to the total travel time, regardless of whether we choose the travel time T, the ray path length s, or the generating parameter σ as the parameter.

7.2.7 Direct method for the Eikonal equation

A method known for directly solving the Eikonal equation uses the principle of least action. This takes advantage of the fact that the ray selects the path with the shortest travel time among all possible paths. Let us consider the two-dimensional case. We cover the entire space with grid points and consider the situation where waves propagate outward from the source. At each step, for each ray path candidate that can be the shortest path, we calculate the travel time along that ray path. Then, we select the ray path with the minimum travel time. This operation is repeated until the wavefront reaches the observation station. By doing this, the travel time at the observation station can be calculated.

Assuming a constant seismic velocity simply within a grid reduces accuracy, so a higher-precision algorithm known as fast marching is known and widely used for complex (non-horizontally-stratified) structures (e.g., Rawlinson and Sambridge 2005[7]).

§7.3 $\tau - p$ (Radon) transform

Travel time curves against epicentral distance become complex due to the multi-valued function. There exists a transform known as $\tau - p$ (Radon) transform into the single-valued function. Here we define intersection time τ by $\tau(p) = T - p_x X$ (this type of transform is known as Legendre transforms in physics). After the transformation from a pair of T and p_x to a pair of τ and p_x, τ becomes the single-valued function even in a case with the positive jump as shown in 7.9.

Once we obtain τ against the ray parameter p_x, we can calculate the travel time T against the epicentral distance X by a relation of $d\tau/dp = -X$[note 6)].

τ is also a useful observable for array analysis of seismic data (A slant stack method of array analysis is a technique of data processing that utilizes the information from densely distributed seismometers at around X). $\tau - p$ transform is a theoretical background of the array analysis[note 7)]

We can extend $\tau - p$ into two dimensions. To define a new variable pair that has the same information to travel time T against the dependent variable $\boldsymbol{X}$, we must consider Legendre transform[note 8)].

$$\tau = T - \boldsymbol{p} \cdot \boldsymbol{X} \tag{7.28}$$

For the transform from $\boldsymbol{p}$ to $\boldsymbol{X}$,

$$\frac{d\tau}{dp_x} = -X, \tag{7.29}$$

$$\frac{d\tau}{dp_y} = -Y, \tag{7.30}$$

$$\tag{7.31}$$

is useful[note 9)].

§7.4 Amplitude: geometrical spreading

[note 6)] From the definition, the derivative of τ with respect to the ray parameter p_x is given by

$$\frac{d\tau}{dp_x} = \frac{dT}{dp_x} - X - p_x \frac{dX}{dp_x} = \frac{dT}{dp_x} - X - \frac{dT}{dX}\frac{dX}{dp_x} = -X. \tag{7.27}$$

[note 7)] For details on practical data analysis, read a textbook by Zhou (Practical Seismic Data Analysis[12]).

[note 8)] Strictly speaking, the Legendre transform requires convexity with respect to the dependent variable. Therefore we need to divide T into retrograde and prograde branches before the transform

[note 9)] This relation can be proven as in a one-dimensional case.

As in a two-layer medium, the conservation of energy along a ray path leads to a theory for amplitudes of a ray theoretical Green's function for phases (e.g. P wave and S wave).

Here we consider seismic wave propagations in a stratified Earth model. When a seismic wave is radiated with the emergency angle of i_0 from the source, the infinitesimal solid angle $d\Omega_0 = \sin i_0 di_0 d\phi_0$ gives the conservation of energy. Here r_1 is the radius of the Earth, and ϕ is azimuth. When a radiated seismic wave with a solid angle reaches a surface point with angular distance Δ from the source,

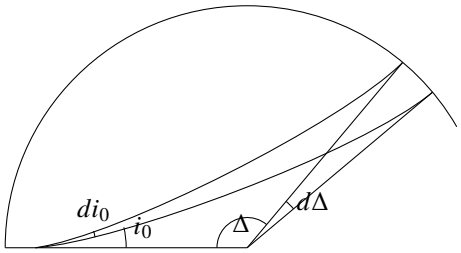

Figure 7.5:

The cross-section area on the surface S_1 is given by

$$dS_1 = r_1^2 \sin\Delta |d\Delta| d\phi_0 \cos i_1. \tag{7.32}$$

From the conservation of energy along the ray path, we obtain

$$E_0 d\Omega_0 = E_1 dS_1. \tag{7.33}$$

The energy at the surface point (the observed station) E_1 is represented by

$$E_1 = E_0 \frac{d\Omega_0}{dS_1} = E_0 \frac{\sin i_0 di_0}{r_1^2 \cos i_1 \sin\Delta |d\Delta|}. \tag{7.34}$$

Here

$$p = \frac{r_0}{\alpha_0} \sin i_0 = \frac{dT}{d\Delta} \tag{7.35}$$

$$\frac{dp}{d\Delta} = \frac{r_0}{\alpha_0} \frac{d \sin i_0}{d\Delta} = \frac{d^2T}{d\Delta^2} \tag{7.36}$$

$$\frac{d \sin i_0}{d\Delta} = \frac{\alpha_0}{r_0} \frac{1}{\cos i_0} \frac{dp}{d\Delta}, \tag{7.37}$$

where r_0 is the distance between the source and the center of the Earth. Then we obtain geometrical spreading $\mathcal{R}$, which gives information on the amplitudes as,

$$\frac{1}{\mathcal{R}^2} = \frac{E_1}{E_0} = \frac{1}{r_1^2} \frac{\alpha_0}{r_0} \frac{\tan i_0}{\cos i_1 \sin\Delta} \left| \frac{d^2T}{d\Delta^2} \right| \tag{7.38}$$

$$= \frac{1}{r_1^2} \frac{\alpha_0^2}{r_0^2} \frac{p}{\cos i_0 \cos i_1 \sin\Delta} \left| \frac{dp}{d\Delta} \right|. \tag{7.39}$$

$dp/d\Delta$ becomes larger with increasing ray density (see Figures in the previous section. This can be interpreted as (1) energy particles are radiated at the source toward every direction, (2) ray represents the trace of the particle (3) how many particles reach the observed station (4) by counting the energy particle, we can infer the amplitude of the phase.

If the heterogeneities of the medium near the source are weak, we can approximate the Green's function with that of an infinite homogeneous medium. By connecting the Green's function for an infinite homogeneous medium to the ray-theoretical Green's function, we can obtain a complete ray-theoretical Green's function, including absolute amplitudes. When a station is located on the free surface, which doubles the amplitudes, the ray-theoretical Green's function of a direct P wave is given by

$$G(\mathbf{x}_r, \mathbf{x}_s, f) = \frac{1}{4\pi\mathcal{R}} \left[\frac{\hat{\boldsymbol{\eta}}_1 \hat{\boldsymbol{\eta}}_2 e^{-2\pi f i T_p}}{\sqrt{\rho_1 \rho_2 \alpha_1^3 \alpha_2}} \right], \tag{7.40}$$

where $\hat{\boldsymbol{\eta}}_1$ and $\hat{\boldsymbol{\eta}}_2$ are polarization vectors at the source and the station, respectively, and T_p is P-wave travel time.

§7.5 Caustic

When

$$\left| \frac{d^2 T}{d\Delta^2} \right| = \infty, \tag{7.41}$$

ray density diverges. This causes divergence of the amplitude in a framework of ray theory. For example, Figure 7.6 shows the concentration of ray paths at the center. This situation is analogous to lighting a fire by focusing sunlight with a magnifying glass. In this case, rays converge at a point known as a "focus". In the case of caustic, the rays focus on a line (e.g. in the case of Figure 7.6, perpendicular to the page, patterns of the ray are homogeneous).

In a region where the spatial scale of amplitude variations is comparable to the wavelength, geometrical ray theory is not appropriate. At such singular points, we need to connect the analytic solution of the original wave equation. When a ray path passes a caustic, it causes a phase jump of 90°. For example, the phase of the PP wave (reflected P wave at the surface) actually is shifted 90°, because it passes caustic one. The wave packet of the PP wave can be represented by the Hilbert transform of the direct P wave mathematically.

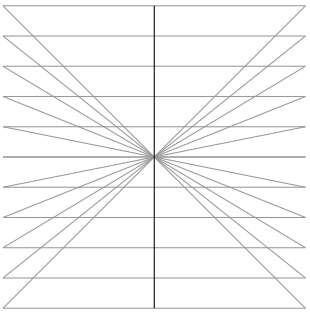

Figure 7.6: Conceptual diagram of a caustic. One can see ray paths concentrating at a point.

Since the ray approximation is broken near caustic, let us consider the 2-D wave equation about a scalar quantity f in polar coordinates with the origin at the caustic:

$$\frac{1}{r}\frac{\partial}{\partial r}\left(r\frac{\partial f}{\partial r}\right)+\frac{1}{r^2}\frac{\partial^2 f}{\partial \phi^2}=-k_0^2 f. \tag{7.42}$$

With the ray approximation, we can assume that typical spatial scales are sufficiently larger than the wavelength, but there exist regions where r is shorter than the wavelength in realistic situations. For simplicity, let us consider the Fourier component $f \propto e^{in\phi}$ with respect to ϕ. Then we have

$$\frac{\partial^2 f}{\partial r^2}+\frac{1}{r}\frac{\partial f}{\partial r}=\left(-k_0^2+\frac{n^2}{r^2}\right)f. \tag{7.43}$$

This is exactly the equation satisfied by the Bessel function. The Bessel function in far-field can be approximated as

$$J_n(kr) \propto \frac{1}{\sqrt{kr}}\cos\left(kr-n\frac{\pi}{2}-\frac{\pi}{4}\right). \tag{7.44}$$

We can see that $\pi/4$ is shifted by 2 times once it passes through the origin (caustic). This is because the change in curvature works better than the derivative with respect to r when viewed in polar coordinates. Here is a rough estimate. For example, in Cartesian coordinates $\cos\left(\sqrt{2}/2k_0x\right)\cos\left(\sqrt{2}/2k_0y\right)$ satisfies the wave equation. If the wavelength corresponding to k_0 is λ_0, the area of this positively inflated region can be written as $(\sqrt{2}\lambda_0/2)^2=\lambda^2/2$. Considering that this is the same as the area of the circle centered at the origin, its radius is $\lambda/(\sqrt{2\pi})$. In other words, the first zero crossing point from the origin in polar coordinates is around 0.39 wavelengths away, which is more extended than $\lambda_0/4$ when considered in plane waves. This summation can be interpreted as giving the phase difference $\pi/4$ [note 10)].

This phase shift can be interpreted from the conservation of energy with a natural extension of the negative cross section dS_2.

$$E_1 dS_1 = E_2 dS_2 \tag{7.45}$$

leads to $A_2 = A_1 i$. This originated from the flip of the ray coordinates before and after a passage at a caustic. In a case of a passage at a focus, the amplitude reverses because the phase flips twice ($i^2=-1$) according to the two directions.

note 10) For an accurate evaluation, we need to approximate the singularity by the Airy function using the WKBJ approximation (see Yomogida's textbook[11] for details). A more physical explanation (corresponding to diffraction) is given in Landau-Lifshitz's classical field theory §59

An example of a caustic is the PP wave, whose phase is shifted relative to the direct P wave. This typical example is intuitively confusing, so it is explained below. Since the ground reflection complicates the behavior, let us consider a mirror image of the hypocenter with respect to the surface (Figure 7.7). If we fold back the ray path of the PP wave radiated downward from the hypocenter at the surface, we can see that it intersects before the observed station. On the other hand, the pP wave radiated from the hypocenter does not intersect. Therefore, the waveforms of the pP and direct-directed waves have the same shape, but the PP wave has a distorted shape to the direct P wave (they are related by the Hilbert transform to each other).

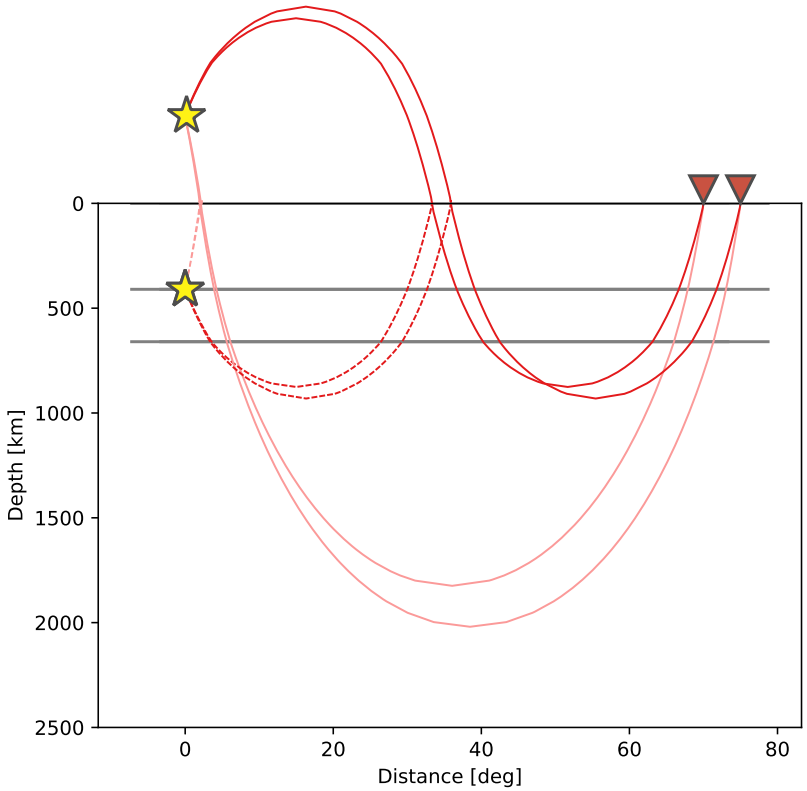

Figure 7.7: Schematic diagram of PP waves passing through caustic. In this figure, we can see that the PP waves intersect, while the pP waves do not.

Translated with www.DeepL.com/Translator (free version)

§7.6 Travel time analysis

Although the generating parameter σ provides insight into this system, it is not directly related to observables. In this section, relations among observables: epicentral distance $X(p_x)$, travel time $T(p_x)$, and ray parameter p_x are presented for a stratified medium[note 11].

At the origin $\boldsymbol{p} = (p_x, \sqrt{\alpha(0)^{-2} - p_x^2})$. The deepest point of the ray z is given by $z = Z(p_x)$. In this case, the corresponding seismic velocity is represented by

$$\alpha(Z) = p_x. \tag{7.46}$$

z component of equation 7.13 leads to the following relation:

$$\frac{dz}{d\sigma} = p_z. \tag{7.47}$$

Let σ be the Σ it takes to reach the deepest point. Since the distance to the deepest point is half of $X(p_x)$, the x component of equation 7.13 becomes

$$\frac{X(p_x)}{2} = \int_0^{\Sigma} p_x d\sigma = \int_0^{Z(p_x)} \frac{dz}{p_z}. \tag{7.48}$$

[note 12] To summarise this,

$$X(p_x) = 2p_x \int_0^{Z(p_x)} \frac{1}{(\alpha^{-2}(z) - p_x^2)^{1/2}} dz \tag{7.49}$$

Next, consider the travel time $T(p_x)$. Since we are now thinking in σ, let dt relate to generating parameter with the equation 7.11,

$$dt = \frac{ds}{\alpha} = \frac{d\sigma}{\alpha^2}. \tag{7.50}$$

As in the case of X, by transforming $d\sigma$ into the integral of dz as well as X, T can be represented by

$$T(p_x) = \int_0^{s_d} \frac{ds}{\alpha} = 2\int_0^{Z(p_x)} \frac{\alpha^{-2}}{(\alpha^{-2}(z) - p_x^2)^{1/2}} dz, \tag{7.51}$$

where s_d is the distance of the ray path from the source to the deepest point.

Finally, let us evaluate τ. Recall the definition:

$$\tau(p_x) = T(p_x) - p_x X(p_x). \tag{7.52}$$

note 11) For details, read the textbook by Shearer[8]

note 12) Since p_x is a conserved quantity, it is often confusing to write $T(p_x) = \int p_x dX = p_x X(p_x)$. In this case. $T(p_x) = \int \boldsymbol{p} \cdot \boldsymbol{ds}$ must be evaluated. This is an example of how inconsistency can arise when considering the physical image of a moving particle if we do not take the generating parameter σ as the parameter instead of the time T.

Substituting the equation derived above, we obtain

$$\tau(p_x) = 2\int_0^{Z(p_x)} \sqrt{\alpha(z)^{-2} - p_x^2}\, dz, \tag{7.53}$$

τ has the advantage that the divergence to infinite disappears from the integral, making the actual evaluation easier.

For typical structures below, let us review the relationship between ray paths and travel time. note 13)

7.6.1 In a case of monotonically increasing seismic velocity with depth

In the simplest case, let us consider travel time for monotonically increasing seismic velocity with depth. Figure 7.8 shows such an example. The ray parameter p_x conserves along the ray path. For this reason, the seismic velocity at the turning depth matches the corresponding apparent horizontal velocity $(1/p_x)$. The ray path dives to the turning depth, then it returns to the surface.

This figure shows that with decreasing parameter $p_x = \sin\theta/\alpha(z)$ (decreasing the emergency angle equivalently), the ray reaches farther (the epicentral distance $X(p)$ becomes longer). In this case, $dX/dp_x < 0$, as shown in the figure, is referred to as prograde. With increasing epicentral distance, the ray density decreases. (This means that ray density can be estimated by dp_x/dX as shown in this figure.) Therefore, the amplitude decreases with the epicentral distance.

note 13) If you are interested in travel time calculations for real one-dimensional structures, please refer to [(2), (3), Crotwell et al. 1999, Buland and Chapman, 1983]

Problem 7.2

1. Let us consider wave propagations in upper xz plane ($z > 0$). When the seismic velocity α is a linear function given by $a + bz$, show that the ray path becomes a circle given by

$$\left(x - \frac{\sqrt{1 - p_x^2 a^2}}{b p_x}\right)^2 + \left(z + \frac{a}{b}\right)^2 = \frac{1}{p_x^2 b^2}. \tag{7.54}$$

   Hint: The equation can be derived from the Hamilton equations and the Eikonal equation.

2. Derive equation 7.51.

3. Show that $T(p_x)$ is given by

$$T(p_x) = \frac{2}{b} \cosh^{-1}\left(\frac{1}{p_x a}\right). \tag{7.55}$$

4. We can calculate a ray path by numerically integrating the Hamilton equation with respect to σ. For example, ray paths in Figure 7.8 are calculated from the integration. Calculate the ray paths numerically in the same manner. Compare the analytic solution of the ray path and the numerical calculation.

   $*$ **Note**: The first parameter of the Hamilton equation describes the change of the location, whereas the second one determines the slowness vector as conserved the total energy along the ray path (in other words, to satisfy the Eikonal equation).

   Hint:

$$\frac{d \cosh^{-1}(z)}{dz} = \frac{1}{\sqrt{z^2 - 1}} \tag{7.56}$$

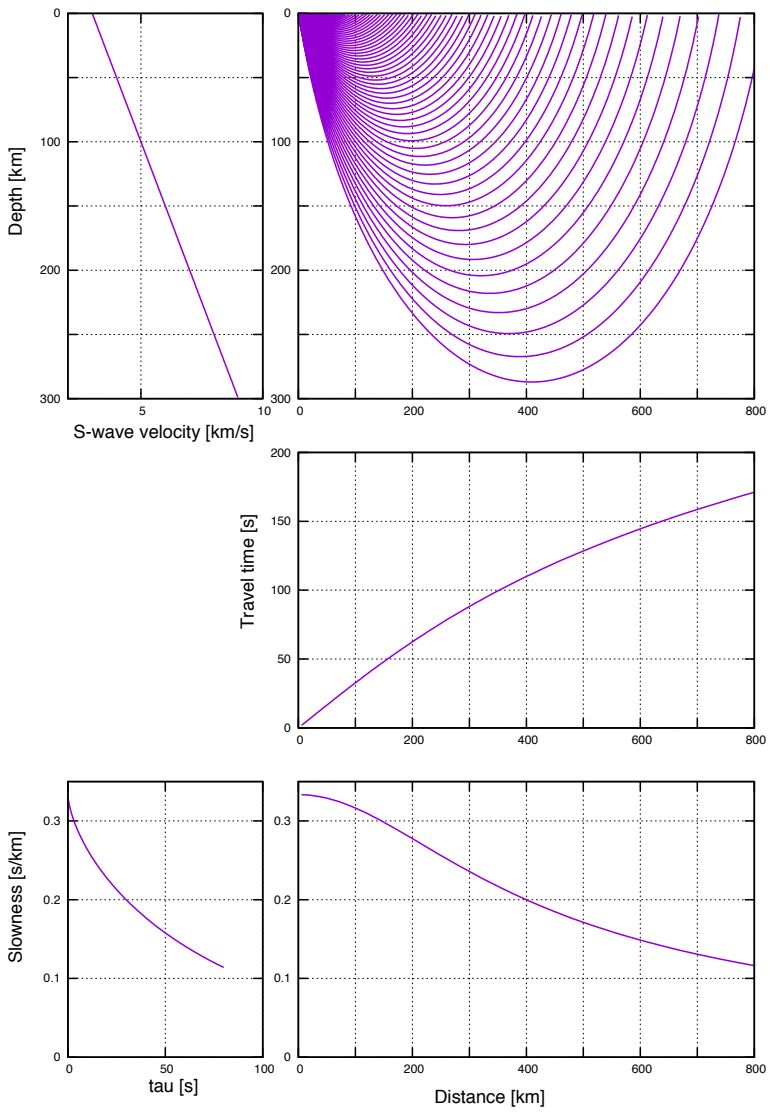

Figure 7.8: Ray paths for linearly increasing seismic structure with depth. We can see a relation of $p_x = dT/dx$.

7.6.2 In a case of a positive seismic jump at a depth

Next, let us consider a positive jump of seismic velocity at a depth.

When a ray path exists in the upper layer, it reaches further with the decreasing emergency angle (prograde dX/dp¡0). When the ray enters the layer of steeply increasing seismic velocity, the ray path backs to the source side according to Snell's law. This feature characterized by $dX/dp > 0$ is referred to as a retrograde ray. When the emergency angle decreases furthermore, it dives into the deeper lower layer, and the ray path becomes prograde again. At the point where $dX/dp = 0$, known as a caustic, the ray path density diverges, causing the amplitudes to diverge. Due to this singularity, ray theory cannot accurately handle the wavefield around the point where $dX/dp = 0$[note 14)].

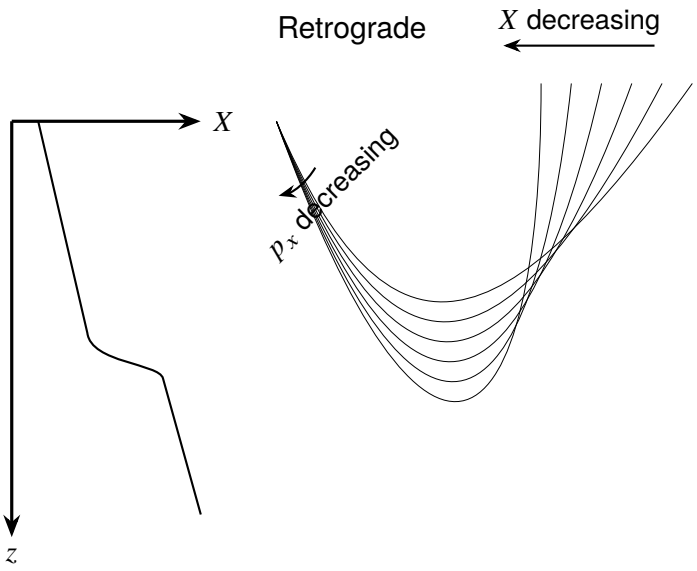

Figure 7.9: Ray paths involving rapidly increasing velocity zone.

Basic features, in this case, are common with those in a two-layer medium discussed in the previous chapter.

note 14)Because the high-frequency approximation is broken down at the point close to the caustic, we must consider an appropriate solution of the wave equation which connects to the ray theoretical solution. Such a solution leads to jumping off the phase of 90° after the passage through the caustic. The phase jump is also discussed in the later section about amplitudes of a ray theoretical solution.

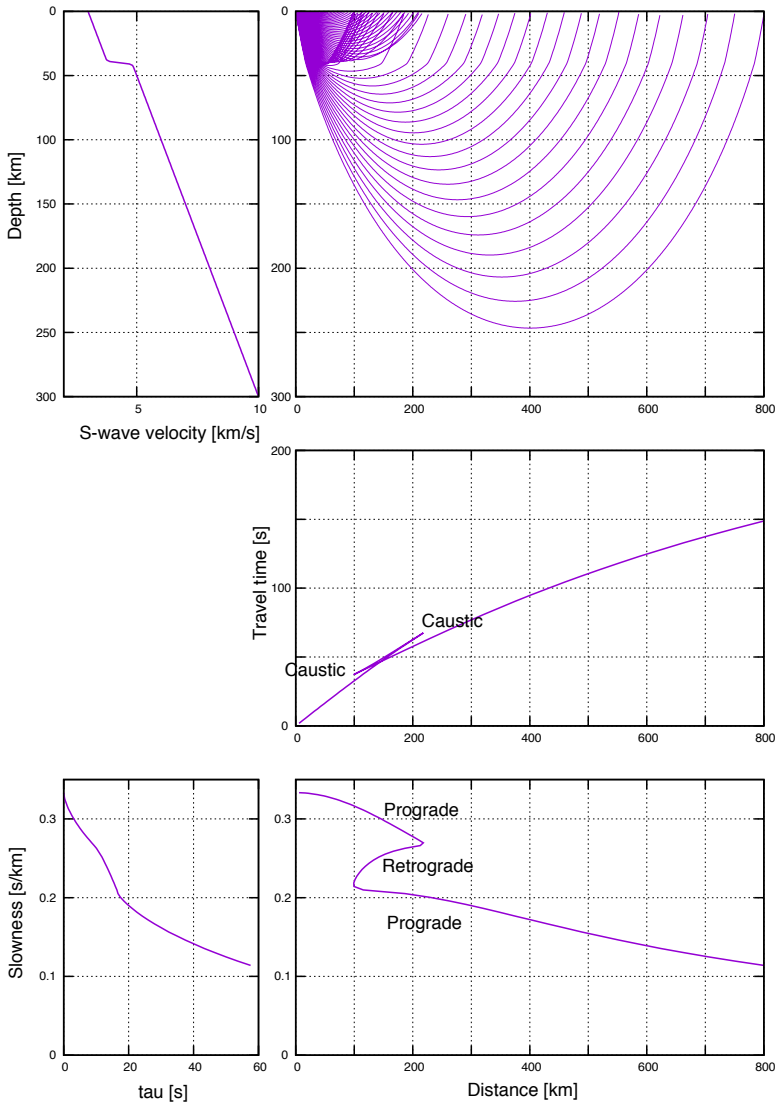

Figure 7.10: Ray paths in a case of positive seismic jump at a depth.

If you only look at the wavefront, you may find it difficult to see the triplication area because they overlap each other. Therefore, let's zoom in on the ray near the triplication area with the wavefront at the same time (Figure 7.11). The retrograde ray corresponds roughly to the green color. The caustic surface is formed at the point where the retrograde starts. When triplication occurs, the rays are folded. The wedge-shaped base of the folded wavefront corresponds to the wavefront that passes through the caustic surface, resulting in a 90-degree phase shift. You can also see that the positive velocity gradient just below the discontinuity bends the rays toward the surface, which increase the amplitude of the retrograde branch. Thus, when considering seismic waves, it is important to consider both the rays and the wavefront together. You can also see that in the $\tau - p$ region, triplication is unfolded and becomes a single-valued function.

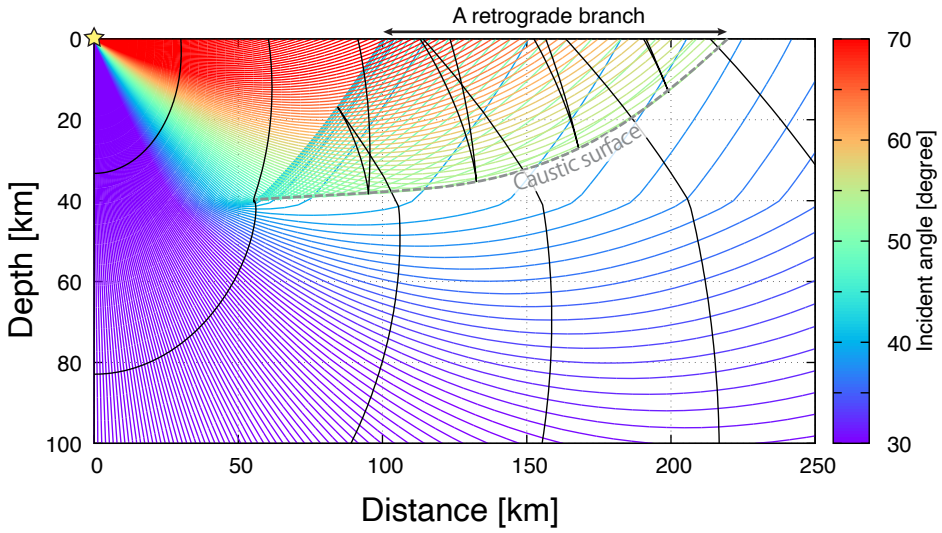

Figure 7.11: Wavefront with positive seismic velocity jump. The emergence angle is shown in color, and the wavefront (isochrones of travel time) is also shown

Consider another example. It is known that a 410 km discontinuity and a 660 km discontinuity exist globally in the Earth's interior. These two discontinuities correspond to phase changes in minerals (corresponding to olivine ⟶spinel and spinel⟶perovskite, respectively). Let's take a look at Figure 7.12. Here is a seismic waveform record in Alaska of an earthquake that occurred in the Aleutians at a depth of about 100 km. The waveforms are complicated, but we can see multiple P-wave packets arriving in $13^\circ \sim 30^\circ$. This is the result of triplication at the 410 km and 660 km discontinuities. The lower figure shows the theoretical travel time. You can see that it roughly represents the characteristics of the observed waveforms.

Let us imagine that there is no information on the Earth's interior. From Figure 7.12, we can see that it is difficult to interpret the waveforms of the P wave except at the first arrival time when there are multiple arrivals. In the figure, this corresponds to the blue rising edge. The rise of the first arriving wave packet is easy to read (because the ground is quiet before the arrival) and can be measured with good accuracy. If we only have information on the first arrivals, it is difficult to distinguish it from the travel time curve for a structure without the discontinuities (e.g, 7.8). In other words, when inferring the internal structure of the earth from the travel time, without

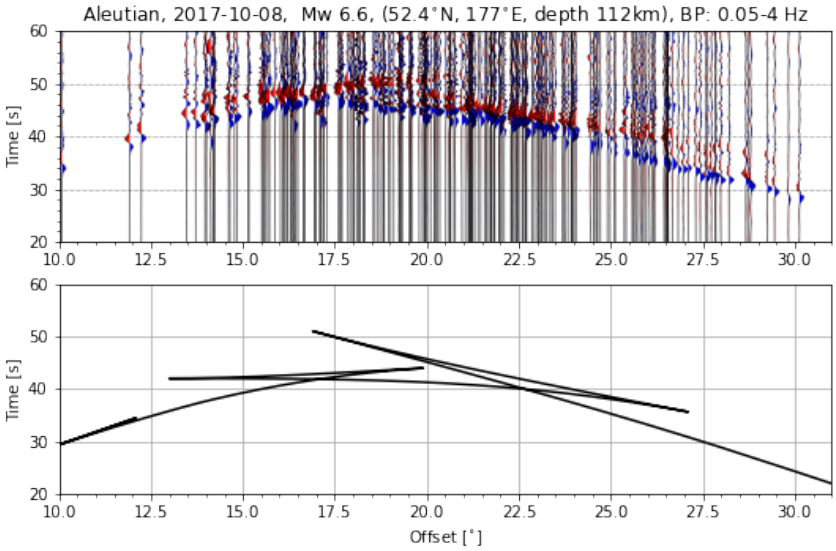

Figure 7.12: A typical example with a positive seismic velocity jump. Velocity waveform (0.05-4 Hz) observed by USArray (Alaska) for an earthquake that occurred in the Aleutians. For a better display, the travel time of the waveform was reduced (specifically, $T(10\ \mathrm{km/s})X$ is plotted against X). Positive amplitudes are shown in red and negative amplitudes are shown in blue. It can be seen that there are multiple arrivals of P-wave wave packets in this distance range. The lower figure also shows the corresponding theoretical travel times, where we can see the triplication corresponding to the positive jumps in the two seismic velocity jumps (410 km discontinuity and 660 km discontinuity).

information on triplication, the information on the internal discontinuity cannot be correctly estimated, and an over smooth structure will be inferred (since the simple model can also explain the measured first arrivals).

Problem 7.3

Let us consider wave propagation in xz plane ($z > 0$) for seismic speed α given by

$$\alpha(z) = 5 + (1 + \tanh(z - 40)) * 2 + \frac{z}{200}. \tag{7.57}$$

By numerical integration of Hamilton equations with respect to σ, calculate the ray paths. And as in Figure 7.9, plot the relations between Travel time and distance, that between distance and slowness, and that between τ and slowness. Then compare the results with two-layered mediums.

7.6.3 In a case of a negative seismic jump at a depth

When a negative jump of seismic velocity with depth exists, rays cannot reach a certain area on the surface known as a shadow zone. Because rays tend to avoid the low-velocity zone, as shown in Figure 7.13, the seismic exploration of the seismic structure becomes difficult in general.

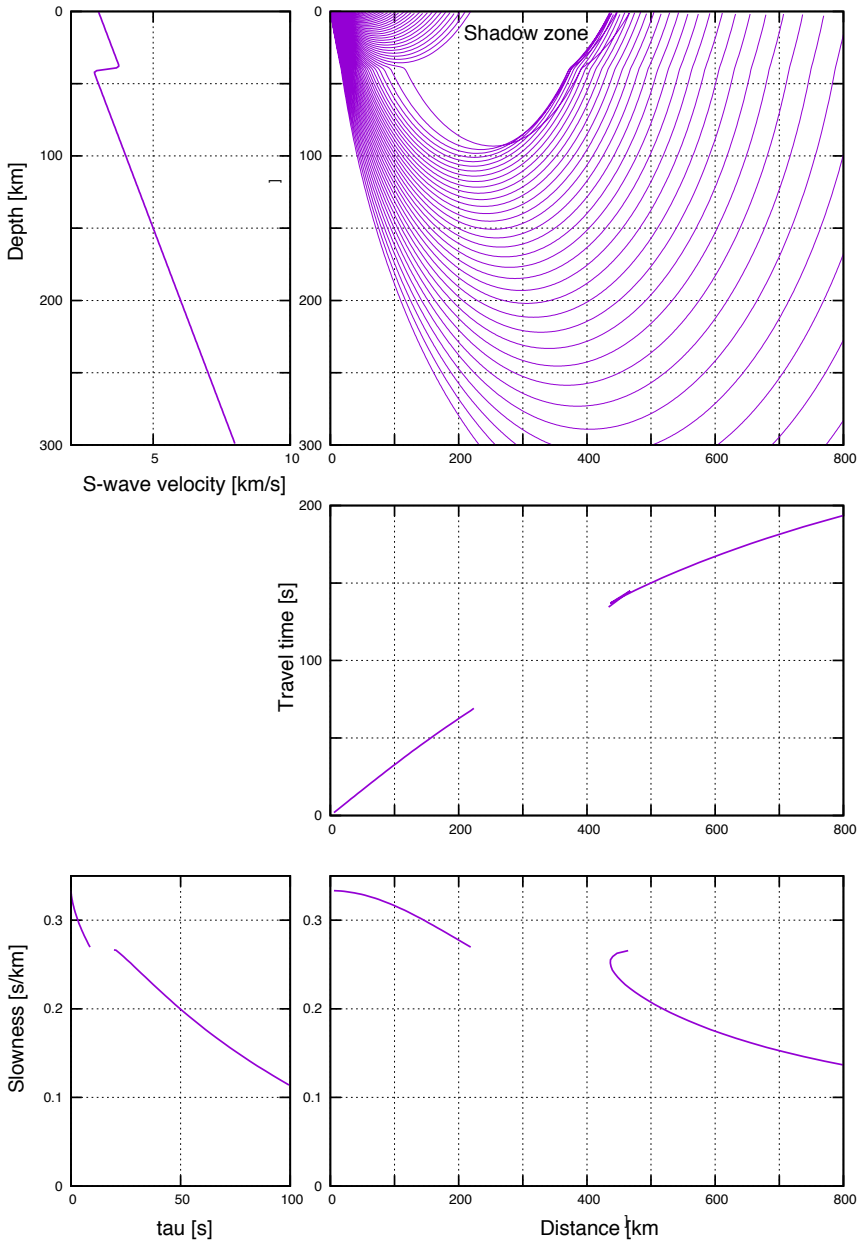

Figure 7.13: Ray paths in a case of negative seismic jump at a depth.

§7.7 1-D inversion

7.7.1 Herglotz-Wiechert inversion

If the seismic velocity structure monotonically increases with depth, we can infer the seismic velocity structure from travel time information. For a given slowness p_x, the corresponding arrival distance $X(p_x)$ is

$$X(p_x) = 2p_x \int_0^{z(p_x)} \frac{dz}{\sqrt{\alpha^{-2}(z) - p_x^2}}. \tag{7.58}$$

Although it may seem abrupt, when the seismic velocity increases monotonically, we can simply transform the integration variable from z to $\eta = 1/\alpha$, which gives

$$X(p_x) = 2p_x \int_{\eta_0}^{p_x} \frac{1}{\sqrt{\eta^2 - p_x^2}} \frac{dz}{d\eta} d\eta. \tag{7.59}$$

Suppose the slowness of the seismic wave observed at a certain distance X_1 is p_1. Dividing both sides by $\sqrt{p_x^2 - p_1^2}$, and integrating with respect to p_x from p_1 to η_0 yields (omitting the details[5]) the depth z_1 where the seismic velocity is $1/p_1$:

$$z_1 = \frac{1}{\pi} \int_0^{X_1} \cosh^{-1}(p_x(X)/p_1) dX. \tag{7.60}$$

This relation is known as the Herglotz-Wiechert formulas. It is important to note that when the travel time T is observed as a monotonically increasing function of distance X, the seismic velocity structure can be uniquely represented by an integral of the observational data. While highly elegant, its application conditions are strict, leaving only limited examples where it can be applied directly.

7.7.2 τ-p inversion

Let us now consider the problem of inferring the structure of the Earth's interior from the travel time of seismic waves measured at the Earth's surface. Suppose we now have a perfectly measured travel time $T(X)$. In this case, the slowness p at location X is

$$p = \frac{dT}{dX}, \tag{7.61}$$

and can be obtained from its direction. The τ can be measured as the interception time (y-intercept) at which the tangent line is extended and intersects at $X = 0$.

Let us assume that the Earth's internal structure consists of n homogeneous layers. Let the thickness of the n layer be ΔZ_n and the seismic wave velocity be α_n (equation7.14). Discretising

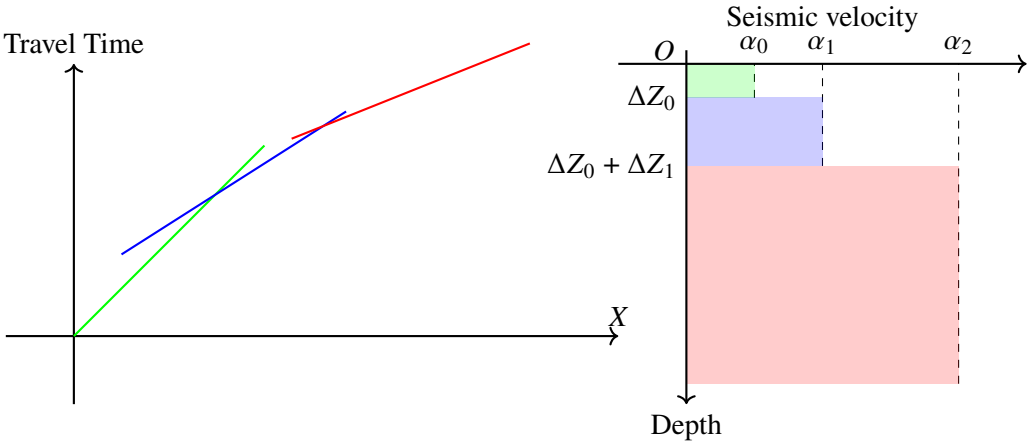

Figure 7.14: Schematic figure of a segmented line approximation of the travel time curve.

the equation for τ (equation7.53), we obtain

$$\tau(p_x) = 2\sum_{1}^{n} \sqrt{\alpha_n^{-2} - p_x^2}\Delta Z_n. \tag{7.62}$$

We can find here that if α_n is known, it is a linear equation. In fact, α_n can be measured from the graph. If each line is a direct wave (red), a head wave in the second layer, and a head wave in the third layer, each slowness corresponds to α_n^{-1}. The we can obtain the following relation:

$$\begin{pmatrix} \tau_1 \\ \tau_2 \\ \vdots \\ \vdots \\ \tau_n \end{pmatrix} = 2\begin{pmatrix} \sqrt{\alpha_0^{-2} - \alpha_1^{-2}} & 0 & 0 & \cdots & \\ \sqrt{\alpha_0^{-2} - \alpha_2^{-2}} & \sqrt{\alpha_1^{-2} - \alpha_2^{-2}} & 0 & \cdots & \\ \cdots & \vdots & & & \\ \sqrt{\alpha_0^{-2} - \alpha_n^{-2}} & \sqrt{\alpha_1^{-2} - \alpha_n^{-2}} & \cdots & & \sqrt{\alpha_{n-1}^{-2} - \alpha_n^{-2}} \end{pmatrix} \begin{pmatrix} \Delta Z_0 \\ \Delta Z_1 \\ \vdots \\ \vdots \\ \Delta Z_n \end{pmatrix}. \tag{7.63}$$

The linear form of the equation means that it is possible to solve the equation from the top layer.

Problem 7.4

Suppose that the travel time T [s] at a point X [km] can be measured at three locations. An earthquake occurred at $X = 0$ on the surface at time $T = 0$. Assume that each observation is $(X_0, T_0) = (15, 3.00)$, $(X_1, T_1) = (80, 13.40)$ and $(X_2, T_2) = (120, 18.20)$, approximate the travel time T by a line connecting these points. Estimate the Earth's internal structure by calculating the $\tau - p$ plot.

§7.8 Seismic tomography

Travel time information can be used to infer not only 1-D structure but also 3-D structure. This technique is called seismic tomography[note 15)]. Let us consider a simplified case here. For simplicity, we assume a 2-D homogeneous medium (Figure 7.15). In the figure, triangles represent observation stations and a star represents a hypocenter. Since a homogeneous medium is assumed, rays are straight lines. Now consider the i-th ray path. Let the travel time anomaly corresponding to the i-th ray path be ΔT_i. As shown in the figure, suppose the region is divided into grids, and each grid position is specified by an index j. Suppose the i-th ray crosses the grid j with a length of l_{ij}. Considering the slowness anomaly Δp_j for each grid, the travel time anomaly ΔT_i can be written as

$$\Delta T_i = \sum_j l_{ij} \Delta p_j . \tag{7.64}$$

By solving this equation using the least squares method, we can determine the slowness anomalies Δp_j.

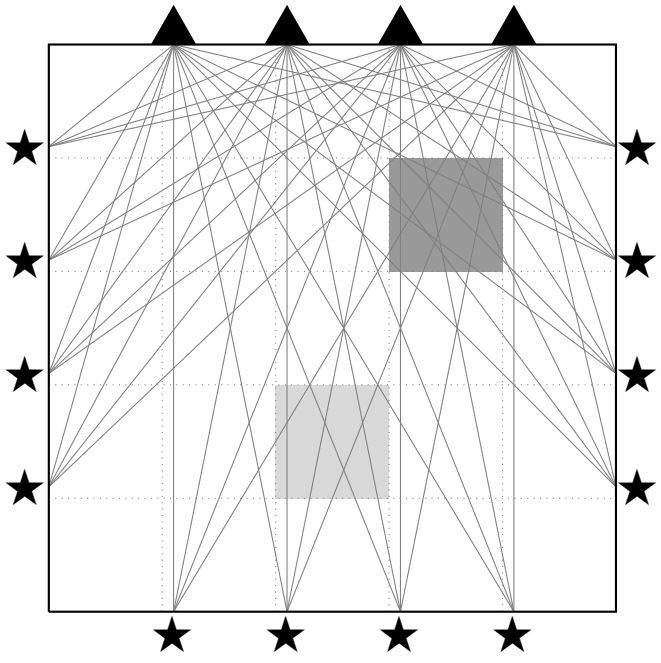

Figure 7.15: Schematic diagram of simplified seismic tomography. Triangles represent observation stations, and stars represent hypocenters. Rays are assumed to be straight lines.

note 15) For details, refer to textbooks by Shearer[8] and Nolet[6]

https://www.eri.u-tokyo.ac.jp/people/knishida/eng/seismology.html

§7.9 Applicability of ray theory

Let us consider the applicability range of ray theory. In order for ray theory to be applicable, high frequency approximation must be valid. In other words, the seismic velocity structure must be sufficiently smooth. Let k be the wavenumber and a be the spatial scale of the velocity anomaly. The condition $ka \gg 1$ must be satisfied. However, considering actual velocity anomalies, it is known that velocity anomalies of various spatial scales exist. This implies that when a seismic wave propagates over a certain distance L, it will cross velocity anomalies of a scale comparable to its wavelength and undergo scattering. This distance is known as the mean free path L. When the propagation distance becomes significantly larger than L, multiple scattering occurs. This is like looking into the interior through frosted glass, making it practically difficult to consider rays. This is because the wave propagation is randomized due to scattering. Figure 7.16 shows a diagram known as the $ka - kL$ diagram. It is important to understand which approximations are reasonable and their application limits depending on each problem setting.

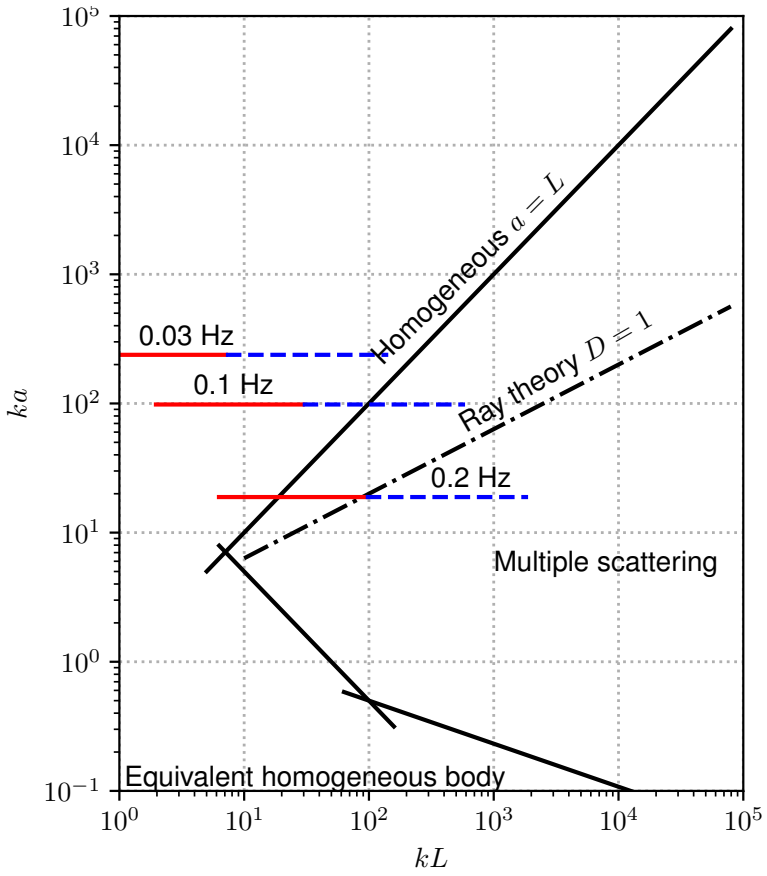

Figure 7.16: $ka - kL$ diagram.

§7.10 Tools for travel time analysis

When we calculate the travel time for a stratified Earth, taup (http://www.seis.sc.edu/taup/) is a common toolkit among seismologists. A direct Eikonal solver using the fast marching algorithm is also common. This algorithm is applicable to a complex medium (non-horizontally-stratified structure). Some different programs using fast marching algorithms are available at a website by Nick Rawlinson (http://rses.anu.edu.au/~nick/). PyKonal,[10] a Python package, is also available.

§7.A IASPEI standard phase list

For details, see http://www.isc.ac.uk/standards/phases/.

7.A.1 CRUSTAL PHASES

Pg	At short distances, either an upgoing P wave from a source in the upper crust or a P wave bottoming in the upper crust. At larger distances also, arrivals are caused by multiple P-wave reverberations inside the whole crust with a group velocity of around 5.8 km/s.
Pb	(alt:P*) Either an upgoing P wave from a source in the lower crust or a P wave bottoming in, the lower crust
Pn	Any P wave bottoming in the uppermost mantle or an upgoing P wave from a source in the uppermost mantle
PnPn	Pn free-surface reflection
PgPg	Pg free-surface reflection
PmP	P reflection from the outer side of the Moho
PmPN	PmP multiple free surface reflection; N is a positive integer. For example, PmP2 is PmPPmP
PmS	P to S reflection/conversion from the outer side of the Moho
Sg	At short distances, either an upgoing S wave from a source in the upper crust or an S wave bottoming in the upper crust. At larger distances also arrivals caused by the superposition of multiple S-wave reverberations and SV to P and/or P to SV conversions inside the whole crust.
Sb	(alt:S*) Either an upgoing S wave from a source in the lower crust or an S wave bottoming in, the lower crust
Sn	Any S wave bottoming in the uppermost mantle or an upgoing S wave from a source in the uppermost mantle
SnSn	Sn free-surface reflection
SgSg	Sg free-surface reflection
SmS	S reflection from the outer side of the Moho
SmSN	SmS multiple free-surface reflections; N is a positive integer. For example, SmS2 is SmSSmS
SmP	S to P reflection/conversion from the outer side of the Moho
Lg	A wave group observed at larger regional distances and caused by the superposition of multiple S-wave reverberations and SV to P and/or P to SV conversions inside the whole crust. The maximum energy travels with a group velocity of approximately 3.5 km/s
Rg	Short-period crustal Rayleigh wave

7.A.2 MANTLE PHASES

§7.B Stratified Earth models

You can find a reference stratified Earth model.

7.B.1 PREM

Preliminary Reference Earth Model http://ds.iris.edu/ds/products/emc-prem/

7.B.2 AK135

http://ds.iris.edu/ds/products/emc-ak135-f/
http://rses.anu.edu.au/seismology/ak135/intro.html

§7.3 Bibliography

[1] K. Aki and P.G. Richards. *Quantitative Seismology*. Univ Science Books, 2nd edition, 2009.

[2] Ray Buland and C H H Chapman. THE COMPUTATION OF SEISMIC TRAVEL TIMES. *Bull. Seismol. Soc. Am.*, 73(5):1271–1302, 1983.

[3] H Philip Crotwell, Thomas J Owens, and Jeroen Ritsema. The TauP toolkit: Flexible seismic travel-time and ray-path utilities. *Seismol. Res. Lett.*, 70(2):154–160, 1999.

[4] F.A. Dahlen and J. Tromp. *Theoretical Global Seismology*. Princeton University Press, Princeton, 1998.

[5] Saito Masanori. *Seismic Wave Theory*. University of Tokyo Press, 2009.

[6] Guust Nolet. *A Breviary of Seismic Tomography: Imaging the Interior of the Earth and Sun*. Cambridge University Press, Cambridge,, September 2008.

[7] N Rawlinson and M S Sambridge. The fast marching method: an effective tool for tomographic imaging and tracking multiple phases in complex layered media. *Explor. Geophys.*, 36(4):341–350, 2005.

[8] P.M. Shearer. *Introduction to Seismology*. Cambridge University Press, third edition, 2009.

[9] V Červený. *Seismic ray theory*. Cambridge University Press, Cambridge, England, 2001.

[10] Malcolm C A White, Hongjian Fang, Nori Nakata, and Yehuda Ben-Zion. PyKonal: A python package for solving the eikonal equation in spherical and cartesian coordinates using the fast marching method. *Seismol. Res. Lett.*, June 2020.

[11] K. Yomogida. *Introduction to Special Functions and Integral Transforms*. Kyoritsu Shuppan, 2007.

[12] H.W. Zhou. *Practical Seismic Data Analysis*. Cambridge University Press, 2014.

P	A longitudinal wave, bottoming below the uppermost mantle; also an upgoing longitudinal wave from a source below the uppermost mantle
PP	Free-surface reflection of P wave leaving a source downward
PS	P, leaving a source downward, reflected as an S at the free surface. At shorter distances, the first leg is represented by a crustal P wave.
PPP	analogous to PP
PPS	PP, which is converted to S at the second reflection point on the free surface; travel time matches that of PSP
PSS	PS reflected at the free surface
PcP	P reflection from the core-mantle boundary (CMB)
PcS	P converted to S when reflected from the CMB
PcPN	PcP are reflected from the free surface N-1 times; N is a positive integer. For example PcP2 is PcPPcP
Pz+P	(alt:PzP) P reflection from the outer side of a discontinuity at depth z; z may be a positive numerical value in km. For example, P660+P is a P reflection from the top of the 660 km discontinuity.
Pz-P	P reflection from the inner side of a discontinuity at depth z. For example, P660-P is a P reflection from below the 660 km discontinuity, which means it is precursory to PP.
Pz+S	(alt:PzS) P converted to S when reflected from the outer side of discontinuity at depth z
Pz-S	P converted to S when reflected from the inner side of discontinuity at depth z
PScS	P (leaving a source downward) to ScS reflection at the free surface
Pdif	(old:Pdiff) P diffracted along the CMB in the mantle
S	Shear wave, bottoming below the uppermost mantle; also an upgoing shear wave from a source below the uppermost mantle
SS	Free surface-reflection of an S wave leaving a source downward
SP	S, leaving a source downward, reflected as P at the free surface. At shorter distances, the second leg is represented by a crustal P wave.
SSS	analogous to SS
SSP	SS converted to P when reflected from the free surface; travel time matches that of SPS.
SPP	SP reflected at the free surface
ScS	S reflection from the CMB
ScP	S converted to P when reflected from the CMB
ScSN	ScS multiple free-surface reflections; N is a positive integer. For example ScS2 is ScSScS
Sz+S	(alt:SzS) S reflection from the outer side of a discontinuity at depth z; z may be a positive numerical value in km. For example, S660+S is an S reflection from the top of the 660 km discontinuity.
Sz-S	S reflection from the inner side of discontinuity at depth z. For example, S660-S is an S reflection from below the 660 km discontinuity, which means it is precursory to SS.
Sz+P	(alt:SzP) S converted to P when reflected from the outer side of discontinuity at depth z
Sz-P	S converted to P when reflected from the inner side of discontinuity at depth z
ScSP	ScS to P reflection at the free surface
Sdif	(old:Sdiff) S diffracted along the CMB in the mantle

Normal Modes

Chapter 8

So far, we have reviewed body waves and surface waves. The frequency band handled in seismology is in the range of $3 \times 10^{-4} \sim 100$ Hz. Oscillations with frequencies lower than approximately 0.005 Hz (5 mHz) are often treated as standing waves (Earth's free oscillations), whereas higher frequencies are typically treated as propagating waves (body waves, surface waves). In the Earth's free oscillation frequency band, the wavelength exceeds 1000 km, making it more convenient to understand them as superpositions of standing waves. The vibration pattern of a standing wave is also referred to as a normal mode.

§8.1 Standing wave of the Earth: Earth's free oscillations

When a huge earthquake occurs, seismic waves with periods around several hundred seconds travel around the Earth multiple times. In such cases, it is easier to understand them represented by a superposition of standing waves rather than as propagating waves as described in the previous section. First, let us look at observed records of earthquakes.

It is known that when a huge earthquake occurs, seismic waves circle the Earth many times. For example, during the recent 2010 Chilean earthquake, surface waves (seismic waves propagating along the Earth's surface) traveling around the Earth were actually recorded by seismometers. A very slow oscillation with a period of 200 seconds was recorded as it propagated. As seismic waves travel around the Earth's surface multiple times, their amplitude decreases, their shape deforms, and they disappear after about a day. Figure 8.1 shows the surface wave recorded by a global broadband seismic network for the earthquake that occurred in Chile on April 1, 2014 (the entire horizontal axis is about 6 hours). We can clearly see the surface wave passing around the world.

On December 26, 2004, a huge earthquake occurred off the coast of Sumatra. Its magnitude exceeded 9, making it the largest earthquake in the last 50 years. In this earthquake, seismometers captured surface waves circling the Earth 8 times. After a day, the seismic waves appeared to have disappeared, but in reality, the Earth continued to vibrate for more than a month. This

earthquake was so massive that the Earth actually kept vibrating for an even longer period.

Figure 8.2 shows the seismogram recorded at the Matsushiro station in Nagano Prefecture, Japan. At a glance, it looks similar to Figure 8.1, but compare the lengths of the horizontal axes. This time, two months of records are plotted. The Sumatra earthquake is recorded near the center. The second panel from the top (bandpass filtered at 0.1-1 mHz) shows that the Earth continued to oscillate even after a month. This recorded pulsing vibration of the entire Earth is called Earth's free oscillation.

Let's look at the actual data to see how it pulses. The lower panel of Figure 8.2 shows seismograms (vertical components) from Germany, the USA, Australia, and Japan about one month after the Sumatra earthquake. Normally, at observation stations around the world, seismic waves are recorded in the order they propagate from the source. What about in Figure 8.2? It shows that all observation stations are moving up and down almost simultaneously. These records indicate that the entire Earth uniformly pulses and repeats expansion and contraction at a period of 1112 seconds. The amplitude of the vibration is about 0.03 mm. At first glance, the amplitude seems small, but only a massive earthquake can cause the entire Earth to pulse. However, once it starts shaking, it has the property of continuing to shake for a long time. During the Sumatra earthquake, it was confirmed to have continued shaking for three months. In addition to the vibration pattern (called a mode) in which the entire Earth repeatedly expands and contracts, a mode in which the whole Earth squashes like a football is also known.

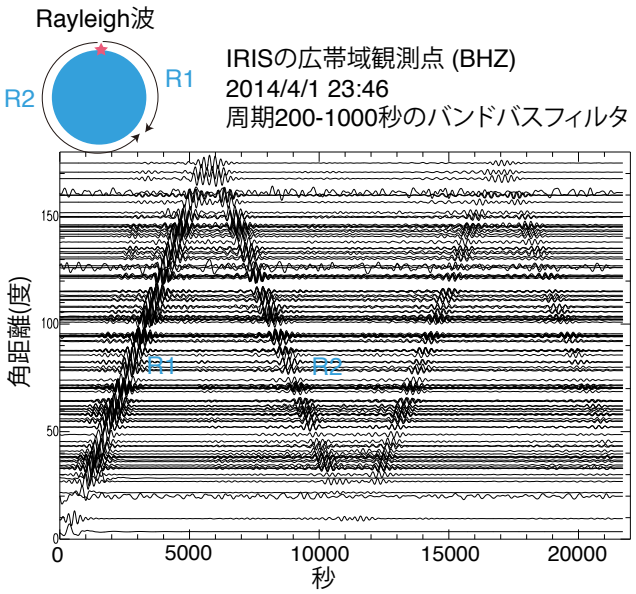

Figure 8.1: Vertical displacement records during the Chilean earthquake on April 1, 2014.

Earthquakes can be likened to striking all the keys of a piano at once. Each piano key corresponds to a vibration pattern (a mode). It is known that any vibration pattern can be reproduced by combinations of hitting many keys. (Although a piano has too few keys to reproduce every sound...). Just as we imagine the shape of an instrument by listening to its sound, seismologists ponder the interior of the Earth by observing its free oscillations with seismometers.

The fundamental reason they can be counted as modes is because the Earth has a finite size. The frequency spacing of the modes is deeply related to the size of the Earth. Mathematically speaking, it reduces to an eigenvalue problem of ordinary differential equations. In the 1D case, it corresponds to a Fourier series expansion, and the vibration pattern of the mode (eigenfunction) corresponds to a sin function.

§8.2 Eigenvalue problem in 1D case: Oscillation of a string

Consider the oscillation of a string of length l. First, let us consider eigenfunctions that satisfy the wave equation:

$$\rho_0 \frac{\partial^2 u(x,t)}{\partial t^2} = \kappa_0 \frac{\partial^2 u(x,t)}{\partial x^2} \tag{8.1}$$

We assume fixed ends as boundary conditions at both ends. The eigenfrequencies and the corresponding eigenfunctions are given by:

$$\omega_n = \frac{n\pi}{l} c_0, \qquad u_n(x) = A_n \sin \frac{n\pi x}{l} \tag{8.2}$$

For normalization, we determine the coefficient A_n to satisfy $(\rho_0 u_i, u_j) = \delta_{ij}$. Calculating the inner product,

$$(\rho_0 u_i, u_j) = \int_0^l \rho_0 u_i^*(x) u_j(x) dx = \rho_0 A_i^* A_j \int_0^l \sin \frac{i\pi x}{l} \sin \frac{j\pi x}{l} dx = \rho_0 |A_i|^2 \frac{l}{2} \delta_{ij} \tag{8.3}$$

Thus, we obtain

$$A_n = \sqrt{\frac{2}{\rho_0 l}} \qquad \text{i.e.} \qquad \underline{u_n(x) = \sqrt{\frac{2}{\rho_0 l}} \sin \frac{n\pi x}{l}} \tag{8.4}$$

which is the normalized eigenfunction $u_n(x)$ [note 1)].

Next, let us consider the response to an impulsive force:

$$\rho_0 \frac{\partial^2 u(x,t)}{\partial t^2} = \kappa_0 \frac{\partial^2 u(x,t)}{\partial x^2} + \delta(x - x_0)\delta(t) \tag{8.5}$$

This problem represents the motion of a rod fixed at both ends when an impulse of 1 [Ns] is applied [note 2)]. Taking the Fourier transform of both sides with respect to time yields:

$$-\omega^2 \rho_0 \tilde{u}(x,\omega) = \kappa_0 \frac{\partial^2 \tilde{u}(x,\omega)}{\partial x^2} + \delta(x - x_0), \tag{8.6}$$

where $\tilde{}$ denotes the Fourier component. Substituting this and the eigenfunction expansion of the wave solution $u(x,\omega)$

$$\tilde{u}(x,\omega) = \sum_{n=1}^{\infty} a_n(\omega) u_n(x) \tag{8.7}$$

[note 1)] From the normalization of the eigenfunction, we can see that u_n^{-2} has dimensions of mass. This value is called the modal mass.

[note 2)] Although the dimensions may seem confusing at a glance, $f(x) = -f_0 \delta(x - x_0)\delta(t)$ has dimensions of [N/m], so f_0 has dimensions of [Ns]. The vibration for an arbitrary force $f(x,t)$ can be represented by a convolution integral with the impulse response (called the Green's function) derived below. For an infinite space, see the Green's function section **??**.

into equation (2), and taking the inner product of both sides with the eigenfunction $u_n(x)$, we obtain

$$\rho_0\omega^2 a_n(\omega) - \rho_0\omega_n^2 a_n(\omega) = -\rho_0 u_n(x_0) \qquad \text{i.}e. \qquad a_n(\omega) = -\frac{u_n(x_0)}{\omega^2 - \omega_n^2} \tag{8.8}$$

Finally, we return to the time domain by applying the inverse Fourier transform [note 3)].

$$a_n(t) = -\frac{1}{2\pi}\int_{-\infty}^{\infty} a_n(\omega)e^{-i\omega t}\,d\omega = -\frac{u_n(x_0)}{2\pi}\int_{-\infty}^{\infty}\frac{e^{-i\omega t}}{\omega^2 - \omega_n^2}\,d\omega \tag{8.9}$$

To evaluate this integral, we treat ω as a variable in the complex plane and integrate along the path shown in Figure 8.3, taking the limit $R \to \infty$. However, since the integral cannot be evaluated if there are poles on the integration path, we perform the integration for a function where the poles are shifted by $-i\epsilon$ ($\epsilon > 0$) from the real axis:

$$g(\omega, t, \epsilon) = \frac{e^{-i\omega t}}{2\omega_n}\left(\frac{1}{\omega - \omega_n + i\epsilon} - \frac{1}{\omega + \omega_n + i\epsilon}\right) \qquad \left(\lim_{\epsilon\to 0} g(\omega, t, \epsilon) = \frac{e^{-i\omega t}}{\omega^2 - \omega_n^2}\right) \tag{8.10}$$

and then take the limit $\epsilon \to 0$. Here, there are four possible combinations to consider depending on whether the two poles are shifted in the positive or negative imaginary direction, but the solution satisfies the differential equation in any case. However, to satisfy the physical condition of causality (i.e., there is no displacement before the external force is applied at $t = 0$), the two poles must be shifted in the negative direction.

For $t > 0$, the poles are enclosed within the integration contour, so:

$$\int_{C1} g(\omega, t, \epsilon)\,d\omega + \int_{C2} g(\omega, t, \epsilon)\,d\omega = -2\pi i\{\mathrm{Res}_{\omega=-i\epsilon+\omega_n} g(\omega, t, \epsilon) + \mathrm{Res}_{\omega=-i\epsilon-\omega_n} g(\omega, t, \epsilon)\} = -\frac{2\pi \sin\omega_n t\; e^{-\epsilon t}}{\omega_n}. \tag{8.11}$$

To prevent this expression from diverging as $t \to \infty$, the poles must be shifted in the negative direction. If they were shifted in the positive direction, it would be multiplied by an $e^{\epsilon t}$ term, which diverges as $t \to \infty$. Taking the limits $R \to \infty$ and $\epsilon \to 0$ in the above equation, the integral along path $C2$ becomes 0, yielding:

$$\int_{-\infty}^{\infty}\frac{e^{-i\omega t}}{\omega^2 - \omega_n^2}\,d\omega = -\frac{2\pi \sin\omega_n t}{\omega_n} \quad (t > 0). \tag{8.12}$$

On the other hand, for $t < 0$, there are no poles within the integration contour, so:

$$\int_{C1} g(\omega, t, \epsilon)\,d\omega + \int_{C3} g(\omega, t, \epsilon)\,d\omega = 0. \tag{8.13}$$

[note 3)] For more details on complex integration, refer to Mathematical Methods for Physicists, Fifth Edition, Arfken, Weber, and Frank Harris,[(1)] or introductory textbooks on special functions and integral transforms.

Taking the limit $R \to \infty$ in the above equation, the integral along path $C3$ vanishes, yielding:

$$\int_{-\infty}^{\infty} \frac{e^{-i\omega t}}{\omega^2 - \omega_n^2} d\omega = 0 \quad (t < 0). \tag{8.14}$$

From the above, the desired $u(x,t)$ for $t > 0$ becomes, based on the string excitation equation:

$$u(x,t) = \begin{cases} \sum_n \frac{u_n^*(x_0)u_n(x)}{\omega_n} \sin\omega_n t & t \geq 0 \\ 0 & t < 0 \end{cases} \tag{8.15}$$

Substituting the normalized eigenfunctions into this equation, the required $u(x,t)$ for $t > 0$ is:

$$u(x,t) = \sum_{n=1}^{\infty} a_n(t)u_n(x) = \sum_{n=1}^{\infty} \left[\frac{2\sin\omega_n t}{\rho_0 l \omega_n} \sin k_n x_0 \sin k_n x \right] \tag{8.16}$$

note 4). Here we define $k_n = n\pi/l$.

To improve visibility, we rewrite the above equation using sum-to-product trigonometric identities note 5).

$$\begin{aligned} u(x,t) = -\frac{1}{2\rho_0 l} \sum_{n=1}^{\infty} \frac{1}{\omega_n} [&\sin(\omega_n t - k_n(x + x_0)) - \sin(\omega_n t + k_n(x + x_0)) \\ &- \sin(\omega_n t - k_n(x - x_0)) + \sin(\omega_n t - k_n(x - x_0))] \end{aligned} \tag{8.17}$$

Looking closely at $\sum_{n=1}^{\infty} \frac{\sin\omega_n t}{\omega_n}$, taking the derivative gives a delta function shape. This means it is related to the Heaviside step function $H(t)$ note 6). It is a bit heuristic, but taking the Fourier series expansion of $H(x) - x/l$ in the interval $0 \leq x < l$, we get:

$$H(x) - x/l = \frac{2}{\pi} \sum_{n=1}^{\infty} \frac{1}{n} \sin k_n x, \tag{8.18}$$

Using this relation to rewrite the equation, we can express it as:

$$u(x,t) = \frac{1}{4\rho_0 c_0} \sum_{n=1}^{\infty} H_p(c_0 t + (x - x_0)) + H_p(c_0 t - (x - x_0)) - H_p(c_0 t - (x + x_0)) - H_p(c_0 t + (x + x_0)), \tag{8.19}$$

note 4) Considering the dimensions of the equation provides a better perspective. When an impulse of 1 [Ns] is applied, we calculate the momentum change, divide by the modal mass to compute the velocity, and then infer the displacement by dividing by the frequency.

note 5) For more details, refer to applied mathematics textbooks.

note 6) The Heaviside step function $H(t)$ is defined as follows:

$$H(t) = \begin{cases} 1 & t > 0 \\ 0.5 & t = 0 \\ 0 & t < 0 \end{cases}$$

where $H_p(x) = H(x) - H(-x)$ for $-l < x < l$, assuming a periodicity of $2l$ in space. Figure 8.4 shows a schematic diagram of the propagation immediately after $t = 0$. At $t = 0$, the first two terms perfectly cancel each other out [note 7)]. Propagation begins from there, and immediately after at $t = t_0$, the displacement spreads out from the center. This can also be interpreted as the string trying to move upwards upon receiving the impulse. When the leftward propagating wave $H_p(c_0t + (x - x_0))$ reaches the left end $x = 0$, its phase reverses to satisfy the boundary condition and reflects (fixed end reflection). The reflection is represented by $H_p(c_0t - (x - x_0))$. Near $x = 0$, it cancels out the amplitude of $H_p(c_0t - (x - x_0))$, so the displacement becomes 0.

The results of summing up to $n = 1, 2, \cdots, 40$ are shown in the left of Figure 8.5 and Figure 8.6. The parameters used are $\rho_0 = 1$[kg/m], $\kappa_0 = 1$ [N], $l = 1$ [m], $x_0 = 0.3$ [m]. In this case, information propagates at speed $c = 1$ [m/s]. A positive amplitude always propagates left and right from the location where the force was applied. When reflected at the fixed end, as shown in Figure 8.4, the sign of one side is reversed. As a result, the reflected wave cancels out the amplitude of the other wave to become 0.

Also, the results when substituting $\sin(\omega_n t)/\omega_n$ with $\exp(-\omega_n^2\tau_0^2)\cos(\omega_n t)$ and setting $\tau_0 = 0.01$ [s] are shown in the right of Figure 8.5 and Figure 8.6 [note 8)]. It can be observed that the pulse propagates in two directions from the source, and the phase reverses at both ends. Furthermore, the propagation velocity is 1 [m/s], which is consistent with the velocity $c_0 = \sqrt{\kappa_0/\rho_0} = 1$ [m/s] calculated from the given parameters.

The following is supplementary information. Next, let us consider the momentum change of the string. Applying an impulse of 1 Ns means that the rod should carry a momentum of 1 Ns until it senses the fixed end. Therefore, we calculate the momentum of the rod. First, for simplicity, we assume $0 < x < l/2$ and consider the time interval $0 < t < x_0/c_0$. The momentum can be written as:

$$\rho_0 \frac{du(x,t)}{dt} = \frac{\delta(c_0t + (x - x_0)) + \delta(c_0t - (x - x_0))}{2}. \tag{8.20}$$

As mentioned in the footnote, the right graph of Figure 8.5 and the graph of Figure 8.6 correspond to velocity waveforms, which is consistent with this analytical solution for the velocity. Integrating this over the entire rod gives a value of 1 [Ns]. In the time interval $x_0/c_0 < t < (l - x_0)/c_0$,

$$\rho_0 \frac{du(x,t)}{dt} = \frac{-\delta(c_0t + (l - x_0)) + \delta(c_0t - (x - x_0))}{2}, \tag{8.21}$$

and integrating over the entire space gives a total momentum of 0 [Ns]. That is, when the wave reaches the left end, because it is a fixed end, it receives a downward impulse of 1 [Ns] (the change in momentum).

8.2.1 Key Points

1. Do not forget the normalization. When κ_0, ρ_0 have spatial distributions, the eigenfunctions will not be orthogonal unless the inner product is defined including the density.

[note 7)] Note that we are considering $H_p(c_0t + (x - x_0))$ and $H_p(c_0t - (x - x_0))$ propagating in opposite directions. This is in the form of d'Alembert's solution and is intuitively easy to understand.

[note 8)] This substitution can be interpreted as taking the time derivative of $\sin(\omega_n t)/\omega_n$ to get a velocity waveform, and applying a low-pass filter with a period of τ_0.

2. When performing complex integration, note that the integration path must be changed depending on the sign of t. From the above discussion, we see that causality is satisfied only when poles exist below the real axis. Note that if a principal value integral is considered, the contribution of the integral around the singularities does not vanish even after taking limits[note 9)].

§8.3 Eigenvalue Problem: The SH Case

First, let us organize the equation of motion (Equation 5.19) and Hooke's law (Equation 5.22) for the plane wave of the SH problem. Here, we take s_y, T_{xz} as variables to consider the boundary conditions. Since the governing equations consist only of partial derivatives with respect to z, the first-order ordinary differential equation with respect to z can be written as:

$$\frac{d}{dz}\begin{pmatrix} s_y \\ T_{xz} \end{pmatrix} = \begin{pmatrix} 0 & \frac{1}{\mu} \\ \omega^2 p^2 \mu - \rho\omega^2 & 0 \end{pmatrix}\begin{pmatrix} s_y \\ T_{xz} \end{pmatrix} \tag{8.22}$$

Also, T_{yx} can be computed from s_y as

$$T_{yx} = \mathrm{i}\omega p \mu s_y. \tag{8.23}$$

We can think of this as integrating the ordinary differential equations from one boundary to find the parameter p that satisfies the required boundary conditions at the other end. This is nothing but an eigenvalue problem.

§8.4 Eigenvalue Problem for a Single-layer Structure

For simplicity, let us consider a case where the structure is homogeneous in the vertical z direction and consider it more concretely. To improve visibility, we rewrite the governing equations as:

$$\frac{d}{dz}\boldsymbol{y} = \boldsymbol{A}\boldsymbol{y}, \tag{8.24}$$

where,

$$\boldsymbol{A} \equiv \begin{pmatrix} 0 & \frac{1}{\mu} \\ \omega^2 p^2 \mu - \rho\omega^2 & 0 \end{pmatrix}, \tag{8.25}$$

$$\boldsymbol{y} \equiv \begin{pmatrix} s_y \\ T_{xz} \end{pmatrix}. \tag{8.26}$$

[note 9)] Instead of complex integration, one can also laboriously solve the problem by considering the continuation of the solution at $t = 0$.

Here, we consider the eigenvalue problem for matrix $\boldsymbol{A}$. Let the i-th eigenvalue be η_i and the corresponding eigenvector be $\boldsymbol{\phi}_i$. From the characteristic equation $|A - \eta_i \boldsymbol{I}| = 0$, we obtain

$$\eta_1 = \omega\sqrt{p^2 - \frac{1}{\beta^2}} \tag{8.27}$$

$$\eta_2 = -\omega\sqrt{p^2 - \frac{1}{\beta^2}} \tag{8.28}$$

The corresponding eigenvectors are

$$\boldsymbol{\phi}_1 = \begin{pmatrix} 1/\mu \\ \eta_1 \end{pmatrix} \tag{8.29}$$

$$\boldsymbol{\phi}_2 = \begin{pmatrix} 1/\mu \\ \eta_2 \end{pmatrix}. \tag{8.30}$$

They satisfy the relation

$$\boldsymbol{A}\boldsymbol{\phi}_i = \eta_i \boldsymbol{\phi}_i. \tag{8.31}$$

In this case, the matrix can be decomposed as

$$\boldsymbol{A} = (\boldsymbol{\phi}_1, \boldsymbol{\phi}_2)\begin{pmatrix} \eta_1 & \\ & \eta_2 \end{pmatrix}(\boldsymbol{\phi}_1, \boldsymbol{\phi}_2)^{-1} \equiv \boldsymbol{\Phi}\boldsymbol{H}\boldsymbol{\Phi}^{-1}, \tag{8.32}$$

where $\boldsymbol{H}$ is a diagonal matrix containing the eigenvalues η_i. By defining $\tilde{\boldsymbol{y}} \equiv \boldsymbol{\Phi}^{-1}\boldsymbol{y}$, we get

$$\frac{d}{dz}\tilde{\boldsymbol{y}} = \boldsymbol{H}\tilde{\boldsymbol{y}}, \tag{8.33}$$

which allows us to solve the differential equation component by component. Summarizing these solutions, the general solution can be written as

$$\boldsymbol{y} = \sum_{i=1}^{2} A_i e^{\eta_i z}\boldsymbol{\phi}_i. \tag{8.34}$$

§8.5 Eigenvalue Problem: The P-SV Case

Here, let us organize the equation of motion (Equation 5.19) and Hooke's law (Equation 5.22) for the plane wave of the P-SV problem. We take s_x, s_z, T_{xz}, T_{zz} as variables to account for the boundary conditions. Since the governing equations consist only of partial derivatives with respect to z, the first-order ordinary differential equation in z can be written as:

$$\frac{d}{dz}\begin{pmatrix} s_x \\ s_z \\ T_{xz} \\ T_{zz} \end{pmatrix} = \begin{pmatrix} 0 & -i\omega p & \frac{1}{\mu} & 0 \\ -i\omega p \frac{\lambda}{\lambda+2\mu} & 0 & 0 & \frac{1}{\lambda+2\mu} \\ -\rho\omega^2 + \omega^2 p^2 \frac{4\mu(\lambda+\mu)}{\lambda+2\mu} & 0 & 0 & -i\omega p \frac{\lambda}{\lambda+2\mu} \\ 0 & -\rho\omega^2 & -i\omega p & 0 \end{pmatrix} \begin{pmatrix} s_x \\ s_z \\ T_{xz} \\ T_{zz} \end{pmatrix} \tag{8.35}$$

Here, T_{xx} can be determined from s_x and T_{zx} as

$$T_{xx} = i\omega p(\lambda + 2\mu)s_x + \lambda \frac{ds_z}{dz}. \tag{8.36}$$

This means the problem is restated as finding the parameter p by integrating the ordinary differential equations from one boundary such that they satisfy the given conditions at the other boundary. This is simply an eigenvalue problem. The problem configuration in the first part of section 5.6.2 corresponds to integrating from the bottom and matching the boundary condition at the surface, while the second part corresponds to starting from the surface and matching the solution at infinity as the boundary condition.

8.5.1 Eigenvalue Problem for Homogeneous Structure

For simplicity, we consider a homogeneous structure in the vertical z direction to examine this more concretely. To improve clarity, we rewrite the governing equations as:

$$\frac{d}{dz}\boldsymbol{y} = \boldsymbol{A}\boldsymbol{y}, \tag{8.37}$$

where,

$$\boldsymbol{A} \equiv \begin{pmatrix} 0 & -\mathrm{i}\omega p & \frac{1}{\mu} & 0 \\ -\mathrm{i}\omega p \frac{\lambda}{\lambda+2\mu} & 0 & 0 & \frac{1}{\lambda+2\mu} \\ -\rho\omega^2 + \omega^2 p^2 \frac{4\mu(\lambda+\mu)}{\lambda+2\mu} & 0 & 0 & -\mathrm{i}\omega p \frac{\lambda}{\lambda+2\mu} \\ 0 & -\rho\omega^2 & -\mathrm{i}\omega p & 0 \end{pmatrix}, \tag{8.38}$$

$$\boldsymbol{y} \equiv \begin{pmatrix} s_x \\ s_z \\ T_{xz} \\ T_{zz} \end{pmatrix}. \tag{8.39}$$

We now consider the eigenvalue problem of the matrix $\boldsymbol{A}$. Assuming the i-th eigenvalue is η_i and the eigenvector is $\boldsymbol{\phi}^i$, the following relationship holds:

$$\boldsymbol{A}\boldsymbol{\phi}^i = \eta_i \boldsymbol{\phi}^i. \tag{8.40}$$

It can thus be decomposed as

$$\boldsymbol{A} = \left(\boldsymbol{\phi}_1, \boldsymbol{\phi}^2, \boldsymbol{\phi}^3, \boldsymbol{\phi}^4\right) \begin{pmatrix} \eta_1 & & & \\ & \eta_2 & & \\ & & \eta_3 & \\ & & & \eta 4 \end{pmatrix} \left(\boldsymbol{\phi}_1, \boldsymbol{\phi}^2, \boldsymbol{\phi}^3, \boldsymbol{\phi}^4\right)^{-1} \equiv \boldsymbol{\Phi} \boldsymbol{H} \boldsymbol{\Phi}^{-1}, \tag{8.41}$$

where $\boldsymbol{H}$ is a diagonal matrix containing η_i. Defining $\tilde{\boldsymbol{y}} \equiv \boldsymbol{\Phi}^{-1}\boldsymbol{y}$, we obtain

$$\frac{d}{dz}\tilde{\boldsymbol{y}} = \boldsymbol{H}\tilde{\boldsymbol{y}}, \tag{8.42}$$

allowing the differential equation for each component to be explicitly solved. The general solution is written as a superposition:

$$\boldsymbol{y} = \sum_{i=1}^{4} A^i e^{\eta_i z} \boldsymbol{\phi}^i. \tag{8.43}$$

8.5.2 Eigenvalues

Let us explicitly derive the eigenvalues. Calculating the determinant of the matrix $\boldsymbol{A} - \eta \boldsymbol{I}$ gives [note 10)]

$$|A| = \left(\eta^2 - \omega^2\left(p^2 - \frac{1}{\alpha^2}\right)\right)\left(\eta^2 - \omega^2\left(p^2 - \frac{1}{\beta^2}\right)\right) = 0, \tag{8.45}$$

which factors into this equation. We observe that these eigenvalues correspond to the vertical propagation of seismic waves. Additionally, η_i represents an evanescent wave when η_i^2 is positive, and a body wave when it is negative.

8.5.3 Eigenvectors

Let us write down the corresponding eigenvectors. For simplicity, we assume the horizontal displacement is finite and normalize it such that $\phi_{i,1} = 1$:

$$\mathbf{A}\begin{pmatrix} \phi_{i,1} \\ \phi_{i,2} \\ \phi_{i,3} \\ \phi_{i,4} \end{pmatrix} = \eta_i \begin{pmatrix} \phi_{i,1} \\ \phi_{i,2} \\ \phi_{i,3} \\ \phi_{i,4} \end{pmatrix}. \tag{8.46}$$

We evaluate row by row, reducing the variables to $\phi_{i,3}$ and $\phi_{i,4}$ to calculate the eigenvectors.

[note 10)] By straightforward cofactor expansion, one computes:

$$\begin{vmatrix} -\eta & a & b & 0 \\ c & -\eta & 0 & d \\ e & 0 & -\eta & c \\ 0 & f & a & -\eta \end{vmatrix} = \eta^4 - \eta^2(df + 2ac + be) + (ed - c^2)(bf - a^2) \tag{8.44}$$

Row 1

From the first row,

$$\phi_{i,2} = -\frac{\mathrm{i}\phi_{i,3}}{\omega p \mu} + \frac{\mathrm{i}\eta_i}{\omega p} \tag{8.47}$$

Row 2

Organizing the second row's components,

$$\eta_i \phi_{i,2} - \frac{1}{\lambda + 2\mu}\phi_{i,4} = -\mathrm{i}\omega p \frac{\lambda}{\lambda + 2\mu} \tag{8.48}$$

Substituting Equation 8.47, we get

$$\frac{\eta_i}{\mu}\phi_{i,3} - \frac{\mathrm{i}\omega p}{\lambda + 2\mu}\phi_{i,4} = \frac{\omega^2 p^2 \lambda}{\lambda + 2\mu} + \eta_i^2 \tag{8.49}$$

Row 4

$$-\rho\omega^2 \phi_{i,2} - \mathrm{i}\omega p \phi_{i,3} - \eta_i \phi_{i,4} = 0 \tag{8.50}$$

Substituting Equation 8.47, we get

$$-\rho\omega^2 \left(-\frac{\mathrm{i}\phi_{i,3}}{\omega p \mu} + \frac{\mathrm{i}\eta_i}{\omega p}\right) - \mathrm{i}\omega p \phi_{i,3} - \eta_i \phi_{i,4} = \tag{8.51}$$

$$\frac{\rho\omega i}{p\mu}\phi_{i,3} - \mathrm{i}\omega p \phi_{i,3} - \eta_i \phi_{i,4} - \frac{\mathrm{i}\rho\omega\eta_i}{p} = 0 \tag{8.52}$$

$$\left(\frac{\mathrm{i}\rho\omega}{\mu p} - \mathrm{i}\omega p\right)\phi_{i,3} - \eta_i \phi_{i,4} = \frac{\mathrm{i}\rho\omega\eta_i}{p} \tag{8.53}$$

2-Component Eigenvalue Problem

Combining the equations for $\phi_{i,3}$ and $\phi_{i,4}$, we obtain

$$\begin{pmatrix} \eta_i & -\frac{\mathrm{i}\omega p\mu}{\lambda+2\mu} \\ \frac{\mathrm{i}\omega}{p}\left(p^2 - \frac{\rho}{\mu}\right) & \eta_i \end{pmatrix} \begin{pmatrix} \phi_{i,3} \\ \phi_{i,4} \end{pmatrix} = \begin{pmatrix} \frac{\omega^2 p^2 \lambda\mu}{\lambda+2\mu} + \eta_i^2 \mu \\ \frac{-\mathrm{i}\rho\omega\eta_i}{p} \end{pmatrix} \tag{8.54}$$

By solving this system, $\phi_{i,3}$ and $\phi_{i,4}$ are explicitly expressed as:

$$\begin{pmatrix}\phi_{i,3}\\ \phi_{i,4}\end{pmatrix} = \begin{pmatrix}\eta_i & -\frac{\mathrm{i}\omega p\mu}{\lambda+2\mu}\\ \frac{\mathrm{i}\omega}{p}\left(p^2-\frac{\rho}{\mu}\right) & \eta_i\end{pmatrix}^{-1}\begin{pmatrix}\frac{\omega^2p^2\lambda\mu}{\lambda+2\mu}+\eta_i^2\mu\\ -\frac{\mathrm{i}\rho\omega\eta_i}{p}\end{pmatrix} \tag{8.55}$$

$$= \frac{1}{\Delta_i}\begin{pmatrix}\eta_i & \frac{\mathrm{i}\omega p\mu}{\lambda+2\mu}\\ -\frac{\mathrm{i}\omega}{p}\left(p^2-\frac{\rho}{\mu}\right) & \eta_i\end{pmatrix}\begin{pmatrix}\frac{\omega^2p^2\lambda\mu}{\lambda+2\mu}+\eta_i^2\mu\\ -\frac{\mathrm{i}\rho\omega\eta_i}{p}\end{pmatrix}, \tag{8.56}$$

$$= \frac{1}{\Delta_i}\begin{pmatrix}\eta_i & \frac{\mathrm{i}\omega p\beta^2}{\alpha^2}\\ -\frac{\mathrm{i}\omega}{p}\left(p^2-\frac{1}{\beta^2}\right) & \eta_i\end{pmatrix}\begin{pmatrix}\rho\beta^2\left(\frac{\omega^2p^2(\alpha^2-2\beta^2)}{\alpha^2}+\eta_i^2\right)\\ -\frac{\mathrm{i}\rho\omega\eta_i}{p}\end{pmatrix} \tag{8.57}$$

$$= \frac{1}{\Delta_i}\begin{pmatrix}\eta_i\rho\beta^2\left(\frac{\omega^2p^2(\alpha^2-2\beta^2)}{\alpha^2}+\eta_i^2\right)+\frac{\omega p\beta^2}{\alpha^2}\frac{\rho\omega\eta_i}{p}\\ -\frac{\mathrm{i}\omega}{p}\left(p^2-\frac{1}{\beta^2}\right)\rho\beta^2\left(\frac{\omega^2p^2(\alpha^2-2\beta^2)}{\alpha^2}+\eta_i^2\right)-\frac{\mathrm{i}\rho\omega\eta_i^2}{p}\end{pmatrix} \tag{8.58}$$

$$= \frac{1}{\Delta_i}\begin{pmatrix}\eta_i\rho\beta^2\left(\left(\omega^2p^2(1-2\frac{\beta^2}{\alpha^2})+\eta_i^2\right)+\frac{\omega^2}{\alpha^2}\right)\\ -\frac{\mathrm{i}\omega\rho}{p}\left(\beta^2\left(p^2-\frac{1}{\beta^2}\right)\left(\omega^2p^2(1-2\frac{\beta^2}{\alpha^2})+\eta_i^2\right)+\eta_i^2\right)\end{pmatrix} \tag{8.59}$$

where Δ_i is the determinant of $\boldsymbol{A}$,

$$\Delta_i = \eta_i^2 - \frac{\omega^2\mu}{\lambda+2\mu}\left(p^2-\frac{\rho}{\mu}\right) \tag{8.60}$$

$$= \begin{cases}\omega^2p^2\left(1-\frac{\beta^2}{\alpha^2}\right), & i=1,2\\ \omega^2\left(p^2-\frac{1}{\beta^2}\right)\left(1-\frac{\beta^2}{\alpha^2}\right), & i=3,4\end{cases} \tag{8.61}$$

Here, let us write out the corresponding eigenvectors case by case for each eigenvalue:

$$(\eta_1,\eta_2,\eta_3,\eta_4) = \omega\left(\sqrt{p^2-\alpha^{-2}},-\sqrt{p^2-\alpha^{-2}},\sqrt{p^2-\beta^{-2}},-\sqrt{p^2-\beta^{-2}}\right) \tag{8.62}$$

For $i=1,2$, which correspond to P-wave propagation,

$$\begin{pmatrix}\phi_{i,3}\\ \phi_{i,4}\end{pmatrix} = \frac{1}{\Delta_i}\begin{pmatrix}\eta_i\rho\beta^2\left(\left(\omega^2p^2(1-2\frac{\beta^2}{\alpha^2})+\eta_i^2\right)+\frac{\omega^2}{\alpha^2}\right)\\ -\frac{\mathrm{i}\omega\rho}{p}\left(\beta^2\left(p^2-\frac{1}{\beta^2}\right)\left(\omega^2p^2(1-2\frac{\beta^2}{\alpha^2})+\eta_i^2\right)+\eta_i^2\right)\end{pmatrix} \tag{8.63}$$

$$= \frac{1}{\Delta_i}\begin{pmatrix}\eta_i\rho\beta^2\left(\left(\omega^2p^2(1-2\frac{\beta^2}{\alpha^2})+\omega^2(p^2-\alpha^{-2})\right)+\frac{\omega^2}{\alpha^2}\right)\\ -\frac{i\omega\rho}{p}\left(\beta^2\left(p^2-\frac{1}{\beta^2}\right)\left(\omega^2p^2(1-2\frac{\beta^2}{\alpha^2})+\omega^2(p^2-\alpha^{-2})\right)+\omega^2(p^2-\alpha^{-2})\right)\end{pmatrix} \tag{8.64}$$

$$= \left(1-\frac{\beta^2}{\alpha^2}\right)\frac{\omega^2p\mu}{\Delta_i}\begin{pmatrix}2\eta_ip\\ -i\omega\left(2p^2-\frac{1}{\beta^2}\right)\end{pmatrix} \tag{8.65}$$

$$= \frac{\mu}{p}\begin{pmatrix}2\eta_ip\\ -\mathrm{i}\omega\left(2p^2-\frac{1}{\beta^2}\right)\end{pmatrix} \tag{8.66}$$

$$\begin{pmatrix}\phi_{i,1}\\ \phi_{i,2}\\ \phi_{i,3}\\ \phi_{i,4}\end{pmatrix} = \begin{pmatrix}1\\ -\frac{\mathrm{i}\eta_i}{\omega p}\\ 2\eta_i\mu\\ -\frac{\mathrm{i}\omega\mu}{p}\left(2p^2-\frac{1}{\beta^2}\right)\end{pmatrix} = \frac{\omega}{p}\begin{pmatrix}\frac{p}{\omega}\\ -\frac{\mathrm{i}\eta_i}{\omega^2}\\ 2\frac{\eta_i\mu p}{\omega}\\ -\mathrm{i}\mu\left(2p^2-\frac{1}{\beta^2}\right)\end{pmatrix} \tag{8.67}$$

On the other hand, for $i = 3, 4$, which correspond to S-wave propagation,

$$\begin{pmatrix}\phi_{i,3}\\ \phi_{i,4}\end{pmatrix} = \frac{1}{\Delta_i}\begin{pmatrix}\eta_i\rho\beta^2\left(\left(\omega^2p^2(1-2\frac{\beta^2}{\alpha^2})+\eta_i^2\right)+\frac{\omega^2}{\alpha^2}\right)\\ -\frac{\mathrm{i}\omega\rho}{p}\left(\beta^2\left(p^2-\frac{1}{\beta^2}\right)\left(\omega^2p^2(1-2\frac{\beta^2}{\alpha^2})+\eta_i^2\right)+\eta_i^2\right)\end{pmatrix} \tag{8.68}$$

$$= \frac{1}{\Delta_i}\begin{pmatrix}\eta_i\rho\beta^2\left(\left(\omega^2p^2(1-2\frac{\beta^2}{\alpha^2})+\omega^2(p^2-\beta^{-2})\right)+\frac{\omega^2}{\alpha^2}\right)\\ -\frac{\mathrm{i}\omega\rho}{p}\left(\beta^2\left(p^2-\frac{1}{\beta^2}\right)\left(\omega^2p^2(1-2\frac{\beta^2}{\alpha^2})+\omega^2(p^2-\beta^{-2})\right)+\omega^2(p^2-\beta^{-2})\right)\end{pmatrix} \tag{8.69}$$

$$= \left(1-\frac{\beta^2}{\alpha^2}\right)\frac{\omega^2\mu}{\Delta_i}\begin{pmatrix}\eta_i\left(2p^2-\frac{1}{\beta^2}\right)\\ -2\mathrm{i}\omega p\left(p^2-\frac{1}{\beta^2}\right)\end{pmatrix} \tag{8.70}$$

$$= \frac{\mu}{p^2-\frac{1}{\beta^2}}\begin{pmatrix}\eta_i\left(2p^2-\frac{1}{\beta^2}\right)\\ -2\mathrm{i}\omega p\left(p^2-\frac{1}{\beta^2}\right)\end{pmatrix} \tag{8.71}$$

$$\begin{pmatrix}\phi_{i,1}\\ \phi_{i,2}\\ \phi_{i,3}\\ \phi_{i,4}\end{pmatrix} = \begin{pmatrix}1\\ -\frac{\mathrm{i}\eta_i}{\omega}\frac{p}{p^2-\frac{1}{\beta^2}}\\ \mu\eta_i\frac{2p^2-\frac{1}{\beta^2}}{p^2-\frac{1}{\beta^2}}\\ -2\mathrm{i}\omega p\mu\end{pmatrix} = \frac{1}{\eta_i}\begin{pmatrix}\eta_i\\ -\frac{\mathrm{i}p}{\omega}\\ \mu\left(2p^2-\frac{1}{\beta^2}\right)\\ -2\mathrm{i}\omega p\mu\eta_i\end{pmatrix} \tag{8.72}$$

The general solution can be formulated as a linear combination of the eigenvectors scaled by the phase contribution of vertical propagation $e^{\eta_i z}$.

8.5.4 Boundary Conditions

In Section 5.6, we analyzed Rayleigh waves propagating in a semi-infinite medium. Here, let us consider a free boundary surface and verify if we obtain identical results.

Assuming a z-axis with upward chosen as positive, let $z = 0$ be the free surface. First, because we are representing a semi-infinite medium, $\mathbf{y}_2$ and $\mathbf{y}_4$ are physically inadmissable as their amplitudes diverge at $z = -\infty$. Hence, the solution must be represented by a linear combination of $\mathbf{y}_1$ and $\mathbf{y}_3$ alone. At the free boundary condition $z = 0$, the stresses T_{xz} and T_{zz} must be zeroes, yielding:

$$\begin{vmatrix}\phi_{1,3} & \phi_{3,3}\\ \phi_{1,4} & \phi_{3,4}\end{vmatrix} = 0. \tag{8.73}$$

By writing out and simplifying this characteristic equation, we acquire

$$16\left(-\frac{1}{\alpha^2}+\frac{1}{\beta^2}\right)p^6 + \left(\frac{16}{\alpha^2\beta^2}-\frac{24}{\beta^4}\right)p^4 + \frac{8}{\beta^6}p^2 - \frac{1}{\beta^8} = 0. \tag{8.74}$$

We assert that this is identical to the characteristic equation of Rayleigh waves, from which we can ascertain the Rayleigh wave phase velocity.

Problem 8.1

1. Derive equation 8.74.

§8.6 Eigenvalue problem for spherically symmetric structure

When considering global-scale oscillations, it is a good approximation to treat the Earth as having structure only varying in the vertical direction, and homogeneous in the horizontal direction (spherically symmetric structure). In this case, the P-SV and SH problems correspond to spheroidal mode and toroidal mode oscillations, respectively. In this section, let us consider the oscillation of a homogeneous sphere, which is the simplest among spherically symmetric structures. For oscillations in more general spherically symmetric structures, refer to Saito's textbook(7) or Dahlen and Tromp (1998).(3)

§8.7 Eigenvibration and eigenfrequency

(4), (6), (7), (11), (13)

§8.8 Normal mode solutions for a homogeneous gas sphere

For simplicity, let us consider the eigenfrequencies and eigenfunctions for a homogeneous gas sphere. Here we assume that the pressure $P(\boldsymbol{x};\omega)$ satisfies the wave equation

$$\nabla^2 P = -\frac{\omega^2}{c^2} P \tag{8.75}$$

The Laplacian in spherical coordinates can be written as

$$\nabla^2 = \frac{1}{r^2}\left(\frac{\partial}{\partial r}r^2\frac{\partial}{\partial r} + {\nabla_h}^2\right) \tag{8.76}$$

$${\nabla_h}^2 = \frac{1}{\sin\theta}\frac{\partial}{\partial\theta}\left(\sin\theta\frac{\partial}{\partial\theta}\right) + \frac{1}{\sin^2\theta}\frac{\partial^2}{\partial\varphi^2} \tag{8.77}$$

We assume that the pressure $P = R(r)Y(\theta,\varphi)$ can be separated by variables in the r, θ, ϕ directions into $R(r)$ and $Y(\theta,\varphi)$.

$$\frac{1}{r^2}\left[\frac{1}{R}\frac{\partial}{\partial r}\left(r^2\frac{\partial R}{\partial r}\right) + \frac{\nabla_h^2 Y}{Y}\right] = -\frac{\omega^2}{c^2}. \tag{8.78}$$

8.8.1 Horizontal direction

Since the right side does not depend on r, θ, or φ, $\frac{\nabla_h^2 Y}{Y}$ must not depend on θ, φ. Y_l^m which satisfies the boundary conditions on the spherical surface is known as a spherical harmonic function characterized by angular order l and azimuthal order m, and it satisfies

$$\nabla_h^2 Y_l^m = -l(l+1)Y_l^m. \tag{8.79}$$

8.8.2 Radial direction

Since the eigenfunction in the horizontal direction can be expressed with spherical harmonics, to find the eigenvalues and eigenfunctions for a homogeneous sphere we need to solve the eigenvalue problem of the ordinary differential equation

$$\frac{1}{r^2 R}\left(\frac{d}{dr}r^2\frac{d}{dr}R\right) = \frac{l(l+1)}{r^2} - \frac{\omega^2}{c^2}. \tag{8.80}$$

The first term on the right hand side represents the horizontal wavenumber, and ω in the second term represents the eigenvalue. The eigenfunctions must satisfy the boundary conditions: (i) pressure $R = 0$ at the surface $r = r_0$, and (ii) finite and continuous at the center $r = 0$. The eigenfunctions are known as spherical Bessel functions $j_l(\omega/cr)$, $n_l(\omega/cr)$. Since j_l takes finite values at the origin and n_l diverges, we know from the second boundary condition that R is proportional to j_l. Furthermore, from the first boundary condition, it must satisfy $j_l(\omega/cr_0) = 0$, and from this condition we can determine the eigenfrequency ω.

§8.9 †Vector spherical harmonics

In the previous section, we considered a gas sphere, but to consider the oscillations of an elastic sphere, we need to consider vector value wave equations instead of scalar ones.

Normal modes of a spherically symmetric Earth can be classified into two types: spheroidal modes and toroidal modes[note 11)]. All wavefields can be represented by a superposition of modes.

To represent spheroidal and toroidal modes, we need to extend spherical harmonics into vectors. The vector spherical harmonics are defined by

$$\boldsymbol{R}_{lm} = Y_l^m \hat{\boldsymbol{r}} \tag{8.81}$$

$$\boldsymbol{S}_{lm} = \nabla_h Y_l^m \tag{8.82}$$

$$\boldsymbol{T}_{lm} = -\hat{\boldsymbol{r}} \times \nabla_h Y_l^m \tag{8.83}$$

Because vector spherical harmonics are more complex, details are omitted, but for instance, eigenfunctions taking vector values satisfy relations with the horizontal Laplacian ∇_h^2, such as $\nabla_h^2 \boldsymbol{T}_{lm} = -l(l+1)\boldsymbol{T}_{lm}$. $\boldsymbol{R}$ and $\boldsymbol{S}$ correspond to spheroidal modes, and $\boldsymbol{T}$ corresponds to toroidal modes. For details, refer to Dahlen and Tromp (1998) p. 872[(3) note 12)].

8.9.1 Spheroidal mode

Spheroidal mode ${}_nS_l$: n represents the number of nodes in the radial direction, and l represents the number of nodes in the horizontal direction. P-SV waves can be represented by superpositions of spheroidal modes.

${}_0S_0$ is a mode of uniform expansion and contraction. This mode can only be excited with observable amplitudes by giant earthquakes. Because it involves only volume changes, the attenuation due to shear deformation is small, and once excited, it is known to continue oscillating for several months.

${}_0S_1$ corresponds to translational motion and cannot exist due to physical constraints. ${}_1S_2$ can exist physically because the inner and outer parts move in opposite directions to conserve momentum (known as the Slichter mode), but its amplitude is small and it is very difficult to detect.

${}_0S_2$ is known as the football mode and is known to have the lowest eigenfrequency among normally observed modes, with a period of about 20 minutes. Figure 8.8 shows the spectrum of the ground motion record observed in Japan during the 2004 Sumatra earthquake. This figure shows that it is excited with an observable amplitude (2 mm) during giant earthquakes. The reason multiple peaks are visible is that the eigenperiod changes depending on the propagation direction due to the Coriolis force effect. Theoretically, Lord Kelvin calculated the eigenfrequencies in the 19th century by approximating the Earth as a homogeneous elastic sphere.(14) Since each eigenfrequency reflects the internal structure of the Earth, active attempts at detection were made until the mid-20th century. The successful detection of the existence of Earth's free oscillations from observation records was first achieved during the 1960 Chilean earthquake using strainmeter records [Benioff et al. (1961)].(2) Since then, observation examples of Earth's free oscillations have accumulated, and research to estimate the Earth's internal structure from the measured eigenfrequencies has been actively conducted.

note 11) Here we assume horizontal heterogeneities are small enough to be ignored.

note 12) The definitions of spherical harmonics and vector spherical harmonics depend heavily on normalization, so it is important to first check which normalization is being followed.

The case of $n = 0$ is particularly called the fundamental mode and corresponds to Rayleigh waves.

8.9.2 Toroidal mode

Toroidal mode ${}_nT_l$: n represents the number of nodes in the radial direction, and l represents the number of nodes in the horizontal direction. SH waves can be described by superpositions of toroidal modes. The $n = 0$ case is particularly called the fundamental mode and corresponds to Love waves.

8.9.3 Correspondence between Earth's free oscillations and surface waves

In Figure 8.1 shown at the beginning of this chapter, we could observe wave groups of Rayleigh waves travelling around the Earth multiple times from the waveform recorded in Japan during the Chilean earthquake. Figure 8.10 shows its Fourier spectrum. The interval at which the wave groups appear corresponds to the time it takes for a surface wave to circumnavigate the Earth. Let us compare the spacing of spectral peaks in Figure 8.10 with the time required for a surface wave to circle the Earth. From the Jeans relation, letting the Earth's radius be R_E, the wavelength λ can be written as

$$\lambda_l = \frac{2\pi R_E}{l + 1/2} \tag{8.84}$$

The eigenfrequency f_l corresponding to l is obtained with phase velocity c_p as

$$f_l = \frac{c_p}{\lambda_l} = \frac{(l + 1/2)c_p}{2\pi R_E} \tag{8.85}$$

Roughly assuming $c_p = 4.5$ km/s, we get $f_{l+1} - f_l \sim 0.1$ mHz, which approximately matches the observed mode spacing.

Focusing on the envelope of the peaks, there seem to be periodic mounds. Let us consider these mounds. The absolute amplitude of the mode with azimuthal quantum number l (assuming $m = 0$), letting the angular distance between the source and observation station be Θ, can be written as

$$|P_l^0(\cos\Theta)| \sim \sqrt{\frac{2}{l\pi \sin\Theta}} |\cos[(l + 1/2)\Theta - \pi/4]| \tag{8.86}$$

Fixing Θ and changing l, we can see that a mound forms approximately every π/Θ and this repeats. For the Chilean earthquake, the angular distance to SGN is 154 degrees. In this case, waves gather at the antipode (directly opposite the source), so it is easier to estimate from the angle from the antipode (180-154) degrees[note 13)]. In this case, the width of a mound is estimated to be 7 in l, matching observations. These phenomena occur simply because the nodes of the mode repeatedly appear.

§8.10 Background Free Oscillations of the Earth

8.10.1 Discovery of Earth's Background Free Oscillations

In the Sun, it is known that turbulence near the surface continuously excites acoustic waves with a period of about 5 minutes. The velocity field of the solar surface is accurately observed

note 13) Of course, one can estimate at $\Theta = 150°$, but in that case care should be taken since l is an integer.

https://www.eri.u-tokyo.ac.jp/people/knishida/eng/seismology.html

from the ground, and the acoustic velocity structure and angular momentum distribution inside the Sun have been investigated in detail from the eigenperiods of the observed acoustic waves (Helioseismology). Kobayashi (1996) considered that a mechanism similar to the excitation mechanism of the 5-minute solar oscillations might also be effective for the Earth, Mars, and Venus. He theoretically estimated the magnitude of atmospheric disturbances and concluded that atmospheric disturbances cause observable levels of oscillations.

Following this, in 1998, Nawa et al. examined the data from the superconducting gravimeter at Syowa Station in Antarctica and discovered a phenomenon in which the solid Earth continuously oscillates in the period band of several hundred seconds even during periods of quiet seismic activity.(8) This was the discovery of Earth's background free oscillations. Because the superconducting gravimeter records in Antarctica contained unique noise associated with tide level fluctuations, the detection was not yet considered conclusive. However, following the detection using the Antarctic data, they were successively detected at observation stations around the world, such as by LaCoste gravimeters installed at IDA stations(12) and STS-1Z seismometers installed at IRIS/GEOSCOPE stations,(5) and their existence became conclusive. Currently, they have been detected at more than 100 observation stations.

Subsequent research has revealed that ocean waves are also deeply involved in the excitation. Research in the broad framework of the atmosphere-ocean-solid Earth coupled system is ongoing[note 14)].

[note 14)] For details, see the review articles by Nishida [2013, 2017].(9), (10)

§8.11 Bibliography

[1] G. Arfken and H. Weber. *Mathematical Methods for Physicists*. Elsevier Science, 2013.

[2] H. Benioff, F. Press, and S. Smith. Excitation of the free oscillations of the earth by earthquakes. *J. Geophys. Res.*, 66:605–619, 1961.

[3] F. Dahlen and J. Tromp. *Theoretical Global Seismology*. Princeton University Press, Princeton, 1998.

[4] F. Gilbert. Excitation of normal modes of the earth by earthquake sources. *Geophys. J. R. Astron. Soc.*, 22:223, 1971.

[5] N. Kobayashi and K. Nishida. Continuous excitation of planetary free oscillations by atmospheric disturbances. *Nature*, 395(September):357–360, 1998.

[6] G. Laske and R. Widmer-Schnidrig. 1.04 - theory and observations: Normal mode and surface wave observations. In G. Schubert, editor, *Treatise on Geophysics (Second Edition)*, pages 117–167. Elsevier, Oxford, Jan. 2015.

[7] S. Masanori. *Seismic Wave Theory*. University of Tokyo Press, 2009.

[8] K. Nawa et al. Incessant excitation of the Earth's free oscillations. *Earth Planet. Space*, 50:3–8, 1998.

[9] K. Nishida. Earth's background free oscillations. *Annu. Rev. Earth Planet. Sci.*, 41(1):719–740, May 2013.

[10] K. Nishida. Ambient seismic wave field. *Proc. Jpn. Acad. Ser. B Phys. Biol. Sci.*, 93(7):423–448, 2017.

[11] M. Saito. *DISPER80; a subroutine package for calculation of seismic normal-mode solutions*, pages 293–319. Acad. Press. San Diego, 1988.

[12] N. Suda, K. Nawa, and Y. Fukao. Earth's background free oscillations. *Science*, 279:2089–2091, 1998.

[13] H. Takeuchi and M. Saito. Seismology: Surface waves and free oscillations. In B. Bolt, editor, *Methos in Computational Physics*, volume 11, pages 217–295. Academic Press, New York, 1972.

[14] W. Thomson. On the rigidity of the earth. *Philosophical Transactions of the Royal Society of London*, 153:573–582, Jan. 1863.

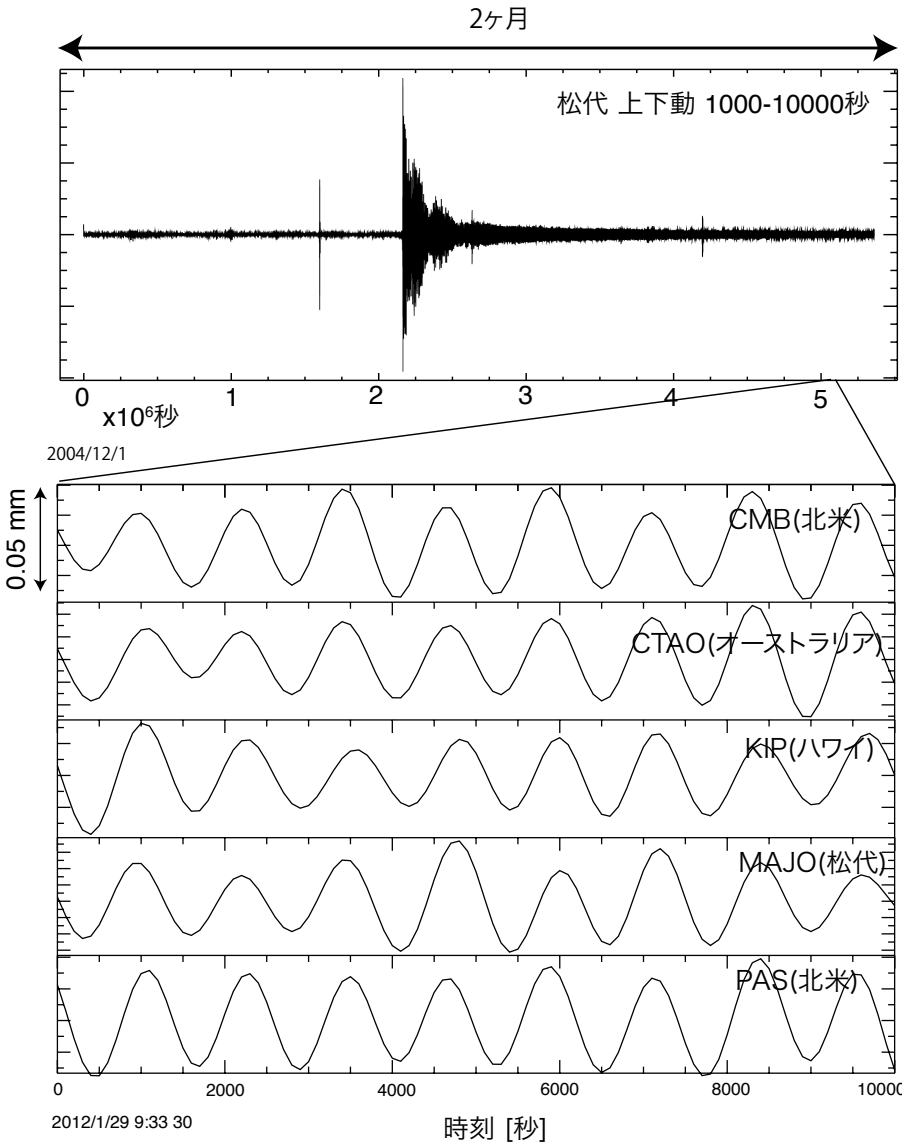

Figure 8.2: Ground motion records of the Sumatra earthquake. Filtered in the period band of 1000-10000 seconds. The upper panel shows the Earth oscillating for more than a month after the Sumatra earthquake. The lower panel is an enlarged view of the oscillations about one month after the earthquake. We can see simultaneous vertical movements around the world. This indicates that the entire Earth is repeatedly expanding and contracting.

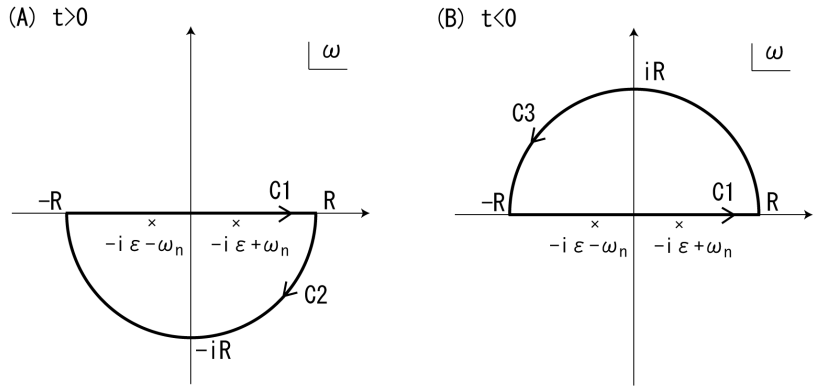

Figure 8.3: Integration path

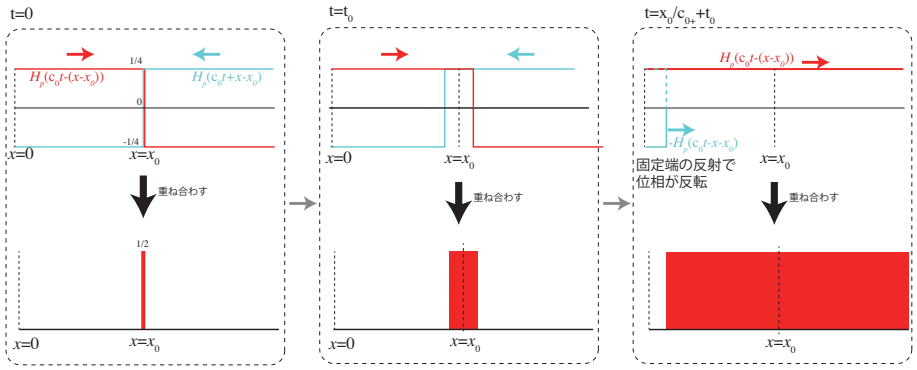

Figure 8.4: Schematic diagram.

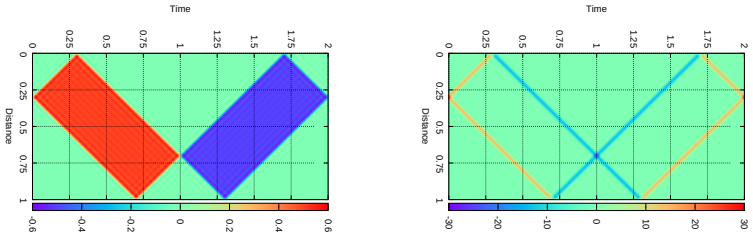

Figure 8.5: Calculated wave propagation.

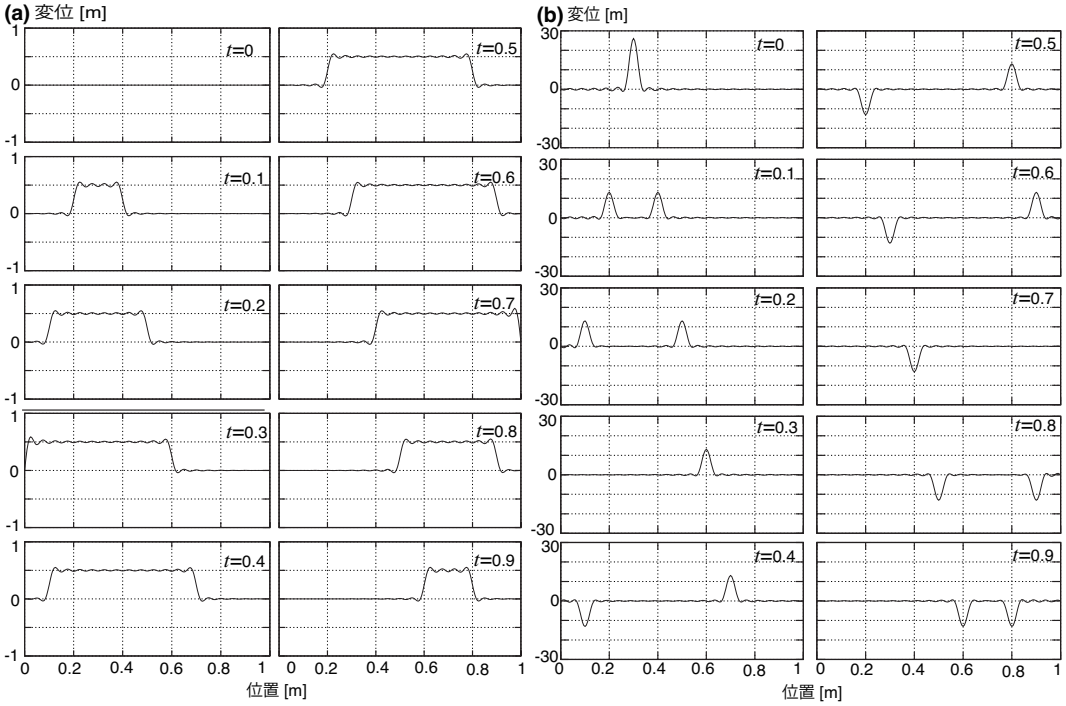

Figure 8.6: (a) Snapshot of calculated waveforms for the impulse response. (b) Snapshot of waveforms when the excitation term is substituted.

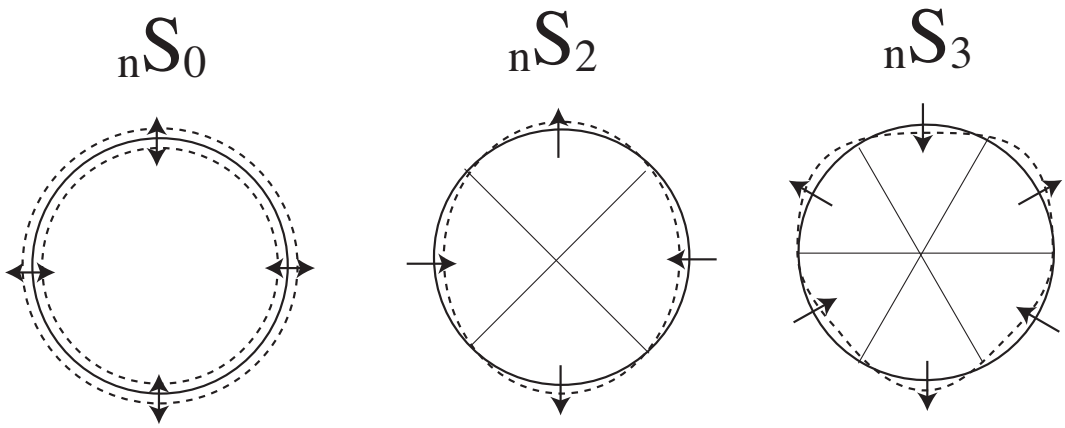

Figure 8.7: Examples of spheroidal modes.

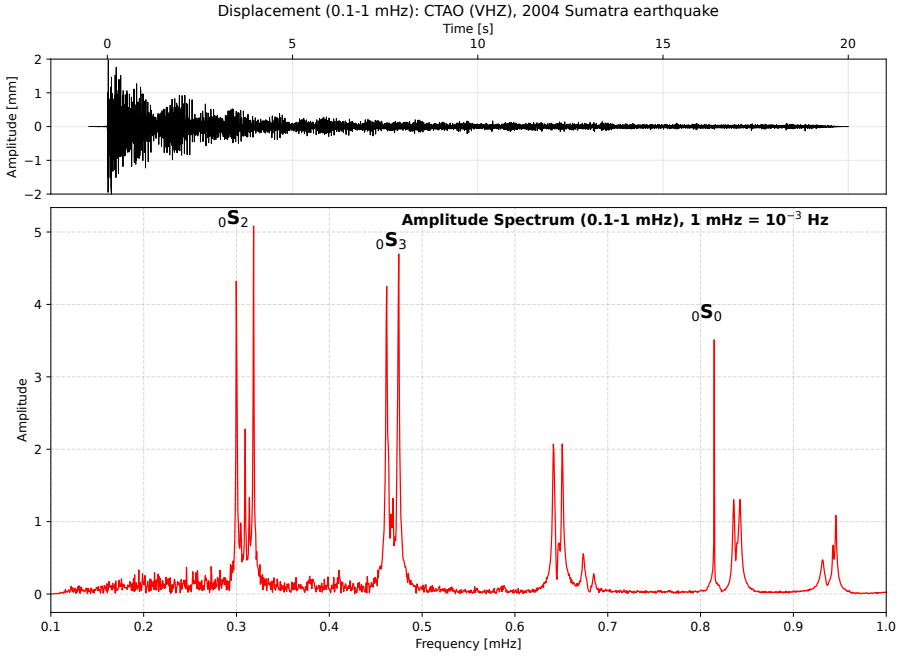

Figure 8.8: Ground motion record during the 2004 Sumatra earthquake.

https://www.eri.u-tokyo.ac.jp/people/knishida/eng/seismology.html

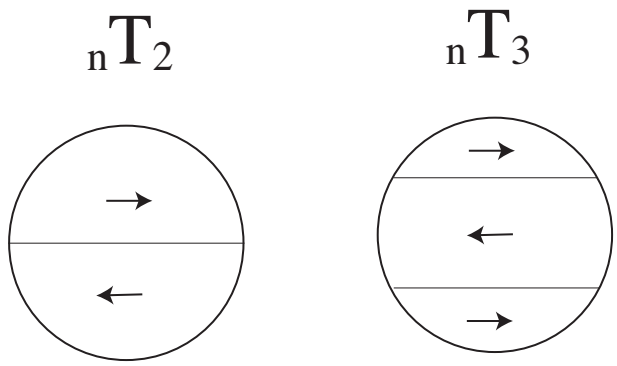

Figure 8.9: Examples of toroidal modes.

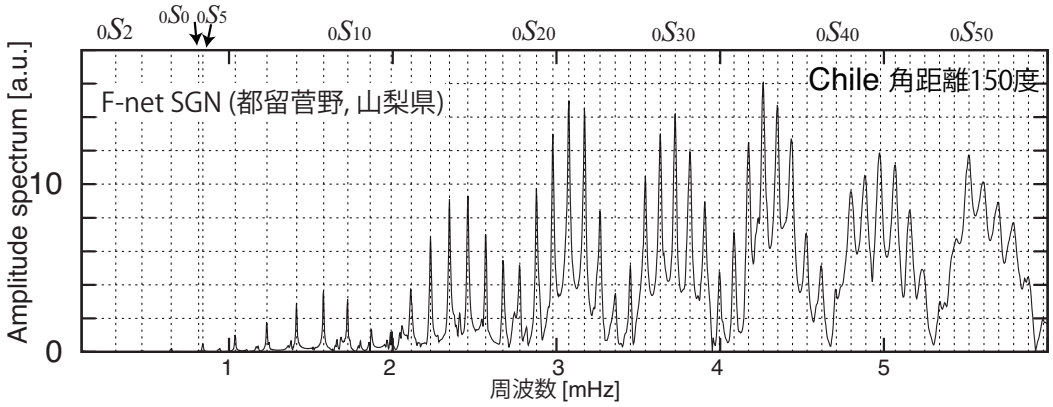

Figure 8.10: Fourier spectrum of the vertical ground motion recorded in Japan during the 2010 Chilean earthquake. We can observe many peaks corresponding to fundamental spheroidal modes. This is because the earthquake was shallow; for deep earthquakes, amplitude of overtones also becomes larger.

Waves in Fluids

Chapter 9

In this chapter, we will explain wave propagation in fluids. When considering wave propagation in the atmosphere and ocean, the restoring force due to gravity plays an essential role. As explained in Chapter **??**, gravity is naturally viewed from an Eulerian perspective, while stress is essentially naturally viewed from a Lagrangian perspective. Thus care must be taken when analyzing it. Therefore, in this chapter, we will first consider a zero-order approximate picture of waves in the atmosphere and ocean, and then explain their behavior based on the governing equations in the latter half.

§9.1 Boundary Waves: Lamb Waves and Ocean Gravity Waves

When considering atmospheric and oceanic waves, the Earth's surface must be treated as a different boundary condition. This is because the atmosphere is a gas and its density is much smaller than that of the ocean. Therefore, for the atmosphere, the surface can be approximated as a fixed boundary (rigid wall), whereas for the ocean, the surface can be approximated as a free boundary. First, as a simple example, we will explain the physical picture of atmospheric Lamb waves and oceanic gravity waves, which are boundary waves with amplitudes near the surface, in a simplified manner.

9.1.1 Lamb Waves

Considering sound waves in the ocean, do horizontally propagating sound waves exist near the water surface? As explained in Section 5.6.1, if the presence of the atmosphere can be neglected and the water surface can be regarded as a free boundary surface, horizontally propagating sound waves cannot exist. How about considering sound waves in the atmosphere?

For the atmosphere, the surface of the Earth can be approximated as a rigid wall. Therefore, we can see that we need to consider the boundary condition where the vertical displacement is 0. In other words, sound waves that repeatedly compress and expand only in the horizontal

direction can exist. These are known as atmospheric Lamb waves. As we will explain in detail later, strictly speaking, atmospheric Lamb waves arrive at a hydrostatic equilibrium in the vertical direction, and propagate at the speed of sound while repeatedly compressing and expanding in the horizontal direction.

It is known that when a large explosion occurs in the atmosphere, Lamb waves are actually generated and orbit the Earth. Recently, it was observed during the 2022 eruption of the Hunga Tonga-Hunga Ha'apai volcano (Figure 9.1). It has been reported that they were recorded by barometers worldwide during atmospheric nuclear tests along with the 1960s.[8] Also, it is known that atmospheric Lamb waves are steadily excited not only during volcanic eruptions but also continuously by meteorological phenomena.[9]

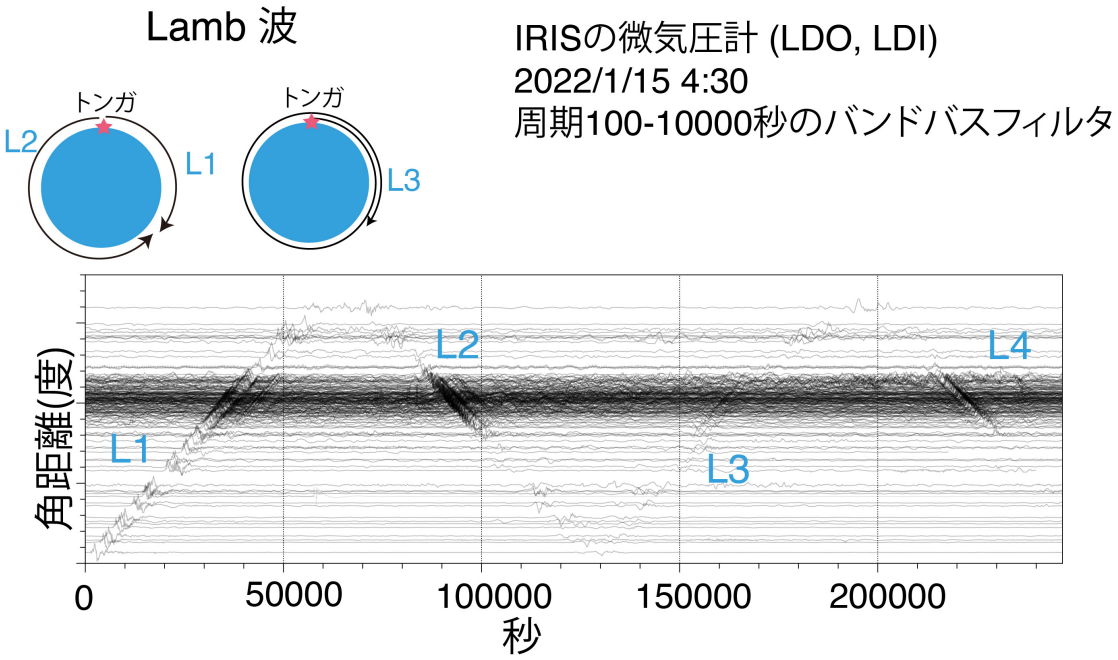

Figure 9.1: Barometer records when the Hunga Tonga-Hunga Ha'apai volcano erupted in 2022. The horizontal axis corresponds to a period of about 3 days, and the vertical axis corresponds to angular distances from 0° to 90°. You can see Lamb waves orbiting the Earth with a propagation speed of about 300 m/s.

9.1.2 Oceanic Gravity Waves

From the ocean's point of view, the sea surface behaves as a free end. As stated earlier, when considering sound waves propagating in a semi-infinite medium, horizontally propagating sound waves cannot exist due to the effect of the free surface. However, gravity waves, whose restoring force is gravity, exist in the ocean. First, let us build a physical picture of their behavior.

Shallow Water Waves

Oceanic gravity waves are called shallow water waves when their wavelength is longer than the water depth. Tsunamis are an example. Here let's roughly consider the physics behind the propagation.

Let the horizontal flow velocity be $\mathrm{i}\omega s_x$ and the vertical flow velocity be $\mathrm{i}\omega s_z$. When the wavelength is sufficiently long compared to the water depth, the flow can be considered two-dimensional, and the horizontal flow velocity becomes constant relative to the vertical direction. Assuming the water depth is H, considering the conservation of mass, we obtain

$$\mathrm{i}\omega \frac{ds_x}{dx} H + \mathrm{i}\omega\eta = 0 \tag{9.1}$$

where η represents the surface elevation.

The horizontal flow dominates and the pressure gradient generated by the sea surface fluctuation drives the flow. Therefore, the equation of motion becomes

$$-\rho\omega^2 s_x = -\frac{\partial \rho g \eta}{\partial x} \tag{9.2}$$

Eliminating s_x, we get

$$-\omega^2\eta = gH\frac{\partial^2\eta}{\partial x^2} \tag{9.3}$$

which indicates that the propagation velocity of shallow water waves is $\sqrt{gH}$.

Deep Water Waves

Although it may seem somewhat top-down, let us try to construct an intuitive physical picture for the case where the wavelength is sufficiently short compared to the water depth.

When considering a wave with angular frequency ω, the physical quantities that determine the system are only g and ρ. If we try to determine the propagation velocity from dimensional analysis, we find that the combination yielding velocity is only g/ω. It is expected that the propagation velocity becomes slower as the frequency increases. This is because the restoring force due to gravity works two-dimensionally near the water surface, whereas the mass moved by the wave is proportional to the cube of its wavelength.

Let's consider how the conservation of mass and the equation of motion balance. When the wavelength is shorter than the depth, the resulting flow is limited to a depth of roughly the wavelength near the water surface. Letting the wavelength be λ, the conservation of mass implies

$$\mathrm{i}\omega \frac{ds_x}{dx}\lambda \propto -\mathrm{i}\omega\eta \tag{9.4}$$

Recalling the relation that the wavelength $\lambda = 2\pi/k$, we have

$$\frac{ds_x}{dx} \propto -k\eta \tag{9.5}$$

Considering the flow directly beneath the sea surface, it is driven by the pressure gradient caused by fluctuations in the surface elevation. Therefore, the equation of motion reads

$$-\rho\omega^2 s_x = -\frac{\partial \rho g \eta}{\partial x} \tag{9.6}$$

Eliminating s_x, we have

$$-\omega^2\eta \propto \frac{g}{k}\frac{\partial^2\eta}{\partial x^2} \tag{9.7}$$

In other words, the phase velocity of deep water waves is proportional to g/ω. Since this is an order-of-magnitude estimation, the proportionality coefficient cannot be evaluated. However, as derived later, we'll see that the proportionality coefficient is exactly 1. Because the group velocity is given by $\frac{d\omega}{dk}$, it can be deduced to be $g/(2\omega)$.

As an example, let us look at ocean bottom pressure gauge records during the 2022 eruption of the Hunga Tonga volcano. Figure 9.2 shows the running spectrum of the ocean bottom pressure gauge records observed in the Tohoku region. The vertical axis represents frequency, and the horizontal axis represents time. We can observe that the arrival time is linearly delayed in proportion to the frequency. Because the arrival time can be calculated by dividing the epicentral distance by the group velocity, we understand that it illustrates the dispersion characteristic of deep water waves.

Problem 9.1

1. From Figure 9.2, one can estimate the distance from the observation station to the Hunga volcano. Read the numerical values from the figure and evaluate that distance.

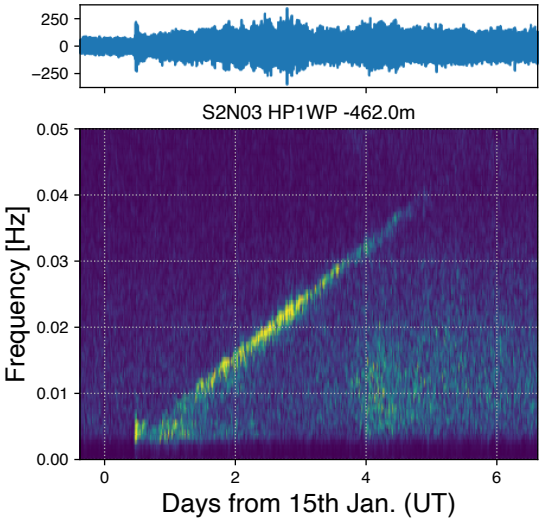

Figure 9.2: Oceanic gravity waves excited when the Hunga Tonga volcano erupted in 2022. It can be seen that the arrival time is delayed as the frequency becomes higher. This indicates that the group velocity is inversely proportional to frequency. We used ocean bottom pressure gauges from the S-net observation stations.

9.1.3 Wake Waves

In the introduction, we used the waves created by ducks on the water surface as an example to explain dispersion. Let us consider this in more detail here. The waves created by ducks are known as wake waves. For example, assume a ship is moving to the right at 20 m/s. Assuming simply that the ship is generating concentric waves at each time step, one can represent the wake wave by integrating the two-dimensional Green's function along the movement of the ship. Figure 9.3 reveals an actual calculation result. We can observe a pattern similar to the waves originated by ducks (known as the Kelvin wave pattern). Furthermore, if one were to observe the V-shaped waves at a single point in space, we recognize that higher-frequency components arrive later, reflecting the effects of dispersion.

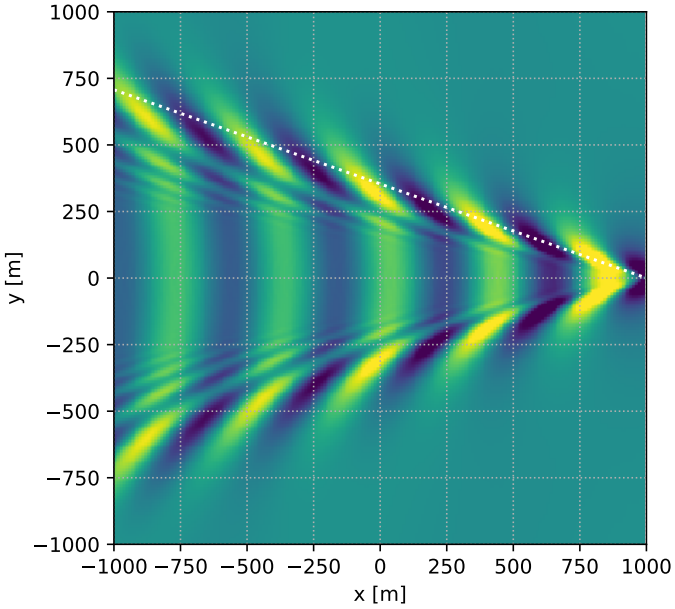

Figure 9.3: An example of a wake wave. The ship moves at 20 m/s and the upper limit of frequency is 0.25 Hz.

First, let us examine the phase velocity at frequency ω. For simplicity, assume there is no dispersion. Let the ship be moving toward the right at speed V in Figure 9.4(a). Similar to when analyzing the forerunner wave in Section 6.4.4, let us reflect on Huygens' principle. Two surfaces of equal phase extend backwards from the ship. This is known as a Mach cone (or shock cone). Assuming the angle is denoted by θ as in (b), the relation $\sin\theta = c_p/V$ is held between the phase velocity c_p and the ship speed V.

In the case of deep water waves, the problem becomes more complex because the group velocity is $1/2$ of the phase velocity. As shown in Figure 9.4(b), because the wave group progresses only $1/2$ relatively to the phase, the amplitude enlarges along the thick red line depicted in the figure. Let the included angle of this line be α. Since the phase itself is parallel to the constant-phase plane, slanted lines align along the thick red line as shown in Figure (b). The phase velocity

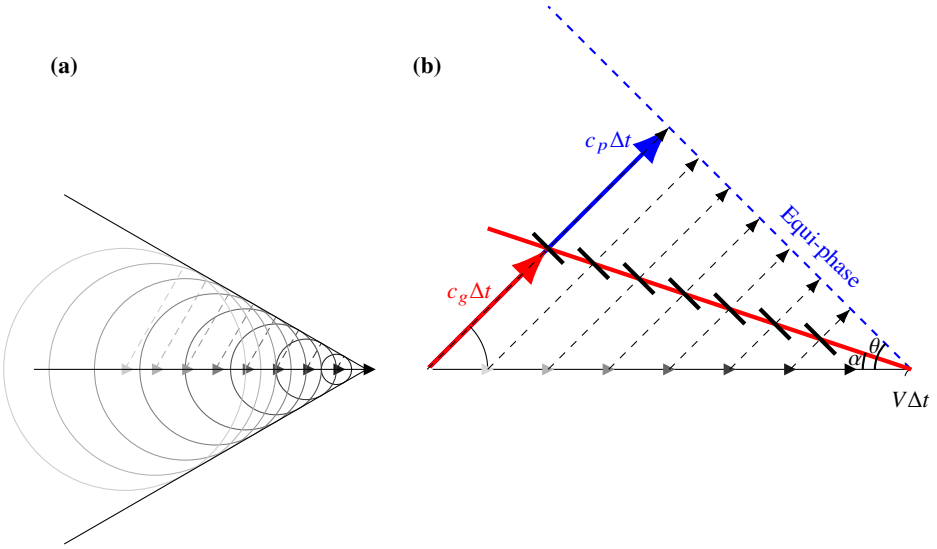

Figure 9.4: (a) Case with no dispersion. It corresponds to the shock cone formed by shock waves. (b) Schematic diagram of wake wave generation. It is vital to understand the relationship between the group velocity and phase velocity.

($c_p = g/\omega$) and the group velocity ($c_g = g/(2\omega)$) are dependent on the frequency, indicating the angles α and θ depend strictly on frequency.

Now, let us examine the relationship between the angles α and θ. Through geometric interactions and trigonometric addition formulas, α and θ relate as follows:

$$\tan\alpha = \frac{1}{2}\frac{\tan\theta}{1+\frac{\tan^2\theta}{2}} \tag{9.8}$$

By differentiating with respect to $\tan\theta$ as a variable, we find that $\tan\alpha$ reaches its local maximum precisely at $\tan\alpha = \sqrt{2}/4$. Recalling the method of stationary phase (Section 6.4.5), it is expected that contributions near the local maximum of $\tan\alpha$ are large. This occurs because wave components of various wavelengths overlap in phase, consequently enhancing the amplitude. Regardless of the boat's speed, waves exhibit huge amplitudes at a constant angle α. Simply put, assuming the boat radiates waves equally at all frequencies, the angle α formed by the wave group is independent of frequency and equates to $\arctan\left(\sqrt{2}/4\right) \sim 19°$.

In Figure 9.3, not only the wave groups aligned at angle α can be seen, but also wavefronts orthogonal to the propagating direction. Let us think about these low-frequency groups of waves. Assuming the speed of the boat is unchanged, the regions on the left of the peak correspond to slower waves in Figure 9.5, while the right side corresponds to faster waves. Simply put, the portion to the left of the maximum corresponds to the wavefronts currently under theoretical consideration. The equi-phase surfaces are fundamentally orthogonal to the advancing direction, while the wave groups tend to be concentrated close to the x-axis. It suggests that a wavefront progresses horizontally along the x-axis at a very low frequency, remaining perpendicular to the direction. Clearly, this is the component we detected in Figure 9.3.

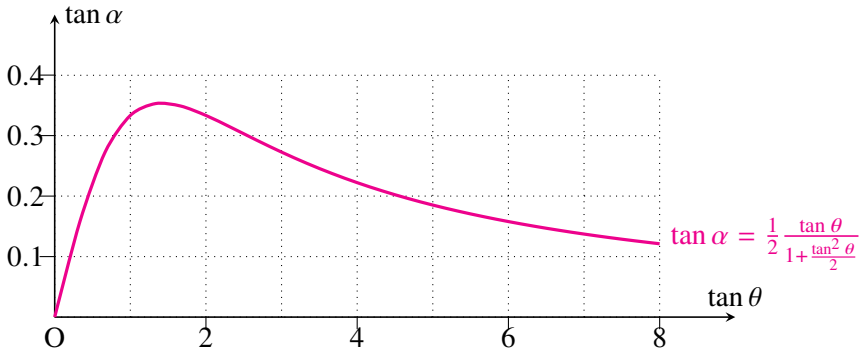

Figure 9.5: Relationship between the angle θ formed by equal-phase surfaces and angle α of the wave group. Fixing the speed of the ship, values right of the local maximum refer to faster waves, while left refers to slower waves. Because we derive with the angle θ, the wave propagation speed is constantly slower than the moving speed of the ship. Hence, a low-frequency cutoff establishes automatically from $g/2\omega = V$.

Problem 9.2

1. Derive equation 9.8.
2. Assuming the ship propagates at 20 m/s and radiates equally across all frequencies. Deduce the dominant frequency operating as a wave group.
3. Providing a figure mirroring Figure 9.4(b) as θ approaches 90°, elaborate on the characteristics of the resulting wave groups.

§9.2 Fluid motion incorporating the effect of gravity

Here we will consider the equations that describe wave propagation in the atmosphere and ocean.

When considering wave propagation in the atmosphere and ocean, the effect of gravity plays an important role compared to the propagation of seismic waves in solid bodies. The effects of gravity can be broadly divided into two. Here let us look at each effect [note 1)].

The first is hydrostatic pressure. When assuming hydrostatic equilibrium is reached, the vertical pressure gradient and gravity balance each other. In the case of the atmosphere, pressure and density decrease exponentially, and in the case of the ocean, hydrostatic pressure increases proportionally to the water depth. When considering the initial stress that balances gravity in

[note 1)] For details, refer to Chapter 6.14 Adjustment to Equilibrium in a Stratified Compressible Fluid of Gill's textbook.[5] For a more detailed understanding of atmospheric sound waves, the out-of-print textbook by Gossard[6] is a good resource.

https://www.eri.u-tokyo.ac.jp/people/knishida/eng/seismology.html

a steady state, care is required because the Eulerian perspective differs from the Lagrangian perspective.

The second effect is its role as a restoring force. As mentioned earlier, the atmosphere is density-stratified (becomes progressively thinner with altitude) due to gravity. Therefore, when oscillating vertically, buoyancy becomes an important restoring force. In this case, we need to consider not only sound waves but also gravity waves with gravity as the restoring force. It is easy to envision waves forming on the interface between oil and water in a dressing.

Assuming the time constant we are focusing on is sufficiently shorter than the rotation period, effects of Earth's rotation such as centrifugal and Coriolis forces are neglected. Also, for simplicity, advection effects such as mean winds are assumed to be negligible.

In the low-frequency band, atmospheric gravity waves, which have gravity as a restoring force, play an important role. When considering atmospheric gravity waves, the change in the gravitational potential caused by density changes can be approximated as being sufficiently smaller than buoyancy. Therefore, the gravitational potential here is neglected as being sufficiently smaller than the gravitational acceleration g_0, but the effect of g_0 is taken into account (the Boussinesq approximation? The Cowling approximation ignores self-gravity)[(1), (3)note 2)].

Let us summarize this into the form of differential equations with the vertical displacement U and stress T_{zz} as independent variables. We assume homogeneity in the horizontal direction. The complication arises because everything except stress takes Eulerian perturbations, whereas stress is Lagrangian. This is because the stress caused by deformation (Lagrangian) is added to the initial stress prior to deformation. Let the position before deformation be $\boldsymbol{x}$, the position after deformation be $\boldsymbol{r}$, and the displacement be $\boldsymbol{s} \equiv (U, V)^T = \boldsymbol{r} - \boldsymbol{x}$. The stress at position $\boldsymbol{r}$ is $-p_0(\boldsymbol{x}) + T_{zz}$. The hydrostatic pressure $p_0(\boldsymbol{r})$ at position $\boldsymbol{r}$ is $\approx p_0(\boldsymbol{x}) - \rho_0 g_0 U$. Hence, the Eulerian stress perturbation at position $\boldsymbol{r}$ is $T_{zz} + \rho_0 g_0 U$.

Equation of motion

$$-\rho_0\omega^2 V = \frac{d(T_{zz} + \rho_0 g_0 U)}{dx} \tag{9.9}$$

$$-\rho_0\omega^2 U = \frac{d(T_{zz} + \rho_0 g_0 U)}{dz} - g_0 \boldsymbol{\nabla} \cdot (\rho_0 \boldsymbol{s}) \tag{9.10}$$

The last term in the second equation is the result of substituting the mass conservation equation (Section **??**) into the buoyancy term.

From the horizontal component

$$V = -\frac{\mathrm{i}k}{\rho_0\omega^2}(T_{zz} + \rho_0 g_0 U) \tag{9.11}$$

note 2) When calculating seismic waves, it is also possible to incorporate a fluid layer to account for the effects of the outer core or the ocean.[(4), (7), (10)]

From the vertical component

$$-\rho_0\omega^2 U = \frac{d(T_{zz}+\rho_0 g_0 U)}{dz} - \boldsymbol{\nabla}\cdot(\rho_0 \boldsymbol{s})g_0 \tag{9.12}$$

$$= \frac{d(T_{zz}+\rho_0 g_0 U)}{dz} - \left(\mathrm{i}kg_0\rho_0 V + \frac{d(\rho_0 U)}{dz}\right) \tag{9.13}$$

$$= \frac{dT_{zz}}{dz} - \mathrm{i}kg_0\rho_0 V \text{ substituting horizontal component equation}$$

$$= \frac{dT_{zz}}{dz} + \frac{k^2 g_0}{\omega^2}(T_{zz}-\rho_0 g_0 U) \tag{9.14}$$

Assuming adiabatic deformation, from the equation of state (which must be considered in a Lagrangian manner: Section **??**),

$$-\rho_0\boldsymbol{\nabla}\cdot(\boldsymbol{s}) = \frac{T_{zz}}{c_s^2} \tag{9.15}$$

Summarizing,

$$\frac{d}{dz}\begin{pmatrix} U \\ T_{zz}\end{pmatrix} = \begin{pmatrix} \frac{k^2 g_0}{\omega^2} & \frac{1}{C}-\frac{k^2}{\rho\omega^2} \\ -\rho\omega^2+\frac{k^2\rho g_0^2}{\omega^2} & -\frac{k^2 g_0}{\omega^2}\end{pmatrix}\begin{pmatrix} U \\ T_{zz}\end{pmatrix} \tag{9.16}$$

where z represents altitude, U is vertical displacement, and T_{zz} is stress. Here C is the bulk modulus, which is related to the sound speed c_s, density ρ, pressure p, and specific heat ratio γ by

$$C = \rho c_s^2 = \rho\left(\frac{\gamma p}{\rho}\right). \tag{9.17}$$

By simply taking the pressure as $p = -T_{zz}$, it may seem to match the hydrodynamic formulation. However, since the pressure perturbation is also taken as Eulerian in the fluid case, to compare with hydrodynamics results, it is necessary to consider the change in hydrostatic pressure due to deformation as $p = -T_{zz} + \rho_0 g_0 U$[note 3)].

9.2.1 Ocean gravity waves

For simplification, density is approximated as a constant. Also, since the speed of sound is sufficiently faster than the speed of oceanic gravity waves, we set $1/C = 0$. The eigenvalues of the matrix are $\pm k$, and the corresponding eigenvectors are

$$\begin{pmatrix} 1 \\ \rho_0 g_0\left(1-\frac{\omega}{kg_0}\right)\end{pmatrix}, \begin{pmatrix} 1 \\ \rho_0 g_0\left(1+\frac{\omega}{kg_0}\right)\end{pmatrix}, \tag{9.18}$$

note 3) In elastic bodies, hydrostatic pressure arises from a decrease in timescale longer than viscous relaxation. Since the deformation of seismic waves is sufficiently shorter than the viscous relaxation timescale, the hydrostatic pressure preserves its pre-deformation value (can be considered frozen). It is possible to consistently handle it as Eulerian, but conventionally in seismology, only stress is often handled in a Lagrangian manner.

https://www.eri.u-tokyo.ac.jp/people/knishida/eng/seismology.html

As for the solution, it must satisfy the boundary conditions $U = 0$ at the seabed and $T_{zz} = 0$ at the water surface (because stress is treated in a Lagrangian manner). Letting the water depth be H, from the boundary conditions we get

$$\tanh kH = \frac{\omega^2}{kg_0}, \tag{9.19}$$

This equation signifies the dispersion relation for oceanic gravity waves.

9.2.2 Waves in the atmosphere

When considering that the atmosphere has reached hydrostatic equilibrium, the vertical pressure gradient and gravity balance. As a result, pressure and density attenuate exponentially. Let H_s be defined as the scale height, which is the altitude interval over which the pressure drops to $1/e$. The scale height is an important physical quantity characterizing the atmospheric structure. In this section, let us consider an atmospheric structure that is density-stratified.

To be consistent with the description in meteorology (fluid dynamics), the stress is rewritten as pressure p viewed from an Eulerian perspective, and the vertical displacement U is rewritten as vertical velocity w.

$$P = \sqrt{\rho}(-T_{zz} + \rho g U) \tag{9.20}$$

$$W = \frac{\mathrm{i}\omega U}{\sqrt{\rho}}. \tag{9.21}$$

Changing variables and rearranging the equation,

$$\frac{d}{dz}\boldsymbol{x}(z) = \boldsymbol{A}(z)\boldsymbol{x}(z), \tag{9.22}$$

where,

$$\boldsymbol{A}(z) = \begin{pmatrix} \frac{1}{2}\left(\frac{g}{c^2} - \frac{N^2}{g}\right) & -\frac{k^2}{i\omega}\frac{\omega^2 - L(k)^2}{L(k)^2} \\ \frac{N^2-\omega^2}{i\omega} & -\frac{1}{2}\left(\frac{g}{c^2} - \frac{N^2}{g}\right) \end{pmatrix}, \tag{9.23}$$

$$\boldsymbol{x}(z) = \begin{pmatrix} P(z) \\ W(z) \end{pmatrix}. \tag{9.24}$$

There are two important frequencies characterizing waves in the atmosphere: the buoyancy frequency (Brunt-Väisälä frequency) N and the acoustic cut-off frequency N_a, which satisfy the following relations:

$$L(k)^2 \equiv k^2 c^2, \tag{9.25}$$

$$N^2 \equiv \frac{g}{H_\rho} - \frac{g^2}{c^2}, \tag{9.26}$$

$$N_a \equiv \frac{c}{2H_\rho}, \tag{9.27}$$

where H_ρ is a quantity called the density scale height, defined by

$$H_\rho = -\frac{dz}{d\ln\rho}. \tag{9.28}$$

There are two frequencies characterizing waves in the atmosphere: the buoyancy frequency (Brunt-Väisälä frequency) N, and the cut-off frequency N_a, which are defined as follows:

$$\begin{aligned} N^2 &= -\frac{g}{\rho_0}\frac{d\rho_0}{dz} - \frac{g^2}{c_s^2}, \\ N_a &= \frac{c_s}{2H_s}, \end{aligned} \tag{9.29}$$

where g is the gravitational acceleration, ρ_0 is the density, z is the altitude, and c_s is the speed of sound.

First, let us consider the buoyancy frequency N. Consider a small volume element. Due to density stratification, buoyancy occurs. Negative buoyancy acts when moving upwards, and positive buoyancy acts when moving downwards. As a result, oscillation takes place. This frequency is the buoyancy frequency.

Next, let us consider the cut-off frequency N_a. N_a is the lowest frequency limit at which sound waves can exist. Below this frequency, sound waves cannot exist. As can be seen from the definition, the wavelength of the sound wave at frequency N_a is $4\pi H_s$. That means the wavelength of the sound wave becomes sufficiently thicker than the atmospheric thickness H_s, so it can no longer be supported as a sound wave. N_a is always higher than the buoyancy frequency N. Elaborating broadly on the actual atmosphere, though it varies with altitude, the buoyancy frequency is roughly around 400 seconds, and the cut-off frequency is around 300 seconds.

Here, for simplicity, we consider an isothermal atmosphere. In the case of an isothermal atmosphere, the speed of sound is constant, meaning the scale height is constant, so we can write $\boldsymbol{x}(z) \sim e^{\lambda r}$. Thus, the characteristic equation is,

$$\det(\boldsymbol{A} - \lambda \boldsymbol{I}) = \lambda^2 + \frac{f(\omega^2)}{c^2\omega^2} = 0, \tag{9.30}$$

where f is defined as

$$f(\omega^2) = \omega^4 - (L(k)^2 + N_a^2)\omega^2 + L(k)^2 N^2. \tag{9.31}$$

Here, let two characteristic frequencies ω_+^2 $\omega_-^2 (\omega_+^2 > \omega_-^2)$ be the solutions to the characteristic equation satisfying the relation:

$$f(\omega^2) = 0. \tag{9.32}$$

Figure 9.6 shows the dispersion relation of atmospheric gravity waves and sound waves. The two frequencies ω_+ and ω_- classifying atmospheric gravity waves and sound waves allow us to divide the propagation modes. The region where they can propagate vertically as sound waves is indicated in blue, and the region where they can propagate vertically as gravity waves in red. The white region $(\omega_- < \omega < \omega_+)$ corresponds to the evanescent region[note 4)] where λ^2

[note 4)] In seismology, it is called an inhomogeneous wave, and in the atmosphere and ocean, it is also called an external wave, but physically refers to the same phenomenon.

https://www.eri.u-tokyo.ac.jp/people/knishida/eng/seismology.html

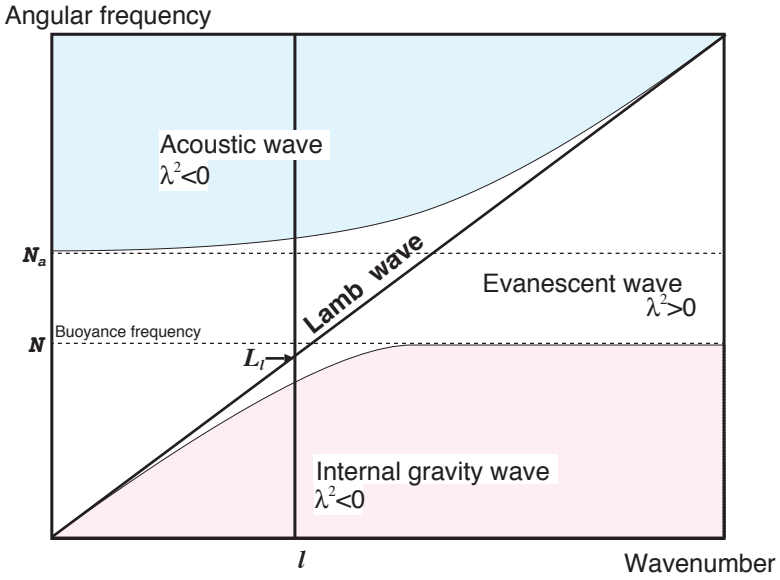

Figure 9.6: Dispersion relation of atmospheric gravity waves and sound waves. Two frequencies ω_+ and ω_- characterizing atmospheric gravity waves and sound waves act as a divide between regions where propagation as a wave in the vertical direction is possible, and the evanescent region where it cannot.

is positive, and decays exponentially in the vertical direction. The slanted line corresponds to the Lamb wave. As explained in the previous section, the Lamb wave acts as a sound wave horizontally and reaches hydrostatic equilibrium vertically. In other words, it is a boundary wave located only near the lower end of the atmosphere, with its energy attenuating proportionally to $\exp(-z/H_s)$[note 5)]. The blue and red regions correspond to internal waves[note 6)]. Because λ^2 is negative, it can propagate in the vertical direction. The acoustic wave region (blue) satisfies the condition $\omega > \omega_+$. Also, the acoustic wave region (blue) always exists on the shorter-period side of the cut-off frequency N_a. The other region, the internal gravity wave region (red), satisfies the relation $\omega < \omega_-$. This region consistently exists on the lower-frequency side of the buoyancy frequency N. In this way, the defining frequencies N_a, $L(k)$, and N play an important role in understanding wave propagation behaviors in the ocean and atmosphere.

Assuming the high-frequency limit constraint for an acoustic wave, λ^2 ($L_l N \ll \omega^2$ and $N_a \ll \omega$) can be approximated as

$$\lambda^2 = -\frac{1}{c^2}(\omega^2 - L(k)^2). \tag{9.33}$$

In this case, ω_+ can be estimated as

$$\omega_+ \sim L(k) \propto v. \tag{9.34}$$

[note 5)] Lamb waves have been observed during total solar eclipses, atmospheric nuclear tests, and volcanic eruptions. Multi-orbit Lamb waves travelling numerous times around the Earth have also been detected. Recently, consistently excited Lamb waves believed to be sourced by atmospheric phenomena have also been discovered.[(9)]

[note 6)] Corresponds to body waves in seismology.

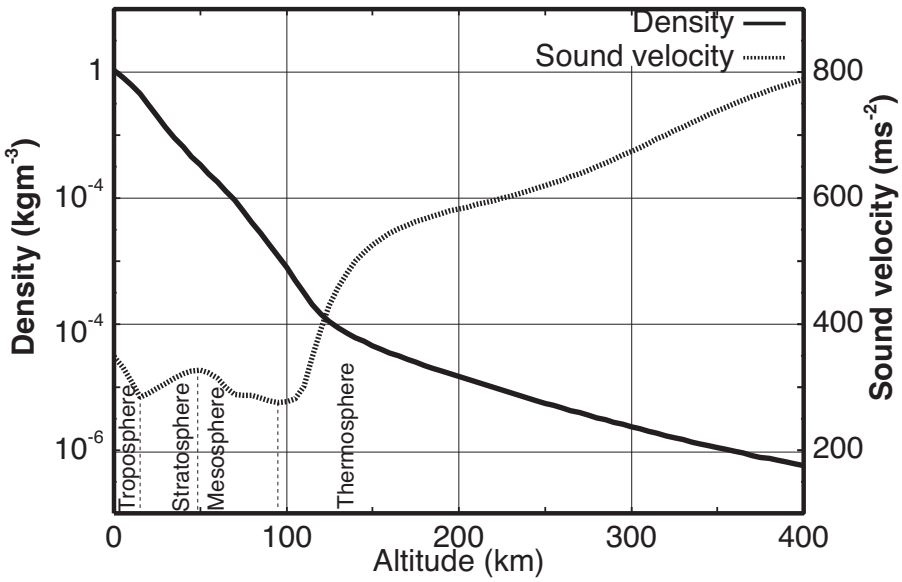

Figure 9.7: Atmospheric sound speed and density structure. Displaying the model in June for the equatorial region from CIRA86.[2]

From this, it can be understood that when a high-frequency sound wave enters a high-sound speed (high-temperature) region like the thermosphere, it will reflect.

Here, let us reflect critically upon the behavior of sound waves at low frequencies. ω_+ can be evaluated by the cut-off frequency N_a. Therefore,

$$\omega_+ \sim N_a \sim \frac{v}{H_\rho} \propto \frac{\sqrt{T}}{T} \propto v^{-1}. \tag{9.35}$$

In other words, it is found that sound waves reflect in low-temperature regions, because as evident from the equation, the vertical wavelength of the acoustic wave is blocked by the atmospheric thickness (scale height H_ρ), while concurrently the scale height intensifies linearly with temperature.

Figure 9.8 depicts the altitude distribution of $\omega_+/2\pi$ formulated based on the COSPAR INTERNATIONAL REFERENCE ATMOSPHERE: 1986 (CIRA86) model (Figure 9.7). Comparing Figure 9.8 with Figure 9.7, we understand the relationship between v and ω_+. From this configuration we verify that an mHz-band acoustic wave will reflect upon joining the lower sound-speed sections of the mesosphere. This occurrence is referred to as inverted refraction. For this reason, fundamental acoustic modes and 1st higher modes are trapped in an elevation window from the surface ascending accurately to circa 100 km. The atmospheric mode trapping operates extensively shaped locally via inversed deflection (inverted refraction) through underlying low-sound gradients spanning the mesosphere. Modes beyond the 2nd higher mode barely trap because they predominantly progress extending fully over heights beyond 100 km dispersing effectively. Vertical wavenumbers dictate dynamically relying exclusively upon metrics gauging lengths separating surface to the upper reflective limits. Inherently yielding shorter footprints than hor-

izontal dimensions uniformly, horizontal propagation group speeds belonging securely to these trapped configurations function very slowly (owing fully to repetitively reflecting vertically and dynamically traveling horizontally) (at estimations nearing 10 m/s orders).

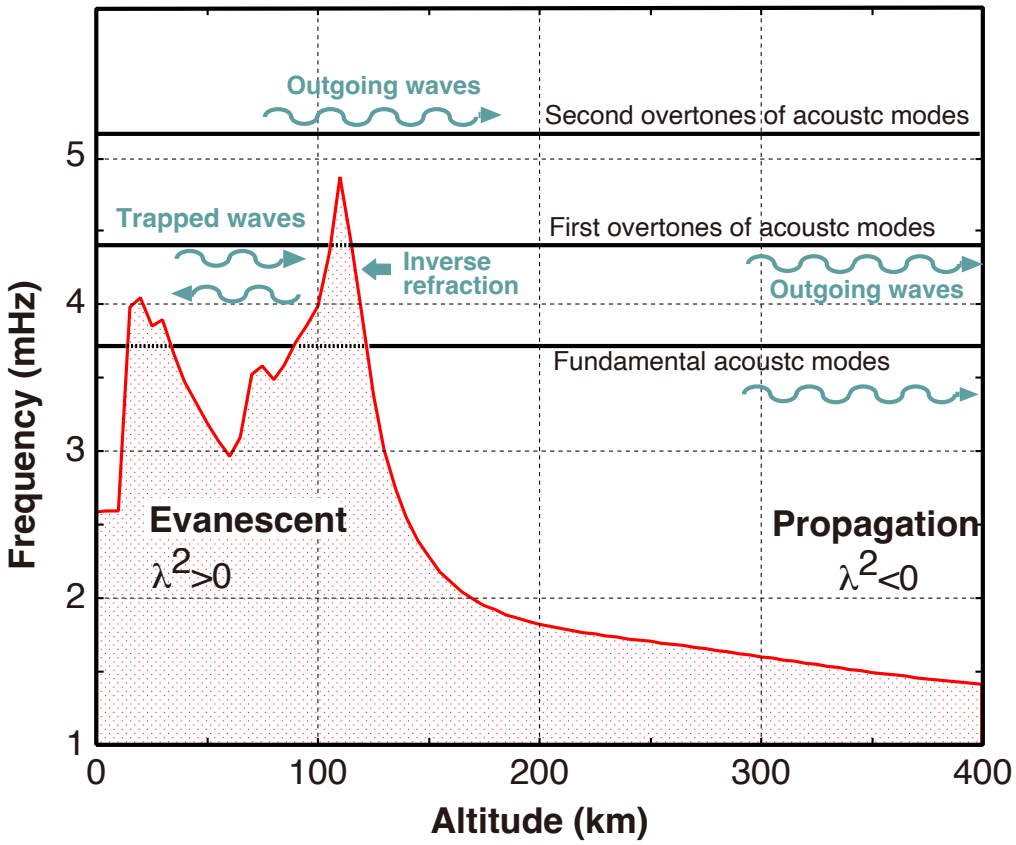

Figure 9.8: Distribution over elevation of characteristic frequency $\omega_+/2\pi$. Computations were formulated utilizing the June variables from COSPAR INTERNATIONAL REFERENCE ATMOSPHERE: 1986 (CIRA86) models precisely assessing $l = 29$ regarding the horizontal metric derived fundamentally within limits defining spherical harmonics.

Wavenumber-Frequency Spectrum

As shown in Figure 9.6, it is standard practice to consider wave propagation in the wavenumber-frequency domain. Especially when dispersion is strong, waveforms in the time domain become complex, often making interpretation difficult. Mathematically, considering it in the time-distance domain and considering it in the wavenumber-frequency domain are essentially equivalent. Throughout this material, various plotting methods will appear. It might be quite difficult if you are not used to them, but since there are standard plotting methods depending on the field, with a little training you will come to understand the key points of the figures.

§9.3 Bibliography

[1] T. Beer. *Atomspheric waves*. Adam Hilger, London, 1974.

[2] CIRA86: Part II Middle Atmosphere Models. *Adv. Space Res.*, 10, 1990.

[3] T. Cowling. The non-radial oscillations of polytropic stars. *Mon. Not. Roy. Astron. Soc.*, 101:369–373, 1941.

[4] F. Dahlen and J. Tromp. *Theoretical Global Seismology*. Princeton University Press, Princeton, 1998.

[5] A. E. Gill. *Atmosphere-ocean dynamics*, volume 30. Academic press, 1982.

[6] E. E. Gossard and W. Hooke. *Waves in The Atmosphere*. Elsevier Amsterdam, 1975.

[7] S. Masanori. *Seismic Wave Theory*. University of Tokyo Press, 2009.

[8] N. Murayama. Pressure waves produced by the nuclear explosion on october 30, 1961-preliminary report. *Journal of the Meteorological Society of Japan. Ser. II*, 40(4):222–231, 1962.

[9] K. Nishida, N. Kobayashi, and Y. Fukao. Background Lamb waves in the Earth's atmosphere. *Geophysical Journal International*, 196(1):312–316, Nov. 2014.

[10] M. Saito. *DISPER80; a subroutine package for calculation of seismic normal-mode solutions*, pages 293–319. Acad. Press. San Diego, 1988.

Seismic Interferometry

Chapter 10

§10.1 Introduction

To understand the Earth's internal structure, the propagation of seismic waves is a crucial clue. Traditionally, seismic velocity structures have been imaged by observing the ground motions caused by earthquakes. Since the 2000s, it has become common to investigate the Earth's interior by analyzing random ground motions induced by phenomena other than earthquakes, a technique known as Seismic Interferometry [note 1)]. In this chapter, based on the knowledge we have learned so far, we will explain the principles of seismic interferometry.

In this text, we will focus on microseisms induced by ocean swells as the random wavefield (see Section 4.8). Another important random wavefield is the seismic coda wave (multiply scattered seismic waves; for details, see Sato, Fehler and Maeda, 2012[31]). Seismic interferometry using coda waves is also widely researched (e.g., Campillo and Paul, 2003[5]), but we will omit the details here due to time constraints. If you are interested, please refer to the aforementioned review papers and textbooks.

§10.2 A brief history of Seismic Interferometry

The idea of seismic interferometry dates back to the 1950s. The spatial autocorrelation (SPAC) method proposed by Aki (1957)[2] pioneered the concept of seismic interferometry. There are also pioneering works in the fields of ocean acoustics by Cox (1973)[7] and exploration seismology

note 1) See recent review papers (e.g., Snieder and Larose, 2013[37]) and textbooks (e.g., Schuster, 2009;[32] Sato, Fehler and Maeda, 2012;[31] Nakata et al., 2019[21]). Seismic interferometry is not limited to the Earth but has been applied to various phenomena, including laboratory scales (e.g., Lobkis and Weaver, 2001[17]), architectural structures (e.g., Snieder and Wapenaar, 2010[35]), helioseismology (e.g., Gizon et al., 2010[11]), and ocean acoustics (e.g., Roux and Kuperman, 2004[30]).

by Claerbout (1968).[6] Aki's idea, however, remained unnoticed for a while[note 2]. However, 26 years after its publication, in 1983, a research group led by Hiroshi Okada from Hokkaido University paid attention to Aki's method (Okada and Sakajiri, 1983),[27] and it became actively studied primarily as a technique (microtremor survey) to investigate ground characteristics near the surface. Since then, the microtremor survey has become a standard method for estimating very shallow structures near the surface.

The paper that triggered the attention toward seismic interferometry in the field of seismology was Campillo and Paul [2003].[5] They analyzed seismic waves generated in Mexico and demonstrated that the propagation of surface waves could be extracted by computing the cross-correlation of the well-scattered coda wave portion of the seismic records. In 2005, Shapiro et al.[34] took advantage of the fact that microseisms continuously arrive from various directions, and succeeded in estimating the crustal structure of California from how these waves propagate. This technique is called ambient noise tomography. Following this study, similar research has been conducted in numerous regions, including North America, Japan, China, and Europe.

The fundamental observable in seismic interferometry is the cross-correlation function of seismic waveforms between two selected stations. The waveform of the cross-correlation function can be interpreted as if there is a virtual source at one station, and the waveform is recorded at the other station. Let us look at Figure 10.1. It shows the cross-correlation functions between the station in Matsushiro and others. This method has two major advantages.

The first advantage is the ability to virtually place an event even in regions without earthquakes. Usually, in aseismic regions, detailed seismic velocity structures are unknown, so the fact that earthquakes are not required is highly beneficial. Figure 10.1 indeed shows the propagation of Rayleigh waves as if Matsushiro were the epicenter.

The second advantage is that there is no need to wait for an earthquake. Normally, to perform seismic wave tomography analysis, one must wait for a sufficient amount of earthquake data to accumulate. In seismic interferometry, a sufficient quality of data can be secured by observing for a certain period [note 3]. This property, not needing to wait for an earthquake, is extremely advantageous for investigating temporal changes in seismic velocity structures. To detect infinitesimal temporal changes in velocity structure using earthquakes, one must wait for earthquakes to occur repeatedly at the exact same location (known as repeating earthquakes). However, such convenient earthquakes occur very rarely. Calculating the cross-correlation function of a certain pair of stations and observing its temporal variation is equivalent to analyzing records of earthquakes repeatedly occurring at the same location. In fact, temporal structural changes accompanying volcanoes and earthquakes are now actively researched (e.g., Sens-Schönfelder and Wegler, 2006[33]).

Here, we will explain the theoretical background and the principles of seismic interferometry.

[note 2] Aki's work was compiled as his doctoral dissertation. According to his autobiography, the idea was inspired by Wiener's Cybernetics. For his thesis, he independently handled the theory, the design and construction of observational equipment, data collection, and structural estimation. Because this was before the widespread use of computers, he even had to design analog circuits to calculate cross-correlation coefficients. He conducted the observations at the athletic field of the Faculty of Science, The University of Tokyo, and ultimately dug into the field himself to verify the structural estimation results.

[note 3] Depending on the frequency band, roughly speaking, several months is sufficient for 0.05-0.5 Hz, and a few days is often enough for higher frequencies. Of course, a longer observation period is more advantageous to ensure sufficient accuracy.

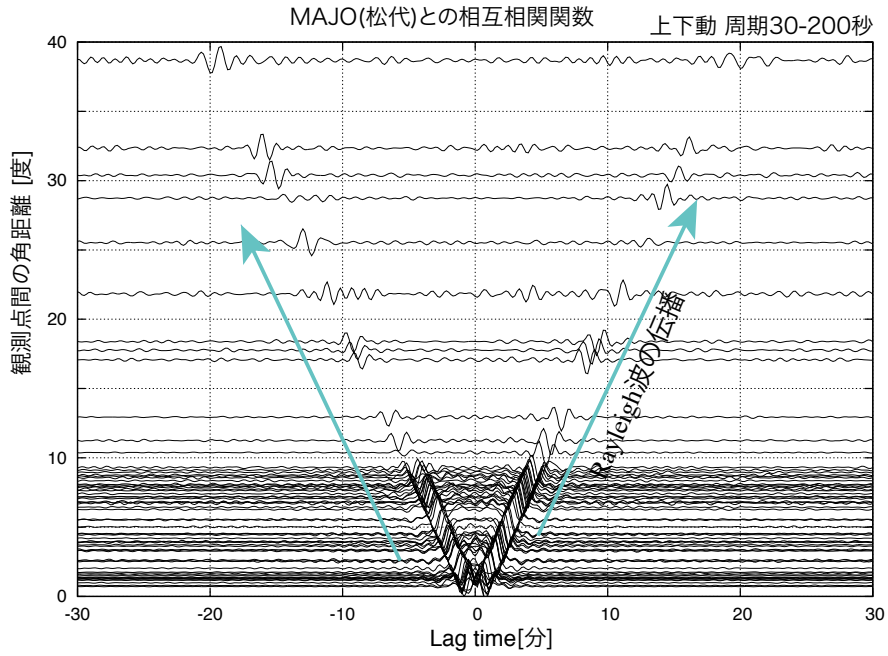

Figure 10.1: Cross-correlation functions of vertical-component records between MAJO (Matsushiro) and other stations, arranged by inter-station distance. A band-pass filter of 20-200 seconds is applied. The propagation of Rayleigh waves is clearly visible. The wave packet with a positive delay time is called the causal part, and the wave packet with a negative delay time is called the acausal part.

For specific application examples, please refer to the review papers mentioned at the beginning.

Rough Earth Club and Smooth Earth Club

SI brings a reunion of different research fields: ocean acoustic (Cox, 1973), seismic exploration (Claebout, 1968), and seismology (Aki 1957). Surprisingly the ideas were proposed independently and simultaneously.

Even in the seismological community, there were different cultures: one is the rough Earth club and smooth Earth club. Keiiti Aki defined them in his letter to V. I. Keilis-Borok, as

> . . . To a geodynamicist, the earth's property is smoothly varying within bodies bounded by large-scale interfaces. Most seismologists also belong to this "smooth earth club" because once you start with an initial model of smooth earth, your data usually do not require the addition of small-scale heterogeneity to your initial model. As summarized well in a recent book by Sato and Fehler (1998), the acceptance of coda waves in the data set is needed for the acceptance of small-scale seismic heterogeneity of the lithosphere. There is an increasing number of seismologists who accept it, forming the "rough earth club." I believe that you are also a member of the rough earth club, judging from the emphasis on the hierarchical heterogeneity

of the lithosphere. . .

(”Seismology of Earthquake and Volcanic Prediction”, Lecture notes, Aki 2003). Seismic wavefield above 1 Hz was a territory of the ”rough Earth club,” whereas that below 0.1 Hz was a territory of the ”smooth Earth club.” The members of the rough Earth club are familiar with stochastic treatments of the seismic wavefield. The recent development of SI means a reunion between the ”rough Earth club” and the ”smooth Earth club.”

The dominant frequency of microseisms at around 0.2 Hz corresponds to the gap between ”*rough Earth club*” and ”*smooth Earth club*”. SI enables us to utilize coherent signals from random seismic wavefields with an assumption of stochastic stationary excitation. Although surface wave tomography was a tool of the ”smooth Earth club,” SI broke the gap. Scattering due to strong lateral heterogeneities in the crust and the sediment was a big barrier for ”*smooth Earth club*.” When we apply SI, the scatterer is important because it enhances the randomness. SI plays a complementary role in the ”smooth Earth club.” This role of SI is true of other communities, such as seismic exploration, acoustic, physical oceanography, and so on.

In this lecture, the next chapter explains the excitation mechanism of microseisms by ocean swell. The next chapter explains the basic principle of SI with a demonstration by a WEB application. Then the last chapter explains some applications, which are done by our group mainly.

§10.3 Theoretical background of Seismic Interferometry: a closed system

To understand the theory of seismic interferometry, let us consider a simple case [note 4)].

First, let us review the definition of the cross-correlation function. I have created a web application (http://www.eri.u-tokyo.ac.jp/knishida/Seismology/wave2Drandom2.html), and it would be easier to understand if you read along while interacting with it interactively.

10.3.1 Cross-correlation analysis

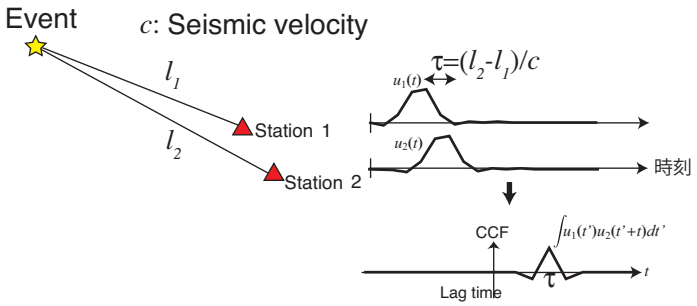

Figure 10.2: Schematic figure of cross-correlation analysis for a pair of seismograms when an earthquake ocurred.

First, we consider a transient phenomenon such as an earthquake or a volcanic explosion. Let us suppose an earthquake occurs at a certain location, as shown in Figure 10.2. For seismograms at stations 1 and 2, we define the cross-correlation function ϕ_{12} as

$$\phi_{12}(t) = \lim_{T\to\infty} \frac{1}{T} \int_0^T u_1(\tau) u_2(t+\tau) d\tau. \tag{10.1}$$

Assuming that the cross-correlation function quickly converges to 0 as $|t|$ increases, we can define its Fourier transform $\Phi_{12}(\omega)$ as

$$\Phi_{12}(\omega) = \langle U_1^*(\omega) U_2(\omega) \rangle \tag{10.2}$$

[note 5)]. In this case, the wave arrives at station 2 delayed by τ seconds relative to station 1 (Figure 10.2, right). As a result, the cross-correlation function has a peak at $t = \tau$. In other words, by

[note 4)] For a comprehensive understanding of the theoretical treatment, Snieder et al. (2010)[38] is highly recommended.

[note 5)] Strictly speaking, when considering a stationary process, the long-term integration is approximated by the ensemble average. Since we are assuming that the wavefield is stationarily excited, $u_i(t)$ is not square-integrable, and therefore its Fourier transform cannot be taken in the usual sense. If you wish to understand it more rigorously, please refer to reference books on time series analysis.

reading the time of the peak of the cross-correlation function, we can measure the difference in seismic wave arrival times (travel-time difference). In practice, precise travel-time differences measured by cross-correlation functions are often utilized to determine hypocenter locations accurately.

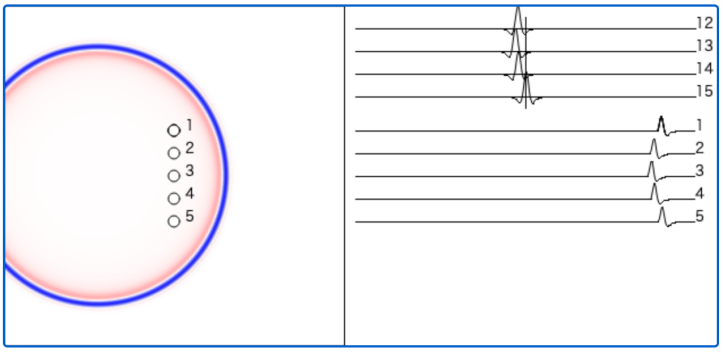

Figure 10.3: Example of simulation results with a point source. The bottom right panel shows the waveforms observed at stations 1 to 5, and the top right panel shows their cross-correlation functions.

In the web application, clicking allows you to place a seismic source at any location, and pressing 's' starts the simulation. In the bottom right, waveforms at stations 1-5 are displayed, and in the top right, their cross-correlation functions (for example, '14' represents the cross-correlation function between 1 and 4) are shown. By reading the peak time of the cross-correlation function, you can measure the travel-time difference. Please give it a try.

Hereafter, we will consider phenomena that can be approximated as statistically random and stationary, such as microtremors and ambient noise, rather than transient phenomena (earthquakes and volcanic eruptions).

10.3.2 SI in a closed system

Here, we consider SI in a closed system. In the case of a finite body, we evaluate CCFs based on a normal mode approach.[17] Because the Earth is a finite-size sphere, this approach is also feasible for multi-orbit propagations on a global scale.[24], [25] For simplicity, this subsection describes a scalar 1-D case, but it can be easily extended to elastic 2-D and 3-D cases.

Repeating seismic experiments

Virtually, we consider repeating seismic experiments in a closed system of a perfect elastic body. Before the initial time $t = 0$, the body did not deform, and a random force $f^k(x)$ was applied to the body at $t = 0$ in the kth experiment, where x is the spatial location. We consider a finite body from $x = 0$ to $x = L$ and impose rigid or free boundary conditions at both ends. The equation of

motions is given by

$$\rho(x)\frac{\partial^2 u^k(x,t)}{\partial t^2} = \kappa(x)\frac{\partial^2 u^k(x,t)}{\partial x^2} + f^k(x)\delta(t), \tag{10.3}$$

where κ is the elastic constant, ρ is the density and u^k is the displacement at the kth experiment. After the force is applied, the displacement is measured at the stations. These experiments are repeated K times. Note that we cannot consider a persistent force in this system because no attenuation leads to an infinite increase in the amplitude over time.

We evaluated the displacement $u^k(x,t)$ by a convolution between the force $f^k(x)$ and the Green's function. The Green's function can be written in terms of normal mode theory[8] as

$$G(x,x';t) = \sum_n \frac{\mathcal{U}_n(x)\mathcal{U}_n(x')}{\omega_n}\sin(\omega_n t), t \geq 0, \tag{10.4}$$

where ω_n is nth eigenfrequency and $\mathcal{U}_n$ is nth eigen function, which satisfies orthonormality:

$$\int_0^L \rho(x)\mathcal{U}_n(x)\mathcal{U}_{n'}(x)dx = \delta_{nn'}. \tag{10.5}$$

Then, the displacement can be represented by the convolution

$$u^k(x,t) = \sum_n A_n^k \mathcal{U}_n(x)\frac{\sin(\omega_n t)}{\omega_n}, \tag{10.6}$$

where $A_n^k = \int_0^L \mathcal{U}_n(x)f^k(x)dx$. We consider the energy partition of the modes for a random external force in the next section.

Energy partition of modal energy

This subsection discusses the energy balance of each mode: how the work done by external forces is distributed to the kinematic and elastic energy. First, we evaluate the work done by the external force can be given by

$$\int_0^\infty \int_0^L v_n^k(x,t)f^k(x)\delta(t)dxdt = (A_n^k)^2, \tag{10.7}$$

where the particle velocity v_n^k of nth mode in the kth experiment is written by $v_n^k = A_n^k\mathcal{U}_n(x)\cos(\omega_n t)$.

The kinetic energy of nth mode T_n can be evaluated by integrating the kinetic energy density in space as

$$T_n = \int_0^L \frac{\rho}{2}(v_n^k)^2 dx = \frac{1}{2}(A_n^k)^2\cos^2(\omega_n t). \tag{10.8}$$

The elastic energy V_n, on the other hand, can be evaluated by integrating the strain energy density in space. The partial integral with the boundary condition leads to

$$V_n = \int_0^L \frac{\kappa}{2}\left(A_n^k \frac{\partial \mathcal{U}_n}{\partial x}\frac{\sin(\omega_n t)}{\omega_n}\right)^2 dx = \frac{1}{2}(A_n^k)^2 \sin^2(\omega_n t). \tag{10.9}$$

The total energy $T_n + V_n$ is

$$T_n + V_n = (A_n^k)^2, \tag{10.10}$$

which balances the work done by external forces.
Here, we consider an excitation by random force F_i^k at location x_i as

$$f^k(x) = \sum_{i=0}^{I-1} F_i^k \delta(x_i), \tag{10.11}$$

where I is the number of the force. We also assume that $F_i^k(x)$ is white noise as

$$\langle F_i^k F_{i'}^k \rangle_k = \bar{F}^2 \delta_{ii'}, \tag{10.12}$$

where $\langle\rangle_k$ is ensemble average with respect to k.

White noise

Here we will consider an external force f applied randomly. Let us define the external force as random fluctuations that contain all wavenumber components equally. Having such property is called white noise[note 6)]. Therefore, its power spectrum $\Phi(f)$ is constant.

Let us consider this more concretely. Look at the left diagram in Figure 10.4. Consider an external force $f^k(i\Delta x)$ discretized with a spatial interval Δx. At each position $i\Delta x$, we roll a dice randomly (assuming it follows a normal distribution with mean 0 and variance 1). Now let's consider the autocorrelation function $\phi(x, x')$. We define the autocorrelation function as

$$\phi(x, x') = \lim_{N\to\infty} \frac{1}{N} \sum_{k=0}^{N-1} f^k(x') f^k(x' + x). \tag{10.13}$$

Now, we assume that there is absolutely no correlation in the external force if the distance between two points is separated by $\Delta x/2$. Then ϕ becomes a function of only $x - x'$, and letting $\xi \equiv x - x'$, we get

$$\phi(\xi) = \begin{cases} 1 & |\xi| \le \Delta x \\ 0 & \text{otherwise.} \end{cases} \tag{10.14}$$

By expanding $\phi(\xi)$ into a Fourier series, we obtain $\Phi(k_n) = \Delta x$, where k_n is the wavenumber $2n\pi/L$. The power spectrum (one-sided spectrum) is $2\Delta x$ (Figure 10.4).

The theoretical calculation has been done. What happens if we actually create numerical data and calculate it? Let's generate white noise using random numbers and perform Fourier analysis.

[note 6)] This is an analogy with sunlight. Generally, white implies containing all frequency components, red implies being rich in low frequencies, and blue implies being rich in high frequencies.

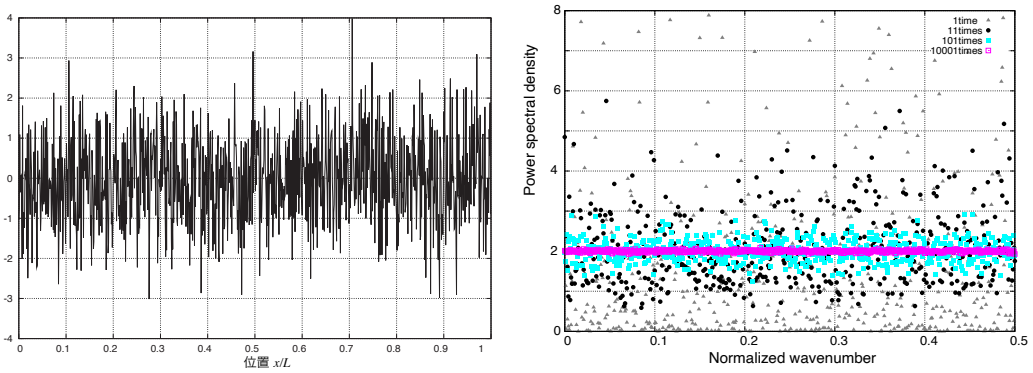

Figure 10.4: Left: external force $f^k(x)$ with white noise characteristics. Right: the result of calculating the power spectrum. As the number of ensemble averages increases, the estimated value approaches 1.

First, let's consider one extracted window. Let's consider the Fourier spectrum at wavenumber k_n[note 7)]. Since $f(x_k)$ is a random number, its Fourier component $F(k)$ is also a random number. Since the power spectrum can be calculated as $|F(k)|^2$, it does not take a constant value but takes a random value[note 8)]. The gray dots on the right of Figure 10.4 are the actually calculated points. This is slightly strange. It is supposed to be $\Phi(f) = 1$, but with just one discrete Fourier transform, we can only see that it is on the same order of magnitude as 2. Why is this?

This is because the autocorrelation function is a statistical quantity. It does not become a meaningful value unless averaged over many ensembles (here k is the index assigned to ensemble elements). More specifically, the estimation error becomes 100%. Although it seems very odd at first glance, this behavior arises because we are statistically evaluating only one sample.

So let us perform the Fourier series expansion many times and take the ensemble average. You will see that it gradually approaches 2[note 9)]. As such, the power spectrum is ultimately a statistical quantity, so the estimation error becomes too large unless averaged sufficiently. For example, consider the case where we sample and average N times. If the time series follows a normal distribution, the estimation error is $1/\sqrt{N}$. The way the error decreases according to N can also be seen from the figure.

note 7) For actual calculation, space must be discretized and a discrete Fourier transform must be performed. Ensuring consistency between the discrete Fourier transform and the Fourier series expansion gives

$$F(k_n) = \Delta x \sum_{j=0}^{N-1} f(x_j) e^{-i2\pi k_n x_j} = \Delta x F^{DFT}(k_n).$$

note 8) More precisely, it follows a χ^2 distribution.

note 9) Just to confirm, we are currently considering a time series with a variance of 1 in the time domain. From Percival's formula, the integral of the power spectrum becomes 2×0.5, which matches.

Equipartition of energy

To simplify the problem, we consider the constant density ρ_0. The expected value of the cross-correlation of A_n can be evaluated as follows.

$$\langle A_n^k A_{n'}^k \rangle_k \sim \frac{I\bar{F}^2}{L\rho_0} \int_0^L \mathcal{U}_n(x)\mathcal{U}_{n'}(x)dx = \frac{I\bar{F}^2}{L\rho_0}\delta_{nn'} \equiv \mathcal{E}\delta_{nn'}, \tag{10.15}$$

where $\mathcal{E}$ is the modal energy. The amplitudes of the different modes A_n do not correlate with each other, and the total energy of each mode is distributed equally. The expected value of the modal energy is constant for each mode when the external force f is white noise. When a system meets this condition, we call the state the equipartition of energy. We note that the fluctuation-dissipation theorem in physics[4] requires a thermal equilibrium that satisfies the equipartition of energy. Equation 10.12 can be derived from the principle of equal a priori probabilities in the case.

CCFs under the equipartition of energy

Here we define a CCF $\phi^k(x_1, x_2; \tau)$ between $u^k(x_1)$ and $u^k(x_2)$ under the equipartition of energy as,

$$\phi^k(x_1, x_2; \tau) \equiv \lim_{T\to\infty} \frac{1}{T} \int_0^T u^k(x_1, t)u^k(x_2, t + \tau)dt, \tag{10.16}$$

where x_1 shows the location of station 1, and x_2 shows that of station 2. We note that there are two types of CCF definitions. The sign of the second term of the other type is flipped.

The ensemble average of $\phi(x_1, x_2; t)$ over K time experiments is defined by the ensemble average $\left\langle \phi^k(x_1, x_2; \tau) \right\rangle_k$. Then, the CCF can be represented by

$$\frac{d}{d\tau}\phi(x_1, x_2; \tau) = -\frac{\mathcal{E}}{2}(G(x_1, x_2; \tau) - G(x_2, x_1; -\tau)), \tag{10.17}$$

which relates the CCF to Green's function.[36] The frequency dependence of this equation differs slightly from Aki's formulation (e.g.,[13]). Although the formulation showed that the Hilbert transform of the CCF can be related to Green's function, the difference can be attributed to spectral normalization.

Compared to CCFs for real data, the biggest problem is the assumption of the equipartition of energy. Because the excitation sources are distributed near the surface, fundamental modes dominate the observed wave field. Energy is not partitioned equally among different mode branches. Indeed, the observed dominance of fundamental modes (e.g.,[22]) shows that the energy is not equally distributed in the radial direction. When considering a single-mode branch, the energy is distributed equally in the horizontal direction if the external force is white noise distributed on the entire surface.

Although the theory assumed K experiments, practically, only one observation is possible. Therefore, the ensemble averages need to be replaced by time averages to calculate the CCFs of observed data for persistent external forces (e.g., ocean waves). However, no attenuation in a closed system causes the problem of diverging amplitudes without attenuation; that is, the seismic

wave field in a closed system never meets the equilibrium for persistent sources. Physically, it is natural to consider the equilibrium between the energy dissipation due to attenuation and the work performed by external forces.[10], [14]

We note that the term Green's function is often used in a less mathematically rigorous sense in studies on SI. Mathematically, a CCF converges to the Green's function only in limited cases. A similar situation occurs in quantum field theory. The Green's function refers to CCFs, although it does not satisfy the mathematical definition.[51]

10.3.3 CCFs for homogeneous source distribution in a 2-D homogeneous medium

For ANT, we explicitly express the CCFs between all pairs of three-component seismometers in an open system when multimode Love and Rayleigh waves dominate the ambient seismic wave field. We evaluated the CCFs for the surface waves in a 2-D problem with a membrane approximation (e.g.,[40], [42]–[44]). We show an expression of the mixed-component CCFs of surface waves.

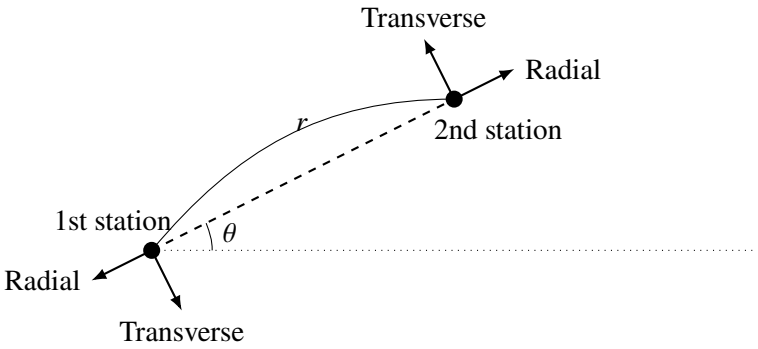

Figure 10.5: Schematic of the geometry of a pair of stations with separation distance r and the coordinate. The figure shows the radial and transverse directions for the station pair. To simplify the equation, the signs of the directions are different from those of other studies. The difference changes the signs of CCF in the components of RR, TT, RZ, and ZR.

An arbitrary seismic wave field $\mathbf{u}(r, \theta; \omega)$ in 2-D can be represented by a superposition of multimode Love and Rayleigh waves as

$$\mathbf{u}(r, \theta; \omega) = \sum_{n=0}^{\infty} \sum_{m=-\infty}^{\infty} f_{n,m}^{Ray}(\omega) \left[U_n(\omega) \mathbf{P}_m(r, \theta; \omega) + V_n(\omega) \mathbf{B}_m(r, \theta; \omega) \right] + f_{n,m}^{Love}(\omega) W_n(\omega) \mathbf{C}_m(r, \theta; \omega), \tag{10.18}$$

where $f_{n,m}^{Ray}(\omega)$ is forcing for Rayleigh waves, and $f_{n,m}^{Love}$ is forcing of Love waves. U_n and V_n are eigenfunctions of the nth overtone of the Rayleigh wave, and W_n is the eigenfunction of the

nth overtone of the Love wave, which has a real value. The basis functions $\mathbf{P}_m$, $\mathbf{B}_m$ and $\mathbf{W}_m$ are given by

$$\mathbf{P}_m(r,\theta;\omega) = \hat{\mathbf{z}} J_m\left(\frac{\omega r}{c_n^{Ray}(\omega)}\right) e^{im\theta}, \tag{10.19}$$

$$\mathbf{B}_m(r,\theta;\omega) = \frac{c_n^{Ray}(\omega)}{\omega r}\left[\hat{\mathbf{r}}\frac{\partial}{\partial r} + \frac{\hat{\boldsymbol{\theta}}}{r}\frac{\partial}{\partial \theta}\right] J_m\left(\frac{\omega r}{c_n^{Ray}(\omega)}\right) e^{im\theta}, \tag{10.20}$$

$$\mathbf{C}_m(r,\theta;\omega) = \frac{c_n^{Love}(\omega)}{\omega r}\left[\frac{\hat{\mathbf{r}}}{r}\frac{\partial}{\partial \theta} - \hat{\boldsymbol{\theta}}\frac{\partial}{\partial r}\right] J_m\left(\frac{\omega r}{c_n^{Love}(\omega)}\right) e^{im\theta}, \tag{10.21}$$

where $c_n^{Ray}(\omega)$ phase velocity of nth overtone of Rayliegh wave, and $c_n^{Love}(\omega)$ is nth overtone of Love wave.

An assumption of equipartition of energy leads to

$$\langle f_{n,m}^{Ray*} f_{n',m'}^{Ray}\rangle U_n(\omega) U_{n'}(\omega) \equiv P_n^{Ray}(\omega)\delta_{nn'}\delta_{mm'}, \tag{10.22}$$

$$\langle f_{n,m}^{Love*} f_{n',m'}^{Love}\rangle W_{n'}(\omega) W_n(\omega) \equiv P_n^{Love}(\omega)\delta_{nn'}\delta_{mm'}, \tag{10.23}$$

$$\langle f_{n,m}^{Ray*} f_{n',m'}^{Love}\rangle = \langle f_{n,m}^{Love*} f_{n',m'}^{Ray}\rangle = 0, \tag{10.24}$$

$$R_n(\omega) \equiv V_n(\omega)/U_n(\omega), \tag{10.25}$$

where $P_n^{Ray}(\omega)$ is the power spectrum of nth overtone of Rayleigh wave, and P_n^{Love} is the power spectrum of nth overtone of Love wave.

The mixed-component cross-spectra for multimode Rayleigh waves are written as,

$$\begin{bmatrix} \Phi_{ZZ}^{Ray} & \Phi_{ZR}^{Ray} & \Phi_{ZT}^{Ray} \\ \Phi_{RZ}^{Ray} & \Phi_{RR}^{Ray} & \Phi_{RT}^{Ray} \\ \Phi_{TZ}^{Ray} & \Phi_{TR}^{Ray} & \Phi_{TT}^{Ray} \end{bmatrix} = \sum_{n=0}^{\infty}\left\{ P_n^{Ray}(\omega) \begin{bmatrix} J_0\left(\frac{\omega r}{c_n^{Ray}}\right) & -R_n J_1\left(\frac{|\omega| r}{c_n^{Ray}}\right) & 0 \\ -R_n J_1\left(\frac{|\omega| r}{c_n^{Ray}}\right) & -\frac{R_n^2}{2} J_{0-2}\left(\frac{\omega r}{c_n^{Ray}}\right) & 0 \\ 0 & 0 & -\frac{R_n^2}{2} J_{0+2}\left(\frac{\omega r}{c_n^{Ray}}\right) \end{bmatrix}\right\}, \tag{10.26}$$

where a cross-spectrum represents the CCF in frequency domain. The mixed-component cross-spectra for multimode Love waves are written as,

$$\begin{bmatrix} \Phi_{ZZ}^{Love} & \Phi_{ZR}^{Love} & \Phi_{ZT}^{Love} \\ \Phi_{RZ}^{Love} & \Phi_{RR}^{Love} & \Phi_{RT}^{Love} \\ \Phi_{TZ}^{Love} & \Phi_{TR}^{Love} & \Phi_{TT}^{Love} \end{bmatrix} = \sum_{n=0}^{\infty}\left\{ P_n^{Love}(\omega) \begin{bmatrix} 0 & 0 & 0 \\ 0 & -\frac{1}{2} J_{0+2}\left(\frac{\omega r}{c_n^{Love}}\right) & 0 \\ 0 & 0 & -\frac{1}{2} J_{0-2}\left(\frac{\omega r}{c_n^{Love}}\right) \end{bmatrix}\right\}, \tag{10.27}$$

where $J_{0-2}(z) \equiv J_0(z) - J_2(z)$ and $J_{0+2}(z) \equiv J_0(z) + J_2(z)$. Z represents the vertical component, and R and T represent the horizontal components according to the polarization direction (Figure 10.5).

These equations are identical to the result of.[13] A similar formulation for DAS observation is given by.[20] We note that the difference of sign Φ_{RZ}^{Ray}, Φ_{RR}^{Ray} and Φ_{TT}^{Ray} originates from the definition of the radial and transverse directions, which differ from this study. Using this formulation, cross-spectra for Rayleigh waves lead to a symmetric relation between the RZ and ZR components as $\Phi_{RZ}^{Ray} = \Phi_{ZR}^{Ray}$, whereas cross-spectra for body waves lead to an antisymmetric relation as $\Phi_{RZ}^{body} = -\Phi_{ZR}^{body}$.[39]

Attenuation becomes significant when considering a seismic wave field in sediment above 0.1 Hz.[23], [28], [29] However, physically plausible attenuation measurements are practically difficult (e.g.,[15], [46]) because there is ambiguity between the source heterogeneities and the attenuation. Although new techniques have been developed to overcome this problem (e.g.,[3], [16], [18]), they are beyond the scope of this study. Even if the physically plausible attenuation estimation is difficult, apparent Q measurements are feasible for better fitting a synthetic cross-spectrum to an observation (e.g.,[23]).

§10.4 SI in an open system

Next, we consider SI in an open system. The formulations in an open system depend on the source-receiver configuration: (1) random point sources distributed over the whole space, (2) random sources distributed on a closed curve, and (3) uncorrelated plane wave incidents from various directions. This subsection describes the relationship between the different configurations of an open system. Mathematically, the theory of an open system differs from that of a closed system. We cannot use normal mode theory for an open system because the system loses energy from the radiation boundary.

For ANT, CCFs are usually formulated in an open system, which better approximates the source-receiver configuration. Because the surface wave can be formulated as a 2-D problem with a membrane approximation (e.g.,[40], [42]–[44]), we can consider them as a 2-D potential problem in an open system. For ANT, we explicitly express the mixed-component CCFs of surface waves in a simplified case at the end of the subsection.

10.4.1 Seismic excitation by an infinite number of sources

We consider one realization of the background seismic wave field excited by an infinite number of sources in an open system. When external force acts on the body at a location $\mathbf{r}$ and time $t = 0$, the 2-D wave equation is given by

$$\frac{\partial^2 \psi(\mathbf{r}, t)}{\partial t^2} = C(\mathbf{r})\nabla^2 \psi(\mathbf{r}, t) + \sum_{i=0}^{\infty} \delta(\mathbf{r}_i - \mathbf{r})\delta(t) f_i \tag{10.28}$$

where $C(\mathbf{r})$ is phase velocity, and f_i is ith external force at the location $\mathbf{r}_i$ ($i = 0, \cdots, \infty$). The potential $\psi(x,t)$ is given by

$$\psi(\mathbf{r},t) = \sum_{i=0}^{\infty} g^{2D}(\mathbf{r}-\mathbf{r}_i;t) f_i, \tag{10.29}$$

where g^{2D} is the Green's function in time domain.
The Fourier component of the potential $\psi(\mathbf{r},t)$ is written by

$$\Psi(\mathbf{r},\omega) = \sum_{i=0}^{\infty} G^{2D}(\mathbf{r}-\mathbf{r}_i;\omega) f_i, \tag{10.30}$$

where G^{2D} is the Green's function in frequency domain. In this paper, we define the Fourier transform as follows,[8]

$$X(\omega) = \int_{-\infty}^{\infty} x(t) e^{-i\omega t} dt. \tag{10.31}$$

We note that the Fourier convention depends on the literature. For example,[1]'s definition has the opposite sign in the exponential term.

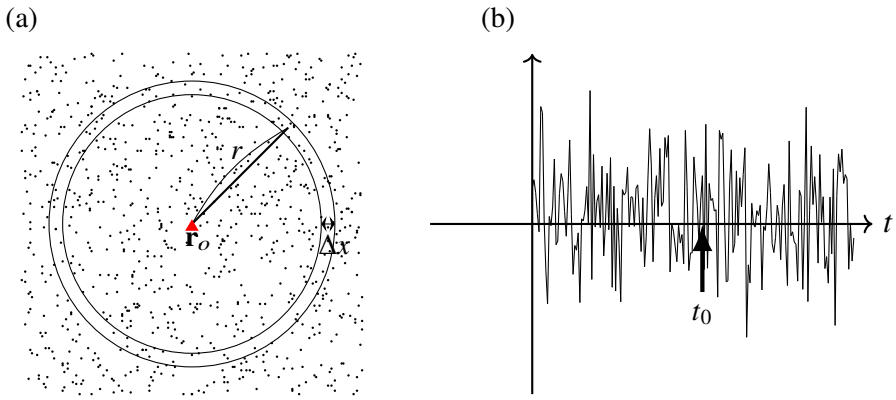

Figure 10.6: Schematic figure for random sources in 2-dimension. (a) Source distribution in space. The red triangle shows the observed station. (b) Potential $\psi(\mathbf{r}_o,t)$ observed at the origin $\mathbf{r}$ at time t. The wave packet at time t_0 is traveled from the source within the concentric circle with radius r shown in (a).

Here, we consider a potential $\psi(\mathbf{r}_o,t_0)$ in a simplified case with constant phase velocity as $C(\mathbf{r}) = C_0$, where $\mathbf{r}_o$ is the location of the origin and time denotes an arbitrary positive time. The $\psi(\mathbf{r}_o,t_0)$ is represented by the sum of the arrivals excited by sources along the concentric circle with radius $r = C_0 t_0$. The typical separation of the sources is assumed to be Δx. Within the circle with the band Δx, about $2\pi r/\Delta x$ sources are distributed (Figure 10.6 left). Because the amplitude decay is proportional to $r^{1/2}$, the mean square amplitude $\psi(\mathbf{r}_o,t_0)$ is estimated to be about $2\pi r/(\Delta x(r^{1/2})^2) = 2\pi/\Delta x$, which does not depend on the distance r. Therefore, after

$t > 0$, the fluctuations of ψ last for a semi-infinite time with the same mean squared amplitudes (Figure 10.6 right).

10.4.2 Random sources distributed on a closed curve

The second source configuration is random sources on an arbitrary curve enclosing stations. Now, we observe the potential ψ at $\mathbf{r}_o$ within the circle with radius r (Figure 10.6). Based on the representation theorem, the wave excited by distributed sources outside the circle can be completely reproduced from the stresses and displacements on the circle (e.g.,[1]). The contribution of the sources within the circle for the CCF can be neglected because the contribution from the sources outside the circle becomes infinitely large when considering infinitely long times. These features mean that it is equivalent to persistent sources distributed only on the circle. Suppose that uncorrelated random sources with white spectra on an arbitrary surface enclose stations in a heterogeneous medium. In this case, the time derivative of the corresponding CCF represents the exact Green's function between a pair of stations.[47]

The web demo of seismic interferometry at http://www.eri.u-tokyo.ac.jp/knishida/Seismology/wave2Drandom2.html simulates this condition (Figure 10.7).

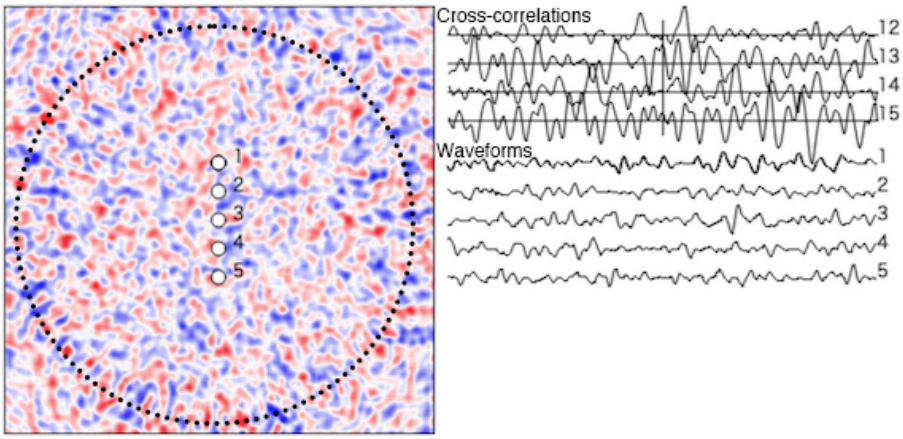

Figure 10.7: Example of a wavefield when random external forces are distributed on a circle. Excitation is assumed to be continuous in time.

10.4.3 Uncorrelated plane wave incidents

The third source configuration is uncorrelated plane wave incidents from various directions. Assuming that the source-station distances are sufficiently longer than the aperture of the seismic array, the assumption leads to a plane-wave approximation.[13), (19] The above discussions for a homogeneous source distribution lead to the identical formulation of CCFs regardless of the source configurations, as shown in the following subsection. When we consider a heterogeneous source distribution, the first source configuration is the most flexible to represent the source,

and the second and third are gradually less flexible. The flexibility of the first two source configurations causes a complex dependence of a CCF on the locations of the two stations. In contrast, the inflexibility of the third source configuration causes a simple dependence of the CCF only on the relative location between the stations (only the distance and the azimuth). In many cases, the ocean swell activities are far enough away from the stations to approximate the phenomenon well. For simplicity, we will use the third source configuration to represent CCFs based on plane wave incidents in the following subsections.

Here, for simplicity, we again assume that the time average is the same as the ensemble average. That is, we suppose that an external force $f_i^k(\omega)$ is distributed on the circumference. Let us consider the situation where such excitation of seismic waves is repeated N times, and we take their ensemble average. Assuming that an external force f_i is completely uncorrelated with other excitation sources f_j, and that f is white, we can write

$$\langle f_i^{k*} f_j^k \rangle_k = \delta_{ij} f_0^2, \tag{10.32}$$

where $\langle \cdot \rangle_k$ represents the ensemble average over k. From this, the cross-spectrum (the Fourier transform of the cross-correlation function) Φ_{12} can be written as

$$\begin{aligned} \Phi_{12}(\omega) \equiv \langle \Phi_{12}^k \rangle_k &= \sum_{i,j} G^{2D*}(\boldsymbol{r}_1 - \boldsymbol{r}_i, \omega) G^{2D}(\boldsymbol{r}_2 - \boldsymbol{r}_j, \omega) \langle f_i^k(\omega) f_j^k(\omega) \rangle_k \\ &= \sum_i G^{2D*}(\boldsymbol{r}_1 - \boldsymbol{r}_i, \omega) G^{2D}(\boldsymbol{r}_2 - \boldsymbol{r}_i, \omega) f_0^2. \end{aligned} \tag{10.33}$$

If the number of excitation sources is sufficiently large and the sources surround the observation points, the summation in the above equation can be replaced by a line integral:

$$\Phi_{12} = f_0^2 \int_{l_s} G^{2D*}(\boldsymbol{r}_1 - \boldsymbol{r}_s, \omega) G^{2D}(\boldsymbol{r}_2 - \boldsymbol{r}_s, \omega) dl_s. \tag{10.34}$$

This takes the form of spatially integrating the convolution integral of the Green's functions. This equation is the fundamental equation in seismic interferometry.

10.4.4 Evaluation of the integral: Relationship between cross-correlation and Green's function

To evaluate this integral, let us consider the source distribution shown in Figure 10.8. The position of the source is represented by the distance r_s and angle ϕ_s from the origin.

For simplicity, we approximate that the Green's function is proportional to $e^{ikr-\pi/4}/\sqrt{kr}$. This approximation is valid when the distance r is longer than the wavelength[note 10)]. Then,

$$\Phi_{12} \propto \int_{l_s} \frac{e^{ik(r_{2s}-r_{1s})}}{k\sqrt{r_{1s}r_{2s}}} dl_s, \tag{10.35}$$

note 10) Specifically, the Green's function can be written as:

$$G^{2D}(\boldsymbol{r}, t) = -\frac{1}{2\pi} \frac{H\left(t - \frac{r}{c}\right)}{\sqrt{t^2 - \frac{r^2}{c^2}}}.$$

https://www.eri.u-tokyo.ac.jp/people/knishida/eng/seismology.html

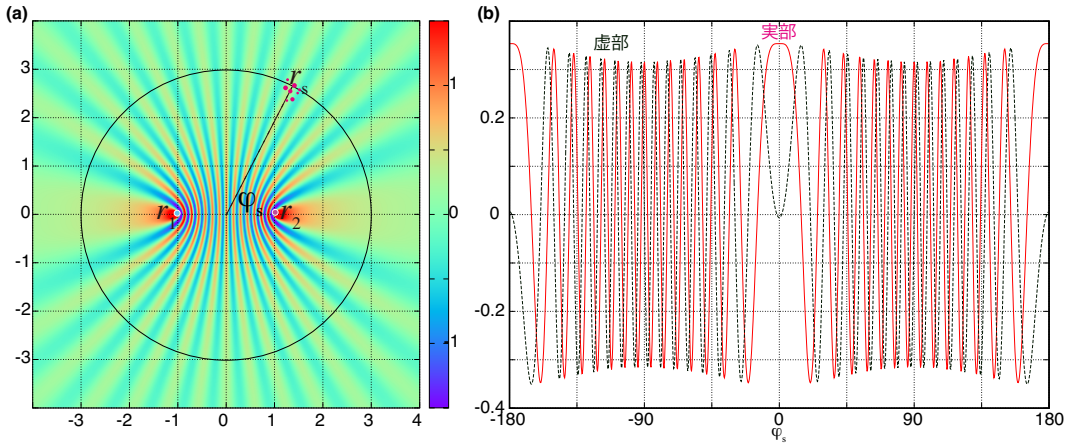

Figure 10.8: (a) Plot of the integrand with respect to ϕ_s at a fixed r_s. (b) Values along the circle at $r_s = 3$ (see Figure 10.8(a)).

where r_{1s} and r_{2s} are the distances between station 1 ($\boldsymbol{r}_1$), station 2 ($\boldsymbol{r}_2$), and the source $\boldsymbol{r}_s$, as shown in Figure 10.8. As seen in the equation, the phase difference at stations 1 and 2 for the wave radiated from the point source $\boldsymbol{r}_s$ is determined by the difference in distance divided by the wavelength. The curves of equal phase difference form hyperbolas with the observation points as foci. Thus, along the path passing through the two stations, the phase change is gradual (stationary point), while in other regions, it oscillates rapidly (Figure 10.8). When considering the problem of random excitation, the contribution from the sources along the path between the two observation points (called the stationary zone) becomes dominant, and the influence of sources in other regions cancels out (method of stationary phase, see e.g., Yomogida, 2007). Moreover, since the imaginary part is antisymmetric with respect to ϕ_s, it cancels out when the source distribution is uniform[note 11)].

Below, we try a slightly more intuitive explanation from a different perspective. As shown by the red dots in Figure 10.8, when random sources are distributed in a limited area, the wavefield observed far enough away can be represented by a superposition of multipoles (monopole, dipole, quadrupole, etc.) (known as multipole expansion). Let us consider the case where ϕ_s is around 70° as shown in the figure. In this case, the probability of a node falling between the two stations is random. Therefore, the probability that the waves from r_s are in-phase at the two stations is equal to the probability that they are out-of-phase. On the other hand, when ϕ_s is 0 or π (the case of the stationary zone), since the direction to the two stations is the same from the source's

In the frequency domain:

$$G^{2D}(\boldsymbol{r},\omega) = -\frac{i}{4}H_0^{(2)}(\omega r/c) \propto \frac{1}{\sqrt{kr}}e^{ikr-\pi/4},$$

where the wavenumber k is defined as $k \equiv \omega/c$, $H_0^{(2)}$ is the Hankel function of the second kind, and $H()$ is the Heaviside step function.

note 11) The rapidly oscillating property of the integrand is important. This is because even if the excitation sources are not uniformly distributed, the contribution from the stationary zone is expected to be dominant. The robustness of the cross-correlation waveform against the source distribution is a crucial point in data analysis.

perspective, the waves from r_s are always in-phase. In other words, only when the excitation sources are located in the stationary zone do they contribute to the cross-correlation waveform.

Problem 9.2

Although evaluated in the frequency domain above, let us consider it in the time domain to understand the shape of the cross-correlation waveform. Here we consider the situation as shown in the accompanying figure. The term written as $G^{2D*}(\boldsymbol{r}_1 - \boldsymbol{r}_s, \omega)G^{2D}(\boldsymbol{r}_2 - \boldsymbol{r}_s, \omega)$ in the frequency domain can be represented by a convolution integral of Green's functions in the time domain (by inverse Fourier transform).

1. Calculate the cross-correlation function when an external force is applied at the position shown in the figure.
2. Consider the case where the external forces are distributed on the circumference shown in the figure. Average the cross-correlation function calculated in (1) with respect to the angular direction, and evaluate the cross-correlation function. Note here that the contribution of the external forces inside the hyperbola in the figure is dominant.
3. Discuss the relationship between the time at which the cross-correlation function reaches its peak value and the distance between the observation points.

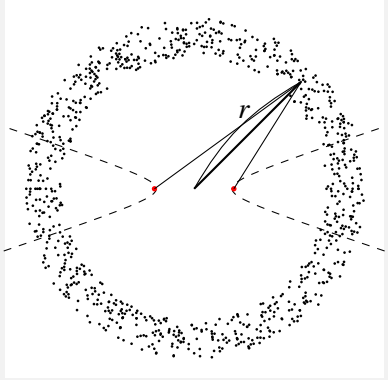

The contribution of the integral was roughly estimated above. Here, following Wapenaar and Fokkema (2006),[48] we consider it further by assuming that u satisfies the radiation boundary condition on l_s:

$$\frac{\partial u}{\partial n} = -iku. \tag{10.36}$$

Combining this with Rayleigh's reciprocity theorem, we can relate the cross-correlation function

and Green's function as follows[note 12)]:

$$\Phi_{12} = f_0^2 \int_{l_s} G^{2D*}(\boldsymbol{r}_1 - \boldsymbol{r}_s, \omega) G^{2D}(\boldsymbol{r}_2 - \boldsymbol{r}_s, \omega) dl_s, \tag{10.37}$$

$$\sim f_0^2 \frac{\rho c}{2i\omega} \left(G^{2D*}(\boldsymbol{r}_1 - \boldsymbol{r}_1, \omega) - G^{2D}(\boldsymbol{r}_1 - \boldsymbol{r}_2, \omega) \right). \tag{10.38}$$

This takes the form where the derivative of the cross-correlation function is proportional to the Green's function[note 13)].

An important point to note here is that attenuation is not considered, and because a radiation boundary condition is used, free-boundary surfaces such as surface reflections cannot be taken into account. Considering a realistic setting, it cannot be interpreted as the Green's function unless excitation sources are also distributed underground surrounding the region of interest. Therefore, for the actual cross-correlation function, the amplitude of body waves will be smaller compared to the Green's function (roughly speaking, an earthquake record). The problem of being unable to extract body waves well, especially surface reflections, can be avoided to some extent by using coda waves (e.g., Tonegawa et al., 2009[41]).

Problem 9.3

Run the web demo of seismic interferometry at http://www.eri.u-tokyo.ac.jp/knishida/Seismology/wave2Drandom2.html to observe the wave propagation and discuss its correspondence with the theory.

§10.5 Conditions for application of surface wave tomography

Let us consider the difference in ray geometry between ANT and earthquake surface wave tomography. In the case of regional-scale earthquake surface wave tomography with source-receiver paths, the target area is surrounded by earthquakes, which are limited along active tectonic areas (Figure 10.9 (a)). Because most ray paths travel across the area, the travel-time anomalies reflect the seismic structure along lines over the scale. Because the perturbations of the inferred phase/group velocity map strongly depend on the damping of the tomographic inversion, the absolute velocities tend to be ambiguous. Although the damping problem is common in

note 12) See Wapenaar and Fokkema (2006)[48] for details.

note 13) The spatial autocorrelation method (SPAC method) by Aki (1957) is discussed under the assumption that plane waves are incident randomly from afar. While the general framework is similar to the discussion in this chapter, the details differ. For example, based on the SPAC method for the 2-D case (see Nakahara, 2006), the Hilbert transform of the cross-correlation function yields the Green's function. This originates from the fact that the wave incident from afar differs from the Green's function and the plane wave $\exp(i(\omega t - \boldsymbol{k} \cdot \boldsymbol{x}))$.

ray theoretical inversion, including ANT, an initial local 1-D model for ANT constructed from multimode dispersion measurements using subarrays (see section **??**) can mitigate the ambiguity.

In contrast, in the case of ANT with a dense array, the distribution of the ray path is uniform (Figure 10.9(b)). Above 0.05 Hz, CCFs with longer separation distances (typically longer than 1000 km) become complex. Ray paths with separation distances shorter than 1000 km enable us to infer tomographic maps even in regions with strong lateral heterogeneities above 0.1 Hz. This situation is similar to earthquake tomography using the two-station method (e.g., [(9), (12),]), which measures the phase differences between seismograms for two stations on a common great-circle path. The drawbacks of the two-station method are (1) that it requires both stations to be located close to the common great circle path, which reduces the available ray paths, and (2) that the longer earthquake-receiver distance tends to cause the wave propagation to enter the regime of multiple scattering at a higher frequency (Figure **??**).

The shape of the sensitivity kernel is elliptical along the ray path, and the width at the midpoint is proportional to $\sqrt{\lambda r_{12}}$, where λ is the wavelength. Because the lengths of ray paths of earthquake data become longer in general, the widths become wider than those of ANT. The wider width tends to average the anomalies within the fat ray, and the averaging over a long distance makes restoring the small-scale image difficult.

(a) Earthquake surface wave tomography (b) ANT

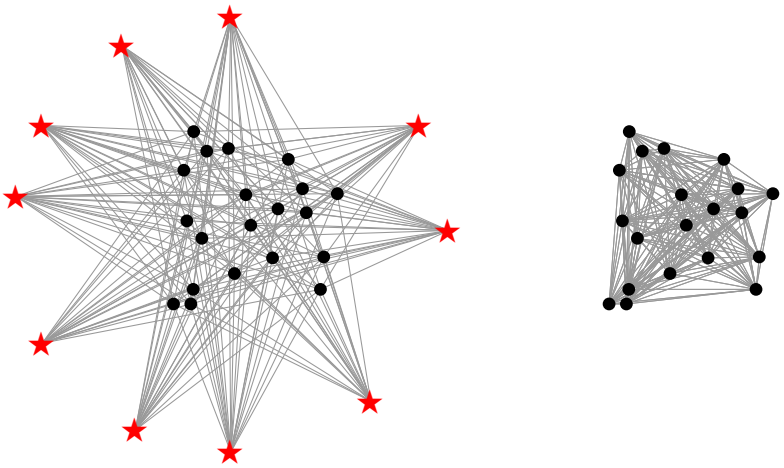

Figure 10.9: (a) A typical example of earthquake-receiver geometry for earthquakes. The gray lines show ray paths between the earthquakes and the stations. Red stars show the earthquakes, and black dots show stations. (b) A typical example of station geometry for ANT. The lines show ray paths between the station pairs.

The advantages of ANT are the homogeneous path distribution and the shorter ray paths. These features enable us to estimate phase/group velocity maps above 0.1 Hz.

Summary: pros and cons of cross-correlation of microseisms

- We can use information from short-distance paths.

- ○ Even at periods shorter than 0.05 Hz, it is less susceptible to scattering and attenuation effects.
- × If there is a bias in the distribution of excitation sources, apparent travel-time anomalies may occur.

Summary: pros and cons of Ambient noise tomography

- ○ The paths do not depend on the earthquake distribution, and there is less bias in the path density.
- ○ In the case of array observations, it is possible to estimate a good initial model (local 1-D structure).
- × If there is a bias in the distribution of excitation sources, apparent travel-time anomalies may occur. This is particularly serious when estimating azimuthal anisotropy or attenuation structure.

ToDO: Relationship between seismic interferometry using a spring-mass model and Brownian motion

§10.6 An application for seismic monitoring

In considering the dynamics of phenomena occurring inside the Earth, it is extremely important to capture temporal changes in velocity structure. This is because volcanic eruptions and earthquakes are expected to cause changes in stress and strain states, accompanied by changes in velocity structure and anisotropy.

When actually trying to determine temporal changes in underground structure, it is ideal to repeat seismic tomography using controlled sources. However, in many cases this is not realistic. On the other hand, when using natural earthquakes, uncertainties caused by the uncertainty of the source and the bias in the source distribution lead to uncertainties in the velocity structure. Therefore, even if a temporal change is apparently observed, it is unclear whether it is just noise or a true velocity change.

In contrast, seismic interferometry is a very effective method for detecting temporal changes in underground structure. This is because by calculating the cross-correlation function over divided periods, we can virtually observe repeating earthquakes. Let us consider the simplest example. We observe earthquakes at two points on the surface, and continuously monitor changes in the cross-correlation function of the records. In this case, localized structural changes between the two points can be monitored moment by moment. Although we will not discuss the details here, pioneering studies include Sens-Schönfelder and Wegler (2006) (Merapi volcano, Indonesia)[33] and Wegler and Sens-Schönfelder (2007) (analysis of the Chuetsu earthquake).[50]

§10.7 Practical problems when applying actual data

10.7.1 Azimuthal dependence of incident waves

To consider the azimuthal dependence of the incident wave amplitude, we consider Cox's equation[7]

$$\sum_{m=0}^{\infty} i^m J_m\left(\frac{\omega r}{c(\omega)}\right)\left[a_m(\omega)\cos(m\zeta) + b_m(\omega)\sin(m\zeta)\right] \tag{10.39}$$

In this case, the travel-time anomaly can be written as

$$\begin{aligned}\delta t &= \frac{B''(0)}{2t\omega^2 B(0)} \text{for the causal part} \\ &= \frac{B''(180)}{2t\omega^2 B(180)} \text{for the acausal part}\end{aligned} \tag{10.40}$$

(Weaver et al., 2009).[49] Using this equation, it is possible to correct the anisotropy of the incident wave.

10.7.2 Finite frequency effects

When applying seismic interferometry, it is not obvious whether it is sufficient to consider the same sensitivity kernel as for normal earthquakes.[45] It is known that when the excitation sources are isotropic and homogeneous, the sensitivity kernel of surface waves is the same as that of earthquakes,[26] but when the excitation sources are uneven, strict corrections are necessary.

§10.8 Bibliography

[1] K Aki and P G Richards. *Quantitative Seismology*, volume 2. W. H. Freeman, San Francisco, 1980.

[2] Keiiti Aki. Space and time spectra of stationary stochastic waves, with special reference to microseisms. *Bull. Earthq. Res. Inst.*, 35:415–457, 1957.

[3] D C Bowden, V C Tsai, and F C Lin. Site amplification, attenuation, and scattering from noise correlation amplitudes across a dense array in long beach, CA. *Geophys. Res. Lett.*, 42(5):1360–1367, March 2015.

[4] Herbert B Callen and Theodore A Welton. Irreversibility and generalized noise. *Phys. Rev.*, 83(1):34–40, July 1951.

[5] Michel Campillo and Anne Paul. Long-range correlations in the diffuse seismic coda. *Science*, 299(5606):547–549, January 2003.

[6] Jon F Claerbout. SYNTHESIS OF a LAYERED MEDIUM FROM ITS ACOUSTIC TRANSMISSION RESPONSE. *Geophysics*, 33(2):264–269, April 1968.

[7] Henry Cox. Spatial correlation in arbitrary noise fields with application to ambient sea noise. *J. Acoust. Soc. Am.*, 54(5):1289–1301, 1973.

[8] F A Dahlen and J Tromp. *Theoretical Global Seismology*. Princeton University Press, Princeton, 1998.

[9] A M Dziewonski and A L Hales. Numerical analysis of dispersed seismic waves. In Bruce A Bolt, editor, *Methods in Computational Physics: Advances in Research and Applications*, volume 11, pages 39–85. Elsevier, Amsterdam, January 1972.

[10] Y Fukao, K Nishida, N Suda, K Nawa, and N Kobayashi. A theory of the earth's background free oscillations. *J. Geophys. Res.*, 107(B9):2206, September 2002.

[11] Laurent Gizon, Aaron C Birch, and Henk C Spruit. Local helioseismology: Three-Dimensional imaging of the solar interior. *Annu. Rev. Astron. Astrophys.*, 48(1):289–338, August 2010.

[12] K Hamada and K Yoshizawa. Interstation phase speed and amplitude measurements of surface waves with nonlinear waveform fitting: Application to USArray. *Geophys. J. Int.*, 202(3):1463–1482, 2015.

[13] Matthew M Haney, T Dylan Mikesell, Kasper van Wijk, and Hisashi Nakahara. Extension of the spatial autocorrelation (SPAC) method to mixed-component correlations of surface waves. *Geophys. J. Int.*, 191(1):189–206, October 2012.

[14] Naoki Kobayashi and Kiwamu Nishida. Continuous excitation of planetary free oscillations by atmospheric disturbances. *Nature*, 395(September):357–360, 1998.

[15] Xin Liu and Yehuda Ben-Zion. Theoretical and numerical results on effects of attenuation on correlation functions of ambient seismic noise. *Geophys. J. Int.*, 194(3):1966–1983, September 2013.

[16] Xin Liu, Gregory C Beroza, Lei Yang, and William L Ellsworth. Ambient noise love wave attenuation tomography for the LASSIE array across the los angeles basin. *Sci Adv*, 7(22), May 2021.

[17] Oleg I Lobkis and Richard L Weaver. On the emergence of the green's function in the correlations of a diffuse field. *J. Acoust. Soc. Am.*, 110(6):3011, 2001.

[18] Fabrizio Magrini and Lapo Boschi. Surface-wave attenuation from seismic ambient noise: Numerical validation and application. *J. Geophys. Res.*, 126(1), January 2021.

[19] Hisashi Nakahara. A systematic study of theoretical relations between spatial correlation and green's function in one-, two- and three-dimensional random scalar wavefields. *Geophys. J. Int.*, 165(3):1097–1105, December 2006.

[20] Hisashi Nakahara, Kentaro Emoto, and Takeshi Nishimura. Extending the formulation of the spatial autocorrelation (SPAC) method to strain, rotation and tilt. *Geophys. J. Int.*, 227(1):287–302, June 2021.

[21] Nori Nakata, Lucia Gualtieri, and Andreas Fichtner. *Seismic Ambient Noise*. Cambridge University Press, March 2019.

[22] K Nishida. Ambient seismic wave field. *Proc. Jpn. Acad. Ser. B Phys. Biol. Sci.*, 93(7):423–448, 2017.

[23] K Nishida, H Kawakatsu, and K Obara. Three-dimensional crustal S wave velocity structure in japan using microseismic data recorded by hi-net tiltmeters. *J. Geophys. Res.*, 113(B10):B10302, October 2008.

[24] K. Nishida, N. Kobayashi, and Y. Fukao. Origin of earth's ground noise from 2 to 20 mhz. *Geophys. Res. Lett.*, 29(10):1413, May 2002.

[25] K Nishida, Jean-Paul Montagner, and Hitoshi Kawakatsu. Global surface wave tomography using seismic hum. *Science*, 326(5949):112, October 2009.

[26] Kiwamu Nishida. Two-dimensional sensitivity kernels for cross-correlation functions of background surface waves. *C. R. Geosci.*, 343(8-9):584–590, September 2011.

[27] H. Okada and N. Sakajiri. Estimation of subsurface structure using slightly long-period microtremors. *Geophysical Bulletin of Hokkaido University*, 42:119–143, October 1983.

[28] G a Prieto, J F Lawrence, and G C Beroza. Anelastic earth structure from the coherency of the ambient seismic field. *J. Geophys. Res.*, 114(B7):1–15, July 2009.

[29] Germán a Prieto, Marine Denolle, Jesse F Lawrence, and Gregory C Beroza. On amplitude information carried by the ambient seismic field. *C. R. Geosci.*, 343(8-9):600–614, September 2011.

[30] Philippe Roux and W A Kuperman. Extracting coherent wave fronts from acoustic ambient noise in the ocean. *J. Acoust. Soc. Am.*, 116(4):1995–2003, October 2004.

[31] H Sato, M C Fehler, and T Maeda. *Seismic wave propagation and scattering in the heterogeneous earth*. Springer, 2012.

[32] B.F. Schutz. *Geometrical Methods of Mathematical Physics*. Cambridge University Press, 1980.

[33] C Sens-Schönfelder and U Wegler. Passive image interferometry and seasonal variations of seismic velocities at merapi volcano, indonesia. *Geophys. Res. Lett.*, 33(21):L21302, November 2006.

[34] Nikolai M Shapiro, Michel Campillo, Laurent Stehly, and Michael H Ritzwoller. High-resolution surface-wave tomography from ambient seismic noise. *Science*, 307(5715):1615–1618, March 2005.

[35] R Snieder. Extracting the building response using seismic interferometry: Theory and application to the millikan library in pasadena, california. *Bull. Seismol. Soc. Am.*, 96(2):586–598, April 2006.

[36] Roel Snieder. Extracting the green's function from the correlation of coda waves: A derivation based on stationary phase. *Physical Review E*, 69(4):046610, April 2004.

[37] Roel Snieder and Eric Larose. Extracting earth's elastic wave response from noise measurements. *Annu. Rev. Earth Planet. Sci.*, 41(1):183–206, May 2013.

[38] Roel Snieder and Kees Wapenaar. Imaging with ambient noise. *Phys. Today*, 63(9):44–49, September 2010.

[39] Ryota Takagi, Hisashi Nakahara, Toshio Kono, and Tomomi Okada. Separating body and rayleigh waves with cross terms of the cross-correlation tensor of ambient noise. *J. Geophys. Res.*, 119(3):2005–2018, March 2014.

[40] Toshiro Tanimoto. Modelling curved surface wave paths: membrane surface wave synthetics. *Geophys. J. Int.*, 102:89–100, 1990.

[41] Takashi Tonegawa, Kiwamu Nishida, Toshiki Watanabe, and Katsuhiko Shiomi. Seismic interferometry of teleseicmic S -wave coda for retrieval of body waves: an application to the philippine sea slab underneath the japanese islands. *Geophys. J. Int.*, 178(3):1574–1586, September 2009.

[42] Jeroen Tromp and F A Dahlen. Variational principles for surface wave propagation on a laterally heterogeneous Earth—II. frequency-domain JWKB theory. *Geophys. J. Int.*, 109(3):599–619, June 1992.

[43] Jeroen Tromp and F a Dahlen. Variational principles for surface wave propagation on a laterally heterogeneous Earth-I. time-domain JWKB theory. *Geophys. J. Int.*, 109(3):581–598, June 1992.

[44] Jeroen Tromp and F a Dahlen. Variational principles for surface wave propagation on a laterally heterogeneous Earth-III. potential representation. *Geophys. J. Int.*, 112(2):195–209, February 1993.

[45] Jeroen Tromp, Yang Luo, Shravan Hanasoge, and Daniel Peter. Noise cross-correlation sensitivity kernels. *Geophys. J. Int.*, 183(2):791–819, November 2010.

[46] Victor C Tsai. Understanding the amplitudes of noise correlation measurements. *J. Geophys. Res.*, 116(B9):B09311, September 2011.

[47] Kees Wapenaar, Deyan Draganov, Roel Snieder, Xander Campman, and Arie Verdel. Tutorial on seismic interferometry: Part 1–basic principles and applications. *Geophysics*, 75(5):75A195, 2010.

[48] Kees Wapenaar and Jacob Fokkema. Green's function representations for seismic interferometry. *Geophysics*, 71(4):SI33, 2006.

[49] Richard Weaver, Berenice Froment, and Michel Campillo. On the correlation of non-isotropically distributed ballistic scalar diffuse waves. *J. Acoust. Soc. Am.*, 126(4):1817, October 2009.

[50] U Wegler, C Sens-Schönfelder, and C Sens-Schönfelder. Fault zone monitoring with passive image interferometry. *Geophys. J. Int.*, 168(3):1029–1033, March 2007.

[51] Alexandre Zagoskin. *Quantum Theory of Many-Body Systems*. Springer, New York, 2014.

Index